Transport Canada
Development

Transports Canada
Développement

TP 5958E

Analysis and Assessment of the Homopolar Linear Synchronous Motor for Urban Transit Applications

Summary Report

Prepared for
Transportation
Development Centre

Transport Canada

JULY 1984

Canada

CA2 OT
UQU 32
84
R023
c.2

CIGGT Project No. PRO-096

CIGGT Report No. 84-2
Transport Canada Report No. TP-5958E

SUMMARY

ANALYSIS AND ASSESSMENT OF THE HOMOPOLAR LINEAR SYNCHRONOUS MOTOR FOR URBAN TRANSIT APPLICATIONS

A.R. Eastham
G.E. Dawson
D.L. Atherton
S.B. Dewan
G.R. Slemon
R. Ong
W.J. Ballantyne
L.W. Coathup

This study was conducted by CIGGT for the
Transportation Development Centre of
Transport Canada under Contract No. OSD-82-00047

Canadian Institute of Guided Ground Transport
Queen's University at Kingston, Ontario
K7L 3N6

July 1984

Library and Information Centre
Centre de Documentation (GSL)
RECEIVED – REÇU LE
JUL 25 1985
Government Publication Officielle
Transport Canada / Transports Canada

This report resulted from research conducted through the Canadian Institute of Guided Ground Transport. The report represents the views of the authors and does not necessarily have the endorsement of the University or the other participating organizations.

Ce rapport est également disponible en français.

REPORT DOCUMENTATION FORM

1. Transport Canada Report No	2. TDC Project No	3. Recipient's Catalogue No.
TP 5958E	4603	

4. Title and Subtitle	5. Report Date
ANALYSIS AND ASSESSMENT OF THE HOMOPOLAR LINEAR SYNCHRONOUS MOTOR FOR URBAN TRANSIT APPLICATIONS Summary Report	July 1984
	6. Performing Organization Report No. 84-2
7. Author(s) A.R. Eastham, G.E. Dawson, D.L. Atherton, S.B. Dewan, G.R. Slemon, R. Ong, W.J. Ballantyne, L.W. Coathup	8. Transport Canada File No. D1465-288-2
9. Performing Organization Name and Address Canadian Institute of Guided Ground Transport (CIGGT) c/o Queen's University Kingston, Ontario K7L 3N6	10. DSS File No. 10DS.T8200-2-2501
	11. DSS or Transport Canada Contract No. OSD-82-00047
12. Sponsoring Agency Name and Address Transportation Development Centre (TDC) Suite 2421, 1000 Sherbrooke Street West Montreal, Quebec H3A 2R3	13. Type of Report and Period Covered Summary, July/82-June/84
	14. Sponsoring Agency Code
15. Supplementary Notes Summary of "Analysis and Assessment of the Homopolar Linear Synchronous Motor for Urban Transit Applications," TP 5957E (CIGGT Report No. 84-2)	16. TDC Project Officer M. Audette, M. Denis C.A. Versailles

17. Abstract

The homopolar linear synchronous motor (HLSM) is a machine which has the three-phase armature and the dc excitation on the same side of the airgap. The track is a coarsely slotted passive steel structure. The modulation of the dc field, produced by this track saliency, along the length of the machine locks into the travelling magnetic wave produced by three-phase ac excitation of the armature winding. Speed of the machine is controlled by armature excitation frequency. The objectives of this project were to evaluate the HLSM as (i) an alternative to the linear induction motor (LIM) for urban transit, and (ii) a machine capable of providing both suspension and propulsion/braking for transportation vehicles. Computer-aided design studies, using finite element analysis with saturable steel characteristics included, were conducted to determine the electromagnetic field distribution in the HLSM and to evaluate the parameters in a two-reactance equivalent circuit model of the machines for performance computation. It has been shown that the HLSM can be designed to meet the performance specifications for an urban transit vehicle and can operate at a high power factor/efficiency product, typically of 0.9 or higher. This leads to low kVA power-conditioner requirements and to excellent energy efficiency. However, the HLSM is considerably larger, two to three times heavier, and has a much higher normal force than a LIM of equivalent performance. While the HLSM is not attractive as a drive for urban transit vehicles, its high normal force makes it feasible for integrated suspension/propulsion applcations. The HLSM is therefore of interest for passive guideway Maglev vehicles.

18. Key Words	19. Distribution Statement
Homopolar linear synchronous motor; Urban transit drives and control; Finite element analysis; Energy management and drive efficiency; Integrated suspension/propulsion system	Available from TDC

20. Security Classification (of this report)	21. Security Classification (of this page)	22. No. of Pages	23. Price
unclassified	unclassified	26	

TDC CDT 79-005

FORMULE DE DOCUMENTATION POUR RAPPORT

1 Nº du rapport Transports Canada	2 Nº de l'étude — CDT	3 Nº de catalogue du destinataire
TP 5958E	4603	

4 Titre et sous-titre	5 Date du rapport
ANALYSIS AND ASSESSMENT OF THE HOMOPOLAR LINEAR SYNCHRONOUS MOTOR FOR URBAN TRANSIT APPLICATIONS Rapport Sommaire	juillet 1984
	6 Nº du rapport de l'organisme exécutant 84-2
7 Auteur(s) A.R. Eastham, G.E. Dawson, D.L. Atherton, S.B. Dewan, G.R. Slemon, R. Ong, W.J. Ballantyne, L.W. Coathup	8 Nº de dossier Transports Canada D1465-288-2
9 Nom et adresse de l'organisme exécutant Canadian Institute of Guided Ground Transport (CIGGT) Queen's Unversity Kingston, Ontario K7L 3N6	10 Nº de dossier — ASC 10DS.T8200-2-2501
	11 Nº de contrat — ASC ou Transports Canada OSD-82-00047
12 Nom et adresse de l'organisme parrain Centre de developpement des transports (CDT) 1000 o., rue Sherbrooke, Suite 2421 Montréal, Québec H3A 2R3	13 Genre de rapport et période visée Sommaire, Juil/82-Juin/84
	14 Code de l'organisme parrain
15 Remarques additionnelles Sommaire de "Analysis and Assessment of the Homopolar Linear Synchronous Motor for Urban Transit Applications," TP 5957E (CIGGT Report Nº 84-2)	16 Agent de projet — CDT M. Audette, M. Danis, C.A. Versailles

17 Resumé

Le moteur linéaire synchrone homopolaire est une machine triphasée dont l'induit et la source de courant continu d'excitation se trouvent du même côté de l'entrefer. Les rails, en acier et rainurés, constituent une structure passive. La modulation du champ continu introduite par la géometrie de la voie le long de l'axe longitudinal de la machine se retrouve dans l'onde magnétique progressive produite par l'excitation des enroulements d'induit par un courant alternatif triphasé. La vitesse de la machine est commandée par la fréquence du courant d'excitation. Le présent projet avait pour objectifs d'évaluer ce type de moteur (i) comme solution de remplacement au moteur linéaire d'induction pour le transport urbain et (ii) en tant que machine capable d'assurer la sustentation, la propulsion et le freinage d'un véhicule de transport urbain. Nous avons effectué des études de conception assistée par ordinateur fondées sur la méthode des éléments finis en vue de déterminer la distribution du champ électromagnétique dans le cas du moteur linéaire synchrone homopolaire et d'évaluer les paramètres d'un circuit à deux réactances équivalent à ce dernier pour en déterminer le comportement. Il a été démontré qu'il est possible de concevoir des moteurs linéaires synchrones homopolaires qui répondent aux exigences de rendement imposées aux véhicles de transport urbain et dont la valeur du produit facteur de puissance/rendement soit assez élevée, de 0,9 ou plus dans un cas type. On parvient ainsi à obtenir des moteurs qui nécessitent un inverseur de faible capacité et qui possèdent un excellent rendement énergétique. Toutefois, le moteur linéaire synchrone homopolaire est beaucoup plus encombrant, de deux à trois fois plus lourd et développe une force normale beaucoup plus élevée qu'un moteur linéaire d'induction de rendement équivalent. Bien qu'il ne soit par intéressant pour la propulsion des véhicules et transport urbain, le moteur linéaire synchrone homopolaire, grâce à sa force normale élevée, peut être exploité dans le cadre des systèmes intégrés de propulsion et de sustentation. Ce type de moteur présente donc un certain intérêt pour les véhicules à sustentation magnétique à voie passive.

18 Mots-clés	19 Diffusion
Moteur linéaire synchrone homopolaire; Moteurs et commandes pour véhicules de transport urbain; Méthode des éléments finis; gestion de l'énergie et rendement; Systèmes de propulsion et de sustentation intégrés	Disponible sur présentation d'une demand à CDT

20 Classification de securite (de ce rapport)	21 Classification de securite (de cette page)	22 Nombre de pages	23 Prix
sans cote	sans Cote	26	

CDT TDC 79-005

LIST OF TABLES

1. HLSM Specifications and Guidelines 4

2. Relative Features of HLSM and LIM 14

LIST OF FIGURES

1. (a) The HLSM configuration, with staggered-pole track and diamond-shaped armature windings
(b) A vehicle concept using HLSMs for integrated suspension and propulsion 3

2. The two-reactance, equivalent-circuit model of the HLSM 5

3. Finite element plots of the excitation field distribution in the HLSM, in:
(a) a polar transverse half section
(b) a longitudinal wavelength 7

4. The open circuit characteristics of the University of Toronto experimental machine at 10 mm gap; test results, finite element computations, and analysis based on the fundamental component of the air gap performance function . . . 8

5. Flux distribution due to armature mmf in the d-axis and the q-axis of the developed model of the staggered-pole HLSM:
(a) a sketch of the flux distribution showing diagonal yoke flux for the d-axis mmf only
(b) finite element plots of the flux distribution in one pole pitch of the machine 10

6. Armature current, complex power, and $\eta \cos \phi$ as a function of speed at full thrust specification for the HLSM design detailed in Appendix A 12

7. Thrust control of the HLSM:
(a) the current angle versus speed algorithm
(b) schematic of possible control scheme 13

TABLE OF CONTENTS

1. INTRODUCTION 1

2. HLSM CONFIGURATION 2

3. DESIGN SPECIFICATIONS AND GUIDELINES 2

4. MODELLING OF THE HLSM 4
   4.1 Equivalent Circuit 4
   4.2 Field Distributions 5
      4.2.1 Field Excitation 5
      4.2.2 d- and q-Axis Reactances 9

5. DESIGN STUDIES, PERFORMANCE AND CONTROL 11
   5.1 Urban Transit Drive 11
   5.2 Comparison with LIM 12
   5.3 Integrated Suspension and Propulsion 15

6. CONCLUSIONS 16

REFERENCES 17

Appendix A: DESIGN OF THE HLSM FOR URBAN TRANSIT PROPULSION

1. INTRODUCTION

Linear electric drives provide guided vehicles with a reliable level of propulsive or braking thrust. Such drives are essential for non-contact vehicles with primary magnetic or air cushion suspension, and are desirable for short-headway, wheeled vehicles when guideway or rail conditions are such that adhesion cannot be guaranteed. The linear induction motor (LIM) has been considered for many vehicles, and has found its main application in low-speed urban transit systems, such as the Birmingham Maglev People Mover, and the Urban Transportation Development Corporation's (UTDC) intermediate-capacity transit system (ICTS).[1]

As is well known, the main disadvantage of the LIM is its low power factor/efficiency product. UTDC's LIM operates with an $\eta \cos \phi$ of 0.40 to 0.42. This is reflected in the capacity of the inverter -- a 325 kVA unit is required for a LIM of nominal rating 120 kW. This disadvantage of the LIM has stimulated researchers to examine linear counterparts of the synchronous motor, which can achieve a high power factor through excitation control. Iron-cored heteropolar linear synchronous drives are used for both the low-speed M-BAHN[2] and the high-speed TRANSRAPID[3] systems in West Germany. An air-cored heteropolar linear synchronous drive has been developed for the JNR high-speed Maglev vehicle,[4] and is also proposed for the Canadian Maglev system.[5]

These heteropolar drives incorporate "long stators" - active guideway windings to which three-phase currents of variable frequency and amplitude are fed to control the speed and thrust of a vehicle. The homopolar configuration of the LSM was conceived as a means of replacing these long stator windings with a passive salient structure in the track. Under contract to the Transportation Development Centre of Transport Canada, we have conducted detailed computer-aided design studies, using the finite element method with non-linear magnetization characteristics, to evaluate the potential of the homopolar linear synchronous motor (HLSM).

In our examination of the HLSM, it was noted that the normal force between the vehicle-borne component and the passive track is substantial, and typically 6 to 10 times the available thrust. It becomes

feasible, therefore, to consider using the machine as an integrated suspension/propulsion system (ISPS), as proposed by Boldea.[6] We have used our design studies to evaluate the potential and control requirements of the HLSM, both as an urban transit drive and as an ISPS.

2. HLSM CONFIGURATION

The HLSM can have one of two basic configurations;[7]

- staggered pole track, with diamond shaped armature windings
- transverse bar track, with figure-of-eight shaped armature windings

The first design, as shown in Figure 1(a), was considered the most appropriate for transit and ISPS applications for two reasons:

- the salient ferromagnetic structure can be prefabricated in sections to the required tolerance and can be mounted more simply to the guideway structure
- the armature coils are of conventional diamond-shaped design, allowing the magnitude of the central gap between the two active sides of the motor to be selected from field considerations rather than from coil geometry limitations.

For wheeled transit, the staggered pole track would replace the centrally mounted reaction rail of a single-sided LIM drive. For ISPS applications, two staggered pole "rails" would be mounted to the underside of the guideway structure, as indicated in Figure 1(b).

3. DESIGN SPECIFICATIONS AND GUIDELINES

The HLSM design studies were conducted for a typical transit vehicle, units of which could form four- or six-car trains, dependent on required system throughput. For propulsion-only and ISPS applications, a consistent set of specifications and guidelines was defined, as given in Table 1. The allowable current densities were based on a thermal analysis and on experience with the operation of UTDC's ICTS LIM.[1]

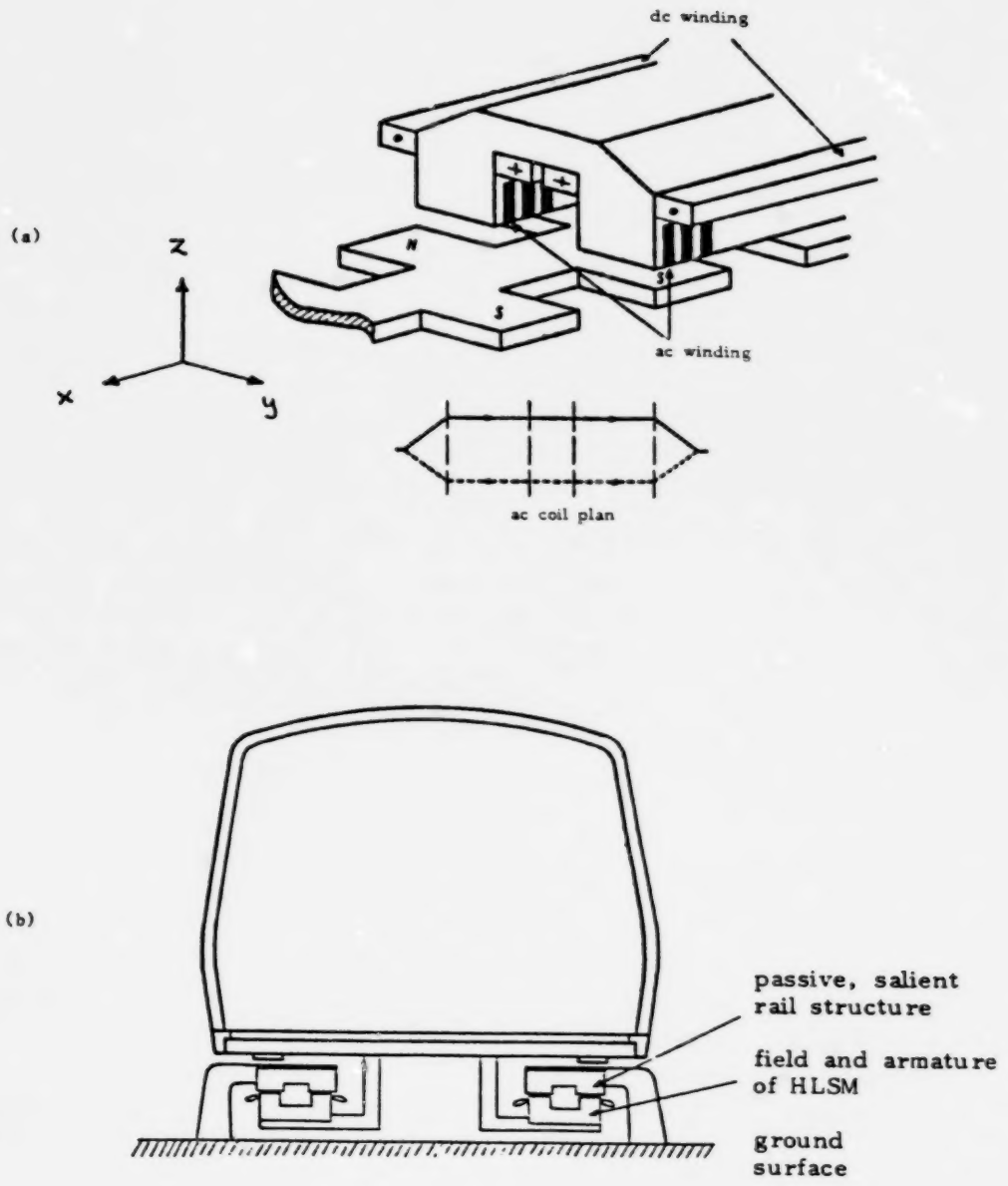

Figure 1 (a) The HLSM configuration, with staggered-pole track and diamond-shaped armature windings
(b) A vehicle concept using HLSMs for integrated suspension and propulsion

TABLE 1

HLSM SPECIFICATIONS AND GUIDELINES

Vehicle capacity	75 passengers
Mass (fully loaded, but without motors)	18,300 kg
Cruising speed	22 m/sec
Number of HLSMs per car: - propulsion only	2
- ISPS	4
Peak thrust per car: - motoring	26 kN
- braking	28 kN
Available power supply voltage	600 V d.c.
Nominal (polar) clearance	12 mm
Allowable current densities;	
Field coil	4 A/mm2
Armature coils: - under maximum thrust	7.5 A/mm2
- rms over duty cycle	5.0 A/mm2

4. MODELLING OF THE HLSM

4.1 Equivalent Circuit

The performance characteristics of the HLSM were computed from a conventional, salient-pole, two-reactance-equivalent circuit model of the machine, as shown in Figure 2. Armature resistance was calculated from winding geometry. Armature leakage reactance was determined by summing the conventional machine components of slot, tooth tip, end winding, and harmonic leakage, with an additional component due to the central crossover portion of armature winding. The latter was computed from the voltage induced per unit width of an iron-free section of armature winding. The d- and q-axis armature reactances and the induced voltage were computed from the field distribution determined by finite element analysis, as described below.

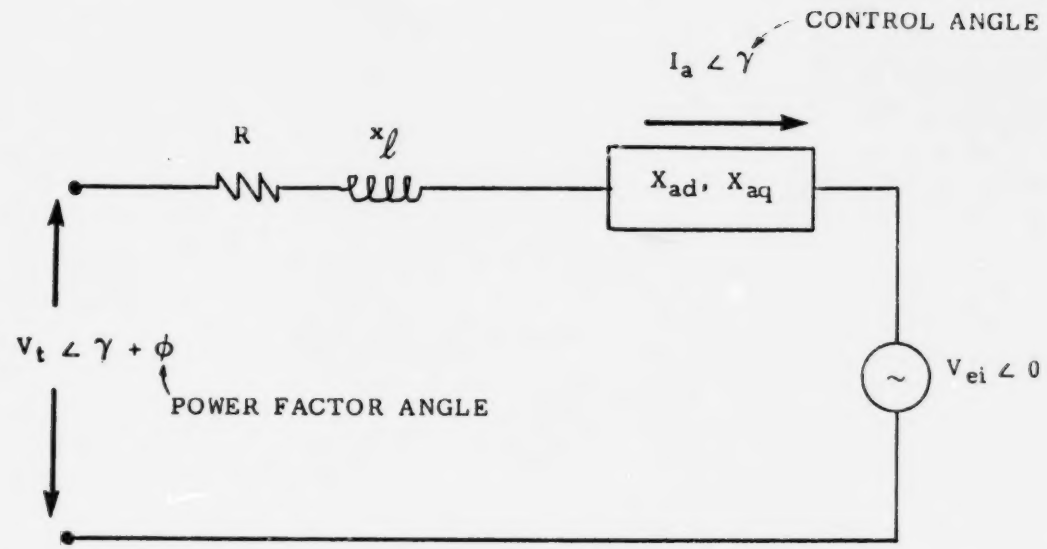

Figure 2 The two-reactance, equivalent-circuit model of the HLSM

4.2 Field Distributions

It is recognized that the armature and excitation field distributions in the staggered pole HLSM are not confined to either longitudinal or transverse sections of the machine. We have used a two-dimensional magnetostatic finite element program to determine the field in various sections of the machine such that the three-dimensional distribution can be evaluated to good accuracy. The finite element computations included non-linear magnetization characteristics for the yoke and track (cast steel) and for the armature laminations (silicon steel).

4.2.1 Field Excitation

The voltage, V_{ei}, was computed as the fundamental component of the voltage induced in the armature winding by the modulation of the excitation field produced by track saliency. The field modulation was evaluated by first considering a transverse half-section of the HLSM, as shown in Figure 3(a). To determine the total excitation flux per armature wavelength, the air gap in Figure 3(a) was set to be:

$$g_{effective} = G * C * g \qquad (4.2)*$$

* Equation numbers in main report.

where: g is the minimum (polar) air gap of the HLSM

C is Carter's coefficient, representing the effective gap increase due to armature slotting

G is Green's coefficient, representing the effective gap increase due to the coarse track saliency.

The applicability of both Carter's and Green's coefficients to the geometry of the HLSM was checked by finite element computations. For both air gap coefficients, the agreement between the analytical expressions and finite element results was within 5 per cent.

One wavelength of the longitudinal section of the machine was then considered, as shown in Figure 3(b). This section includes the actual polar air gap, the armature slot structure, and the track saliency; the depth of the interpolar region being selected, by finite element computations, to provide the same reluctance as the actual interpolar geometry of the HLSM. The vector potential boundary conditions of the longitudinal section were adjusted to introduce the same total flux per wavelength as was found from the transverse section. The saliency of the track now distributes this flux to produce a modulation of the air gap field.

The transverse field distribution in the polar and interpolar regions and the longitudinal field distribution allowed the total flux linkage in the armature winding to be determined as a function of position. The induced voltage is given by:

$$V_{ei} = 2\sqrt{2}\,\pi f\, N k_w\, \phi_{1max} \qquad (4.1)$$

where: f is the supply frequency,

N is the number of armature turns/phase,

k_w is the winding factor,

ϕ_{1max} is the amplitude of the fundamental flux per pole.

The finite element method for determining induced voltage was validated by comparison with data obtained by Slemon[8] on a three-pole test HLSM. The open-circuit characteristics from numerical analysis and

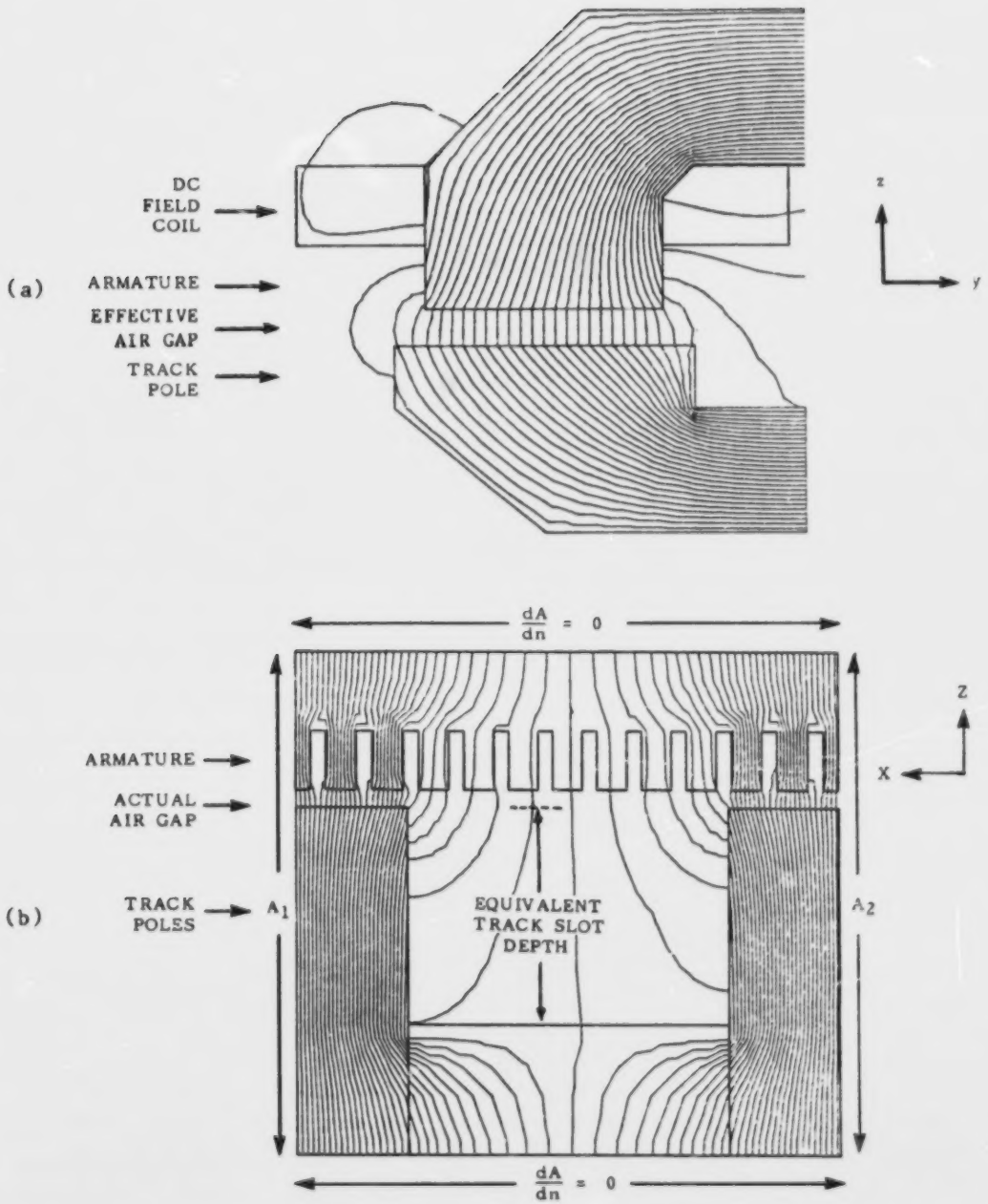

Figure 3 Finite element plots of the excitation field distribution in the HLSM, in:
(a) a polar transverse half section
(b) a longitudinal wavelength

test results are shown in Figure 4. The discrepancy in the saturated region is considered to be due to an uncertainty in the magnetization characteristics of the steels used in the test machine. Below saturation, agreement is good, indicating the usefulness of the finite element technique in HLSM analysis and design studies.

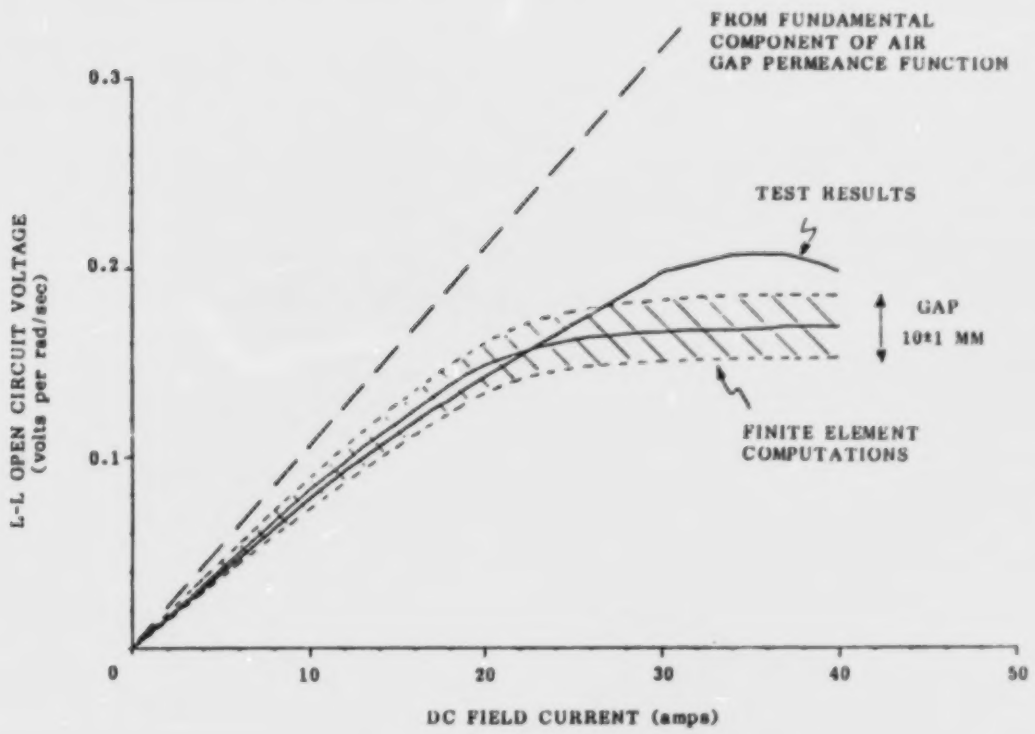

Figure 4 The open circuit characteristics of the University of Toronto experimental machine[8] at 10 mm gap; test results, finite element computations, and analysis based on the fundamental component of the air gap permeance function.[9]

For comparison, the open circuit characteristic determined from equation (2), but using the fundamental component of the flux modulation based on an ideal air gap permeance function[9] is also shown in Figure 4. It is apparent that the shape and reluctance of the magnetic circuit must be taken into account in evaluating the capabilities of the HLSM.

The normal force may also be evaluated from the known excitation field distribution, as:

$$F_z = \int \frac{B_z^2}{2\mu_o} \, dA \qquad \text{over the surface area of the armature} \qquad (9.1)$$

4.2.2 d- and q-Axis Reactances

Consideration of the armature flux distribution in the HLSM reveals that the field is not, in general, restricted to longitudinal paths but that significant flux can cross diagonally over the yoke of the machine. This flux path cannot be represented in the section of Figure 3(a), and was modelled in a manner similar to that used by Baudon.[10] Conceptually, the yoke is cut longitudinally and the entire machine is folded down to yield the two-dimensional geometry shown in Figure 5.

Typical flux paths are shown for armature mmf in the d-axis and in the q-axis of the machine. The q-axis distribution consists of strong loops of field in the polar regions and weaker loops in the interpolar regions. No flux crosses the yoke and track. However, with armature mmf in the d-axis, it is energetically favourable for significant flux to cross the yoke and track diagonally. This flux crosses two small air gaps, rather than one small and one large gap if restricted to a longitudinal path.

For finite element computation, one wavelength of the machine was discretized, and the results for the d- and q-axis conditions are also shown in Figure 5. The required boundary condition of zero normal component of flux (because of field symmetry) was established by assigning a very low relative permeability (0.0001) to two thin boundary regions. This had the effect of introducing a "magnetic insulator." The return path for the diagonal flux was provided by the outer regions of very high relative permeability (900,000), simulating a magnetic "short circuit."

Having determined the armature field distributions, the d- and q-axis inductances can be computed from the fundamental components of armature flux linkage per pole:

(a)

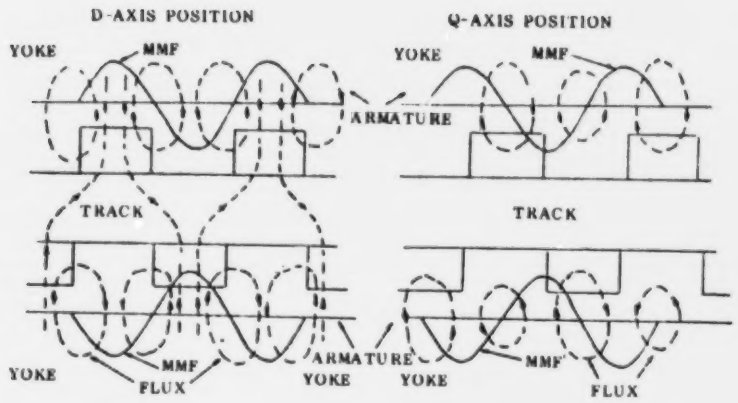

(b)

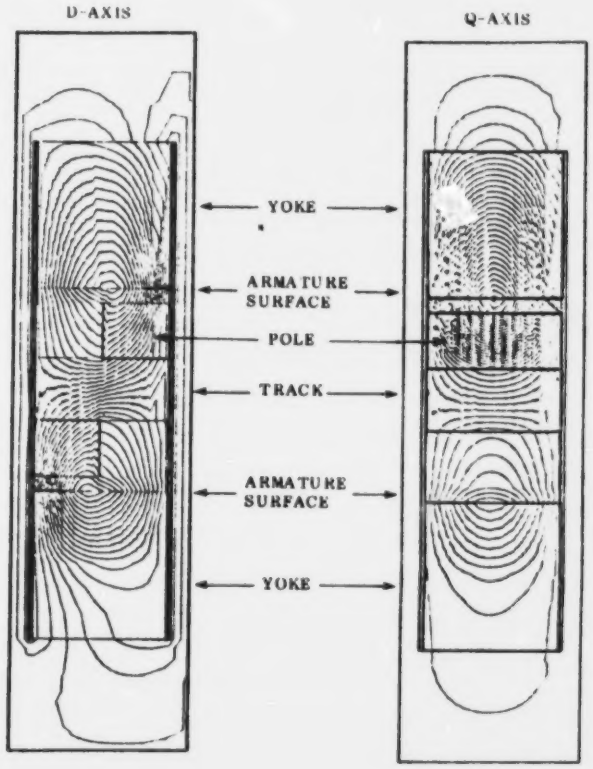

Figure 5 Flux distribution due to armature mmf in the d-axis and the q-axis of the developed model of the staggered-pole HLSM:
(a) a sketch of the flux distribution showing diagonal yoke flux for the d-axis mmf only
(b) finite element plots of the flux distribution in one pole pitch of the machine.

$$L_{d,q} = 2 \Phi_{d,q} N k_w / I_a \qquad (4.5)$$

In contradiction with analytical expressions based on Fourier analysis of an idealized armature field distribution, often quoted in the literature (e.g.[9]), the finite element technique predicts $x_{aq} > x_{ad}$ for the HLSM, as found experimentally by Balchin and Eastham.[10] This is believed to be a result of the characteristic saliency of the homopolar machine -- each side of the HLSM has one track pole every wavelength rather than every pole pitch as in a conventional synchronous or reluctance machine. An uncertainty remained in the evaluation of x_{ad} and x_{aq}. However, it was shown by sensitivity analysis that the ability of the HLSM to meet performance specifications was insensitive to applicable changes in these parameters.

5. DESIGN STUDIES, PERFORMANCE AND CONTROL

Iterative design studies were conducted to identify machines for propulsion-only and for ISPS applications which best meet the specifications and guidelines given in Table 1. The finite element technique was used for magnetic circuit design and to evaluate V_{ei}, x_{ad} and x_{aq}. Mechanical performance and terminal characteristics were then determined from conventional equivalent circuit expressions.

5.1 Urban Transit Drive

The design of the machine considered to be best suited as an urban transit drive is detailed in Appendix A. In order to achieve the objective of high $\eta \cos \phi$, it was necessary to design a strong field-weak armature machine, with a tooth/slot width ratio of 2. Some performance characteristics are given in Figure 6. For brevity, only the propulsion characteristics under full thrust requirements are shown. Armature current, complex power and $\eta \cos \phi$ are shown as a function of speed for full field excitation of 24 kAt. In braking, the maximum armature current is 265 A, and the complex power reaches 185 kVA.

A variable-voltage variable-frequency inverter is required for speed control. A power transistorized or GTO voltage source unit seems most appropriate, and must be controlled to make the current waveform close to sinusoidal, particularly at low speed, to minimize thrust harmonics.

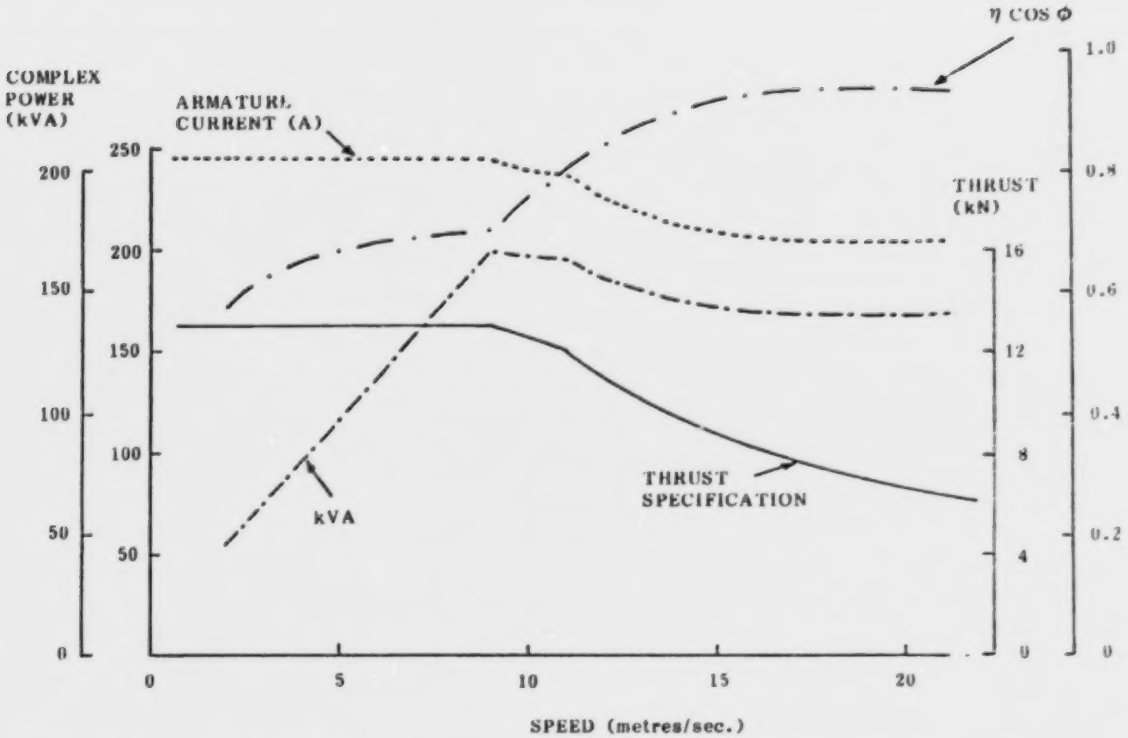

Figure 6 Armature current, complex power, and $\eta \cos \phi$ as a function of speed at full thrust specification for the HLSM design detailed in Appendix A.

In order to minimize both armature heating and energy drawn from the power rails (600 V d.c.), an appropriate objective for the control system is to drive the vehicle over a specified speed/distance profile at minimum armature current. This can be achieved by controlling the angle of the armature mmf with respect to the q-axis of the motor, as detected by track pole reluctance or proximity sensors. Optimum current angle versus speed characteristics in motoring and in braking provide appropriate control algorithms, and can be identified from computations based on the equivalent circuit parameters of the HLSM, as shown in Figure 7(a). A possible control scheme for an urban transit HLSM is then shown in simplified block diagram form in Figure 7(b).

5.2 Comparison with LIM

A detailed comparison of the design features of the HLSM with a LIM of comparable performance (UTDC's ICTS LIM[1]) is given in Appendix A.

(a)

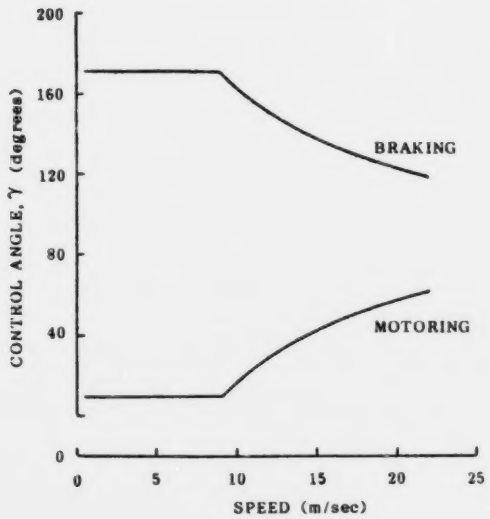

(b)

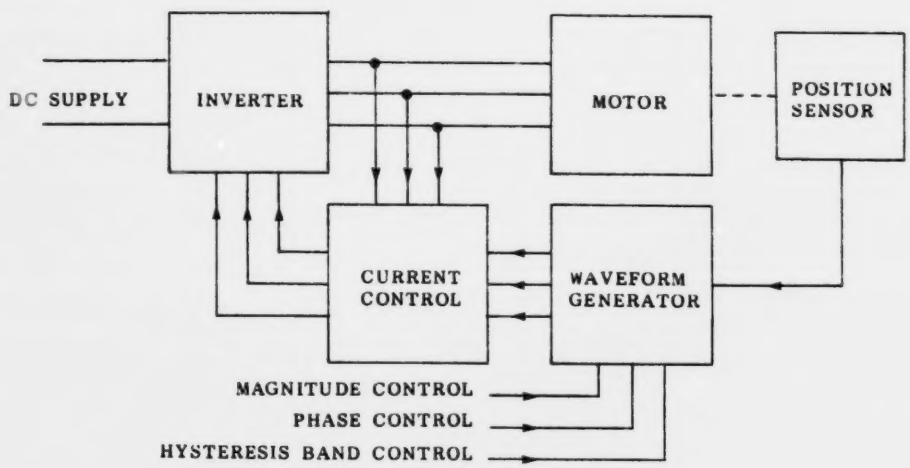

Figure 7 Thrust control of the HLSM:
(a) the current angle versus speed algorithm
(b) schematic of possible control scheme

A comparison of the general characteristics of the two machines is given in Table 2. It is apparent that the HLSM is larger, heavier, requires a deeper guideway component and has a considerably higher normal force than the LIM. The HLSM, however, operates at a much higher power factor efficiency product, and therefore requires an inverter of lower capacity.

TABLE 2

RELATIVE FEATURES OF HLSM AND LIM

	HLSM	LIM
Motor size	2.35 m long x 0.65 m wide x 0.18 m high	1.90 m long x 0.52 m wide x 0.10 m high
Mass of electromagnetic components of motor	1410 kg	422 kg
Depth of guideway component	8 cm	3 cm
Maximum normal force	90 kN	25 kN
Power factor x efficiency (above 15 m/sec)	typically 0.8*	typically 0.4*
Inverter capacity	200 kVA	325 kVA
Energy drawn by four-car train per km of corridor	5.4 kWh/km**	9.6 kWh/km**
Peak power demand of four-car train	1,260 kW	1,580 kW

* Includes losses in field coils
** Assumes full regenerative receptivity in the power line.

The effect of the latter characteristic has been quantified by means of an energy management model in which a transit vehicle can be run over a modelled corridor to evaluate its mechanical and electrical performance. LIM- and HLSM-propelled vehicles were simulated over a 21 km corridor with fifteen stations at varying separations, with a dwell time at each of 20 secs. Grades were included with a maximum of 6 per cent. The mass differential (one tonne per motor) between the HLSM and

the LIM was included. Maximum acceleration of 1.27 m/sec^2 and deceleration of 1.00 m/sec^2 were used. The corresponding energy drawn from a 600 V d.c. line (taking into account converter efficiencies) per km of corridor, and the peak power demand of a typical four-car train are given in Table 2.

In spite of the attractive energy and power characteristics of an HLSM drive, the increased size, mass and normal force would pose serious problems for urban transit. The addition of almost one tonne of unsprung mass to each axle would have major implications in truck dynamics. This, together with the high vertical force, would impose unacceptable penalties on the trackwork and vehicle. It must, therefore, be concluded that the HLSM, as a propulsion-only unit, is not viable for urban transit applications.

5.3 Integrated Suspension and Propulsion

The above design studies resulted in an HLSM which had a thrust capability of 13 kN and which produced a normal force of 93 kN, for a potential lift/thrust ratio of 7.1. In a controlled electromagnetic suspension mode (see Figure 1(b)), this HLSM would have a lift/weight ratio of 6.7, could support a payload of 8000 kg, and could provide a vehicle with an acceleration of up to 0.14 g (1.42 m/sec^2). It is feasible, therefore, to consider using the HLSM as an integrated suspension/propulsion system (ISPS), as proposed by Boldea.[6]

In the simulation of the propulsion-only HLSM over a typical transit corridor it was apparent that the machine should be operated at close to full field flux to achieve optimum performance. Under low thrust cruise conditions, it was desirable to reduce the field excitation by no more than 20 per cent. In the ISPS mode, it would be necessary to maintain constant field flux and to dynamically control the excitation in response to variations in the air gap. Performance evaluation, using the equivalent circuit model, has shown that this mode of operation produces very little degradation in the electrical characteristics of the HLSM under thrust control.

It is apparent, therefore, that independent normal force and thrust control is possible with the HLSM. Chopper control of the field excitation, with feedback from gap sensors and accelerometers, can be

used to maintain a stable electromagnetic suspension. To achieve optimum electrical characteristics, control angle versus speed characteristics (similar to those of Figure 7(a)) can be defined, and thrust can be controlled simply by adjusting the magnitude of the armature current at the specified speed dependent current angle, γ.

In practise, the two centrally-mounted, eleven-pole HLSMs of an urban transit drive would be replaced by four corner-mounted, six-pole HLSMs for ISPS operation. Most of the design features of the HLSMs could remain unchanged from those given in Appendix A. The only significant change would be a doubling of the armature conductors per slot from 8 to 16 and a halving of the armature current to keep the impedance of the machine compatible with the available power supply (up to 230 V/phase from a 600 V d.c. line).

6. CONCLUSIONS

The computer-aided design studies reported here have allowed the HLSM to be compared with the LIM as a non-contact urban transit drive. The basic trade-offs are apparent. The HLSM can be operated at high $\eta \cos \phi$, resulting in an appreciable saving in inverter capacity over the LIM. As a consequence, some savings in operating costs, in terms of lower energy/km and lower peak power demand, can be achieved with the HLSM. However, this machine is much larger and heavier. It requires a deeper guideway component, and its normal force exceeds that of a LIM by a factor 3-4. These latter factors make it evident that the HLSM cannot be considered a viable urban transit drive.

As an integrated suspension/propulsion system (ISPS), the high normal force would be used for vehicle suspension in a controlled electromagnetic mode. The thrust/braking force could then be controlled, at high $\eta \cos \phi$, independent of the suspension force. Unlike the TRANSRAPID and M-BAHN drives, the HLSM ISPS uses an inexpensive passive salient guideway structure, but requires propulsion power transfer to the vehicle. While the ROMAG (now MAGTRANSIT) LIM ISPS also has a passive guideway, the HLSM operates at higher $\eta \cos \phi$ and requires a power conditioner of lower capacity and mass, resulting in savings in capital and operating costs.

It appears that the application most suited to the characteristics of the HLSM is integrated suspension/propulsion. In this mode of operation, the HLSM offers ease of control and high energy efficiency -- it merits detailed evaluation in comparison with other ISPS designs for both intercity and urban transportation.

REFERENCES

1. BALLANTYNE, W.J. "LIM Design for Urban Transit." Proc. of International Conference on "Maglev Transport - Now and for the Future, Solihull, England, October 1984.

2. BIVENS, J.A. "M-BAHN - Advanced Maglev Technology Reality," Proc. Second International Symposium on Advanced Propulsion and Control for Urban Transit, Baltimore, MD., U.S. Dept. of Transportation, 1984, pp. 223-7.

3. GLATZEL, K., KHURDOCK, G. and ROGG, D. "The Development of the Magnetically Suspended Transportation System in the Federal Republic of Germany," IEEE Trans. on Vehicular Technology, 1980, Vol. VT-29, pp. 3-16.

4. OHTSUKA, T. and KYOTANI, Y. "Recent Progress in Superconducting Magnetic Levitation Tests in Japan," Proc. IEEE IAS Annual Meeting, 1980, IEEE Publ. No. 80CH1575-0, pp. 238-43. See also Proceedings of the Second International Seminar on Superconductive Magnetic Levitated Train, Miyazaki, Japan, November 1982.

5. HAYES, W.F. and TUCKER, H.G. "Design Concept and Comparative Performance of an Electrodynamic Maglev Transportation System for the Toronto-Montreal Corridor of Canada," Proc. of International Conference on Maglev Transport - Now and for the Future, Solihull, England, October 1984.

6. BOLDEA, I. "MAGNIBUS - The Romanian Linear Inductor (Synchronous) Motor (Passive Guideway) Maglev," Proc. of International Conference on Maglev Transport - Now and for the Future, Solihull, England, October 1984.

7. EASTHAM, J.F. "Iron-Cored Linear Synchronous Machines," Electronics & Power, 1977, Vol. 23, pp. 239-42.

8. SLEMON, G.R., DEWAN, S.B., BURKE, P.E., STRAUGHAN, A. and BHATIA, R. "Study of an Analytical Model of the Homopolar Linear Synchronous Motor," Transport Canada Report No. TP2856E, December 1980.

9. NASAR, S.A. and BOLDEA, I. Linear Motion Electric Machines, John Wiley & Sons, 1976.

10. BAUDON, Y. "Moteur Lineaire Synchrone," Final Report to D.G.R.S.T. (No. 76-7-0126), July 1979.

11. BALCHIN, M.J. and EASTHAM, J.F. "Characteristics of a Heteropolar Linear Synchronous Machine with Passive Secondary," Electric Power Applications, 1979, Vol. 2, pp. 213-8.

APPENDIX A

DESIGN OF THE HLSM FOR URBAN TRANSIT PROPULSION

(i) Cross-section

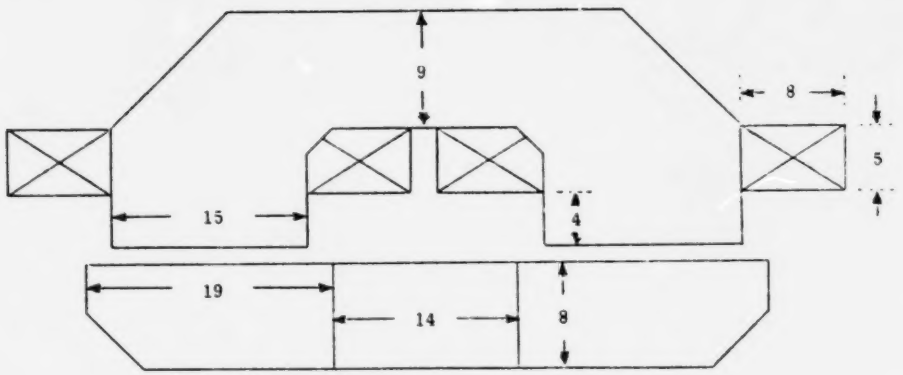

dimensions in cm

(ii) Field Winding of HLSM

Total MMF:	24 - 28 kiloamp. turns
Per coil:	
Number of turns:	500
Current:	24 - 28 A
Cross-section	50 mm x 80 mm
Fill factor (allowing for cooling passages):	0.75
Conductor cross-section:	6 mm^2
Resistance:	9.0 ohms
Conductor current density:	4 - 4.7 A/mm^2
Driving voltage (two coils in series):	504 volts
Winding loss:	10.4 - 14.1 kW

(iii) Armature Windings (of HLSM and LIM of equivalent performance)

	HLSM	LIM
Number of phases:	3	3
Number of poles:	11	6
Pole pitch:	183.3 mm	286.8 mm
Active width of armature:	150 mm (each side)	216 mm
Number of slots:	71 (each side)	79
Half-filled slots:	5 (at each end)	7 (at each end)
Slot pitch:	30.6 mm	23.9 mm
Slot width:	10.2 mm	15.7 mm
Tooth width:	20.4 mm	8.2 mm
Slot depth:	40.0 mm	54.9 mm
Number of slots/pole/phase:	2	4
Number of conductors/slot:	8	8
Slot fill factor:	0.69	0.58
Coil pitch:	5/6	7/12
Coil overhang (each side):	80 mm	152 mm
Conductor cross-section:	35 mm^2	62.6 mm^2
Number of turns/phase:	88	96
Frequency range:	0-60 Hz	5-50 Hz
Maximum available phase voltage:	230 V	270 V
Voltage limit (break point):	10-11 m/sec	12-13 m/sec
At peak thrust:		
Current:	250 A	465 A
Conductor current density:	7.2 A/mm^2	7.4 A/mm^2

(iv) Equivalent Circuit Parameters of HLSM

Per-phase, at 60 Hz:		
Armature resistance:		0.083 ohms
Leakage reactance:		
Slot leakage:	0.261 ohms	
Tooth-top leakage:	0.109 ohms	
End-winding leakage:	0.063 ohms	
Harmonic leakage:	0.036 ohms	
Central gap leakage:	0.079 ohms	0.548 ohms
Direct axis, x(ad):		
. from stored energy expression		0.875 ohms
. from finite element computation		0.622 ohms
Quadrature axis, x(aq):		
. from stored energy expression		0.631 ohms
. from finite element computation		1.000 ohms
Induced voltage:	fundamental component of rate of change of flux linkage	

Centre de développement
des transports
1000 o., rue Sherbrooke
Suite 2421
Montréal, Québec
H3A 2R3
Télex 05-24713

Transportation
Development Centre
1000 Sherbrooke St. W.
Suite 2421
Montreal, Quebec
H3A 2R3
Telex 05-24713

Library and Information Centre
Centre de Documentation (GSL)
RECEIVED – REÇU LE
JUN 25 1985
Government Publication Officielle
Transport Canada / Transports Canada

Canadian Institute of
Guided Ground Transport
Queen's University
at Kingston, Ontario

A.R. Eastham et al

CIGGT Report No. 84-2
Transport Canada Report No. TP-5957E

CA2 ON
UQU 325
84
R02
c.2

CIGGT Project No. PRO-096

CIGGT Report No. 84-2
Transport Canada Report No. TP-5957E

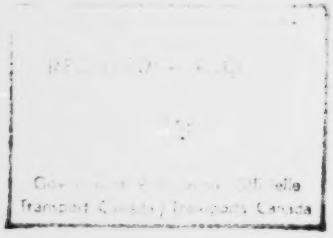

ANALYSIS AND ASSESSMENT OF THE HOMOPOLAR LINEAR SYNCHRONOUS MOTOR FOR URBAN TRANSIT APPLICATIONS

A.R. Eastham
G.E. Dawson
D.L. Atherton
S.B. Dewan
G.R. Slemon
R. Ong
W.J. Ballantyne
L.W. Coathup

This study was conducted by CIGGT for the Transportation Development Centre of Transport Canada under Contract No. OSD-82-00047.

Canadian Institute of Guided Ground Transport
Queen's University at Kingston, Ontario
K7L 3N6

July 1984

ACKNOWLEDGEMENTS

We would particularly like to thank Mr. M. Audette, the TDC Project Officer, Mr. I. Duncan of the Ontario Ministry of Transportation and Communications, and Mr. R.M. Renfrew, formerly of the Urban Transportation Development Corp. and now Executive Director of the Canadian Institute of Guided Ground Transport, for their interest and guidance in the analysis and assessment of the Homopolar Linear Synchronous Motor.

ISBN 0 88911 255 8

This report resulted from research conducted through the Canadian Institute of Guided Ground Transport. The report represents the views of the authors and does not necessarily have the endorsement of the University or the other participating organizations.

REPORT DOCUMENTATION FORM

1. Transport Canada Report No	2. TDC Project No	3. Recipient's Catalogue No
TP 5957E	4603	

4. Title and Subtitle	5. Report Date
ANALYSIS AND ASSESSMENT OF THE HOMOPOLAR LINEAR SYNCHRONOUS MOTOR FOR URBAN TRANSIT APPLICATIONS	July 1984
	6. Performing Organization Report No: 84-2

7. Author(s)	8. Transport Canada File No
A.R. Eastham, G.E. Dawson, D.L. Atherton, S.B. Dewan, G.R. Slemon, R. Ong, W.J. Ballantyne, L.W. Coathup	D1465-288-2

9. Performing Organization Name and Address	10. DSS File No
Canadian Institute of Guided Ground Transport (CIGGT) c/o Queen's University Kingston, Ontario K7L 3N6	10DS.T8200-2-2501
	11. DSS or Transport Canada Contract No: OSD-82-00047

12. Sponsoring Agency Name and Address	13. Type of Report and Period Covered
Transportation Development Centre (TDC) Suite 2421, 1000 Sherbrooke Street West Montreal, Quebec H3A 2R3	Final, July/82-June/84
	14. Sponsoring Agency Code

15. Supplementary Notes	16. TDC Project Officer
	M. Audette, M. Denis C.A. Versailles

17. Abstract

The homopolar linear synchronous motor (HLSM) is a machine which has the three-phase armature and the dc excitation on the same side of the airgap. The track is a coarsely slotted passive steel structure. The modulation of the dc field, produced by this track saliency, along the length of the machine locks into the travelling magnetic wave produced by three-phase ac excitation of the armature winding. Speed of the machine is controlled by armature excitation frequency. The objectives of this project were to evaluate the HLSM as (i) an alternative to the linear induction motor (LIM) for urban transit, and (ii) a machine capable of providing both suspension and propulsion/braking for transportation vehicles. Computer-aided design studies, using finite element analysis with saturable steel characteristics included, were conducted to determine the electromagnetic field distribution in the HLSM and to evaluate the parameters in a two-reactance equivalent circuit model of the machines for performance computation. It has been shown that the HLSM can be designed to meet the performance specifications for an urban transit vehicle and can operate at a high power factor/efficiency product, typically of 0.9 or higher. This leads to low kVA power-conditioner requirements and to excellent energy efficiency. However, the HLSM is considerably larger, two to three times heavier, and has a much higher normal force than a LIM of equivalent performance. While the HLSM is not attractive as a drive for urban transit vehicles, its high normal force makes it feasible for integrated suspension/propulsion applications. The HLSM is therefore of interest for passive guideway Maglev vehicles.

18. Key Words	19. Distribution Statement
Homopolar linear synchronous motor; Urban transit drives and control; Finite element analysis; Energy management and drive efficiency; Integrated suspension/propulsion system	Available on request from CIGGT or sponsoring agency

20. Security Classification (of this report)	21. Security Classification (of this page)	22. No. of Pages	23. Price
unclassified	unclassified	133 + append.	

TDC CDT 79-005

FORMULE DE DOCUMENTATION POUR RAPPORT

1 N° du rapport Transports Canada	2 N° de l'étude — CDT	3 N° de catalogue du destinataire
TP 5957E	4603	

4 Titre et sous-titre	5 Date du rapport
ANALYSIS AND ASSESSMENT OF THE HOMOPOLAR LINEAR SYNCHRONOUS MOTOR FOR URBAN TRANSIT APPLICATIONS	juillet 1984
	6 N° du rapport de l'organisme exécutant 84-2
7 Auteur(s) A.R. Eastham, G.E. Dawson, D.L. Atherton, S.B. Dewan, G.R. Slemon, R. Ong, W.J. Ballantyne, L.W. Coathup	8 N° de dossier Transports Canada D1465-288-2
9 Nom et adresse de l'organisme exécutant Canadian Institute of Guided Ground Transport (CIGGT) Queen's Unversity Kingston, Ontario K7L 3N6	10 N° de dossier — ASC 10DS.T8200-2-2501
	11 N° de contrat — ASC ou Transports Canada OSD-82-00047
12 Nom et adresse de l'organisme parrain Centre de developpement des transports (CDT) 1000 o., rue Sherbrooke, Suite 2421 Montréal, Québec H3A 2R3	13 Genre de rapport et période visée final, juil./82-juin/84
	14 Code de l'organisme parrain
15 Remarques additionnelles	16 Agent de projet — CDT M. Audette, M. Danis, C.A. Versailles

17 Resume

Le moteur linéaire synchrone homopolaire est une machine triphasée dont l'induit et la source de courant continu d'excitation se trouvent du même côté de l'entrefer. Les rails, en acier et rainurés, constituent une structure passive. La modulation du champ continu introduite par la géometrie de la voie le long de l'axe longitudinal de la machine se retrouve dans l'onde magnétique progressive produite par l'excitation des enroulements d'induit par un courant alternatif triphasé. La vitesse de la machine est commandée par la fréquence du courant d'excitation. Le présent projet avait pour objectifs d'évaluer ce type de moteur (i) comme solution de remplacement au moteur linéaire d'induction pour le transport urbain et (ii) en tant que machine capable d'assurer la sustentation, la propulsion et le freinage d'un véhicule de transport urbain. Nous avons effectué des études de conception assistée par ordinateur fondées sur la méthode des éléments finis en vue de déterminer la distribution du champ électromagnétique dans le cas du moteur linéaire synchrone homopolaire et d'évaluer les paramètres d'un circuit à deux réactances équivalent à ce dernier pour en déterminer le comportement. Il a été démontré qu'il est possible de concevoir des moteurs linéaires synchrones homopolaires qui répondent aux exigences de rendement imposées aux véhicles de transport urbain et dont la valeur du produit facteur de puissance/rendement soit assez élevée, de 0,9 ou plus dans un cas type. On parvient ainsi à obtenir des moteurs qui nécessitent un inverseur de faible capacité et qui possèdent un excellent rendement énergétique. Toutefois, le moteur linéaire synchrone homopolaire est beaucoup plus encombrant, de deux à trois fois plus lourd et développe une force normale beaucoup plus élevée qu'un moteur linéaire d'induction de rendement équivalent. Bien qu'il ne soit par intéressant pour la propulsion des véhicules et transport urbain, le moteur linéaire synchrone homopolaire, grâce à sa force normale élevée, peut être exploité dans le cadre des systèmes intégrés de propulsion et de sustentation. Ce type de moteur présente donc un certain intérêt pour les véhicules à sustentation magnétique à voie passive.

18 Mots-clés	19 Diffusion
Moteur linéaire synchrone homopolaire; Moteurs et commandes pour véhicules de transport urbain; Méthode des éléments finis; gestion de l'énergie et rendement; Systèmes de propulsion et de sustentation intégrés	Disponible sur présentation d'une demande au CIGGT au à l'organisme qui a subentionné l'étude.

20 Classification de sécurité (de ce rapport)	21 Classification de sécurité (de cette page)	22 Nombre de pages	23 Prix
sans cote	sans Cote	133 + append.	

CDT TDC 79-005

TABLE OF CONTENTS

1. INTRODUCTION 1
   1.1 Linear Electric Drives 1
   1.2 Modes of Operation of the HLSM 3
   1.3 Background and Context of Work 6
   1.4 Objectives and Achievements 7

2. REVIEW OF RESEARCH ON THE HLSM 11
   2.1 Development of Research Activities 11
   2.2 Methods of Analysis 13
      2.2.1 Stored Energy Method 14
      2.2.2 Fourier Series 18
      2.2.3 Conformal Transformation 20
      2.2.4 Non-Linear Magnetic Circuit Analysis 21
      2.2.5 Finite Element Method 21

3. FINITE ELEMENT ANALYSIS 23
   3.1 The Finite Element Method 23
   3.2 Variational Formulation 23
   3.3 Boundary Conditions 28
   3.4 B-H Characteristics 28
   3.5 Representation of Excitation 29
      3.5.1 DC Excitation 29
      3.5.2 AC Excitation 29
   3.6 Solution of the Non-Linear Equations 31
   3.7 Field Plotting 35
   3.8 Validation of Solution 35

4. FINITE ELEMENT MODELLING OF THE HLSM 37
   4.1 The Equivalent Circuit 37
   4.2 Induced Voltage 38
      4.2.1 General Approach 38
      4.2.2 Transverse Section 38
      4.2.3 Longitudinal Section 42
      4.2.4 Calculation of Induced Voltage 45
      4.2.5 Validation of Analysis 46
   4.3 Armature Reactance 50
      4.3.1 General Approach 50
      4.3.2 Finite Element Method I 50
      4.3.3 Finite Element Method II 53
      4.3.4 Discussion 56

5. DESIGN AND PERFORMANCE OF THE HLSM FOR URBAN TRANSIT 59
   5.2 Design Approaches 61
      5.2.1 Test Motor 61
      5.2.2 Magnetic Circuit Considerations 62
      5.2.3 Lorentz Force Approach 63
      5.2.4 Finite Element Analysis 64

5.2.5 Equivalent Circuit 64
5.2.6 Review of Design Procedures 65
5.3 Design Characteristics 66
5.4 Performance of the HLSM 71
5.4.1 Motoring Performance 72
5.4.2 Braking Performance 77
5.4.3 Excitation and Armature Field Distribution . . 79

6. CONTROL AND POWER-CONDITIONING 83
6.1 Control 83
6.2 Power-Conditioning 84
6.3 References Related to Power-Conditioning and Control of Synchronous Drives 88

7. PERFORMANCE OVER DUTY CYCLES 91
7.1 Simple Duty Cycle 91
7.1.1 Speed and Thrust Profiles 91
7.1.2 Performance Profiles 93
7.2 Transit Corridor Duty Cycle 97
7.2.1 Energy Management Model 98
7.2.2 Simulation Results 99

8. COMPARISON BETWEEN HLSM AND LIM PROPULSION 103
8.1 Approach 103
8.2 Cost Analysis 104
8.2.1 Cost of the Primary 104
8.2.2 Cost of the Secondary 104
8.2.3 Cost of the PCU 105
8.2.4 Cost of Substations and Power Rail 105
8.2.5 Cost of the Truck and Friction Brakes 106
8.2.6 Cost Analysis Summary 106
8.3 Discussion 107
8.4 Conclusions 108

9. POTENTIAL OF HLSM FOR INTEGRATED SUSPENSION/PROPULSION . . . 109
9.1 Normal Force. 109
9.2 Integrated Suspension/Propulsion System 110
9.3 Control 111
9.4 ISPS Design 113
9.5 Performance 113
9.6 Discussion 116

10. CONCLUSIONS AND RECOMMENDATIONS 121
10.1 Objectives and Achievements 121
10.2 Conclusions 123
10.3 Recommendations 126

11. REFERENCES 129
11.1 A Bibliography of Iron-Cored Linear Synchronous Motors 129
Other References 133

Appendix A: DETERMINATION AND COMPUTATION OF THE HLSM EQUIVALENT-CIRCUIT PARAMETERS

Appendix B: DESIGN PARAMETERS OF THE UNIVERSITY OF TORONTO TEST HLSM

Appendix C: DETERMINATION OF THE CONTROL ANGLE REQUIRED FOR MINIMUM CURRENT, FOR ANY GIVEN SET OF THRUST, SPEED AND FIELD EXCITATION

Appendix D: SIMULATION OF THE HLSM RUNNING ON A DUTY CYCLE

Appendix E: PERMANENT MAGNET HLSM'S

LIST OF TABLES

2.1 A Comparative Evaluation of the LIM and HLSM According to Levi 12

4.1 Air Gap Coefficients for Slemon's Test HLSM 41
4.2 Equal Reluctance Approach: Total Flux Density as a Function of Effective Track Slot Depth for Selmon's Test HLSM 44
4.3 Experimental and Calculated Values of D and Q Axis Inductances for Slemon's Test HLSM, Using an Equivalent Track Slot Depth of 58 mm 51

5.1 HLSM Specifications and Guidelines 59
5.2 Comparative Characteristics of the HLSM and LIM for ICTS Application 67
5.3 Comparative Characteristics of the Armature Windings of the HLSM and LIM for ICTS Application 69
5.4 Field Winding of the HLSM 70
5.5 Equivalent Circuit Parameters of the HLSM 70

7.1 Parameters of the Vehicle and Simple Duty Cycle 91
7.2 Power and Energy Characteristics of LIM and HLSM Drives Over the Vancouver ALRT Corridor 99

8.1 Per-Vehicle Cost Comparison 106
8.2 Wayside Cost Comparison 107

9.1 Design of an HLSM for ISPS Operation 114

10.1 Relative Features of HLSM and LIM 124

LIST OF FIGURES

1.1 Schematics of the linear induction motor and the homopolar linear synchronous motor for urban transit propulsion 2

1.2 Two design options for the HLSM: the transverse bar track design with figure-of-eight shaped armature coils, and the slotted (staggered-pole) track design with conventional diamond-shaped armature coils 4

1.3 A vehicle concept using HLSMs for integrated suspension and propulsion 6

2.1 Dimensional characteristics of the HLSM 14

2.2 Per-phase two-reactance equivalent circuit of the HLSM . . 17

2.3 The model of the HLSM used for non-linear magnetic circuit analysis and an expanded pole pitch showing the assumed air gap field distribution and flux paths for analysis 22

3.1 Transverse half section of a linear hompolar synchronous machine discretized into triangular elements 25

3.2 B-H Characteristics assumed for silicon-steel laminations and for cast steel 30

3.3 Flow chart of the two-dimensional finite element method for non-linear magnetic field problems 32

3.4 Flow chart of the convergence procedure in the non-linear two-dimensional finite element method 34

3.5 DC excitation field distribution in a transverse half plane of the HLSM 36

3.6 Armature field in the longitudinal plane of the HLSM, with ac mmf in the d-axis 36

4.1 The two-reactance equivalent circuit model of the HLSM . . 37

4.2 The field distribution in a transverse half section of the HLSM 39

4.3 Air gap fringing coefficient 40

4.4 The excitation field distribution in one longitudinal wavelength of the HLSM 42

4.5 Configuration used to determine the equivalent track slot depth of the HLSM 43

4.6 Field plots for the geometries used to establish the effective track slot depth 45

4.7 The flux density at half the armature slot depth as a function of Slemon's test HLSM 46

4.8 Polar transverse dc field distribution of Slemon's HLSM and the corresponding flux density 47

4.9 Interpolar transverse dc field distribution of Slemon's HLSM and the corresponding flux density 48

4.10 The open circuit characteristics of the University of Toronto experimental machine 49
4.11 MMF distribution 51
4.12 Longitudinal section of Slemon's HLSM with armature mmf in d-axis 52
4.13 Longitudinal section of Slemon's HLSM with armature mmf in q-axis 52
4.14 Models for the armature flux distribution 54
4.15 D-axis and q-axis configurations for the determination of reactance by finite element method II 54
4.16 Flux distribution due to armature mmf in the d-axis and in the q-axis of the developed model of Slemon's staggered-pole HLSM 55
4.17 D-axis and q-axis flux density calculated at half the armature slot depth as a function of position along the longitudinal section of Slemon's HLSM 58

5.1 Motoring and braking thrust requirements per motor for the HLSM drive 60
5.2 The general configuration of the staggered-pole HLSM selected for urban transit applications 67
5.3 Design details of the HLSM 68
5.4 Meeting the performance specification in motoring, showing the effect of varying dc excitation 73
5.5 Meeting the performance specification in motoring, showing the effect of varying both the magnitude and ratio of X_{ad} and X_{aq} 75
5.6 Meeting the performance specification in braking, showing the effect of varying dc excitation 78
5.7 (a) Polar transverse dc field distribution of the final HLSM design with a doubly corrected air gap 80
(b) Interpolar transverse dc field distribution of the final HLSM design with a corrected air gap 81
(c) Longitudinal field distribution of the HLSM design . . 81
(d) D-axis armature field distribution in the developed model of the HLSM, used to determine X_{ad} 82
(e) Q-axis armature field distribution in the developed model of the HLSM, used to determine X_{aq} 82

6.1 Typical current angle versus speed characteristics for control of the HLSM 83
6.2 Inverter supply to HLSM armature windings 86
6.3 Hysteresis-band control of phase currents, with portion of typical waveform shown for i_c 86
6.4 The basic HLSM control system 87

7.1 The speed-time and grade profile assumed for the simple duty cycle 92
7.2 The motor thrust profile for the simple duty cycle 93
7.3 The armature current profile for the simple duty cycle . . 95
7.4 The control angle, γ, profile for the simple duty cycle . 95

7.5 The kVA profile for the simple duty cycle 96
7.6 The induced voltage per Hertz, V_{ei}/Hz, profile for the simple duty cycle 96
7.7 The armature terminal voltage profile for the simple duty cycle 97
7.8 Characteristics of the Vancouver ALRT corridor 100
7.9 The speed-distance profile for vehicles with LIM drive and with HLSM drive along the Vancouver ALRT alignment 101
7.10 Electrical power and cumulative energy input profiles for a four-car train with LIM drive and with HLSM drive along the Vancouver ALRT alignment 102

9.1 Normal force per pole as a function of (dc mmf/coil)^2 for the urban transit HLSM 110
9.2 A cross-section of vehicle and guideway, showing how HLSMs may be used for integrated suspension and propulsion 111
9.3 Schematic of ISPS control section for the HLSM 112
9.4 Performance characteristics of the ISPS HLSM with dc mmf of 26 kA turns, meeting the performance specification in motoring 117
9.5 Performance characteristics of the ISPS HLSM with dc mmf of 26 kA turns, meeting the performance specification in braking 119

A.1 The per-phase two-reactance equivalent circuit model of the HLSM A.1
A.2 Armature slot dimensions A.3
A.3 Modelling of a 5/6 chorded armature winding to find the cross-over leakage reactance, XCENT A.6

B.1 Dimensions of the University of Toronto test HLSM B.2

C.1 Phasor polygon in the motoring regime C.3
C.2 Phasor polygon in the braking regime C.8

E.1 Demagnetization curves for Alnico, Cobalt-Samarium and Ferrite permanent magnets E.2
E.2 A conceptual design of an HLSM with cobalt-rare earth permanent magnet excitation E.7

1. INTRODUCTION

1.1 Linear Electric Drives

Linear electric drives provide guided vehicles with reliable propulsion and braking. Such drives are essential for electric non-contact vehicles, with primary magnetic or air-cushion suspension, and are desirable for short-headway wheeled vehicles where guideway or rail conditions are such that adhesion cannot be guaranteed.

The linear induction motor (LIM) has been considered for many vehicles, and has found its main application in urban transit or shuttle systems, such as for the Urban Transportation Development Corporation's (UTDC) intermediate-capacity transit system (ICTS) under construction in Vancouver, Scarborough and Detroit, for the WEDWAY shuttle service in Orlando and at Houston International Airport, and for the Birmingham Maglev People Mover in England.

The use of a linear induction motor provides UTDC's ICTS vehicle with normal service acceleration and braking of 1.25 m/sec^2, and allows the 22 m/sec vehicles to be operated at headways as low as 90 seconds. The guideway profile can include grades up to 6 per cent. The lack of rotating components and the non-contact nature of the LIM drive should lead to significant maintenance cost reductions as compared with any rotating machine drive.

The primary of the LIM consists of a distributed three-phase armature winding which is excited from a controllable source -- usually a variable frequency inverter. The secondary of the LIM usually consists of a steel core with an aluminum cap, although other design options are available (e.g. a steel-cored cage rail, or a solid steel strip). The LIM primary can either be carried by the vehicle, as shown in Figure 1.1(a) (as for the ICTS and Birmingham People Mover systems) or be mounted in the track (as for the WEDWAY system). The secondary or reaction component is then located on the opposite side of the airgap.

The main disadvantage of the LIM is its low power factor/efficiency product. This is a consequence of the magnitude of the airgap, which is typically 10-12 mm for transit vehicles. The power-conditioner must provide sufficient excitation to drive flux across the airgap of the

machine. This requires substantial kVAR. The ICTS LIM operates with an $\eta \cos \phi$ of 0.40-0.42. This is reflected in the capacity of the variable-frequency variable-voltage inverter -- a 325 kVA unit is required for a LIM of nominal rating 120 kW.

(a)

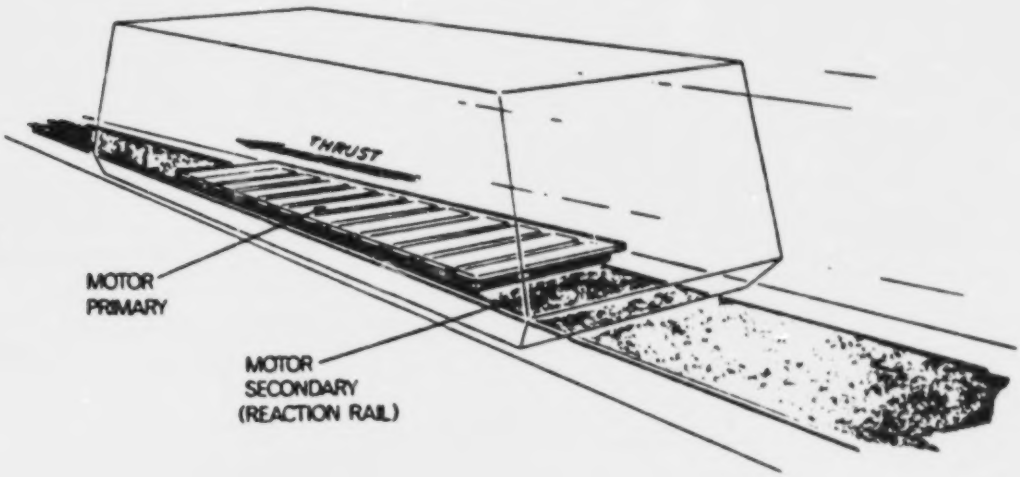

(b)

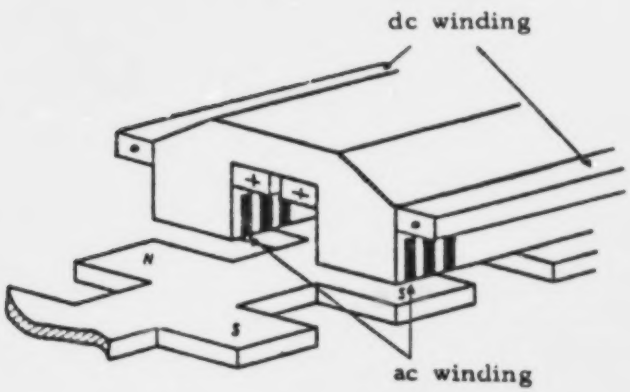

Figure 1.1 Schematics of (a) the linear induction motor, and (b) the homopolar linear synchronous motor, for urban transit propulsion

This characteristic of the LIM leads to low energy efficiency and to high-capacity power-conditioner requirements in comparison with rotary drives. These factors have stimulated researchers to examine linear counterparts of other rotating ac machines, specifically the synchronous motor in view of its high power factor capability through dc

excitation control. Iron-cored heteropolar linear synchronous drives are used for both the low-speed M-BAHN and the high-speed TRANSRAPID Maglev systems in West Germany, while an air-cored heteropolar linear synchronous motor (LSM) has been developed for the JNR high-speed Maglev vehicle and is also proposed for the Canadian Maglev system.

These heteropolar drives incorporate "long stators" -- active guideway windings to which three-phase currents of variable frequency and amplitude are fed to control the speed and thrust of a vehicle. The homopolar configuration of the LSM, on which this report is based, was conceived as a means of replacing these long stator windings with a passive salient structure in the track, as shown in Figure 1.1(b).

This report describes the results of a detailed investigation, analysis and assessment of the homopolar linear synchronous motor for two potential applications:

- as an urban transit drive, in comparison with the linear induction motor
- as an integrated suspension/propulsion system (ISPS) for non-contact transit vehicles.

1.2 Modes of Operation of the HLSM

The HLSM is a synchronous machine with both the ac armature winding anr the dc excitation on the same side of the airgap -- on the component which would be carried by the vehicle. The track is a coarsely slotted, ferromagnetic structure, analogous to the salient-pole rotor of a conventional synchronous machine.

Two design options for the HLSM are shown in Figure 1.2. In both designs, the vehicle component carries a dc field winding running longitudinally around the yoke of the machine. This produces transverse excitation flux which crosses the airgap twice and magnetizes the salient pole track, as shown. The saliency of the track produces a modulation in the magnitude of the airgap flux density along each side of the machine.

A distributed three-phase armature winding is located in the slots shown in Figure 1.2. When connected to a source of three-phase ac, the armature produces an airgap field which moves longitudinally at the

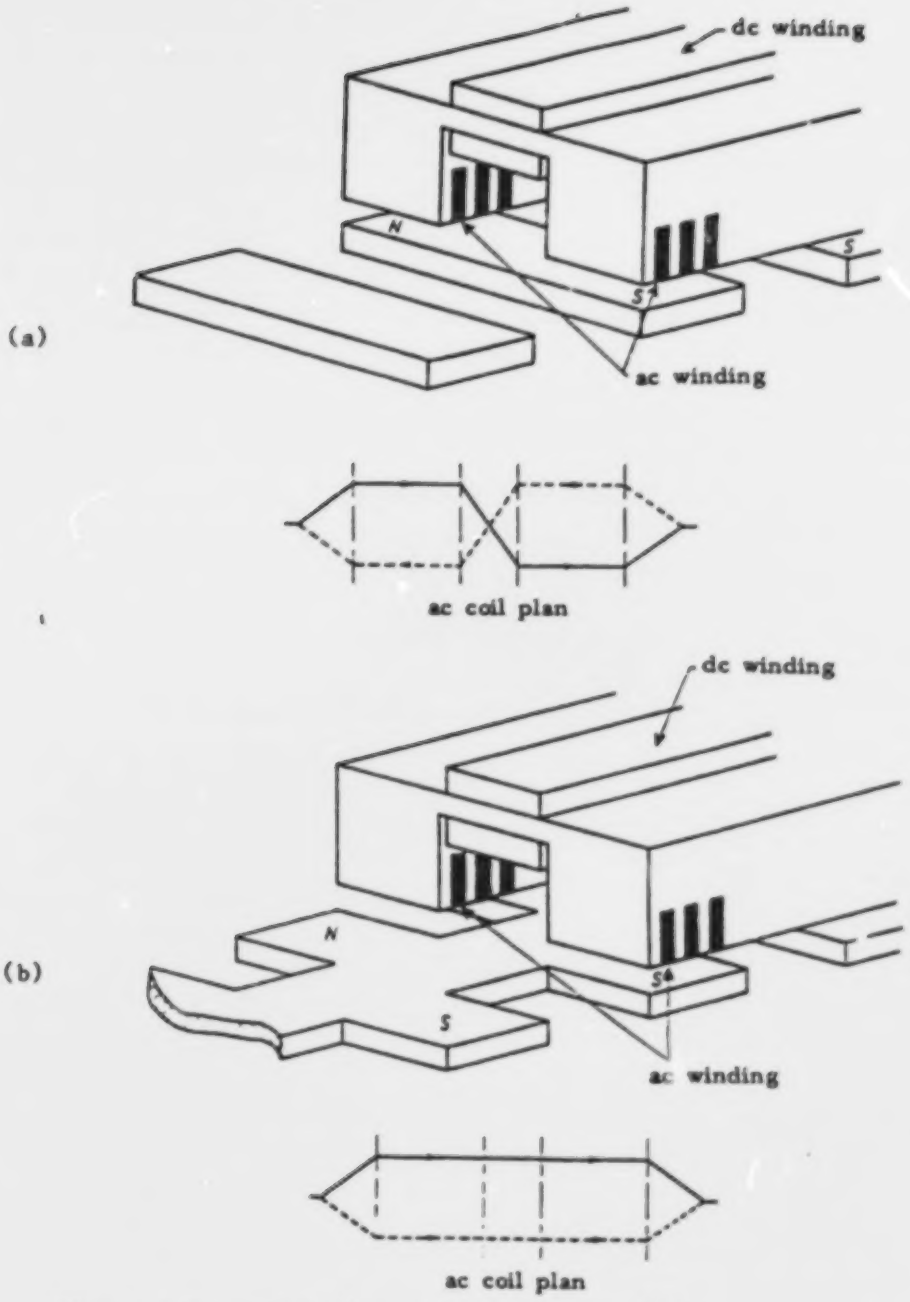

Figure 1.2 Two design options for the HLSM:
(a) the transverse bar track design with figure-of-eight shaped armature coils
(b) the slotted (staggered-pole) track design with conventional diamond-shaped armature coils

characteristic synchronous speed, $v_s = 2\tau f$, where τ is the winding pole pitch, and f is the source frequency. In operation, the travelling armature field locks into the modulated excitation field to provide a thrust force and forward motion of the vehicle at speed v_s. Vehicle speed is therefore controlled by armature frequency. The thrust is determined both by the magnitude of the modulation in excitation field and by the magnitude of the armature current. The terminal characteristics of the HLSM, in particular the power factor and kVA drawn from the supply, can be optimized by controlling the dc excitation and the phase angle at which current is injected into the armature with respect to track pole position.

The two design options shown in Figure 1.2 differ in two respects. The first has a track consisting of simple transverse steel bars. The modulated gap flux densities along each side of the machine have a longitudinal space phase difference of 180°, requiring a similar space phase difference in the armature field. This is achieved by figure-of-eight shaped armature windings, as shown. The second option has a continuous slotted steel and staggered pole track. The modulated gap flux densities along each side of the machine are now in longitudinal space phase, and the armature can carry a conventional diamond-shaped winding.

Both HLSM designs produce high normal forces between vehicle-borne components and the passive track. It will be shown that this force is typically 6-10 times the available thrust. It becomes feasible, therefore, to consider using the machine not only as an urban transit drive but to make use of the high normal force for vehicle suspension in an integrated suspension/propulsion system (ISPS).

After careful consideration of the two designs, Option (b) was considered the most appropriate for transit and ISPS applications for two reasons:

- the salient ferromagnetic structure can be prefabricated in sections to the required tolerances and can be mounted more simply to the guideway structure

- the armature coils are of conventional diamond-shaped design, allowing the magnitude of the central gap between the two active sides of the

motor to be selected from field considerations rather than from coil geometry limitations.

For wheeled transit, the staggered pole track would replace the centrally mounted reaction rail of the single-sided LIM drive shown in Figure 1.1(a). For ISPS applications, two staggered pole "rails" would be mounted to the underside of the guideway structure, as indicated in Figure 1.3.

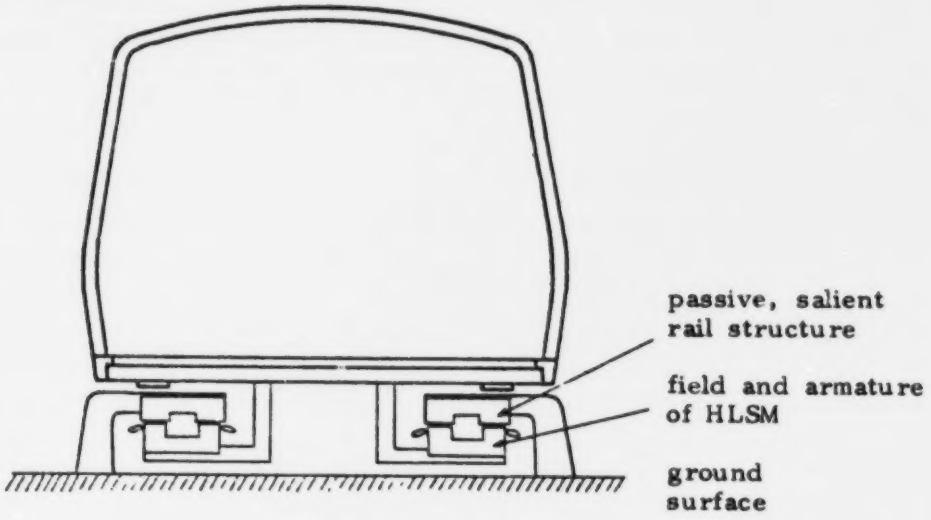

Figure 1.3 A vehicle concept using HLSMs for integrated suspension and propulsion

1.3 Background and Context of Work

During the past years, TDC has funded a number of studies and experimental tests to achieve a better understanding of contactless propulsion motors and to identify novel transportation systems which better meet the needs of Canadian cities.

The Canadian Institute of Guided Ground Transport has administered projects in which researchers from Queen's University, the University of Toronto and McGill University have advanced the state of knowledge of electrodynamic suspension, linear synchronous and linear induction motor propulsion, and integrated suspension/propulsion systems through analysis and experimentation. As a result of studies and tests conducted by both the University of Toronto (under contract to TDC) and

Queen's University (with funding from NSERC), it was established that the HLSM had a number of attractive features which made it a good candidate for propulsion of urban transit vehicles. It was recognized that the potential advantages -- the improved power factor and efficiency -- may be offset by an increase in motor weight. A detailed design analysis and an identification of operational features was therefore needed to determine if the advantages of the HLSM outweighed its disadvantages.

CIGGT therefore undertook to conduct the analysis, design and assessment of the HLSM, both for urban transit and integrated suspension/propulsion applications. The work reported here was conducted by researchers in the Department of Electrical Engineering and in the Physics Department at Queen's University and in the Department of Electrical Engineering at the University of Toronto, in collaboration with engineers at the Urban Transportation Development Corporation. Specific objectives and achievements are described below.

1.4 Objectives and Achievements

The objectives of this contract, as specified in TDC's Work Statement, are listed below. A review of the relevant achievements is given after each item.

(i) Conduct a comprehensive review of the state-of-knowledge of HLSM's and assess analytical approaches.

This was completed in the early stages of the project. The review of the state-of-knowledge and analytical approaches is presented in Section 2.

(ii) Define a design specification for the HLSM, based on ICTS LIM propulsion requirements.

Specifications and design guidelines for an HLSM which could serve as a drive for an ICTS vehicle were developed in consultation with engineers from UTDC. Most of the parameters are directly related to the requirements for and experience with the ICTS LIM drive.

(iii) Develop analytical techniques to assess motor design performance.

A major component of the work reported here, and a major achievement of this project, was the development of a finite element analysis of the HLSM. A three-dimensional representation of the flux distribution in the machine was developed from a two-dimensional analysis of the HLSM, applied to three orthogonal planes in the machine. The analysis included the non-linear magnetization characteristics of the machine steels (Silicon Steel and Cast Steel). The finite element method was used for computer-aided design and to determine parameters in the two reactance equivalent circuit of the machine for performance computation.

(iv) Conduct a design study and evaluate performance achievements of the proposed design.

As noted above, the finite element technique was used and proved to be very effective for design studies and for derivation of the parameters required for performance evaluation. An iterative design procedure was used to determine an HLSM design which would operate at high efficiency and power factor, such that the rating of the inverter power-conditioner would be minimized.

(v) Evaluate the performance and control requirements of the HLSM over a typical duty cycle and over a route having the characteristics of a typical urban transit system.

A typical duty cycle was defined such that the HLSM would be exercised over its full operating range. A 1 km station separation was considered. The vehicle was required to accelerate at 1.2 m/sec^2, cruise at 22 m/sec^2 ascend a 5 per cent grade at full speed, cruise, descend a 5 per cent grade at full speed, cruise, and brake at 1.2 m/sec^2 into the station. A control algorithm, specifying the armature current angle as a function of speed, was selected such that the HLSM would draw minimum armature current at all times. The results showed that the HLSM design could provide the specified performance within the design guidelines. An ICTS vehicle with HLSM drive was then run in simulation over a complete

route, taking the Vancouver ALRT alignment as typical. This allowed the net energy and peak power demand to be evaluated for direct comparison with a vehicle with LIM drive.

(vi) Evaluate the performance and control requirements of the HLSM as an integrated suspension and propulsion system.

The optimized HLSM design exhibited a high normal force, of such a magnitude that it could be used for vehicle suspension. Comparatively little design modification was required to make the HLSM appropriate for ISPS application. This mode of operation was shown to be feasible and a more likely application for the HLSM than simply as an urban transit drive.

(vii) Conduct an HLSM system evaluation as a replacement to the LIM system in the ICTS application.

The assessment of the HLSM as an urban transit drive was conducted in collaboration with UTDC Research & Development Ltd. It was shown that the HLSM could operate with an armature $\eta \cos \Phi$ of typically 0.90-0.92, leading to significant savings in energy consumption and peak power demand as compared with the LIM. However, the HLSM is longer, higher and considerably heavier than the LIM, and has almost four times the normal force. With regard to these features, it was concluded that the disadvantages outweigh the advantages of the HLSM as an urban transit drive. However, the higher normal force allows the HLSM to be considered for ISPS applications. In this mode, the thrust and normal force can be controlled independently by armature and excitation control. Integrated suspension/propulsion is considered to be the preferred application for the HLSM.

2. REVIEW OF RESEARCH ON THE HLSM

2.1 Development of Research Activities

There is a substantial body of published research work on the homopolar linear synchronous motor and on closely related machine configurations, dating from the first known suggestion of its application as a linear drive by Drake et al. in 1968. A comprehensive bibliography has been included in this report as Section 11.

Analysis of the HLSM began with the work of Levi at the Polytechnic Institute of New York in the early 1970s, and gradually spread to other countries involved in linear motor research, primarily at the university and research centre level. World-wide interest in the HLSM developed from the prospect that one of the principal limitations of the linear induction motor, namely its inherently low power factor, could be overcome. Indeed, the early work of Levi predicted highly encouraging design and performance characteristics for the HLSM, as compared with the LIM. As an example, Table 2.1 shows predicted comparative features of the two linear machines as propulsion units for the Tracked Air Cushion Research Vehicle (TACRV) which was tested at the Pueblo high-speed test track in the mid-seventies. However, the very low volume and mass predicted for the HLSM was not substantiated by later experimental work and more detailed analysis.

This early work by Levi led, in the late 1970s, to a substantial design study and experimental evaluation of the HLSM by General Electric in Schenectady, New York, as reported by Haller and Mischler (1978), Kliman et al. (1980), and Nondahl (1980). The Nondahl paper, "Design Studies for Single-Sided Linear Electric Motors," compares LIM and HLSM designs for transportation systems ranging from subway cars to high-speed locomotives, at five power levels from 200 kW to 3,735 kW. At each power level, the HLSM was predicted to be capable of operation at unity power factor, but would have a mass up to three times that of the LIM -- a figure which is substantiated by the work conducted by CIGGT and reported here.

TABLE 2.1

A COMPARATIVE EVALUATION OF THE LIM AND HLSM ACCORDING TO LEVI (1974)

Basic Characteristic		Equivalent Single-Sided TACRV-LIM	Homopolar Inductor
Rail clearance (cm)		0.8	1.5
Power factor		0.575	1.0
Efficiency		0.8	0.91
Weight/Output power (kg/kW)	LIM	0.59	0.29
	Synchronous condensor*	0.66	
	Total	1.25	
Total volume (m^3)		2.2	0.48
Total weight (ton)		18	3.9
Thrust (N)		10^5 (22,500 lbs)	10^5 (22,500 lbs)
Max. suspension force (N)		1.26×10^5	4.5×10^5
Max. guidance force (N)		10^4	8×10^4

* For power factor correction.

Note: The very low volume and mass predicted for the HLSM was not substantiated by later analytical and experimental work.

In parallel with the research in the U.S., a group of U.K. researchers from Nottingham University (Davis et al.), Aberdeen University (Eastham and Balchin), and Brush Electric Machines Ltd (Chahal et al.) pursued configurational studies, analysis and experimental work on a rotating test rig at Nottingham. Some research activities were also evident in the Federal Republic of Germany with the work of Weh at the University of Braunsweig, and in France with the early analysis by Rummich and the subsequent work of Baudon and colleagues at the Institut National Polytechnique de Grenoble.

In terms of progress towards the implementation of HLSMs in a prototype vehicle, the work of Boldea at the Polytechnique Institute in

Timisoara, Romania, must be considered the most advanced. Boldea, in collaboration with Nasar at the University of Kentucky, has made extensive analyses of the HLSM and of its application not merely as a propulsion unit but as an integrated suspension and propulsion system (ISPS). The normal force produced by the HLSM is typically up to ten times higher than the thrust, and can be controlled to provide vehicle suspension in an electromagnetic mode. A test vehicle has been constructed, and has recently (in 1984) been successfully suspended by controlled HLSMs in the Engineering Labs in Timisoara.

In Canada, research in HLSMs was begun in the mid-seventies by Slemon and colleagues at the University of Toronto. After the initial analytical work, Transport Canada funded an experimental study, using a rotating wheel test rig with the staggered pole track configuration. This work was reported in December 1980. In the late 1970s, Atherton and Dawson began independent studies at Queen's University, and a rotating wheel test rig with the transverse bar track configuration was constructed in the Department of Electrical Engineering. The results of these studies showed that the attractive features of unity power factor operation for the HLSM could be attained. In view of the interest in linear drives for urban transit systems, as a result of the intermediate capacity transit system (ICTS) developments at the Urban Transportation Development Corporation (UTDC), it was considered desirable to conduct a detailed analytical investigation and design study of the HLSM specifically for ICTS applications, to determine if this machine could be developed as an improved linear drive for second-generation ICTS-type vehicles. The comparison between the existing LIM drive and the HLSM forms the basis of the work reported here.

2.2 Methods of Analysis

A survey of the literature in Section 11 reveals five distinct approaches to the analysis of the HLSM:

- stored energy
- Fourier analysis
- conformal transformation
- non-linear megnetic circuit analysis
- finite element method

In the following subsections, the assumptions of these methods and corresponding analytical expressions for machine parameters and performance characteristics will be presented. The validity of these techniques for HLSM design and performance evaluation will then be discussed.

2.2.1 Stored Energy Method

The machine geometry considered for the stored energy (and other) techniques is shown in Figure 2.1. It is assumed that the permeability of motor and track steel is infinite, i.e. the field energy of the ferromagnetic material is zero.

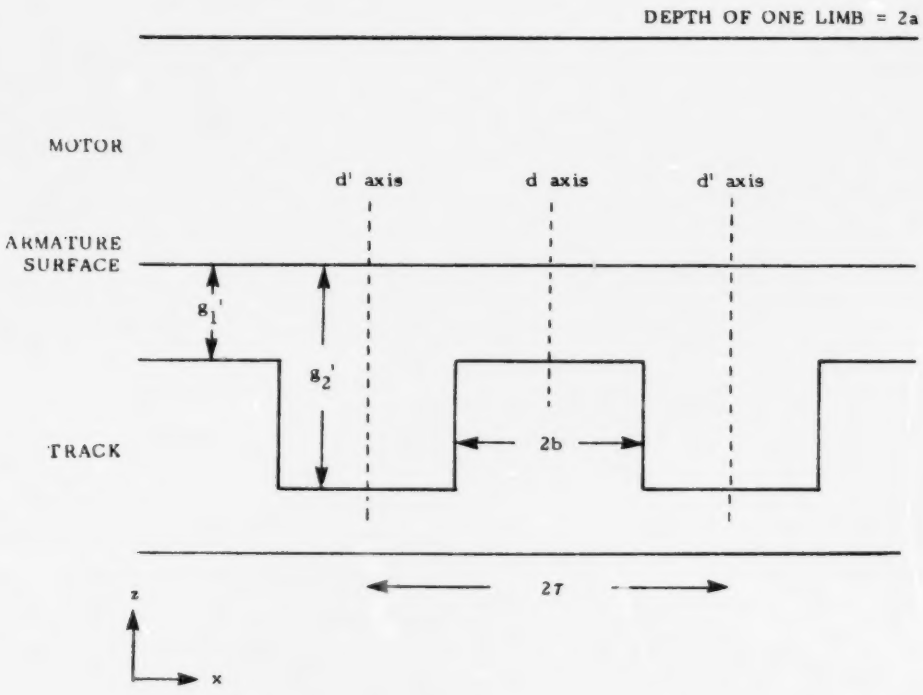

Figure 2.1 Dimensional characteristics of the HLSM. g_1' and g_2' are the polar and interpolar Carter's coefficient corrected air gaps

The mmf distribution is taken to be:

$$F(x) = F_0 + F_1 \cos\left(\frac{\pi x}{\tau} + \theta\right) \qquad (2.1)$$

where: $2F_0$ is the total dc mmf

F_1 is the amplitude of the ac mmf

and $$F_1 = \frac{3\sqrt{2}\, N_{ph}\, I_{rms}\, k_w}{P} \qquad (2.2)$$

where P is the number of pole pairs along each side of the machine.

The components of field intensity in the air gap are taken as:

$$H_{dc} = \frac{F_0}{g_1'} \; ; \; \frac{F_0}{g_2'}$$

$$H_{ac} = \frac{F_{ac}}{g_1'} \; ; \; \frac{F_{ac}}{g_2'}$$

The energy, W_m, stored in the air gap of the HLSM is then:

$$W_m = 2\,\mu_0\, aP \int_{-b}^{2\tau - b} H^2\, g(x)\, dx \qquad (2.3)$$

Thrust force, F_x, is given by:

$$F_x = \frac{\partial W_m}{\partial x} = \frac{\pi}{\tau}\,\frac{\partial W_m}{\partial \theta}$$

giving, after manipulation:

$$F_x = \frac{2\mu_0\, a\, P\, F_1^{\,2}}{g_1'}\left(1 - \frac{1}{k}\right)(\sin 2\theta \sin 2\alpha + 4c \sin\theta \sin\alpha) \qquad (2.4)$$

where: $k = \frac{g_2'}{g_1'}$, $\alpha = \frac{\pi b}{\tau}$, and $c = \frac{F_0}{F_1}$

The thrust expression contains two terms, familiar from conventional salient-pole synchronous machine theory, due to saliency (proportional to sin 2θ) and to excitation (proportional to sin θ). The angle, θ, represents the space phase displacement between the ac mmf and the polar axis of the machine.

Similarly, normal force, F_z, is given by:

$F_z = \frac{\partial W_m}{\partial z}$, leading to:

$$F_2 = \frac{2\mu_0 \, a \, P \, F_1^{\,2} \tau}{g_1'^{\,2} \pi} \left[\left(\alpha + \frac{\pi - \alpha}{k^2}\right) (1 + 2c^2) \right.$$

$$\left. + \left(1 - \frac{1}{k^2}\right) \left(\frac{1}{2} \cos 2\theta \sin 2\alpha + 4c \cos\theta \sin\alpha\right) \right] \qquad (2.5)$$

The above expressions were first derived by Rummich (1972) and were subsequently used by many authors. Their inadequacy lies in the idealized air gap field distribution -- no account is taken of steel reluctance or fringing. Finite element analysis of the machine shows that a knowledge of the field distribution in the HLSM is necessary for performance evaluation. The above expressions yield optimistically high results.

The stored energy method may also be used to determine terminal characteristics of the HLSM, by calculating parameters in the two-reactance equivalent circuit model of the machine, shown in Figure 2.2. This equivalent circuit is the same as that conventionally used for salient-pole synchronous machines, and has been used extensively in the literature. The same equivalent circuit is used in this report, but with parameters determined by finite element analysis using non-linear steel magnetization characteristics.

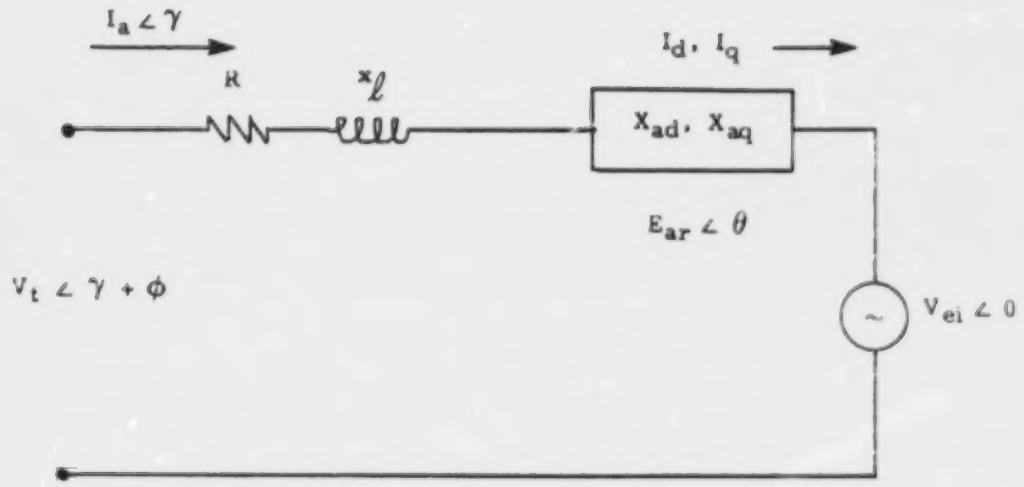

R = per-phase armature resistance
x_l = per-phase armature leakage resistance
x_{ad} = per-phase d-axis armature reactance
x_{aq} = per-phase q-axis armature reactance
V_{ei} = fundamental voltage induced in armature phase by dc excitation
θ = field angle
ϕ = power factor angle

Figure 2.2 Per-phase two-reactance equivalent circuit of the HLSM

With ac mmf in the d-axis ($\theta = 0$), and zero dc excitation, the stored energy in the gap is equated to:

$$W_m \,)\, \theta = 0,\ F_0 = 0 \;=\; \frac{3}{2}\,\frac{x_{ad}}{\omega}\,I^2 \qquad (2.6)$$

Similarly, with ac mmf in the q-axis ($\theta = \pi/2$):

$$W_m \,)_{\theta = \frac{\pi}{2},\ F_0 = 0} \;=\; \frac{3}{2}\,\frac{x_{aq}}{\omega}\,I^2 \qquad (2.7)$$

For a smooth air gap machine:

$$W_m)_{k=1,\ F_0=0} = \frac{3}{2}\frac{x_m}{\omega} I^2 \qquad (2.8)$$

These expressions give:

$$x_{ad} = \frac{1}{\pi}\left[\left(\alpha + \frac{1}{2}\sin 2\alpha\right)\left(1 - \frac{1}{k}\right) + \frac{\pi}{k} \right] x_m \qquad (2.9)$$

$$x_{aq} = \frac{1}{\pi}\left[\left(\alpha - \frac{1}{2}\sin 2\alpha\right)\left(1 - \frac{1}{k}\right) + \frac{\pi}{k} \right] x_m \qquad (2.10)$$

where: $$x_m = \frac{24\,\mu_0\ \omega\tau a\,(k_w N_{ph})}{\pi^2\ P\ k_c\ g} \qquad (2.11)$$

2.2.2 Fourier Series

The Fourier series method uses the same assumptions with regard to steel characteristics (i.e. $\mu \rightarrow \infty$) as the stored energy method, and results in exactly the same expressions for the machine reactances x_{ad} and x_{aq}. Following the method of Lawrenson and Agu (1964) for reluctance machine analysis, an air gap permeance function is defined in terms of harmonic components for the machine geometry shown in Figure 2.1.

$$\Lambda(x) = 2\,\mu_0\, a\, dx \left[\frac{1}{g'_2} + \beta\left(\frac{1}{g'_1} - \frac{1}{g'_2}\right)\right.$$

$$\left. + \frac{2}{\pi}\sum_{n=1}^{\infty}\frac{1}{n}\left(\frac{1}{g'_1} - \frac{1}{g'_2}\right)\sin \pi n \beta \cos\frac{2 n \pi x}{\lambda}\right] \qquad (2.12)$$

Putting $F_{ac} = F_1 \cos(\pi x/\tau - \omega t + \theta)$, a corresponding expression for the air gap flux density as a function of time and space can be developed.

Noting that only the fundamental component of B(x,t) is significant for electromechanical energy conversion, the fundamental flux per pole can be computed from:

$$\phi \text{ per pole} = 4\, a \int_{-\tau}^{\tau} B_1(x,t)\, dx \qquad (2.13)$$

with $\theta = 0$ for ϕ_d, $\theta = \pi/2$ for ϕ_q.

Putting $g_1' = g_2'$, both ϕ_d and ϕ_q reduce to ϕ_m, then $\phi_d/\phi_m = x_{ad}/x_m$ and $\phi_q/\phi_m = x_{aq}/x_m$, yielding the same analytical expressions as in (2.9) and (2.10)

The induced voltage, V_{ei}, in the equivalent circuit of Figure 2.2 can also be found by Fourier analysis. For the machine geometry shown in Figure 2.1, the amplitude of the space fundamental of air gap flux density, $\hat{B}_1$, is given by:

$$\hat{B}_1 = \frac{2}{\pi g_1'} \mu_0 F_0 \left(1 - \frac{1}{k}\right) \sin \alpha \qquad (2.14)$$

The rms value of induced voltage, V_{ei}, is then:

$$V_{ei} = 8\sqrt{2}\, f\, k_w\, N_{ph}\, a\, \tau \hat{B}_1 \qquad (2.15)$$

This induced voltage is subject to the same inaccuracy as the force, as steel saturation is neglected. Finite element analysis shows that Fourier analysis overestimates V_{ei} substantially near the normal operating condition of a well-designed machine.

Once equivalent circuit parameters are found, the per-phase equivalent circuit can be used to find both mechanical output and terminal characteristics of the HLSM.

Power output $P_m = 3\, V_{ei}\, I_a \cos\gamma = F_x\, v_s \qquad (2.16)$

where: $v_s = 2\tau f$

or $P_m = 3\, V_t\, I_a \cos\phi - 3\, I_a^2\, R \qquad (2.17)$

$$\text{Efficiency } \eta = \frac{F_x v_s}{F_x v_s + 3 I_a^2 R} \tag{2.18}$$

$$\text{Power factor, } \cos \phi = \frac{F_x v_s + 3 I_a^2 R}{3 V_t I_a} \tag{2.19}$$

2.2.3 Conformal Transformation

Conformal transformation techniques have been used by Levi et al. (1978) and by Slemon et al. (1980). The technique is an analytical method for the solution of Laplacian fields, and is applicable to determining the field distribution in air/steel structures having regular boundary shapes. The HLSM configuration, as shown in Figures 1.2 and 2.1, lends itself to this type of analysis.

While conformal transformation removes one of the limitations of the stored energy and Fourier series methods by its ability to produce a better representation of the air gap field distribution (i.e. it takes into account fringing into the sides of the track poles), it retains the limitation that the steel is assumed to have very high permability. Boundaries are assumed to be equipotentials. While the saturation characteristics of the HLSM can be simulated by use of correction factors, the usefulness of conformal transformation lies in its ability to provide a better determination of machine reactances and of the induced voltage, at least under low saturation conditions.

Slemon et al. (1980) used this technique to seek the optimum track pole geometry which maximizes the induced voltage, V_{ei}, for a given dc excitation of the machine. V_{ei} may be calculated from the modulation of the dc field, caused by track saliency, by use of (2.15).

From the armature field distribution, with dc mmf set to zero and with ac mmf positioned in the d-axis or in the q-axis, the peak value of the fundamental component of the air gap flux density at the armature surface, $B_{d,q}$, can be determined by Fourier analysis of the field distribution. Then:

$$X_{ad,aq} = 8\,\omega\,\frac{k_w\,N_{ph}}{I_{peak}}\,a\,\frac{\tau}{\pi}\,\hat{B}_{d,q} \qquad (2.20)$$

2.2.4 Non-Linear Magnetic Circuit Analysis

The non-linear magnetic circuit analysis, developed by Atherton (1981), was the first which took into account the saturable characteristics of the machine steels. The method takes the slotted armature and salient pole track structure of the HLSM and, assuming that no flux enters the sides of the track poles, computes the effective reluctance of all flux paths between the surfaces (parallel to the direction of motion) of the armature teeth and track pole, as shown in Figure 2.3. With this model of the field distribution, the modulation of the dc field in the air gap can be found as a function of excitation, allowing the induced voltage, V_{ei}, to be calculated. Superposition of the armature mmf allows the mechanical power of the HLSM to be evaluated as a function of the field angle.

A comparison between the assumed excitation field distribution in Figure 2.3 and the distribution found by finite element analysis (see Figure 4.4) shows that the non-linear magnetic circuit method is inaccurate to the extent that it neglects the flux entering the sides of the rail bars. The non-linear magnetic circuit analysis was used by Atherton for preliminary design and control studies -- the finite element method was used for detailed design studies described in this report.

2.2.5 Finite Element Method

As is evident from comments in the above sections, the finite element method was considered the most appropriate for HLSM design and analysis, in view of its ability to determine the field distribution in two-dimensional sections of the HLSM, while taking into account the saturable characteristics of machine steels.

The analytical basis and application of finite element methods to HLSM design and performance evaluation is fully discussed in Section 3 of this report.

(a)

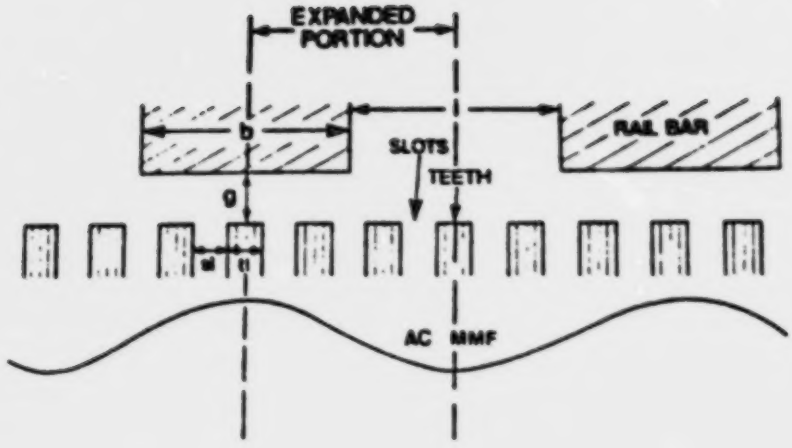

(b)

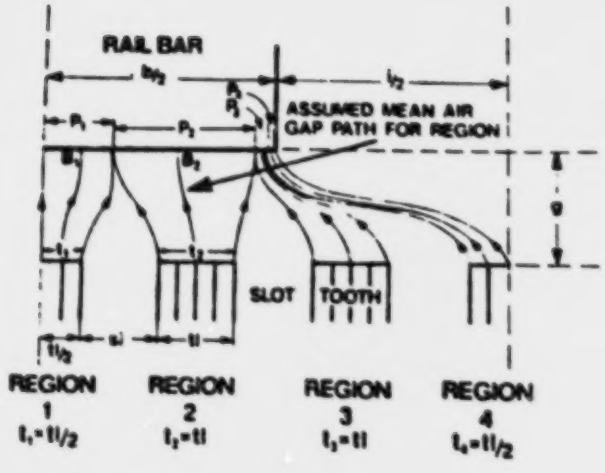

Figure 2.3 (a) The model of the HLSM used for non-linear magnetic circuit analysis
(b) An expanded pole pitch showing the assumed air gap field distribution and flux paths for analysis

3. FINITE ELEMENT ANALYSIS

3.1 The Finite Element Method

The finite element method, as used for analysis and design studies of the HLSM, is a numerical technique for the solution of the magnetic field distribution in a two-dimensional plane of an electromagnetic device. The analytical approach consists of finding a function that minimizes a certain specified energy functional over the entire region.

While three-dimensional finite element analyses are under development, these are computationally complex, and are considered unnecessary for analysis of the HLSM. The use of a two-dimensional program implies that the modelled device or machine is infinitely long and of uniform cross-section in the direction perpendicular to the plane of analysis. However, by considering the field distribution in three orthogonal planes of the HLSM, a clear picture of the three-dimensional field distribution in the machine can be established.

Since the HLSM is a synchronous machine, a magnetostatic analysis is adequate for design studies and performance evaluation. The only eddy currents produced in HLSM operation are those resulting from nonmagnetized steel entering the front end and magnetized steel leaving the rear end of the machine. This is known, from experimental studies, to be of lesser significance than the well-known end-effect in LIMs, because of the high resistivity and discontinuous nature of the steel rail bars.

3.2 Variational Formulation

Consider a two-dimensional field problem in which an electric machine is considered to be infinitely long in the z-direction. All currents are assumed to flow only in the z-direction of the machine. Thus, there will only be a z-directed component of magnetic vector potential, $A(x,y) = A_z(x,y)$. In the region, R, of the x-y plane (the cross-section of the machine), bounded by the line S, the magnetic vector potential satisfies the non-linear Poisson equation:

$$\frac{\partial}{\partial x}\left(\nu \frac{\partial A}{\partial x}\right) + \frac{\partial}{\partial y}\left(\nu \frac{\partial A}{\partial y}\right) = - J \qquad (3.1)$$

subject to appropriate boundary conditions. Here the reluctivity, ν, is both field- and position-dependent, and J is the current density vector in the z-direction of the machine.

In order to achieve a numerical solution to the partial differential equation (3.1), the problem is formulated in variational terms. Thus, the non-linear two-dimensional field problem will be expressed by an energy functional:

$$F = \iint_R \left(\int_0^B \nu \, b \, db \right) dS - \iint_R J \, A \, ds \qquad (3.2)$$

where B is the flux density in the x-y plane of the machine.

The non-linear equation (3.1) is the Euler equation of (3.2). The true solution to the field problem is obtained by searching for a function, A, that minimizes the functional.

The finite element method involves the following basic steps:

(i) discretization of the field region into sub-regions of elements, interconnented at nodal points. Figure 3.1 shows the discretization of a half section of the HLSM.

(ii) identification of each sub-region, e.g. excitation, air ($\mu = 1$), or steel (μ variable, according to a defined non-linear magnetization curve)

(iii) representation of each sub-region by an appropriate trial solution

(iv) application of boundary conditions

(v) assembly and solution of nodal equations in matrix form, to find vector potential distribution at discretization nodes

(vi) calculation of physical quantities (field distribution, induced voltage, force, etc.) as required.

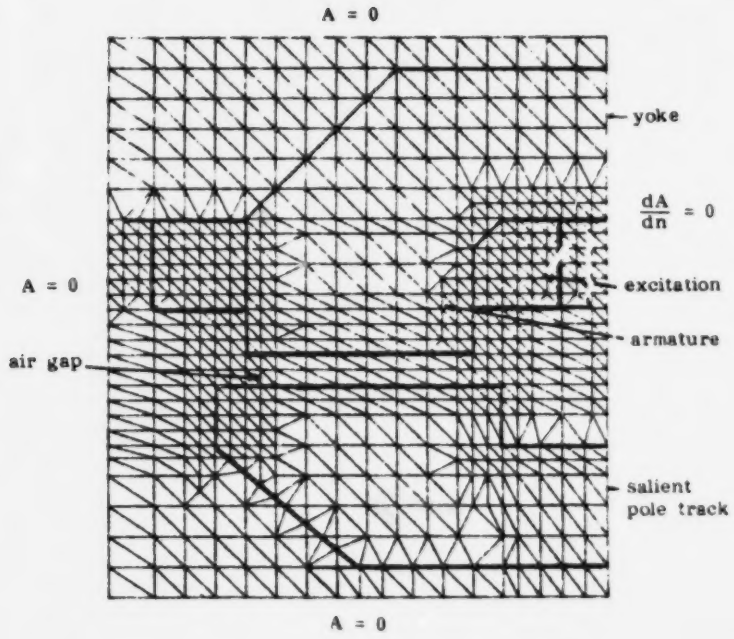

Figure 3.1 Transverse half section of a linear homopolar synchronous machine discretized into triangular elements

Let the region of interest be subdivided into triangular elements, as shown in Figure 3.1. Trial solutions to the field problem of these first-order elements are represented by a first-degree polynomial in terms of the nodal values of the vector potential. Hence, the magnetic vector potential at a point in a triangle is taken as:

$$A = \frac{1}{2\Delta} \sum_{i=1}^{3} (a_i + b_i x + c_i y) A_i \qquad (3.3)$$

where the index, i, ranges over the triangle vertices, l, m, n, and

$$a_l = x_m y_n - y_m x_n \;,\; a_m = x_n y_l - y_n x_l \;,\; a_n = x_l y_m - y_l x_m$$

$$b_l = y_m - y_n \;,\; b_m = y_n - y_l \;,\; b_n = y_l - y_m$$

$$c_l = x_m - x_n \;,\; c_m = x_n - x_l \;,\; c_n = x_l - x_m$$

Δ = area of the triangle

A_l, A_m, A_n = vertex values of A

Differentiating equation (3.3) with respect to x and y, the corresponding magnetic flux density within the triangle is:

$$B = \frac{\partial A}{\partial x} + \frac{\partial A}{\partial y}$$

$$B = \frac{1}{2\Delta} \sum_{i=1}^{n} (b_i A_i + c_i A_i)$$

The magnitude of the flux density is given as:

$$|B| = \frac{1}{2\Delta} \sqrt{(b_l A_l + b_m A_m + b_n A_n)^2 + (c_l A_l + c_m A_m + c_n A_n)^2} \quad (3.4)$$

The minimization of the functional is achieved by setting the first derivative of (3.2) to zero with respect to each of the vertex values of vector potential:

$$\frac{\partial F}{\partial A_i} = 0 \text{ for all } i \quad (3.5)$$

To obtain an approximate solution for A everywhere, the surface integrals of (3.2) are conveniently written in a way that permits evaluation over a triangle at a time. For a typical triangle, say the t^{th}, the surface integral, F_t, is given as:

$$F_t = \iint_t \left(\int_0^B \nu \, b \, db - JA \right) dx \, dy \quad (3.6)$$

Equation (3.5) may now be written as:

$$\frac{\partial F}{\partial A_i} = \sum_{\text{triangles}} \frac{\partial F_t}{\partial A_i} = 0 \qquad (3.7)$$

The summation is carried over all triangles in the subdivision. For each triangle:

$$\frac{\partial F}{\partial A_i} = \iint_t \left[\frac{\partial}{\partial B} \int_0^B \nu \, db \, \frac{\partial B}{\partial A_i} - J \frac{\partial A}{\partial A_i} \right] dx \, dy$$

$$= \iint \left[\nu \, B \frac{\partial B}{\partial A_i} - J \frac{\partial A}{\partial A_i} \right] dx \, dy \qquad (3.8)$$

Unless i is one of the vertices, differentiation with respect to A_i clearly produces zero. Thus, equation (3.8) is an expression in three variables, A_i. The flux density expression, equation (3.4), is substituted into equation (3.8). After some manipulation, equation (3.8) becomes:

$$\frac{\nu}{4\Delta} \begin{bmatrix} b_l b_l + c_l c_l & b_l b_m + c_l c_m & b_l b_n + c_l c_n \\ b_l b_m + c_l c_m & b_m b_m + c_m c_m & b_m b_n + c_m c_n \\ b_l b_n + c_l c_n & b_m b_n + c_m c_n & b_n b_n + c_n c_n \end{bmatrix} \begin{bmatrix} A_l \\ A_m \\ A_n \end{bmatrix} = \begin{bmatrix} 1/3 & J_l \\ 1/3 & \times J_m \\ 1/3 & J_n \end{bmatrix} \qquad (3.9)$$

Matrix equation (3.9) represents the minimization of the energy functional in one triangle. To obtain a corresponding representation of the entire region, an equation corresponding to equation (3.9) is written for each of the triangles in the subdivided region. The resulting assembly of algebraic equations can be combined into a single matrix equation given by:

$$[T] \, [A] = [J] \qquad (3.10)$$

where: [T] is the matrix obtained from the individual element matrices as in equation (3.9)

[A] is the column vector of the vertex values of vector potentials

[J] is the column vector of vertex values of current densities.

3.3 Boundary Conditions

In Figure 3.1, the space surrounding the half section of the HLSM must also be discretized to take into account any leakage field outside the machine structure. The discretization is extended to a distance at which it is considered that the field will be negligibly small. The boundary conditions must then be specified. Two commonly used boundary condition were applied to the analysis of the HLSM:

(i) Dirichlet boundary condition. The value of the vector potential is specified at nodal points on the boundary, i.e.

$$A = g, \text{ along a boundary}$$

This condition was used, usually with g=0, to represent zero normal component of field along a boundary. No field crosses this boundary.

(ii) Neumann boundary condition. The value of the normal derivation of vector potential along a boundary is specified, i.e.

$$\frac{dA}{dn} = p, \text{ along a boundary}$$

For p=0, this boundary condition is automatically incorporated in the field equations, and corresponds to a uniform normal component of field along the boundary. All fields cross this boundary at right angles, and it represents a line of symmetry of the field distribution in a cross-section of a machine or device.

3.4 B-H Characteristics

Numerical methods in which the non-linearity of the ferromagnetic materials is fully considered require a representation of the magnetization curve of the material. A method of linear interpolation, introduced by Trutt et al. (1968), is employed to calculate the

permeability for each triangular element in the material. For a good approximation of the representation of the magnetization curve, a large number of points (typically 30-50) on the curve are specified. Convergence of the solution of the field problem represented by equation (3.10) must be ensured to produce an accurate result, as discussed in Section 3.6.

Those parts of the HLSM which are exposed to time-varying field, i.e. around the armature, must be constructed with laminated material (silicon steel). Those parts which carry dc field and are exposed to little time-varying flux can be fabricated from solid material (cast steel). Magnetization curves for silicon steel and for cast steel are shown in Figure 3.2.

3.5 Representation of Excitation

3.5.1 DC Excitation

A discretization of the transverse half section of the HLSM was shown in Figure 3.1. Each side of the machine has a source of dc mmf, which drives excitation flux across the air gap to magnetize the salient-pole track structure. In finite element analysis, the current distribution is represented by point current sources located at each node in the subregion of excitation. For a dc mmf of NI amp turns, in a coil of cross-sectional area A, the overall current density is NI/A amps/m^2. The nodes of each triangle in the excitation subregion are then assigned a current $NI\Delta/3A$, where Δ is the area of the triangle.

3.5.2 AC Excitation

In a synchronous machine, the ac field distribution under steady-state conditions may be determined by freezing the three-phase ac current at a particular instant of time. The excitation may be represented either by modelling the complete slotting of the armature or by replacement of the actual winding current distribution by an equivalent current sheet. The latter method was considered entirely adequate for HLSM analysis.

In the finite element method, the equivalent current sheet is approximated by discrete current nodes along the armature surface. It is

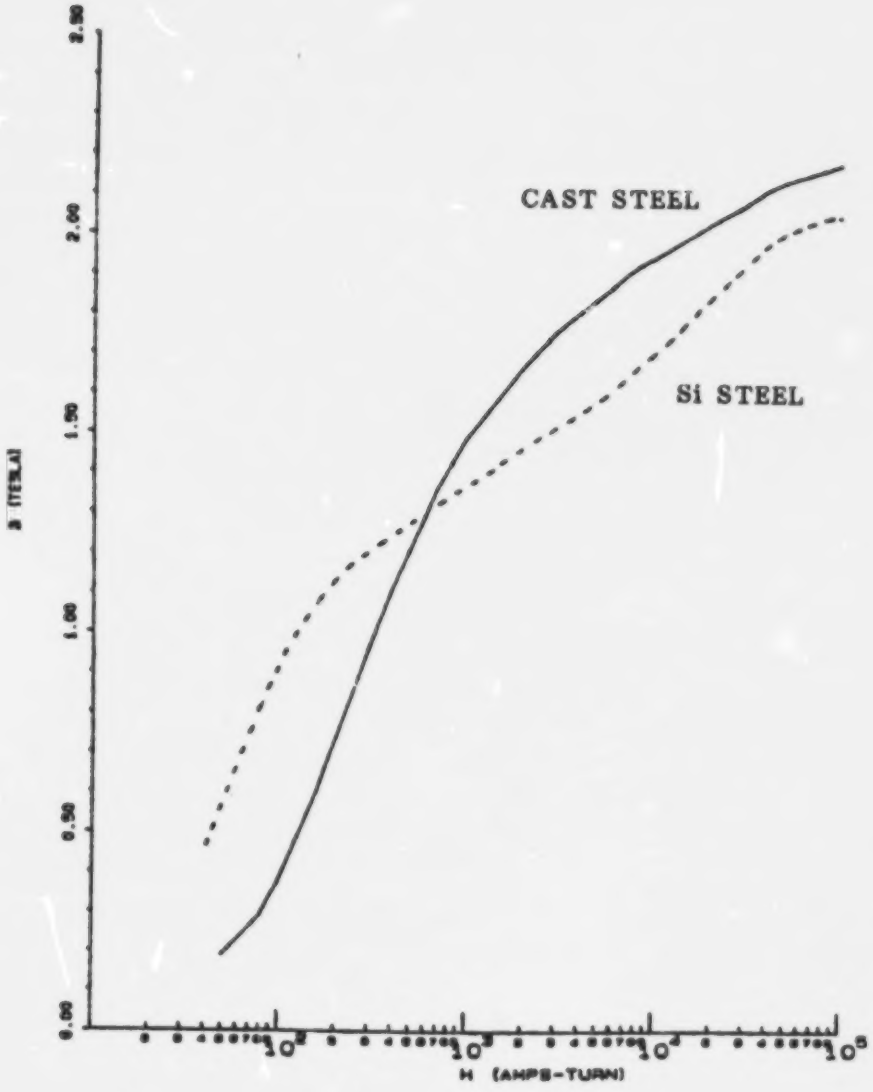

Figure 3.2 B-H characteristics assumed for silicon-steel laminations and for cast steel

necessary to have a sufficient number of current nodes to provide a good representation of the actual armature mmf distribution. The current at each node was determined from the following expression, from Alger (1965):

$$J = J_m \cos (\pi x/\tau + \delta) \qquad (3.11)$$

where:

$$J_m = \frac{3\sqrt{2}\, I_{rms}\, k_w\, N_c\, f_k}{N_n}$$

where: N_c represents the number of conductors per slot

N_n is the number of current nodes along the armature surface

f_k is the amplitude factor to account for the peak value of the fundamental of Fourier analysis of the current waveform

δ is the field angle of the machine

$\pi x/\tau$ is the position of the current nodes along the armature surface

k_w is the winding factor.

3.6 Solution of the Non-Linear Equations

The Gaussian elimination method is used to solve equation (3.10). Due to the symmetry of the global matrix, it can be reduced to a sparse matrix, thus saving computation storage and CPU time. The flow chart for computation of field distributions using the two-dimensional non-linear finite element method is shown in Figure 3.3.

For the non-linear problem, convergence of the solution is achieved through the use of a convergence factor, e, in:

$$\mu'_{new} = \mu_{old} + e\,(\mu_{new} - \mu_{old}) \qquad (3.12)$$

where: μ'_{new} is the relative permeability of each element for the next iteration

μ_{new} is the relative permeability of each element, corresponding to the flux density in each element and the B-H curve

μ_{old} is the previous relative permeability of each element for that particular iteration.

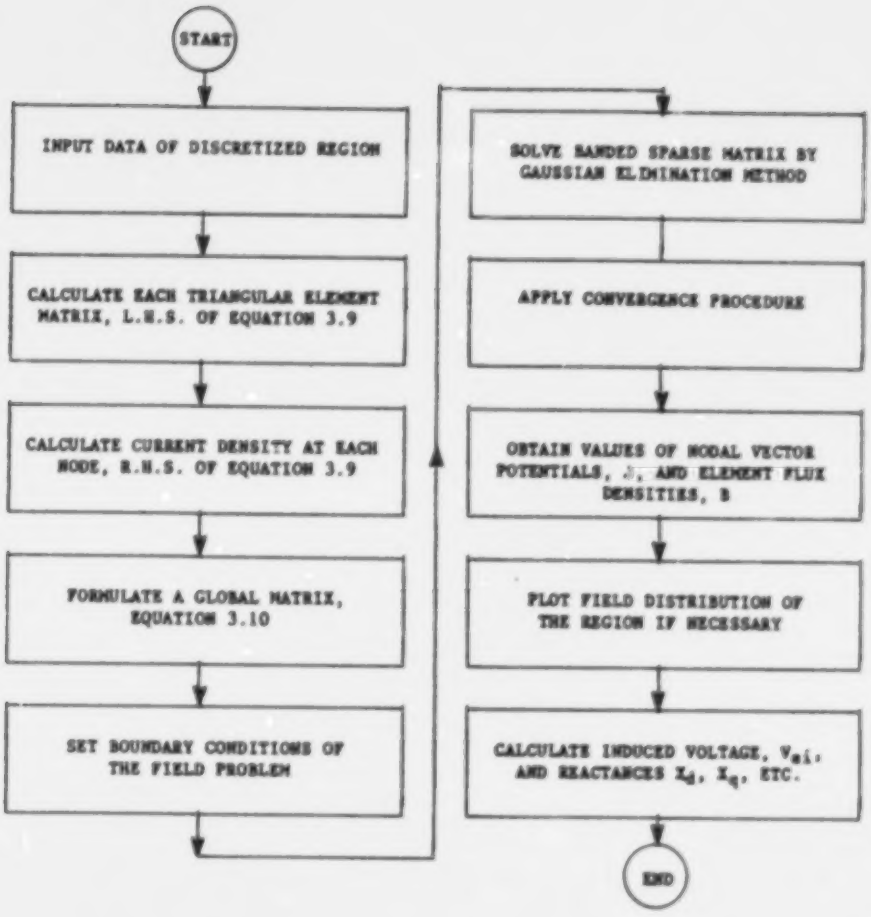
START
INPUT DATA OF DISCRETIZED REGION
CALCULATE EACH TRIANGULAR ELEMENT MATRIX, L.H.S. OF EQUATION 3.9
CALCULATE CURRENT DENSITY AT EACH NODE, R.H.S. OF EQUATION 3.9
FORMULATE A GLOBAL MATRIX, EQUATION 3.10
SET BOUNDARY CONDITIONS OF THE FIELD PROBLEM
SOLVE BANDED SPARSE MATRIX BY GAUSSIAN ELIMINATION METHOD
APPLY CONVERGENCE PROCEDURE
OBTAIN VALUES OF NODAL VECTOR POTENTIALS, A, AND ELEMENT FLUX DENSITIES, B
PLOT FIELD DISTRIBUTION OF THE REGION IF NECESSARY
CALCULATE INDUCED VOLTAGE, V_{ai}, AND REACTANCES X_d, X_q, ETC.
END

Figure 3.3 Flow chart of the two-dimensional finite element method for non-linear magnetic field problems

Initially, the relative permeability of each element is set at a reasonable value for the material. The flux density of each element is then calculated by the finite element program. From the B-H curve, a new value for the relative permeability of each element is calculated corresponding to the first computed flux density. After this first iteration, the relative permeability of each element, as calculated from the B-H curve, is used directly to recompute the element flux density. The above equation (3.12) is applied only after the second iteration.

To obtain an accurate solution, three factors have to be considered to ensure its convergence:

(i) maximum potential change between successive iterations

(ii) average potential change between successive iterations

(iii) permeability change.

The solution is said to converge when the following criteria are met:

(i) maximum potential change between iterations $<$ accuracy limit

(ii) average potential change between iterations $<$ accuracy limit

(iii) permeability change $<$ 5 per cent.

The permeability change is calculated as follows:

$$P_{change} = \frac{\mu_{new} - \mu_{old}}{\mu_{new}} \times 100\% \qquad (3.13)$$

The accuracy limit found to be adequate (see Section 3.8) was, dependent on the field problem, in the range 0.01-0.001 per unit.

Figure 3.4 shows the flow diagram for the convergence of solution of the banded symmetric matrix of equation (3.10). A series of computer runs was made to determine the range of convergence factor which provides the best result. The range of preferred convergence factor was found to be between 0.10 and 0.20 for problems in which the magnetic circuit does not reach saturation. For deep saturation conditions, the preferred convergence factor was considerably less, and was typically 0.01 to 0.02.

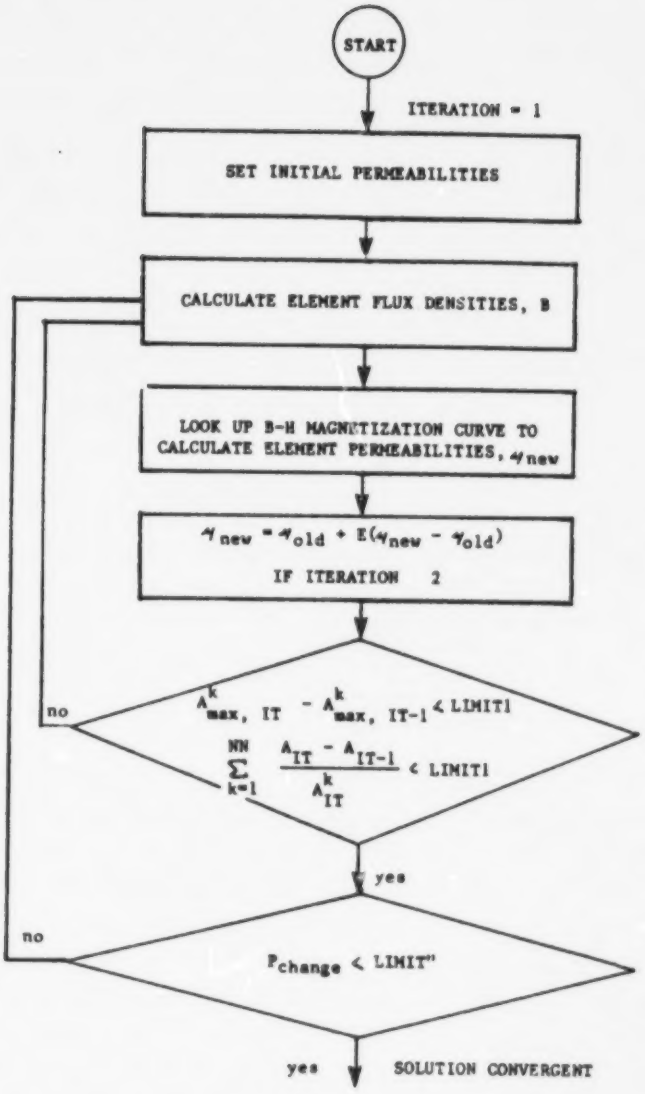

Figure 3.4 Flow chart of the convergence procedure in the non-linear two-dimensional finite element method

3.7 Field Plotting

After a convergent solution has been achieved, the field plot can be generated by plotting contours of constant vector potential, A. The density of "flux lines" in a given field distribution can be selected by specifying a particular increment of vector potential, ΔA, between lines.

A typical transverse dc field distribution, corresponding to the discretization of Figure 3.1, is shown in Figure 3.5. Similarly, a typical ac armature field distribution in the longitudinal plane, with ac mmf in the d-axis of the HLSM, is shown in Figure 3.6.

The discontinuous nature of some of the lines in these and other field plots in this report is a consequence of linear interpolation and the coarseness of the discretization. The finite element solution produces vector potential values at each node in the discretization. The A value at any point on the triangle side is assumed to vary linearly between nodal values. Contours of constant A are plotted by linearly joining appropriate points on triangle sides.

3.8 Validation of Solution

In order to validate the finite element solution, an internal check was incorporated into the computer program. According to Ampere's circuital law:

$$\int \mathbf{H}.d\mathbf{l} = \int \mathbf{J}.d\mathbf{a} \qquad (3.14)$$

Thus, the line integral of H.dl around any closed field line must equal the total current enclosed. In general, the finite element solutions were iterated until this equality was met to within ±1 per cent.

For further validation, derived machine characteristics, e.g. open circuit voltages, reactances, forces, etc., can be compared with experimental results. The HLSM tested by Slemon et al. (1980) has been modelled, and some of its characteristics have been checked against finite element analysis, as discussed in Section 4.

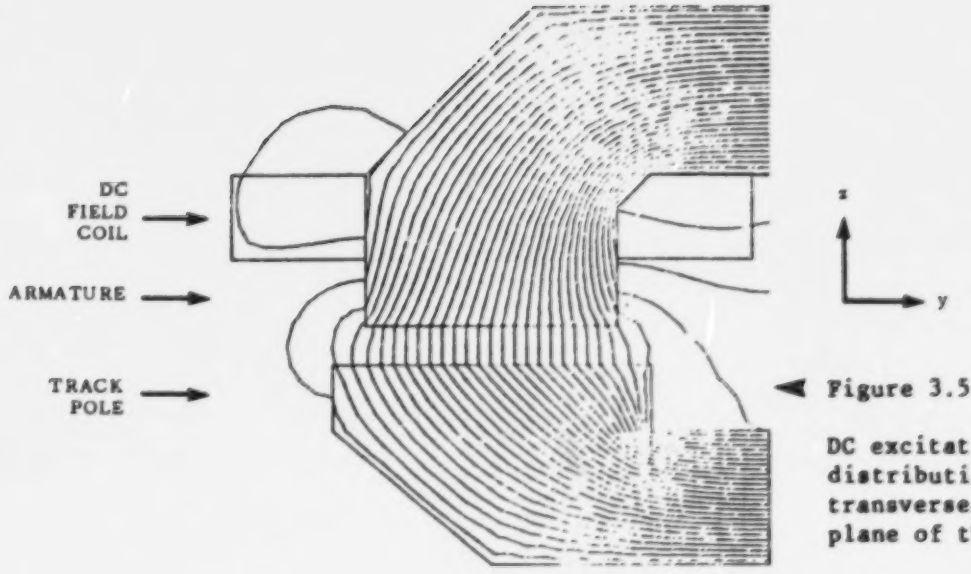

Figure 3.5

DC excitation field distribution in a transverse half plane of the HLSM

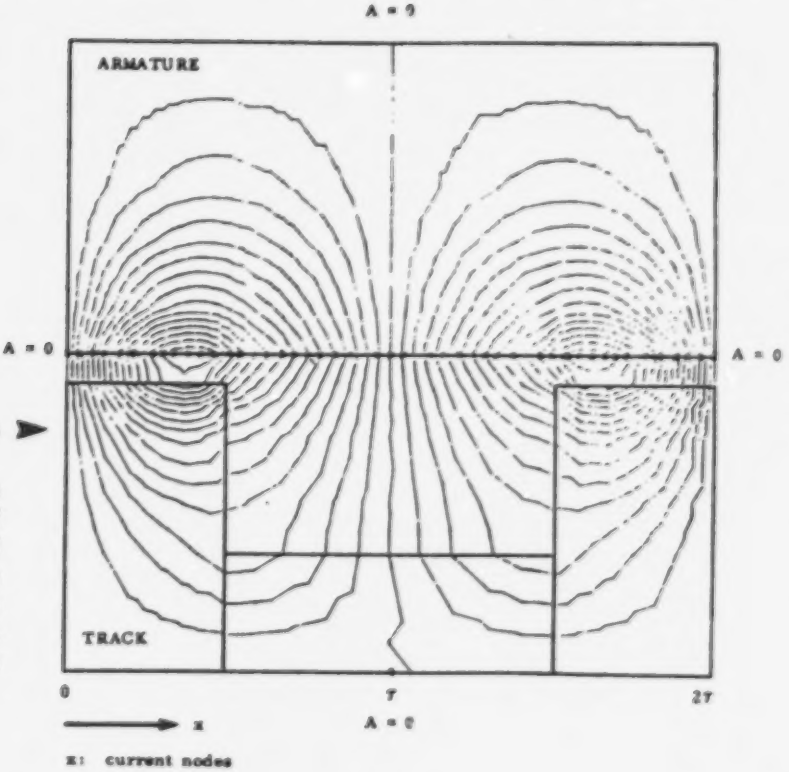

Figure 3.6

Armature field in the longitudinal plane of the HLSM, with ac mmf in the d-axis. The armature current is modelled by 47 current nodes per wavelength along the armature surface.

4. FINITE ELEMENT MODELLING OF THE HLSM

4.1 The Equivalent Circuit

As noted in Section 2, the modelling approach selected for analysis and design studies of the HLSM was the two-reactance equivalent circuit of the machine, with the armature reactance and induced voltage parameters being determined by the finite element method. The equivalent circuit is again shown in Figure 4.1.

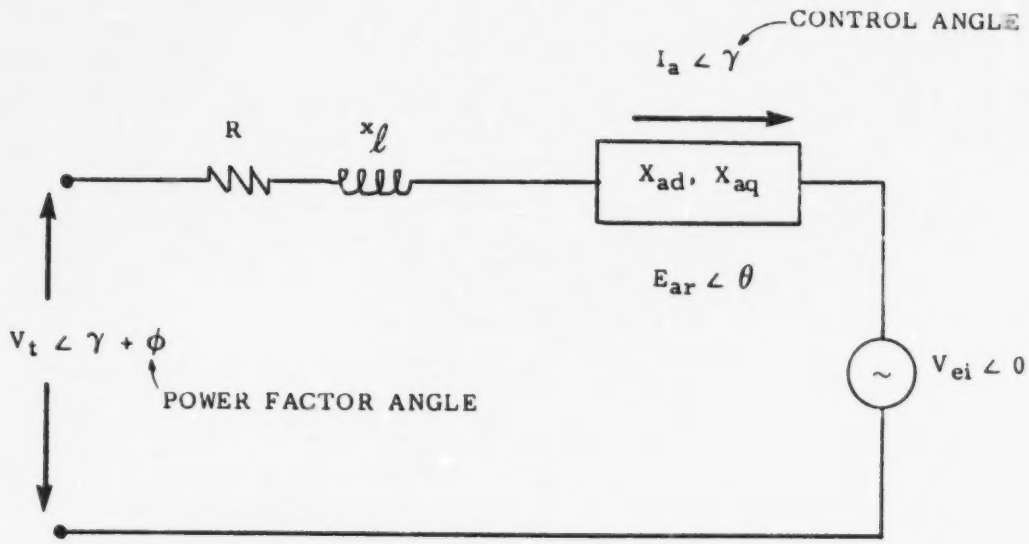

Figure 4.1 The two-reactance equivalent circuit model of the HLSM

Analytical expressions and a program for the computation of parameters in the per-phase equivalent circuit are given in Appendix A. The armature resistance, R, was determined from the armature winding geometry. The leakage reactance, X_L, was determined by summing conventional ac machine expressions for slot leakage, end winding leakage, tooth tip leakage, and harmonic leakage, as given in Liwschitz-Garik and Whipple (1946). An additional leakage component in that part of the armature which crosses the central gap of the HLSM was computed and added into X_L.

The computer program also calculates the armature reactances X_{ad} and X_{aq} from the stored energy/Fourier analysis expressions (2.9, 2.10), the magnetizing reactance of a smooth air gap machine (2.11), and the induced voltage based on Fourier analysis (2.15). These parameters were computed for comparison with those derived by finite element analysis.

4.2 Induced Voltage

4.2.1 General Approach

The voltage, V_{ei}, is induced in the armature winding of the HLSM by the time-varying flux produced by the saliency of the track structure and by forward movement of the machine. The induced voltage is given by:

$$V_{ei} = 2\sqrt{2}\,\pi\, f\, N\, k_w\, \phi_{lmax} \qquad (4.1)$$

where: f is the supply frequency

N is the number of armature turns/phase

k_w is the winding factor

ϕ_{lmax} is the amplitude of the fundamental component of flux per pole

It is, therefore, necessary to evaluate ϕ_{lmax} by finite element analysis. This was achieved by considering the dc field distribution in both transverse and longitudinal planes of the machine.

4.2.2 Transverse Section

In order to determine the total excitation flux per armature wavelength, the field distribution in a transverse half-section of the machine was considered, as shown in Figure 4.2. Since this plane is perpendicular to the armature slotting and track saliency, an effective air gap must be introduced:

$$g_{effective} = G * C * g \qquad (4.2)$$

where: g is the minimum (polar) air gap of the HLSM

C is Carter's coefficient, representing the effective gap increase due to armature slotting

G is Green's coefficient, representing the effective gap increase due to the coarse track saliency.

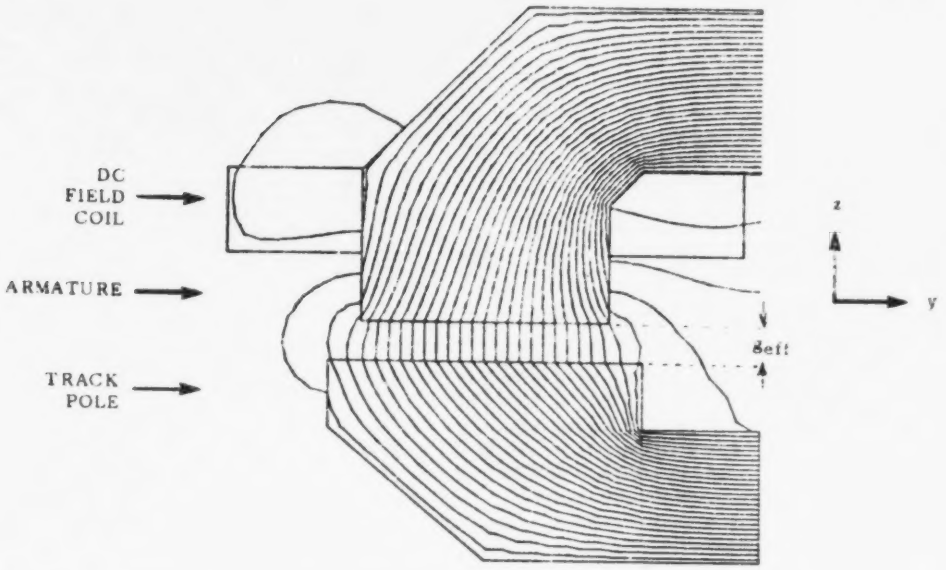

Figure 4.2 The field distribution in a transverse half section of the HLSM

Carter (1900) calculated the ratio of equivalent to actual air gap, as influenced by flux fringing in a slot of infinite depth in a two-dimensional section of an armature. The Carter's coefficient, which is used to calculate the air gap coefficient due to armature slotting in the HLSM, is given as:

$$C = \frac{tw\ (5g + sw)}{tw\ (5g + sw) - sw^2} \qquad (4.3)$$

where: sw is the width of the slot opening

tw is the tooth width

g is the actual air gap.

The top curve in Figure 4.3 gives the variation of Carter's coefficient as a function of slot opening/gap ratio.

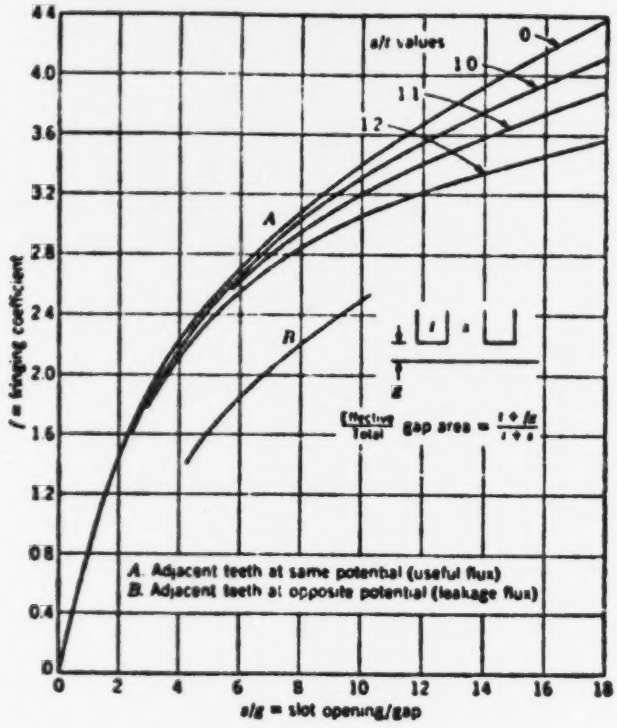

Figure 4.3 Air gap fringing coefficient, from Alger (1965)

Green (see Alger, 1965) extended Carter's coefficient to account for large ratios of slot width to air gap and finite tooth width. Green's modified coefficient is used to calculate the equivalent air gap due to the track saliency of the HLSM. Green's modified coefficient is:

$$G = \frac{tw + sw}{tw + f\,g} \qquad (4.4)$$

where f is the fringing factor obtained from Figure 4.3.

The Carter's coefficient in equation (4.3) can also be obtained from equation (4.4) in the mit s/t = 0.

The applicability of Carter's and Green's coefficients to the geometry of the HLSM was checked by finite element computations on a longitudinal section of the machine. In this case, the ferromagnetic materials were assumed to be infinitely permeable. The air gap coefficient was determined from two modelling steps:

(i) the slot and tooth geometry of the armature was modelled, with the track replaced by a smooth ferromagnetic plane. The armature slots were made infinitely deep. The outer boundaries were set to constant magnetic vector potentials, but with a different value for each boundary. The integral of H.dl of flux lines crossing the actual air gap, g, was determined from the finite element solution.

(ii) The slot and tooth geometry of the armature was replaced by a smooth armature surface, and the vector potential values at the outer boundaries kept the same. The air gap, g_2, was varied to obtain the same value of $\int$ H.dl as in (i) above. The air gap coefficient due to armature slotting is given by the ratio g_2/g_1.

Similarly, the air gap coefficient due to track saliency was determined. This method was used to compute the air gap coefficients G and C for the armature and track slot geometry of Slemon's test HLSM (see Appendix B) at 5, 10 and 15 mm air gaps. A comparison between the air gap coefficients as given by the analytical expressions (4.3) and (4.4) and as computed by finite elements is given in Table 4.1. Close agreement is evident.

TABLE 4.1

AIR GAP COEFFICIENTS FOR SLEMON'S TEST HLSM

Actual Air Gap (mm)	Green's Modified Coefficient (track)	Carter's Coefficient (armature)	Finite Element Results	
			Track	Armature
5	1.681	1.368	1.709	1.369
10	1.541	1.184	1.545	1.192
15	1.454	1.123	1.456	1.131

The field solution for the transverse half section, as shown in Figure 4.2, with an effective air gap of appropriate magnitude, can therefore be used to determine the total excitation flux per wavelength of the HLSM.

4.2.3 Longitudinal Section

Having determined the total excitation flux per wavelength, the longitudinal section of the HLSM, as shown in Figure 4.4, was considered. The actual tooth and slot geometry of the armature, and the actual air gap and track pole length, were represented. However, in view of the staggered pole geometry of the track, it was necessary to determine an equivalent track slot depth.

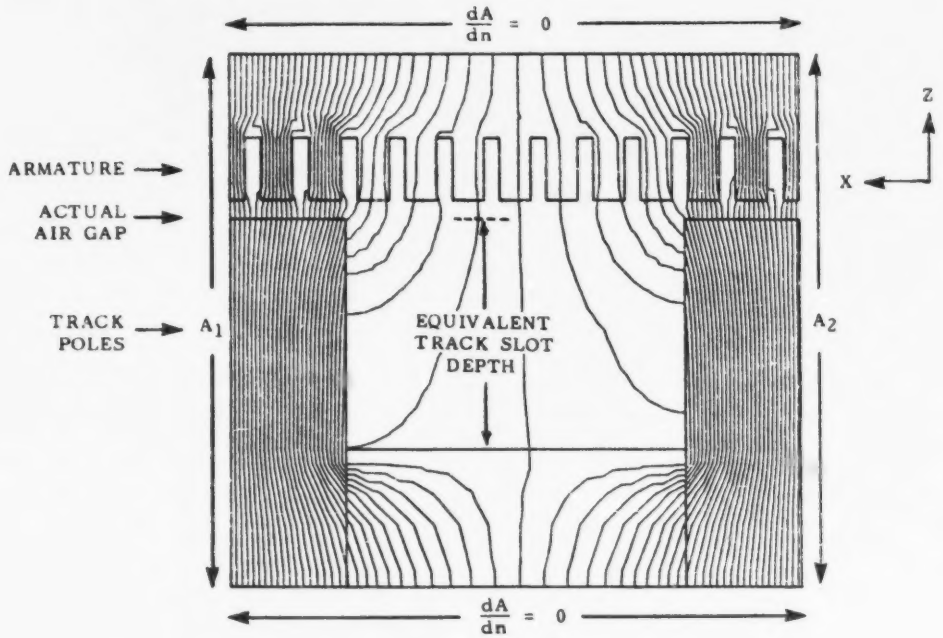

Figure 4.4 The excitation field distribution in one longitudinal wavelength of the HLSM

Figure 4.5(a) shows a section of the armature positioned between track poles. In this region, it is clear that the dc field does not cross the air gap normally but will take a curved interpolar path before it reaches the track yoke. Thus, the effective track slot depth is not

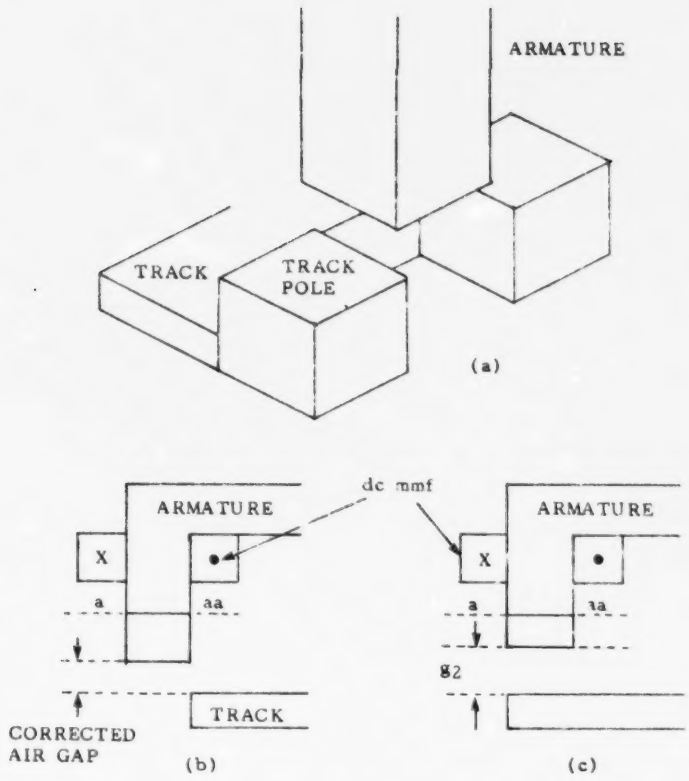

Figure 4.5 Configuration used to determine the equivalent track slot depth of the HLSM

equal to the depth of the track pole. The effective track slot depth is an important factor in determining the modulation of the dc field.

An equal reluctance approach using the finite element method was used to determine the effective track slot depth. With reference to Figure 4.5, there are two basic steps:

(i) The transverse interpolar half section of the machine was used. The air gap was first corrected for armature slotting. For a particular value of dc mmf, with the configuration as shown in Figure 4.5(b), the total flux along the line a-aa was determined.

(ii) Maintaining the same dc mmf, an effective air gap, g_2, in the interpolar region was sought to obtain the same flux along a-aa in Figure 4.5(c).

The reluctance of the path taken by the flux lines in Figure 4.5(b) is equal to that in Figure 4.5(c) when g_2 is adjusted to obtain the same excitation flux. The effective track slot depth is given by g_2 minus the corrected air gap.

The experimental data obtained by Slemon et al. (1980) was used to validate the finite element method of calculating induced voltage. Detailed design parameters of the test HLSM are given in Appendix B. For a dc mmf of 13.6 kA.turns, the mean flux density along line a-aa in Figure 4.5(b) (step 1 of the equal reluctance method) is 1.909 Telsa. The mean flux density along a-aa in Figure 4.5(c), as a function of effective track slot depth, with infinitely permeable armature and track, is listed in Table 4.2. For Slemon's test HLSM, the effective track slot depth can be taken as 58 mm.

TABLE 4.2

EQUAL RELUCTANCE APPROACH: TOTAL FLUX DENSITY AS A FUNCTION OF EFFECTIVE TRACK SLOT DEPTH FOR SLEMON'S TEST HLSM

Effective Track Slot Depth (mm)	Mean Flux Density (Tesla)
20	2.825
30	2.415
40	2.168
50	1.999
55	1.937
58	1.904
60	1.883

Figure 4.6 shows field plots for the two machine configurations used to evaluate the effective track slot depth.

Having established the geometry for a longitudinal wavelength of the HLSM, as in Figure 4.4, the boundary conditions were then established. At the upper and lower boundaries, the Neumann boundary condition (i.e. $dA/dn = 0$) was used. This field enters and leaves these boundaries at right angles. In the HLSM, these field lines would cross the yokes of the machine and track and would join up across the armature and air gap on the opposite side of the motor.

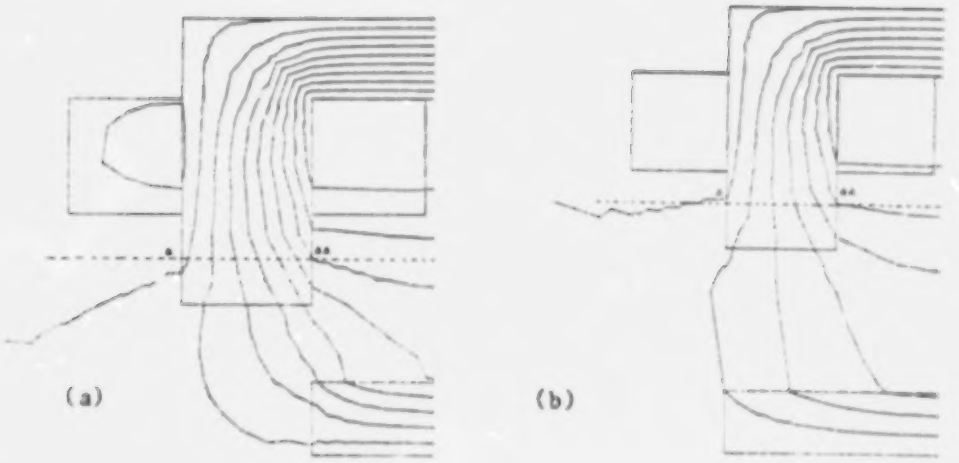

Figure 4.6 Field plots for the geometries used to establish the effective track slot depth:
(a) the interpolar transverse dc field distribution
(b) the field distribution for an equal reluctance condition

The end boundaries were set to constant vector potentials, A_1 and A_2. Thus, no flux would cross these boundaries, as expected for the d-axis of the HLSM. The difference between A_1 and A_2 determines the amount of flux that crosses the section. (A_1-A_2) was adjusted to introduce the same total flux per wavelength as was found from analysis of the transverse section. The saliency of the track distributes this flux to produce a longitudinal modulation of the air gap field, as shown in Figure 4.7.

4.2.4 Calculation of Induced Voltage

The transverse field distributions in the polar and interpolar regions, as shown in Figures 4.8 and 4.9 for Slemon's test HLSM, and the longitudinal field distribution shown in Figure 4.7 allowed the total flux linkage in the armature winding, $\phi(x)$, to be determined as a function of position. The value of ϕ_{1max}, the amplitude of the fundamental flux per pole, in (4.1), as required for computation of the induced voltage, was then determined by Fourier analysis of $\phi(x)$, using a Fast Fourier Transform program.

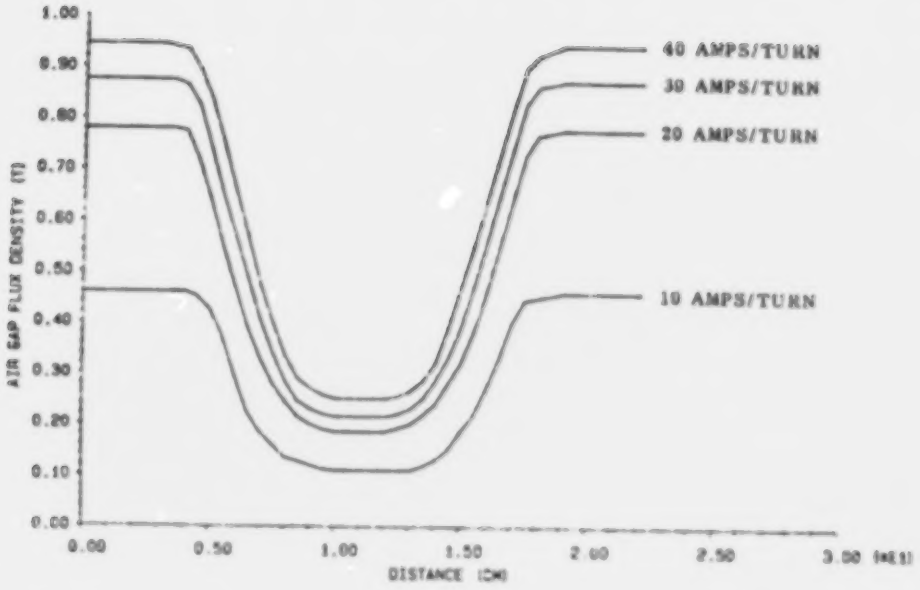

Figure 4.7 The flux density (averaged over a tooth pitch) at half the armature slot depth as a function of longitudinal position over a wavelength of Slemon's test HLSM. These finite element results were calculated for an actual air gap of 10 mm and for four values of dc excitation.

With regard to the operation of the HLSM, it is important to note that the track saliency merely modulates and does not reverse the flux per pole. It is this feature that limits the induced voltage and which forces the HLSM to be larger and heavier than an induction motor or conventional synchronous motor for a given mechanical performance.

4.2.5 Validation of Analysis

The finite element method for determining induced voltage was validated by comparison with data obtained by Slemon et al. (1980) on a three-pole test HLSM. The design parameters of this machine are listed in Appendix B.

The open-circuit characteristics, from numerical analysis and test results, are shown in Figure 4.10. The test results showed some speed dependence (the voltage at 25 m/sec being about 20 per cent lower than that at 5 m/sec), presumably due to eddy current effects at the entry and exit ends of the short (three-pole) test HLSM. For comparison

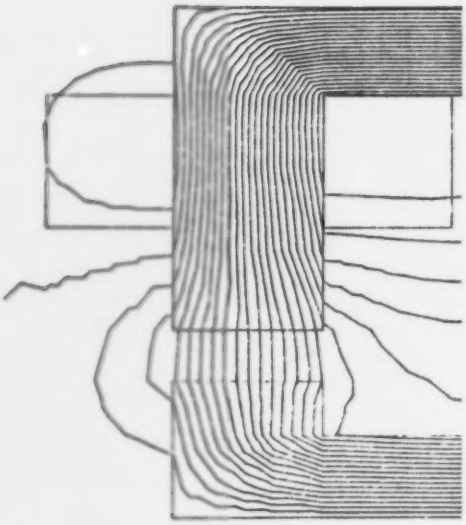

(a)

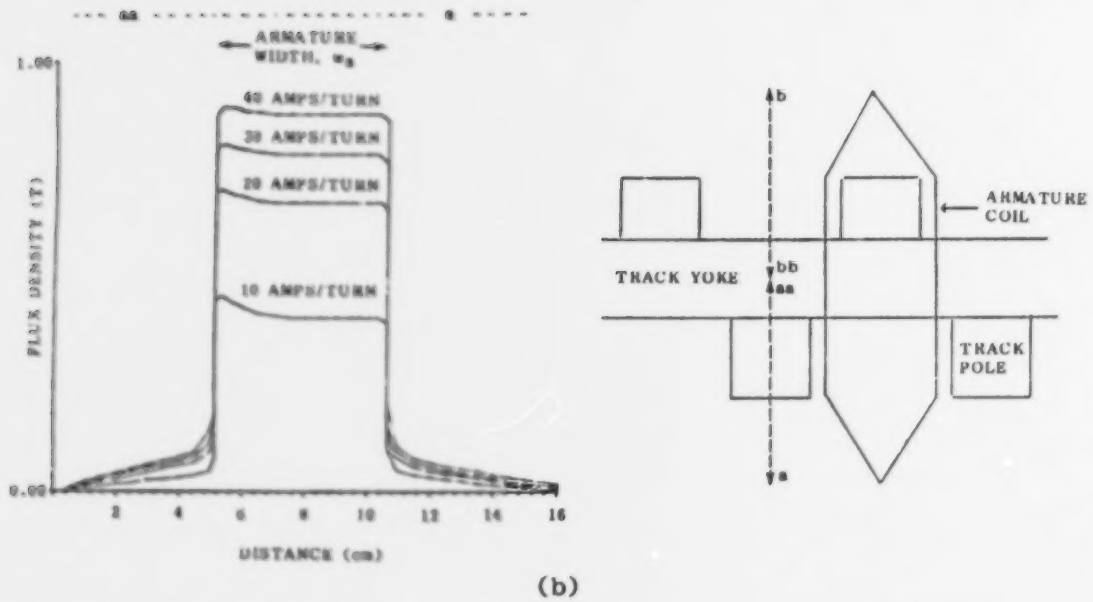

(b)

Figure 4.8 (a) Polar transverse dc field distribution of Slemon's HLSM with a doubly corrected air gap of 18.25 mm (actual air gap of 10 mm) and dc excitation of 30 A/turn; difference between constant vector potential lines = 0.00330 weber/meter.
(b) The corresponding flux density, B_z, shape function across and either side of the armature width.

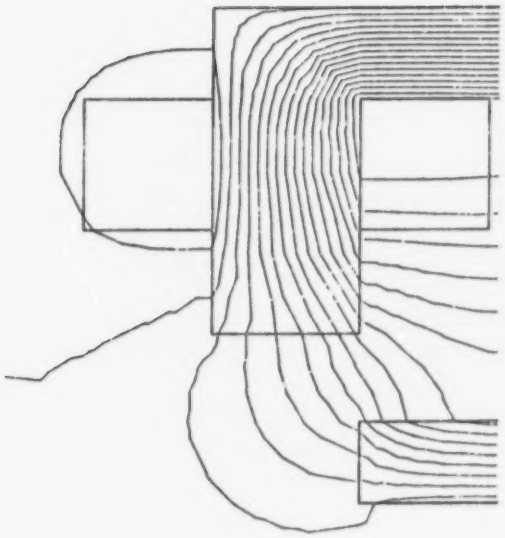

(a)

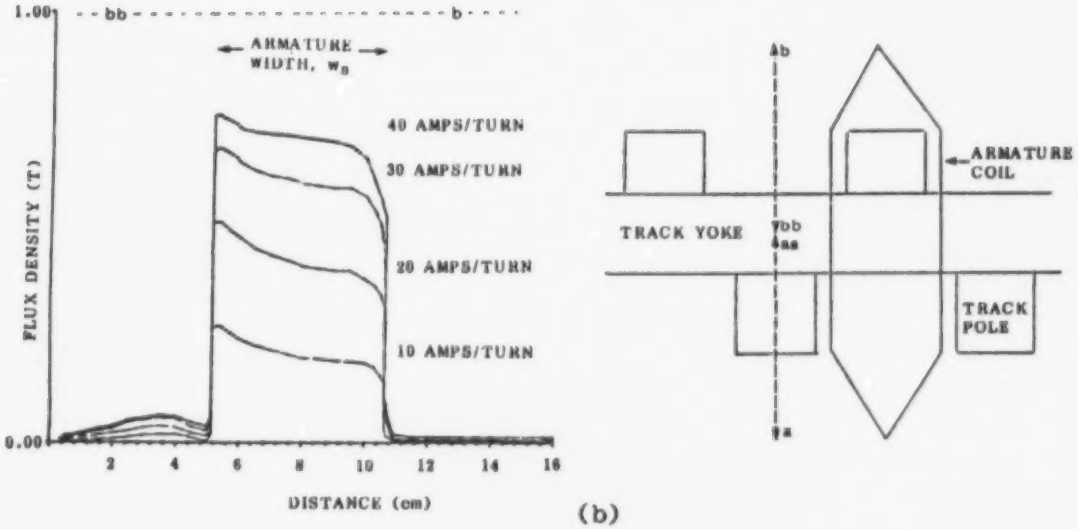

(b)

Figure 4.9 (a) Interpolar transverse dc field distribution of Slemon's HLSM with a doubly corrected air gap of 18.25 mm (actual air gap of 10 mm) and dc excitation of 30 A/turn; difference between constant vector potential lines = 0.00330 weber/meter.
(b) The corresponding flux density, B_z, shape function across and either side of the armature width.

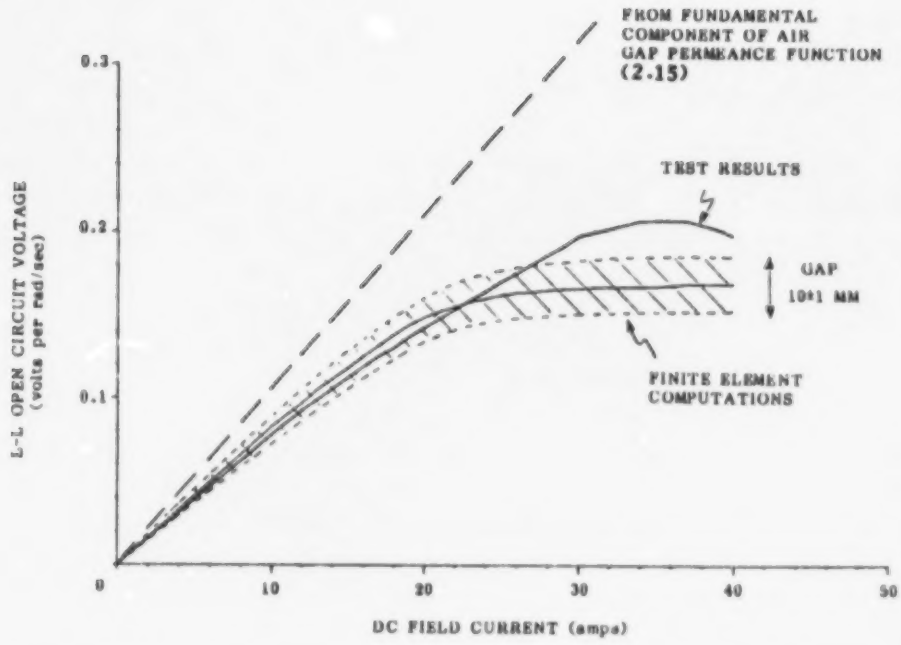

Figure 4.10 The open circuit characteristics of the University of Toronto experimental machine (Slemon et al. (1980)) at 10 mm gap; test results extrapolated to zero frequency, finite element computation and analysis based on the fundamental component of the air gap permeance function

purposes, the open-circuit data were extrapolated to zero speed to remove these end effects.

The discrepancy between finite element computations and test results in the saturated region is considered to be due to an uncertainty in the magnetization characteristics of the steels used in the test machine. The computations were based on the excitation field modulation over a wavelength which was not influenced by the ends of the machine, and the shortness of the test HLSM may also have had an effect.

For comparison, the open-circuit characteristic determined from (2.15), using the fundamental component of the flux modulation based on an idealized air gap permeance function, is also shown in Figure 4.10. It is apparent that this simple analytical approach, as used by many authors in the literature, yields values of induced voltage that are optimistically high, particularly for high dc excitation such that

parts of the magnetic circuit are driven towards saturation. It is apparent that steel reluctance must be taken into account in evaluating the capabilities of the HLSM.

In general, agreement between numerical analysis and experimental results is sufficiently good to show the usefulness of the finite element technique in HLSM analysis and design studies.

4.3 Armature Reactance

4.3.1 General Approach

The d- and q-axis armature inductances, L_{ad} and L_{aq}, as required for the equivalent circuit of the HLSM, were also determined by finite element analysis, and are compared with values from other analytical techniques and with measured values for Slemon's test HLSM in Table 4.3. In general, the inductances can be calculated from the fundamental component of armature flux linkage per pole:

$$L_{ad,q} = \frac{2 \hat{\Phi}_{d,q} N_{ph} k_w}{I_a} \qquad (4.5)$$

where $\hat{\Phi}_{d,q}$ is the maximum fundamental flux per pole due to peak armature current, I_a, with armature mmf located in the d- and q-axes, respectively, of the machine.

Rather than placing the armature current in discrete slots, the mmf distribution is modelled by point currents at nodes along a flat armature surface, representing an equivalent current sheet, as shown in Figure 4.11.

4.3.2 Finite Element Method I

To develop the method for computing $x_{ad,q}$, the geometry of Slemon's test HLSM was considered. Initially, it was assumed that the armature flux distribution would be confined to the longitudinal plane of the machine. Corresponding field plots when the armature mmf is located in the d and q axes of the HLSM are shown in Figures 4.12 and 4.13, respectively.

TABLE 4.3

EXPERIMENTAL AND CALCULATED VALUES OF D AND Q AXIS INDUCTANCES FOR SLEMON'S TEST HLSM, USING AN EQUIVALENT TRACK SLOT DEPTH OF 58 MM

Air Gap (mm)	Experi-* mental Values		Stored Energy/ Fourier Series		Conformal Trans-formation		Finite Element Method I		Finite Element Method II	
	L_{ad} (mH)	L_{aq} (mH)	L_{ad} (mH)	L_{aq} (mH)	L_{ad} (mH)	L_{aq} (mH)	L_{ad} (mH)	L_{aq} (mH)	L_{ad} (mH)	L_{aq} (mH)
5	1.090	1.090	1.010	0.987	1.490	1.460	0.541	1.421	0.866	1.421
10	0.770	0.770	0.628	0.618	0.904	0.869	0.449	0.852	0.721	0.852
15	0.530	0.530	0.461	0.454	0.680	0.660	0.331	0.645	0.622	0.645

* An equivalent synchronous inductance was measured experimentally, and was assigned to both L_{ad} and L_{aq} (see Section 4.3.4).

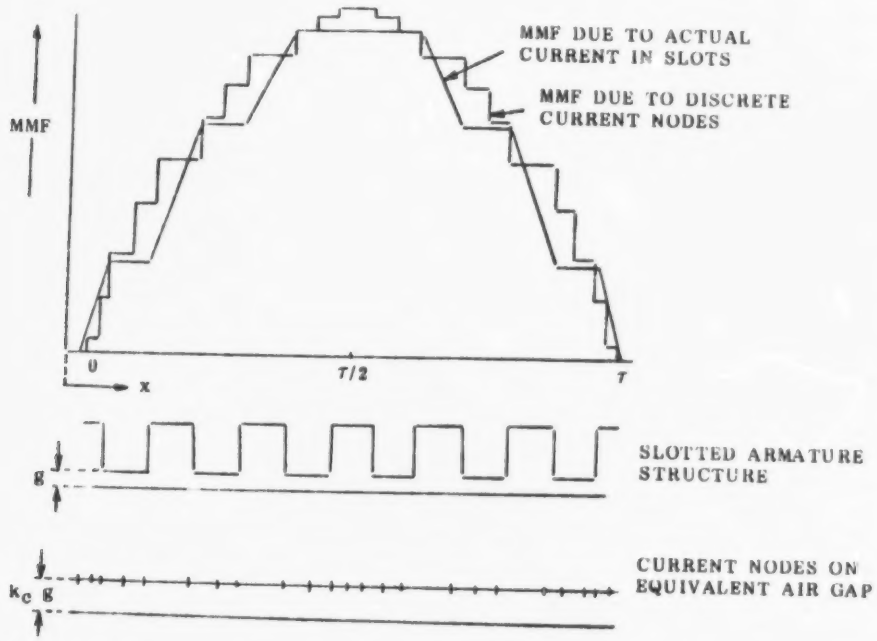

Figure 4.11 MMF distribution: comparison of mmf due to actual currents in slots and mmf due to discrete equivalent current sheet

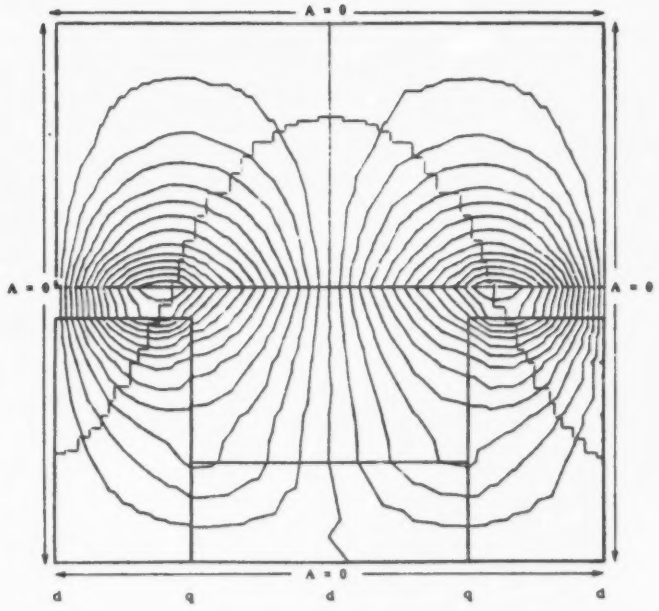

◄ Figure 4.12

Longitudinal section of Slemon's HLSM with armature mmf in d-axis (armature current of 80 A/turn, actual air gap of 10 mm)

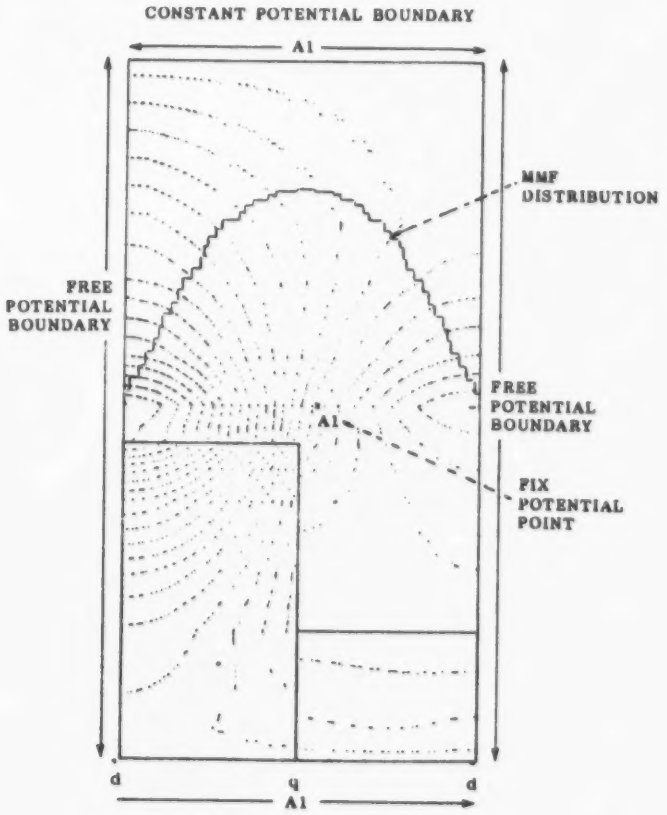

Figure 4.13 ►

Longitudinal section of Slemon's HLSM with armature mmf in q-axis (armature current of 80 A/turn, actual air gap of 10 mm)

As for the induced voltage, the net flux linkage in a complete full-pitch diamond-shaped armature winding, $\phi(x)$, was determined as a function of position from the field plots. The fundamental component was then determined by Fourier analysis to yield $\hat{\phi}_{d,q}$ for (4.5). For Slemon's test HLSM with zero dc excitation, the inductances were found to be independent of armature current over the range 80-240 A.

The finite element values of L_{ad} and L_{aq} developed by this first method were found to differ significantly from those deduced from experimental data, as shown in Table 4.3. This necessitated further analysis, as detailed below.

4.3.3 Finite Element Method II

A more detailed consideration of the armature flux distribution of the complete machine revealed that flux was not, in general, restricted to longitudinal paths but that significant flux could cross diagonally over the yoke of the machine. This flux cannot be represented in the sections of Figure 4.14(a), and so was modelled in a manner similar to that developed by Baudon (1979). Conceptually, the yoke was cut longitudinally and the entire machine was folded down to yield the geometry shown in Figure 4.14(b).

In the modified geometry, the field distribution with the armature mmf in the q-axis is identical to that found for the original longitudinal section. No flux crosses the yoke and track, and the q-axis inductance is therefore unchanged. However, with armature mmf in the d-axis, it is energetically favourable for significant flux to cross the yoke and track diagonally. This flux crosses two small air gaps, rather than the one small air gap and one large air gap which would be the case if the flux were restricted to longitudinal paths.

For finite element computations, the modified geometry of the HLSM was modelled as shown in Figure 4.15. For the d- and q-axis armature mmf's, one complete wavelength (2τ) of the machine was discretized. The required boundary condition of zero normal component of flux (because of field symmetry) was established by assigning a very low relative permeability (0.0001) to two thin boundary regions, as shown. This had the effect of introducing a "magnetic insulator." The return path for the diagonal flux was provided by the outer regions of very high relative permeability, simulating a magnetic "short circuit."

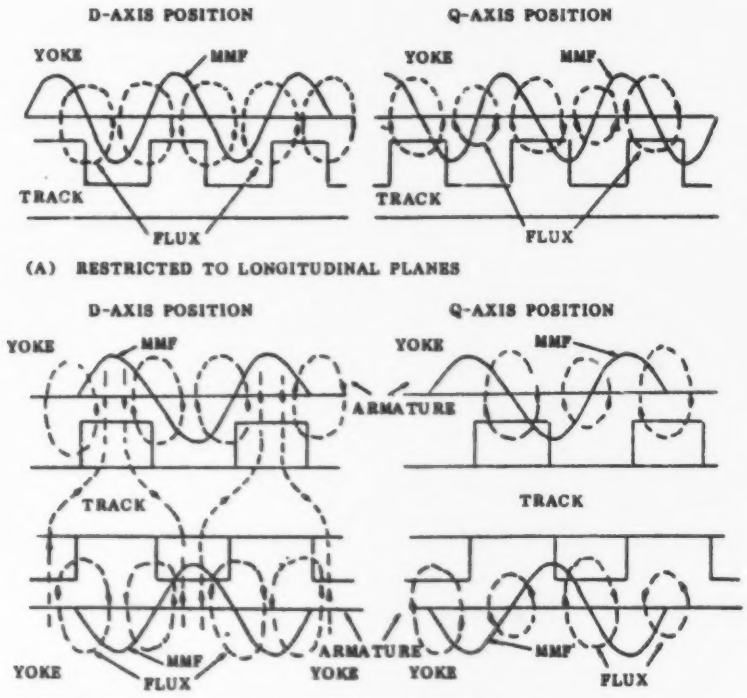

◄ Figure 4.14

Models for the armature flux distribution

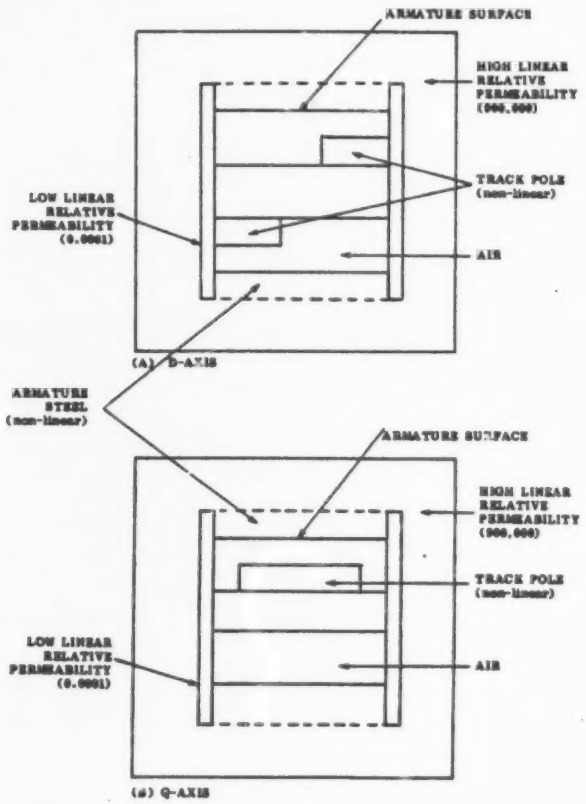

Figure 4.15 ►

D-axis and q-axis configurations for the determination of reactance by finite element method II

The d-axis and q-axis flux distributions corresponding to the geometries of Figure 4.15 are shown in Figure 4.16. The corresponding d- and q-axis inductances, computed from the fundamental components of armature flux linkages, are listed in Table 4.3.

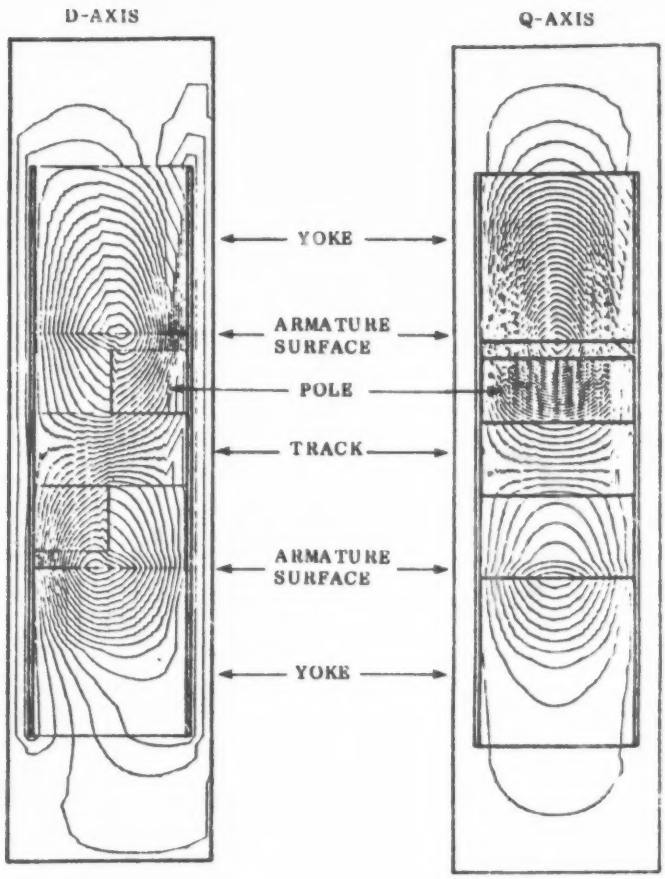

Figure 4.16 Flux distributions due to armature mmf in the d-axis and in the q-axis of the developed model of Slemon's staggered pole HLSM

4.3.4 Discussion

With reference to Table 4.3, it is apparent that there is a significant difference between the various analytical methods and experimental results.

In their evaluation of the HLSM, Slemon et al. (1980) noted that analysis of the reactances by conformal transformation gave the result that L_{ad} and L_{aq} were nearly equal, indicating that their machine could develop little salient torque. This was supported by the shape of the measured thrust/field angle characteristic, which showed a cos γ dependence with insignificant cos 2γ component. For comparison with the experimental results, Slemon et al. averaged the L_{ad} and L_{aq} values found by conformal analysis. The experimental reactance was deduced from open circuit and short circuit characteristics extrapolated to zero speed and was presented by Slemon et al. as an effective non-salient armature reactance. For comparison purposes, this armature reactance has been assigned to both L_{ad} and L_{aq} in Table 4.3.

The armature reactance values calculated from the stored energy/Fourier series expressions (2.9 and 2.10) were also fairly close to each other, but of lower magnitude than the conformal transformation values. In the development of the analytical expression, the following ideal assumptions were made:

(i) Flux crosses perpendicularly from the armature surface to the track. Hence, the flux density in the air gap is given by the mmf divided by the product of permeability and gap length:

$$B_g = \mu_0 \frac{MMF(x))}{g(x)}$$

The finite element field plots in Figures 4.12 and 4.13 (and indeed simple magnetic circuit considerations) show that this assumption is inaccurate.

(ii) Saturation effect is ignored. The finite element method has been used to show that this is valid up to the rated armature current for Slemon's test HLSM of 240 amperes/phase.

The variations of air gap flux density with respect to position along the longitudinal section of the machine with armature mmf in the d-axis and in the q-axis, respectively, are shown in Figures 4.17(a) and (b).

The q-axis condition indicates that, in the interpolar region, the flux density in the ideal condition is much smaller than that calculated from the finite element method. As a result, the value of X_{aq} obtained from the stored energy method appears to be low and inaccurate.

Both finite element models predict a q-axis inductance that is larger than the d-axis inductance. This is considered to be a result of the characteristic saliency of the homopolar machine -- each side of the machine has a pole every wavelength rather than every pole pitch as in the case of the conventionally excited synchronous machine. Balchin and Eastham (1979) have reported the experimental observation of L_q greater than L_d for an HLSM, consistent with the finite element results found here.

It remains to be noted that, in Table 4.3, only the finite element method predicts $L_{aq} > L_{ad}$. Both conformal transformation and stored energy/Fourier series analyses give $L_{aq} < L_{ad}$, in apparent agreement with test data from Slemon's HLSM. These analytical and experimental results leave some uncertainty about the accuracy of the finite element modelling technique for the evaluation of armature reactances. In view of this uncertainty, the computed electrical and mechanical performance of the selected HLSM design for urban transit applications was subjected to a sensitivity analysis to examine the effect of varying both the magnitude and ratio of X_{ad} and X_{aq}. It was found that the HLSM design could achieve the specified performance, for a range of armature reactances from 50 to 150 per cent of computed values, with little change in terminal characteristics and with only minor changes in the control algorithm (see Section 5.4.1). For the purposes of HLSM assessment, the uncertainty in X_{ad} and X_{aq} is considered unimportant.

(a)

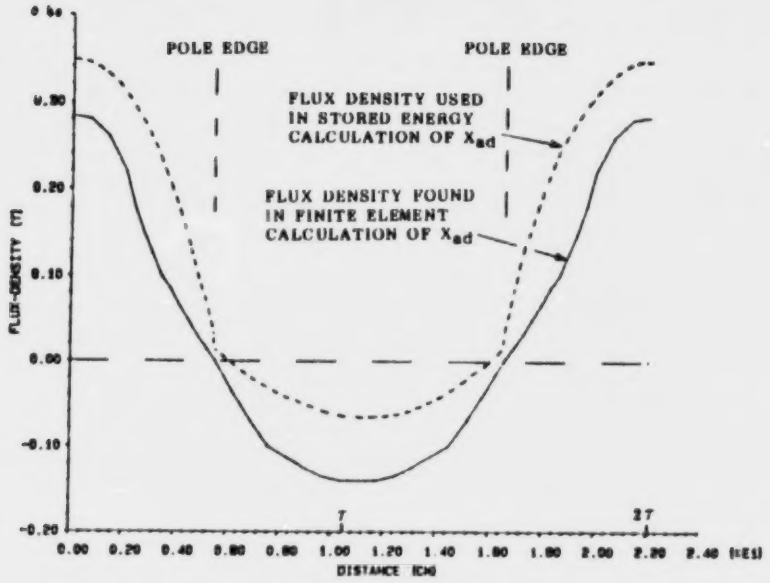
POLE EDGE
POLE EDGE
FLUX DENSITY USED IN STORED ENERGY CALCULATION OF X_{ad}
FLUX DENSITY FOUND IN FINITE ELEMENT CALCULATION OF X_{ad}
FLUX-DENSITY (T)
DISTANCE (CM)

(b)

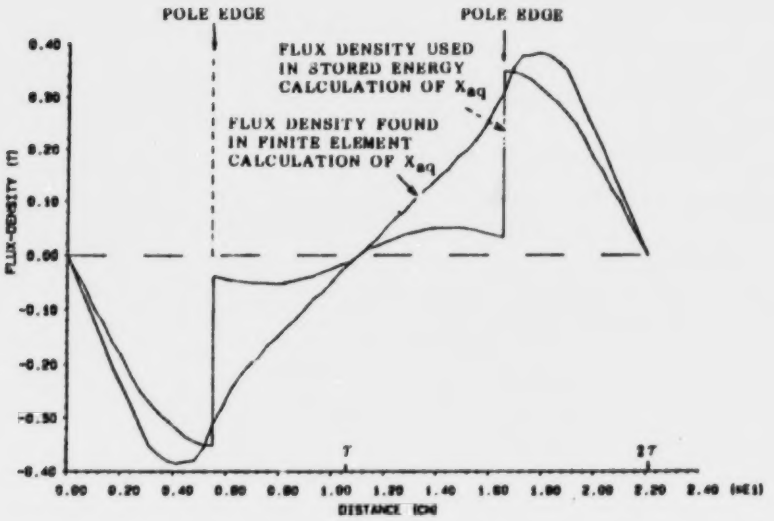
POLE EDGE
POLE EDGE
FLUX DENSITY USED IN STORED ENERGY CALCULATION OF X_{aq}
FLUX DENSITY FOUND IN FINITE ELEMENT CALCULATION OF X_{aq}
FLUX-DENSITY (T)
DISTANCE (CM)

Figure 4.17 (a) D-axis, and (b) q-axis flux density calculated at half the armature slot depth as a function of position along the longitudinal section of Slemon's HLSM, with an equivalent polar air gap of 11.84 mm

5. DESIGN AND PERFORMANCE OF THE HLSM FOR URBAN TRANSIT

5.1 Design Specifications and Guidelines

To assess the application of the HLSM to urban transit, as was the purpose of the work reported here, a design study was conducted for an HLSM that would meet the motor performance requirements of UTDC's intermediate-capacity transit system (ICTS).

A consistent set of specifications and guidelines for propulsion-only and for integrated suspension/propulsion applications was defined, as given in Table 5.1. The maximum thrust and braking force requirements, as a function of speed, are shown in Figure 5.1. These characteristics were established from information made available by UTDC.

TABLE 5.1

HLSM SPECIFICATIONS AND GUIDELINES

Vehicle capacity	75 passengers
Mass (fully loaded, but without motors)	18,300 kg
Cruising speed	22 m/sec
Number of HLSMs per car - propulsion only	2
- ISPS	4
Peak thrust per car - motoring	26 kN
- braking	28 kN
Available power supply voltage	600 V dc
Nominal (polar) clearance	12 mm
Overall width	$\leq$0.65 m
Allowable current densities - field coil	4 A/mm^2
- armature coils	
. under maximum thrust	7.5 A/mm^2
. rms over duty cycle	5.0 A/mm^2
Power factor-efficiency ($\eta \cos \phi$) product	high ($>$0.8)

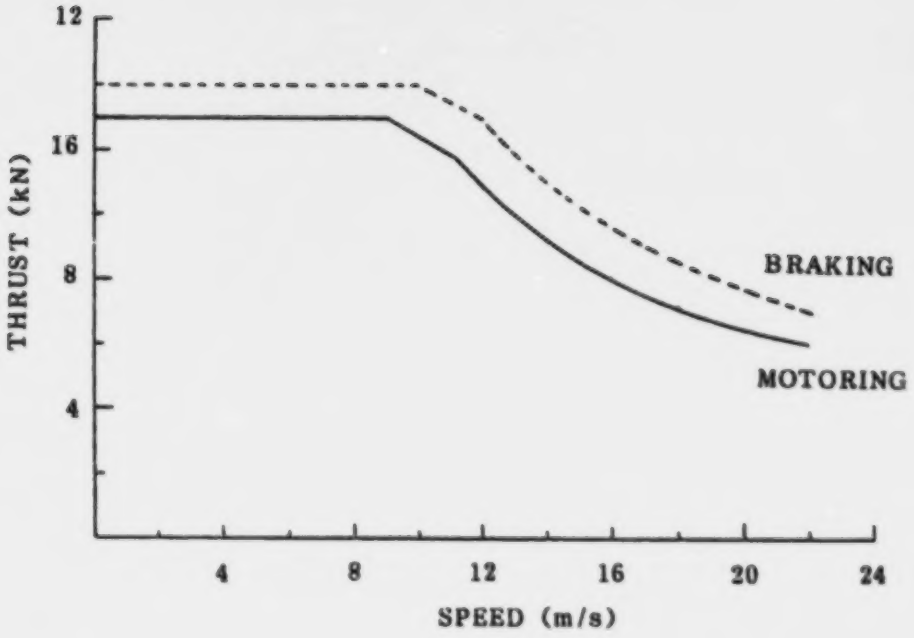

Figure 5.1 Motoring and braking thrust requirements per motor for the HLSM drive

The HLSM design studies were conducted for a typical ICTS vehicle, units of which could form four- or six-car train consists, dependent on required system throughput. The specifications shown in Table 5.1 are identical to those for ICTS, while the allowable current densities were based on thermal considerations and on experience with the operation of the ICTS linear induction motor.

In the winding of a linear machine, the primary thermal path for extraction of heat is along the windings themselves. Rejecting the complications of internal liquid cooling for the HLSM, the armature coils are most effectively cooled by air flow over the end windings, as in the ICTS LIM. However, the geometry of the field coils makes it more difficult to extract the heat, so that a combination of end and side cooling and air flow through the centre of the machine is proposed. In view of the much longer thermal path in the centre of the HLSM, a lower current density for the field coils, as compared with that for the armature coils, is appropriate.

Recognizing the ability of the HLSM to operate at high efficiency and power factor as the potential advantage of the HLSM over the LIM, a primary design objective was to seek a motor with high $\eta \cos \phi$ (>0.8).

5.2 Design Approaches

As is usual in the design of electric machinery for a specific application, various methods were used to iteratively approach a design which is close to optimum within the framework of the performance specifications and guidelines. These methods included consideration of the performance capabilities of test motors (in terms of thrust per unit active area), simple magnetic circuit and Lorentz force calculations, equivalent circuit computations based on analytical values of circuit parameters, and, finally, computer-aided design studies based on the finite element technique.

5.2.1 Test Motor

The characteristics of the HLSM designed and tested at the University of Toronto (Slemon et al., 1980) are given in Appendix B. This motor could achieve a maximum thrust of 15,000 Newtons per m^2 of active area. Scaling to a required thrust of 13 kN, the corresponding active area would be 0.87 m^2.

Taking a maximum width of 0.65 m to allow the HLSM to fit within this dimension of the maximum available ICTS LIM space package and, with allowance for end windings and the central region, taking one half of this width to be active, the total length of the machine would be approximately 2.7 m.

Considering 60 Hz to be a reasonable operating frequency for cruising speed of 22 m/sec, the pole pitch, τ, is given by:

$$\tau = \frac{V_s}{2f} = \frac{22}{2 \times 60} = 0.183 \text{ m} \qquad (5.1)$$

The above motor would therefore require approximately 14 poles.

This simple scaling from known test motor performance gives the first indication of the physical size of the HLSM.

5.2.2 Magnetic Circuit Considerations

Early studies with the HLSM equivalent circuit, using analytical expressions for parameters, indicated that a design requirement would be to make V_{ei} sufficiently high to achieve good $\eta \cos \phi$ operation. To achieve this objective, the HLSM must be a strong field machine, i.e. the design should seek to maximize the modulation of the excitation field. Consequently, an armature tooth/slot width ratio >1 should be selected.

With a tooth/slot width ratio of 2, and an operating flux density (due to excitation alone) in the teeth of 1.5 Tesla, the air gap flux density in the polar regions of the HLSM would be approximately 1.0 Tesla. Assuming the flux density in the interpolar region to be approximately 0.2 Tesla, the amplitude of the excitation field modulation would be 0.4 Tesla.

Again, it must be noted that the modulation of the air gap field is a very important parameter in the operation of the HLSM. From the above considerations, it would be very difficult to design the HLSM to make this modulation amplitude exceed 0.5 Tesla. In comparing the homopolar synchronous motor with a more conventional synchronous machine having excitation and armature coils on opposite sides of the air gap, the latter machine could operate with an excitation field amplitude of 1.5 Tesla or more. Again, it is the low amplitude of excitation field modulation which limits the HLSM performance and which forces the machine to be physically larger than induction or more conventional synchronous machines to produce a required thrust.

Ampere's Circuital Law allows a first estimate of the excitation current requirements of the HLSM to produce a polar gap field of 1 Tesla:

$$\int H.dl = \int J.da \qquad (5.2)$$

which reduces to:

$$\frac{B}{\mu_0} 2 g = N I_{dc} \qquad (5.2)$$

where: B = 1 Tesla

g = 12 mm

giving NI_{dc} = 19.1 kilo-amp. turns.

Multiplying by 1.3 to account for iron reluctance and fringing gives a total dc current requirement of 24.8 kA.t or 12.4 kA.t per coil.

5.2.3 Lorentz Force Approach

The armature current requirements can be estimated by use of the Lorentz force expression:

$$\text{THRUST} = \int J \times B \, da \qquad \text{over the active area of the machine} \qquad (5.3)$$

Assuming sinusoidally distributed air gap field modulation and armature current sheet:

$$B(x) = \hat{B} \sin \frac{\pi x}{\tau}$$

$$J = J_m \sin \left(\frac{\pi x}{\tau} + \gamma\right)$$

where:
$$J_m = \frac{6 \sqrt{2} N_{ph} I_{rms} k_w}{P \tau} \quad A/m \qquad (5.4)$$

Therefore, the maximum thrust (for $\gamma = 0$) is given by:

$$\text{THRUST} = 4 a P \hat{B} J_m \int_0^{\tau} \sin^2 \frac{\pi x}{\tau} \, dx \qquad (5.5)$$

$$= 12 \sqrt{2} a \hat{B} N_{ph} I_{rms} k_w$$

Taking $2a = 0.15$ m

$\hat{B} = 0.4$ Tesla

$k_w \approx 0.9$

and a thrust requirement of 13 kN, gives an armature requirement of $N_{ph} I_{rms} = 2.8 \times 10^4$ amp. turns. This requirement could be met by an armature current of 280 amps in a winding having approximately 100 turns/phase.

5.2.4 Finite Element Analysis

As described in Section 4, finite element analysis was used to determine the excitation field modulation and armature flux distribution of the HLSM. This method allowed the computer-aided design of the magnetic circuit of the machine. Recognizing that the mass of the HLSM will be considerably higher than that of a LIM of equivalent performance, an efficiently designed magnetic circuit is required to minimize motor mass.

5.2.5 Equivalent Circuit

The equivalent circuit used for HLSM analysis has been shown in Figure 4.1. This is the conventional circuit for a salient-pole synchronous machine. Once equivalent-circuit parameters have been determined, the phasor relationships, mechanical performance, and terminal characteristics can be evaluated, and control strategies can be selected to optimize motor performance over its operational duty cycle.

The primary resistance and leakage reactance were determined from armature winding configuration and from conventional ac machine expressions, as detailed in Appendix A.

As noted in Section 2, the induced voltage can be determined once the fundamental component of air gap field modulation is known:

$$V_{ei} = 8 \sqrt{2} f k_w N_{ph} a 7 \hat{B} \qquad (5.6)$$

The modulation amplitude, $\hat{B}$, was initially determined from the above simple magnetic circuit considerations, and later by finite element analysis for more detailed design studies.

In view of the uncertainty in the values of d- and q-axis armature reactances, X_{ad} and X_{aq}, the performance of the HLSM was subjected to a sensitivity analysis with respect to changes in the magnitude and ratio of these parameters. As will be seen, variations in X_{ad} and X_{aq} had little effect on performance, but require the control algorithm to be adjusted to regain optimum performance of the HLSM.

5.2.6 Review of Design Procedure

To design an HLSM to meet the performance specifications and guidelines, the following steps were taken:

(i) scaling of known capabilities of a test motor to gain a first estimate of motor length (see 5.2.1)

(ii) application of magnetic circuit considerations to gain an approximation for:
. the modulation of the air gap field
. the dc excitation requirements.

(iii) consideration of the Lorentz force expression to gain an approximation for ac armature requirements

(iv) establishment of a preliminary HLSM design, which was circulated to research team members for comment

(v) finite element analysis of a transverse section of the HLSM having the largest active width compatible with ICTS drive system space availability (0.65 m)

(vi) selection of armature winding configuration and slot geometry, bearing in mind the maximum available terminal voltage, current density guidelines, and the requirement to maximize excitation flux modulation.

(vii) finite element analysis of a longitudinal section of the HLSM and evaluation of the excitation field modulation

(viii) finite element analysis of armature flux distribution, and evaluation of X_{ad} and X_{aq}

(ix) computation of per-phase armature resistance and reactance

(x) determination of mechanical performance and terminal characteristics from equivalent circuit model

(xi) iteration through steps (iv) to (viii) to seek a magnetically efficient machine design that meets the performance specifications and guidelines, with the criteria of high $\eta \cos \phi$ over a range of speeds, and close to minimum motor mass.

5.3 Design Characteristics

Rather than presenting details of the preliminary and intermediate designs, only the final HLSM design is presented here. Further information on the CAL development of this design is given in the M.Sc. thesis by Ong (1983).

The general configuration of the HLSM is again shown in Figure 5.2, while dimensional details of the transverse section, longitudinal section, and track are shown in Figure 5.3.

The overall dimensional and mass characteristics of the HLSM, in comparison with those of the ICTS LIM of equivalent performance, are listed in Table 5.2, while a comparison of the armature winding configuration is given in Table 5.3. Details of the field winding and of the derived equivalent-circuit parameters of the HLSM are given in Tables 5.4 and 5.5, respectively.

It will be noted that the operating frequency at full speed was selected to be 60 Hz. A 5/6 chorded, 2 slots/pole/phase winding configuration, and a tooth/slot width ratio of 2 were chosen. The track pole/slot ratio was selected to be less than unity (0.67) to take advantage of the small salient thrust produced by the HLSM.

While the motor design presented here has close to minimum mass (for high $\eta \cos \phi$ -- see 5.4), it is apparent from Table 5.2 that the HLSM is considerably longer, higher, and more massive than a LIM of equiva-

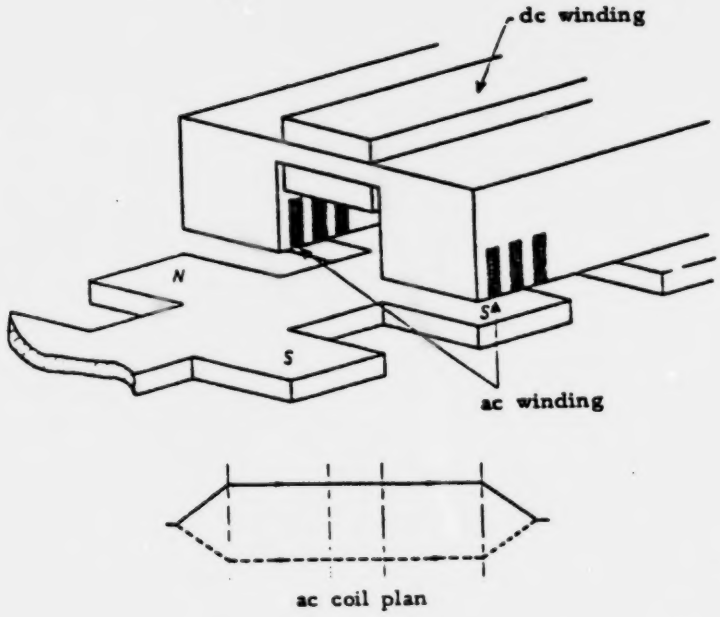

Figure 5.2 The general configuration of the staggered-pole HLSM selected for urban transit applications

TABLE 5.2

COMPARATIVE CHARACTERISTICS OF THE HLSM AND LIM FOR ICTS APPLICATION

	HLSM	LIM
Length (including ends of HLSM field coils)	2.35 m	1.90 m
Width (including end windings of armature)	0.65 m	0.52 m
Height	18 cm	9.9 cm
Mass: steel	1,020 kg	203 kg
armature copper	120 kg	219 kg
field copper	270 kg	-
Total (electromagnetic)	1,410 kg	422 kg
Maximum kVA requirement	200 kVA	325 kVA
Maximum normal force	90 kN	25 kN
Total depth of guideway component	8 cm	3 cm
Mean power dissipation per unit area of motor casing	4.75 kW/m^2	6.0 kW/m^2

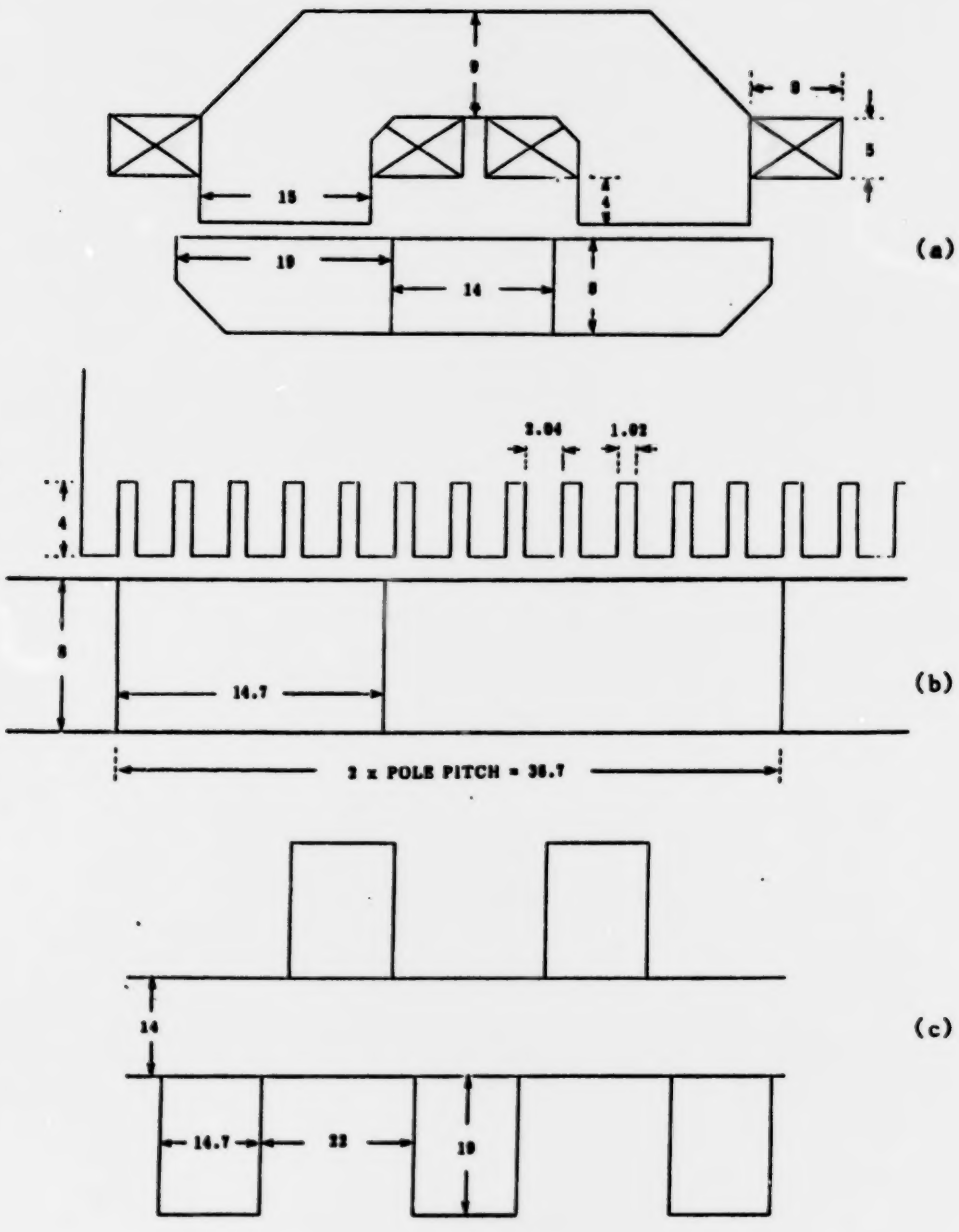

Figure 5.3 Design details of the HLSM:
(a) a transverse section of armature and track
(b) a longitudinal section of armature and track
(c) a plan view of the track

TABLE 5.3

COMPARATIVE CHARACTERISTICS OF THE ARMATURE WINDINGS OF THE HLSM AND LIM FOR ICTS APPLICATION

	HLSM	LIM
Number of phases	3	3
Number of poles	10 + 2 half-strength	6
Pole pitch	183.3 mm	286.8 mm
Active width of armature	150 mm (each side)	216 mm
Number of slots	71 (each side)	79
Half-filled slots	5 (at each end)	7 (at each end)
Slot pitch	30.6 mm	23.9 mm
Slot width	10.2 mm	15.7 mm
Tooth width	20.4 mm	8.2 mm
Slot depth	40.0 mm	54.9 mm
Number of slots/pole/phase	2	4
Number of conductors/slot	8	8
Slot fill factor	0.69	0.58
Coil pitch	5/6	7/12
Coil overhang	80 mm (each side)	152 mm (each side)
Conductor cross-section	35 mm^2	62.6 mm^2
Number of turns/phase	88	96
Frequency range	0-60 Hz	5-50 Hz
Maximum available phase voltage	230 V	270 V
Voltage limit	10-11 m/sec	12-13 m/sec
At peak thrust: current	250 A	465 A
conductor current density	7.2 A/mm^2	7.4 A/mm^2

TABLE 5.4

FIELD WINDING OF THE HLSM

Total mmf		24-28 kiloamp. turns
Per coil:	number of turns	500
	current	24-28 A
	cross-section	50 mm x 80 mm
	fill factor (allowing for cooling passages)	0.75
	conductor cross-section	6 mm^2
	resistance	9.0 ohms
	conductor current density	4-4.7 A/mm^2
Driving voltage (two coils in series)		504 volts
Winding loss		10.4-14.1 kW

TABLE 5.5

EQUIVALENT CIRCUIT PARAMETERS OF THE HLSM
(per-phase at 60 Hz)

Armature resistance			0.0823 ohms
Leakage reactance:	slot leakage	0.261 ohms	
	tooth-top leakage	0.109 ohms	
	end-winding leakage	0.063 ohms	
	harmonic leakage	0.036 ohms	
	central gap leakage	0.079 ohms	0.548 ohms
Direct axis, X_{ad}:	from stored energy expression		0.875 ohms
	from finite element computation		0.622 ohms
Quadrature axis, X_{aq}:	from stored energy expression		0.631 ohms
	from finite element computation		1.000 ohms
Induced voltage			fundamental component of rate of change of flux linkage

lent performance. The electromagnetic components of the HLSM are 3.3 times heavier than those of the LIM. However, a significant reduction of required power conditioner capacity, from 325 kVA to 200 kVA, can be achieved. The HLSM could be made less massive by reducing the strength of excitation, i.e. at the expense of a degraded $\eta \cos \phi$. Mechanical performance and terminal characteristics are presented in the next subsection.

The normal force developed by each HLSM should also be noted. Ninety kN is sufficient to levitate a mass of 9.2 tonnes (i.e. one half of the vehicle mass) in a controlled electromagnetic mode. It is this characteristic of the HLSM that makes it feasible for integrated suspension/propulsion system (ISPS) applications, as discussed in Section 9.

5.4 Performance of the HLSM

The performance of the HLSM, as computed from the two-reactance equivalent-circuit model of the machine, is reported here for both motoring and braking operation. Per-phase armature resistance and leakage reactance were computed as in Appendix A. Induced voltage and armature reactances were computed by finite element analysis, while the effects of variations in the latter parameters were investigated by sensitivity studies.

While power conditioning and control is discussed in Section 6, it is appropriate to note the control mode selected for HLSM operation at this stage. Recognizing that the performance of any large air gap linear machine is thermally limited, the control algorithm selected was that which maintains the phase angle between armature current and induced voltage at the value which results in minimum armature current over the thrust-speed performance specification shown in Figure 5.1. Appendix C describes how this angle can be computed for both motoring and braking operations.

In the following presentation of performance characteristics, the control angle as a function of speed is shown for various excitation and armature reactance conditions. The armature current, complex power, and $\eta \cos \phi$, as a function of speed characteristics, are computed with the control angle set to achieve the minimum armature current condition.

5.4.1 Motoring Performance

Figure 5.4(a)-(d) shows the armature current, complex power, armature η cos ϕ and control angle versus speed characteristics for the urban transit HLSM. For all of these and subsequent characteristics, the motor produces sufficient motoring (or later braking) thrust to achieve the specification in Figure 5.1.

The nominal dc excitation of the HLSM was selected to be 24 kA-turns as being sufficient to drive the magnetic circuit uniformly towards the knee of saturation. The curves in Figure 5.4 show the effect of varying the excitation either side of nominal current, assuming no demagnetizing effect of armature reaction.

It may be noted that, for an excitation of 24 kA.t, the maximum armature current would be 250 A, the maximum complex power requirement would be 170 kVA, the armature η cos ϕ exceeds 0.8 at speeds above 11 m/sec (50 per cent of cruising speed), and η cos ϕ reaches 0.92 at cruising speed. The control angle is maintained at -8°, to take advantage of salient thrust, up to the speed at which the inverter reaches its voltage limit. The control angle must then be increased towards 50° at cruising speed to maintain minimum armature current.

A similar set of motoring characteristics is shown in Figure 5.5(a)-(e), illustrating the effect of changing the magnitude and ratio of X_{ad} and X_{aq}. In Figure 5.5 (a)-(c), the armature current, kVA, η cos ϕ, and control angle versus speed curves are shown for X_{ad} and X_{aq} equal to 0.5, 1.0 and 1.5 p.u. with respect to the values computed from stored energy/Fourier series analysis (see Table 5.5). Figure 5.5(e) shows the effect of changing the ratio of X_{ad} and X_{aq} on the armature current drawn by the HLSM. While the curves are evidently sensitive to changes in X_{ad} and X_{aq}, it is clear that the selected HLSM design could meet the performance specifications, even if the d- and q-axis reactances differ from their nominal values by ±50 per cent, simply by adjusting the control angle algorithm appropriately.

(a) Armature current versus speed

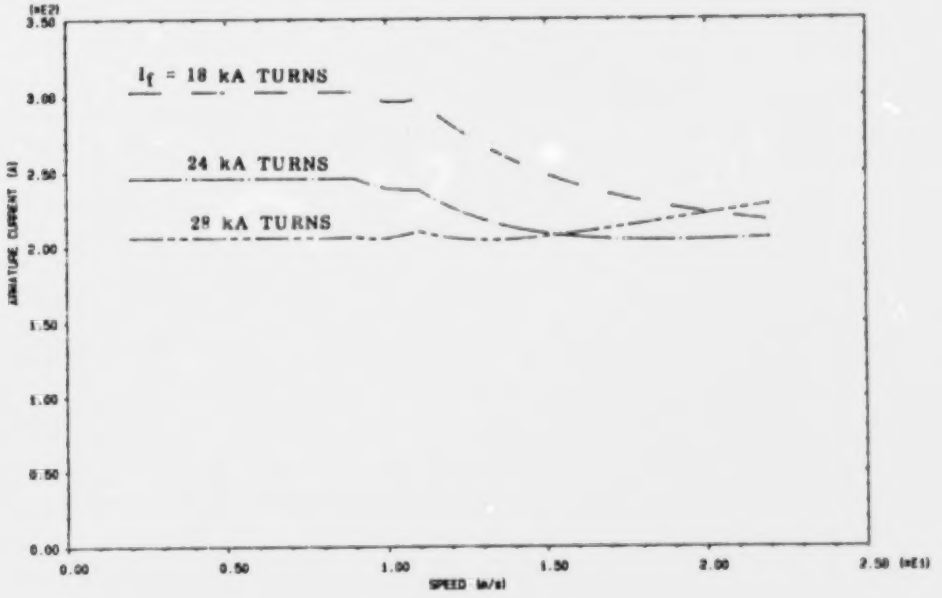

(b) Complex power versus speed

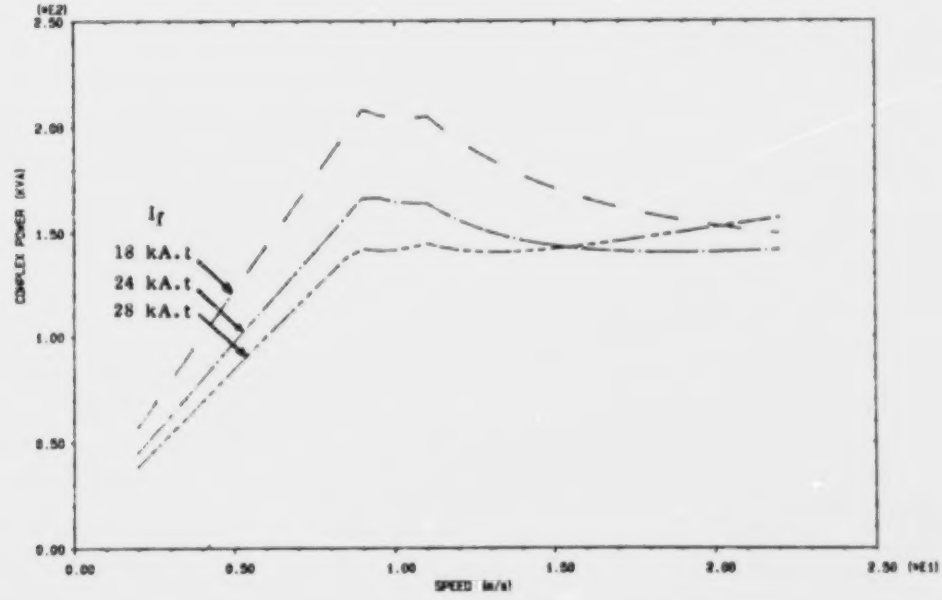

Figure 5.4 Meeting the performance specification in motoring, showing the effect of varying dc excitation

(c) Armature efficiency-power factor product versus speed

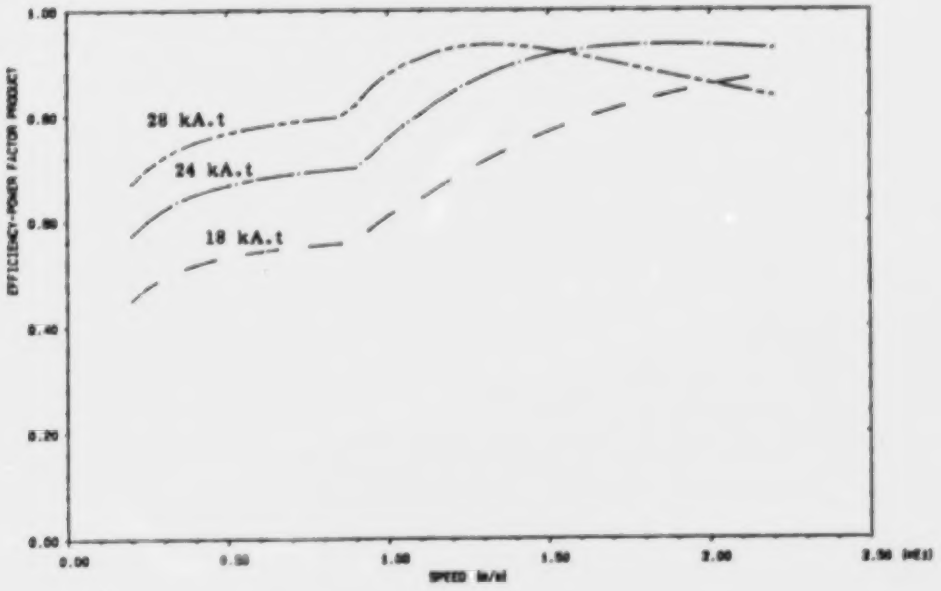

(d) Control angle versus speed

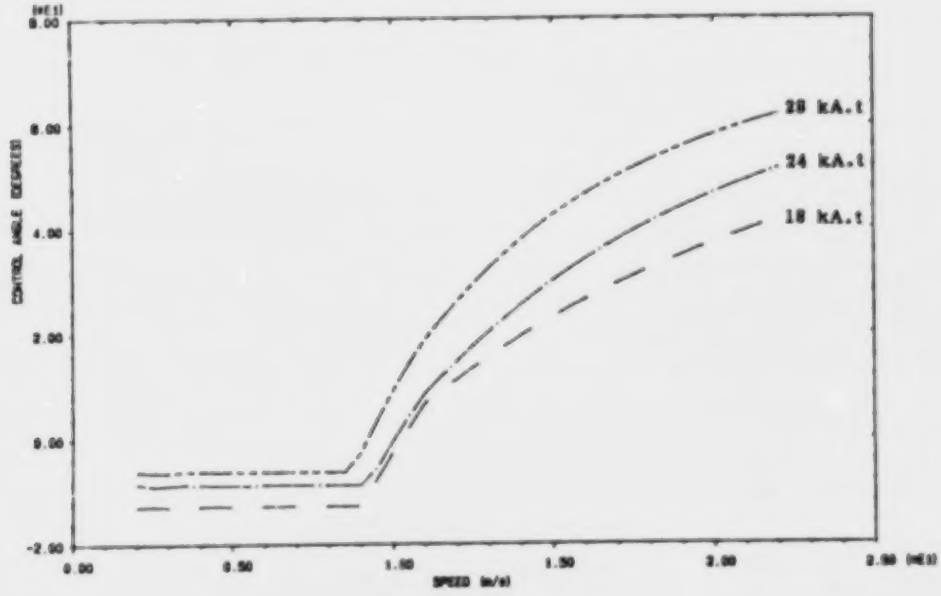

Figure 5.4 (Cont'd)

(a) Armature current versus speed

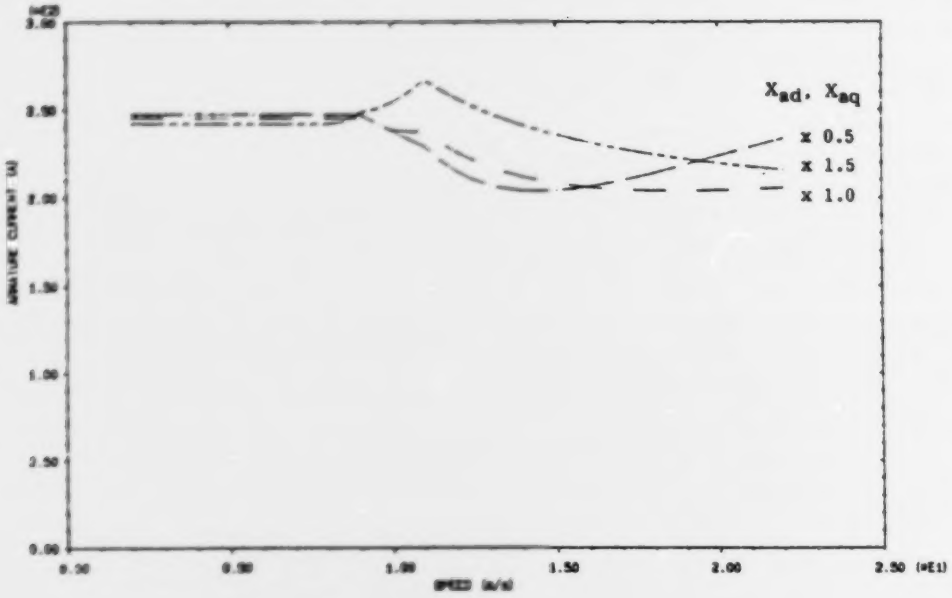

(b) Complex power versus speed

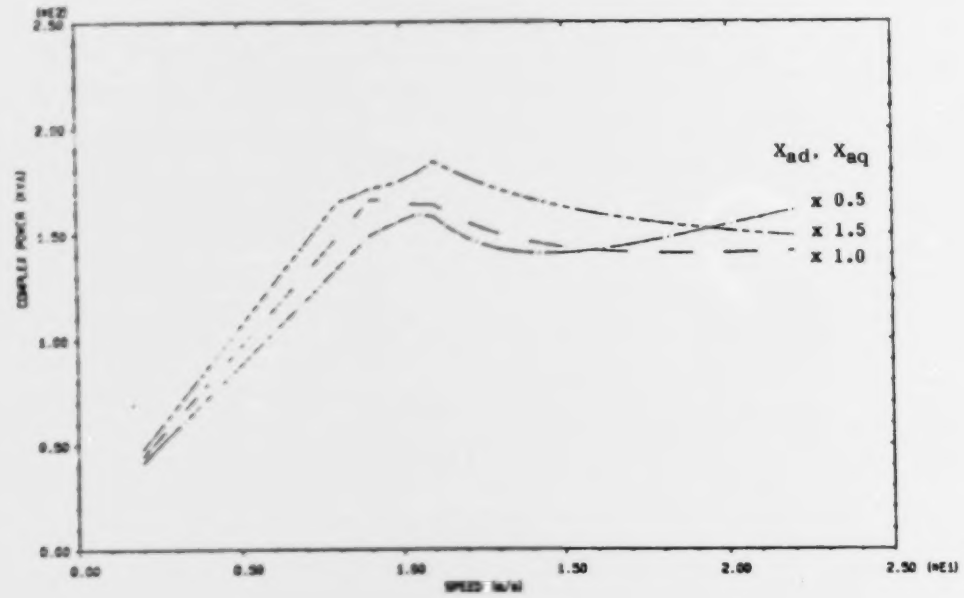

Figure 5.5 Meeting the performance specification in motoring, showing the effect of varying both the magnitude and ratio of X_{ad} and X_{aq}

(c) Armature efficiency-power factor product versus speed

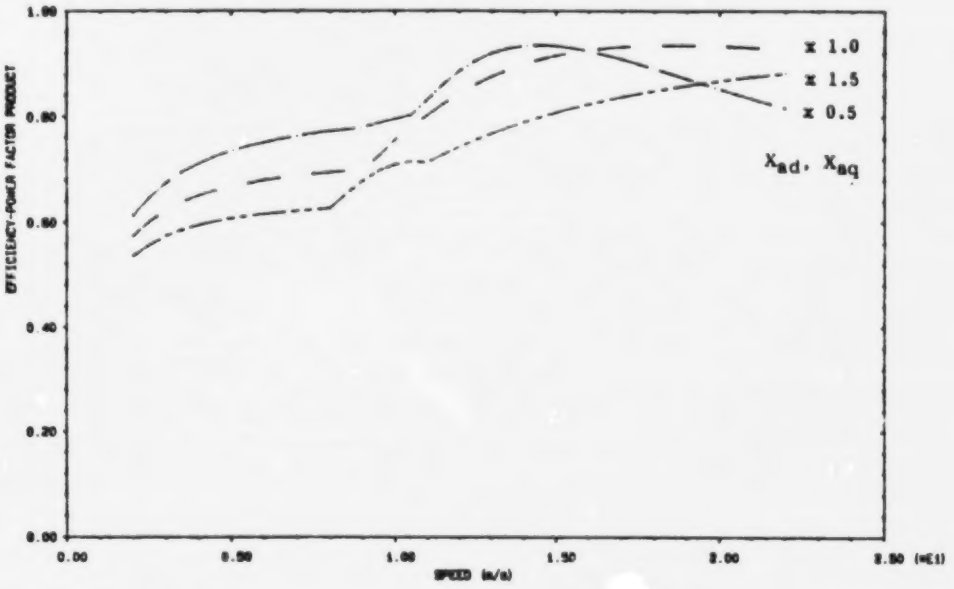

(d) Control angle versus speed

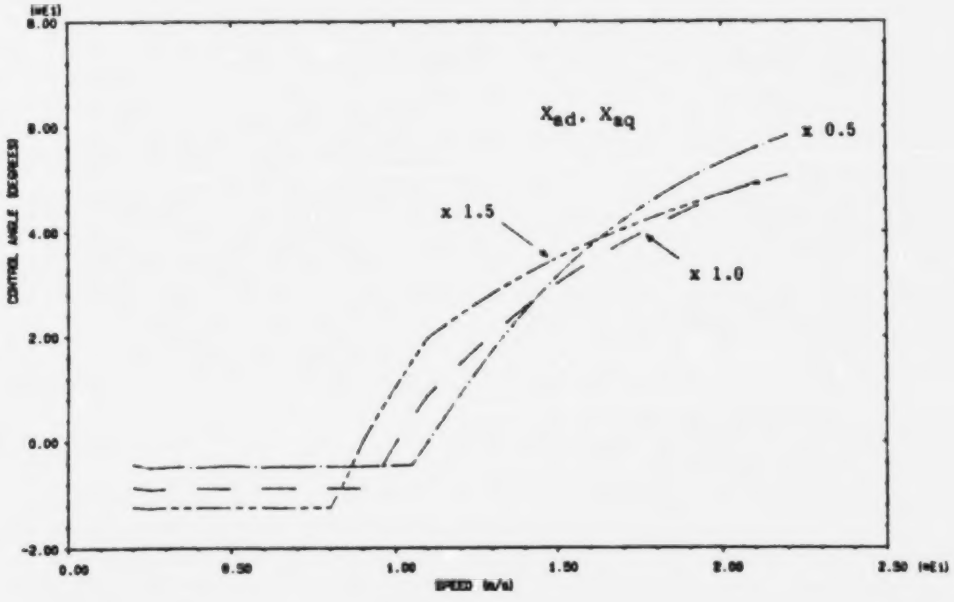

Figure 5.5 (Cont'd)

(e) Armature current versus speed, showing the effect of changing the X_{ad} and X_{aq} ratio

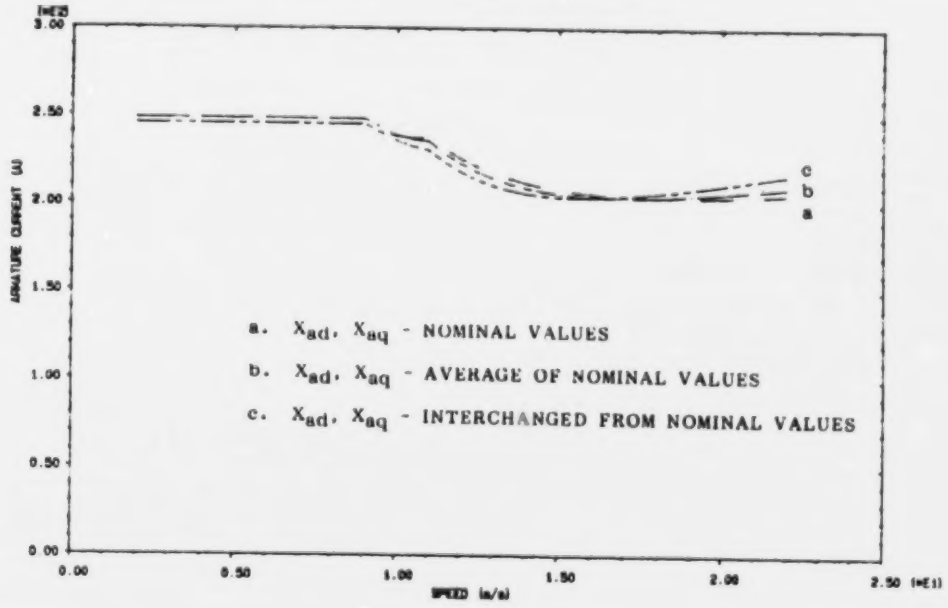

Figure 5.5 (Cont'd)

5.4.2 Braking Performance

Again, a similar set of characteristics is presented for braking operation, to meet the specification in Figure 5.1. Figure 5.6(a)-(c) shows the armature current, kVA, and control angle characteristics as a function of speed, for the same three values of dc excitation as in Figure 5.4. At the nominal value of 24 kA.turns, the maximum armature current is now 265 A, while the complex power requirement reaches 185 kVA. The control angle must now be varied from 188°, up to the break point, to 130° at cruising speed.

The sensitivity to X_{ad} and X_{aq} is not included here as it is very similar to that illustrated for motoring operation.

(a) Armature current versus speed

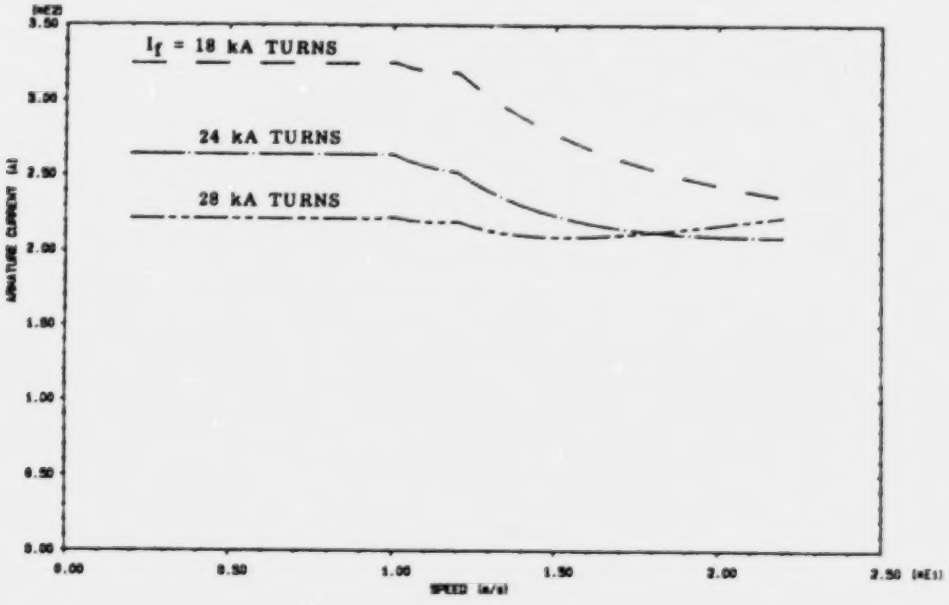

(b) Complex power versus speed

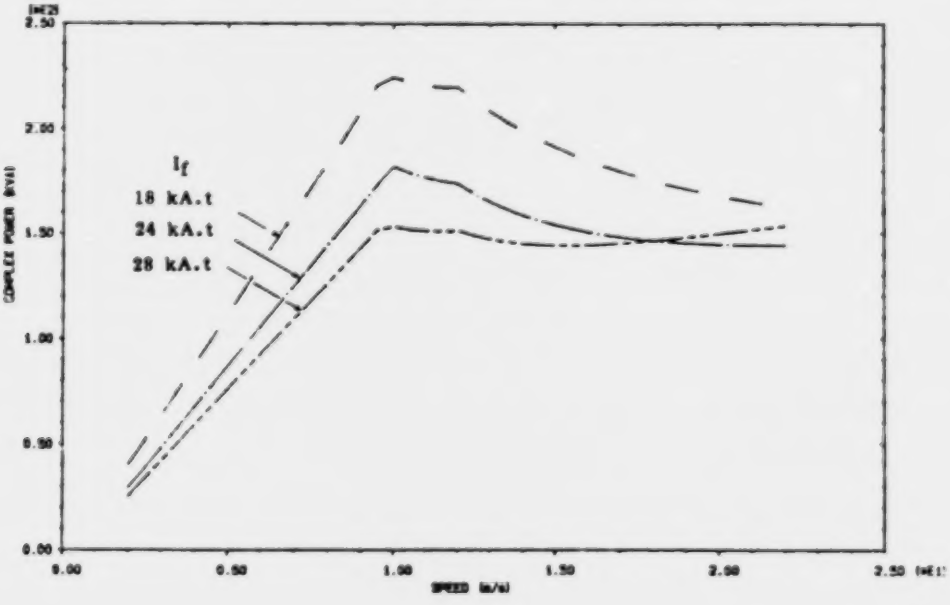

Figure 5.6 Meeting the performance specification in braking, showing the effect of varying dc excitation

(c) Control angle versus speed

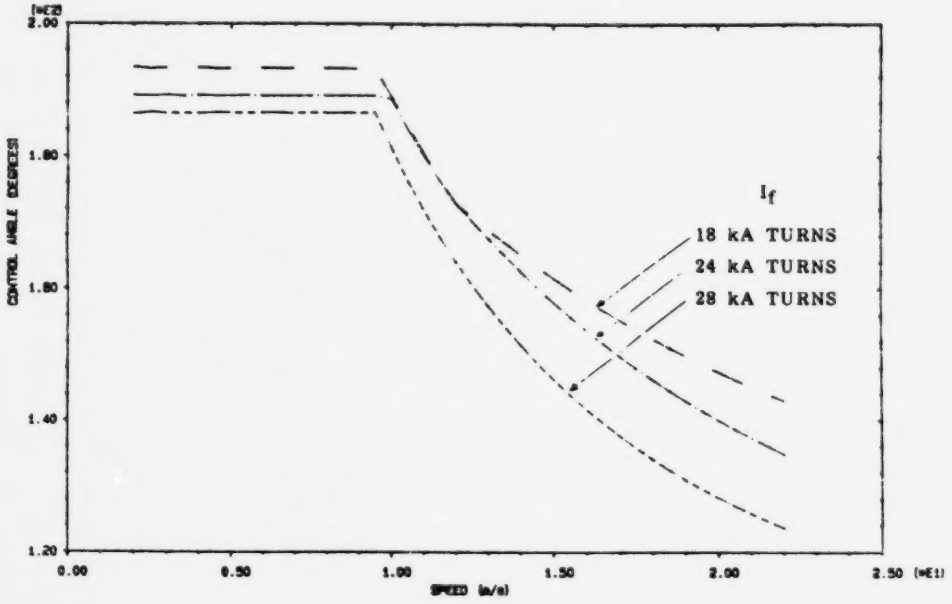

Figure 5.6 (cont'd)

5.4.3 Excitation and Armature Field Distribution

To illustrate the field distribution in the final HLSM design, Figure 5.7 shows finite element plots for the following conditions:

(a) a transverse polar excitation field distribution

(b) a transverse interpolar excitation field distribution

(c) a longitudinal excitation field distribution

(d) a d-axis armature field distribution

(e) a q-axis armature field distribution

The finite element field distributions in Figures 5.7(a)-(c) were used to find the modulation of the dc field to determine armature-induced voltage, while Figures 5.7(d)-(e) show armature field distributions for a model of the HLSM (as discussed in Section 4.3.3) developed to evaluate X_{ad} and X_{aq}.

The performance characteristics presented in this section were computed for the HLSM operating at its full thrust requirement. The performance of the HLSM over a typical duty cycle and over a typical transit corridor is presented in Section 7.

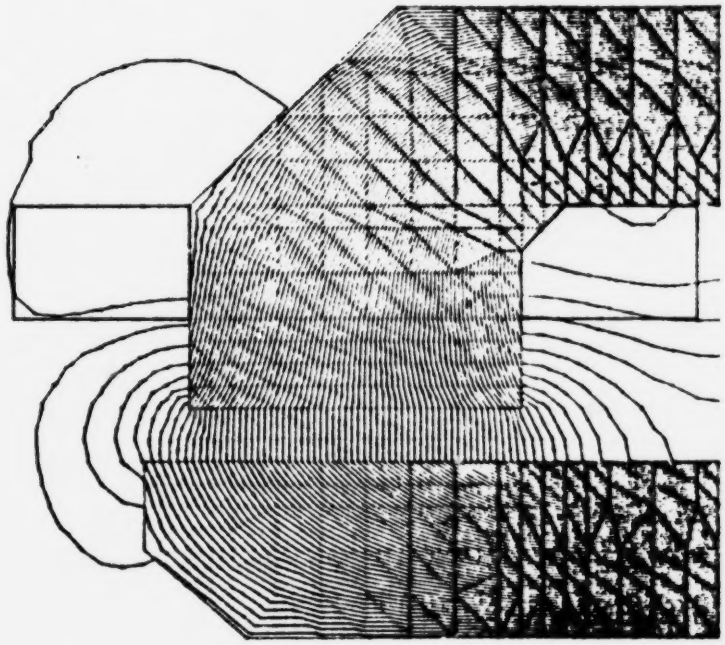

Figure 5.7(a) Polar transverse dc field distribution of the final HLSM design with a doubly corrected air gap (actual air gap is 12 mm). The dc excitation per side is 14,000 ampere-turns. Difference between constant vector potential lines is 0.002 weber/meter.

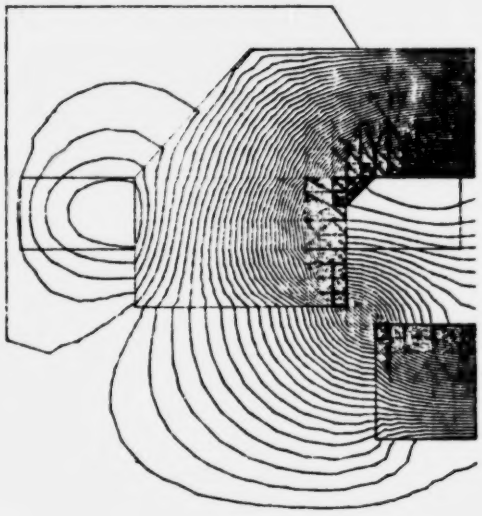

Figure 5.7(b) Interpolar transverse dc field distribution of the final HLSM design with a corrected air gap (actual air gap is 12 mm). The dc excitation per side is 14,000 ampere-turns. Difference between constant vector potential lines is 0.0007 weber/meter.

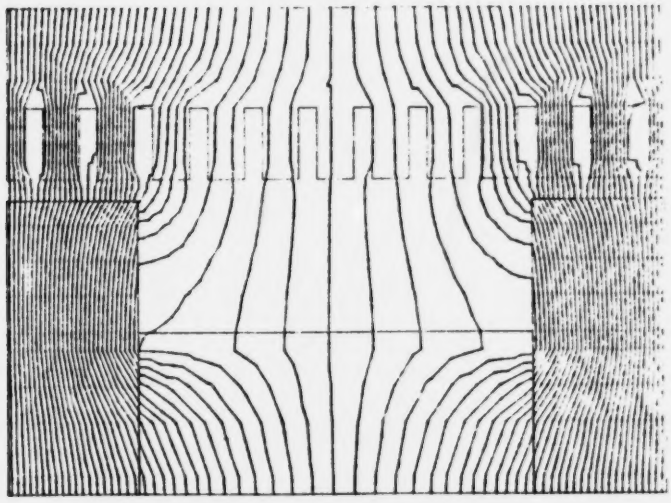

Figure 5.7 (c) Longitudinal field distribution of the final HLSM design. The dc excitation per side is 14,000 ampere-turns and the difference between constant vector potential lines is 0.004 weber/meter.

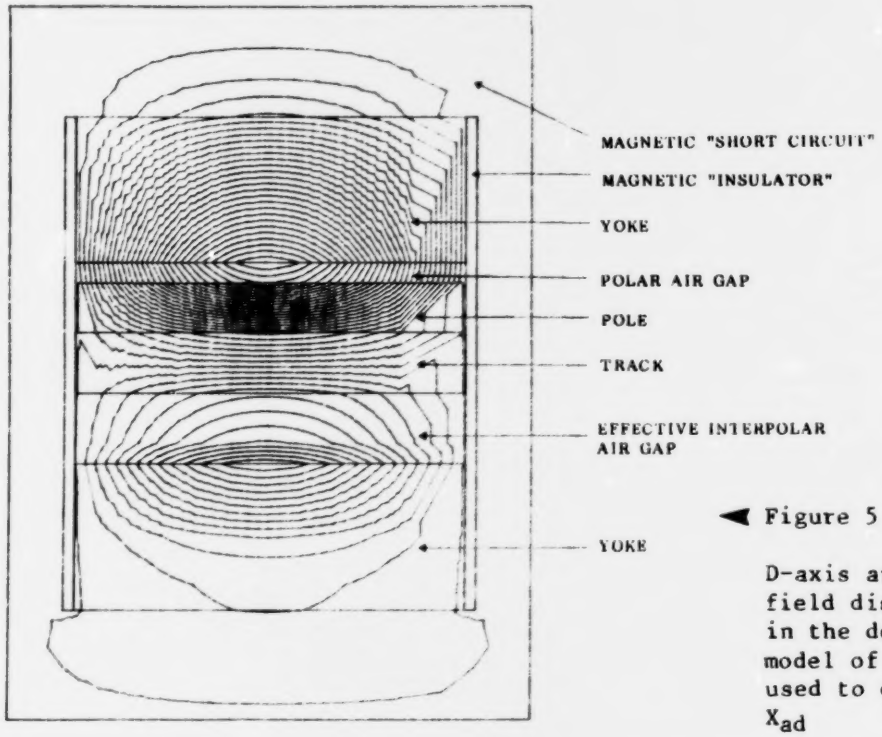

◄ Figure 5.7(d)

D-axis armature field distribution in the developed model of the HLSM, used to determine X_{ad}

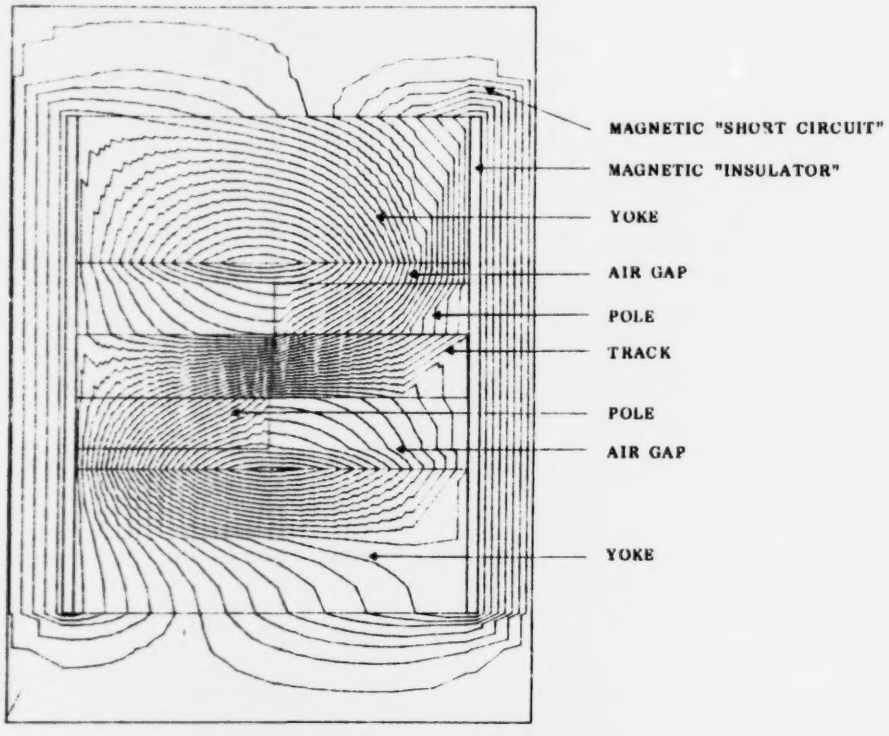

Figure 5.7(e) ►

Q-axis armature field distribution in the developed model of the HLSM, used to determine X_{aq}

6. CONTROL AND POWER-CONDITIONING

6.1 Control

The performance of any large air gap linear machine is limited by the magnitude of current that can be carried by its windings. This thermal limitation makes it appropriate to control the machine such that performance per unit current is optimized. It was shown in Section 5.4 that the HLSM can be controlled by varying frequency, magnitude and angle of the armature current according to the speed and thrust requirements of a vehicle. Once the parameters in the two-reactance equivalent circuit model of the machine are known, a current angle, γ, versus speed characteristic can be determined which results in minimum armature current over the thrust-speed performance specification of the drive. Typical current angle versus speed characteristics for motoring and braking operations were discussed in Section 5.4, and are illustrated in Figure 6.1.

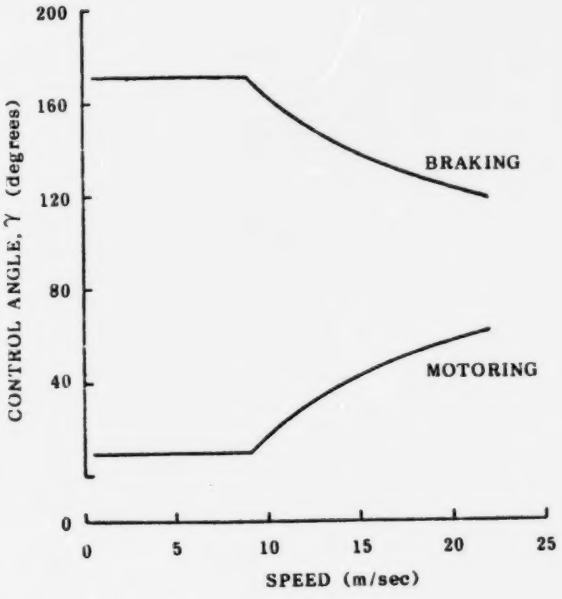

Figure 6.1 Typical current angle versus speed characteristics for control of the HLSM. γ is the phase angle between the armature current and V_{ei}, the voltage induced by the excitation field (modulated by track saliency)

Control of the thrust of the HLSM would be achieved principally through control of the current supplied to the armature windings. In addition, some control of field current would be needed in the constant power region of operation to optimize use of the available power supply.

To effectively control current angle γ, it will be necessary to detect the longitudinal position of the track poles relative to the armature windings. No detailed study has been carried out to select the best detector system. The ferromagnetic nature of the track poles, however, lends itself well to magnetic detection, which should be highly reliable and free from environmental noise.

6.2 Power-Conditioning

Ideally, the currents supplied to the armature windings should be a balanced set of sine waves with equal magnitudes and equal phase displacement between phases. To the extent that the currents contain harmonic components, there will be thrust oscillations which may cause objectionable vibration and noise. Since the dominant vibration frequency is six times that of the armature current frequency, this factor becomes most important for starting and low-speed operation.

The three armature phase windings can never be made identical because of the finite length of the motor. Thus, these windings will be slightly unbalanced. If the armature supply is a balanced set of voltages, the currents will be somewhat unbalanced, leading to loss of torque capability and to increased stator losses. It is, therefore, desirable to have direct means of controlling the phase currents in magnitude, wave shape and phase angle.

Selection of the appropriate type of power-conditioner is limited by the constraints discussed above. Current-source inverters employing a controlled dc current link and thyristor switching are used with numerous induction and synchronous motor drives. They are, however, inappropriate for this application. The 120° square-wave phase current contains harmonics which would result in unacceptable thrust oscillation at low speed. Previous experiments (Ref. 2 in Section 6.3) have, however, shown that this waveform is acceptable at higher speeds where thrust oscillation frequencies are well above the natural frequencies of the motor mounting.

The major disadvantages of the current-source inverter for this application are associated with its volume and weight, dominated by the large inverter capacitors which are required. An alternative form of inverter is required which will combine low weight and volume with an ability to control the magnitude, phase and waveform of the phase currents. No detailed study has been carried out to define the optimum inverter for this application but experience with LIM and rotating drives suggests the use of an inverter employing gate turnoff or power transistors with means to control the output current magnitude and waveshapes. This can be accomplished using the structure of a standard voltage source inverter as shown in Figure 6.2, with hysteresis-band control of each phase current. In this system, the inverter switches are controlled to maintain the current in each phase within a narrow hysteresis band around the desired value, as shown in Figure 6.3.

The basic elements of the control system are shown in Figure 6.4. The desired phase angle between the track pole and the stator mmf is added (presumably digitally) to the signal from the motor position sensor to obtain the required phase angle of the phase current. The desired current magnitude is derived from the thrust command. Hysteresis band signals are then added to and subtracted from the desired current waveform signals, and the results are compared with the actual phase current to produce the transistor switching signals.

Provision can be made for controlling the width of the hysteresis band. A narrow band will produce a lower value of noise in the motor thrust, a feature which may be important at low speed. A wider band reduces the number of switching operations and this increases the efficiency of the inverter. If, however, the band is too wide, the phases of the currents may not be controlled with sufficient accuracy. This would have little effect on the thrust but could have a significant effect on motor power factor in the high-speed, voltage-limited region of operation.

In the constant power region, operation is limited by the magnitude of the available armature voltage. If the armature current, and therefore the armature voltage, is to be sinusoidal, the inverter is subject to a 15 per cent derating as compared with a standard voltage source inverter. This derating can be reduced substantially by adding a third harmonic to each phase current waveform. The third harmonic has no

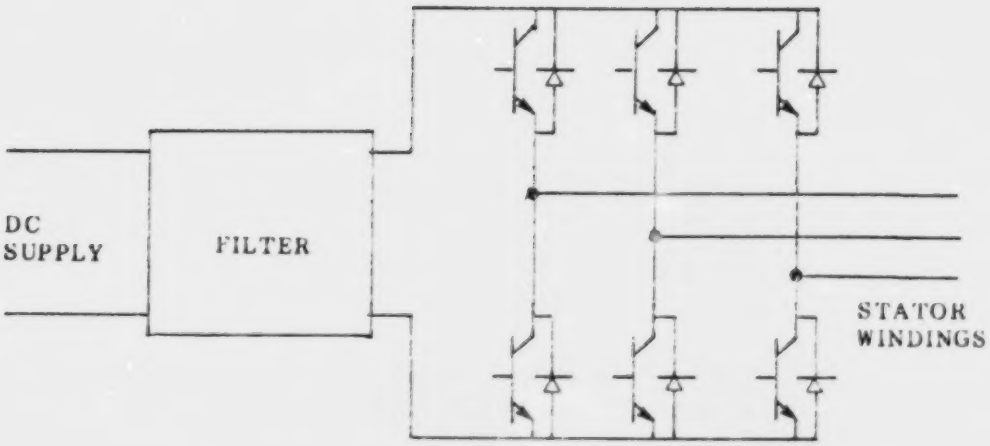

Figure 6.2 Inverter supply to HLSM armature windings

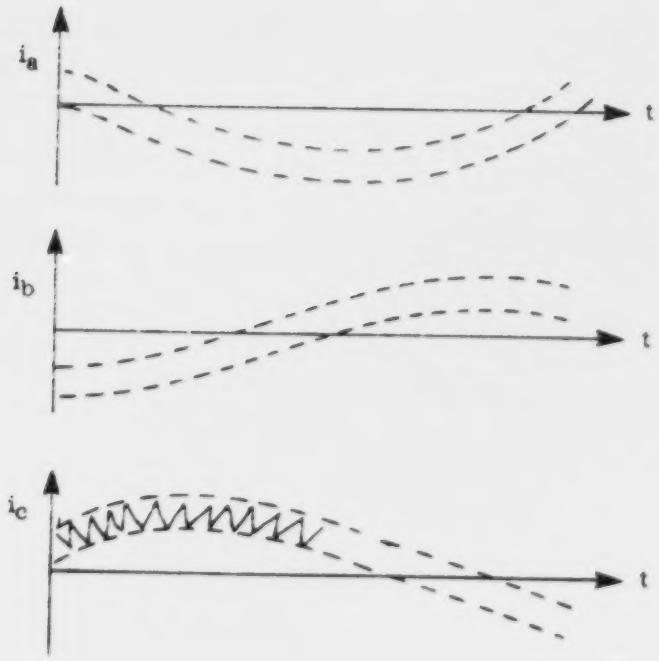

Figure 6.3 Hysteresis-band control of phase currents, with portion of typical waveform shown for i_c

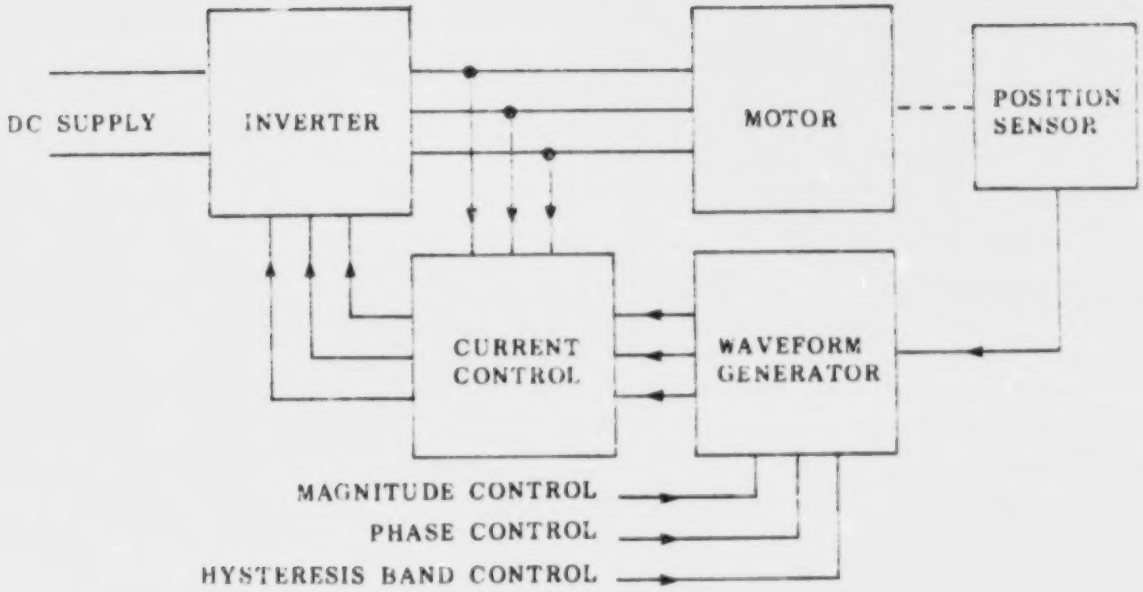

Figure 6.4 The basic HLSM control system

effect on thrust but, by appropriate choice of magnitude and phase, it can result in an increased ratio of fundamental component to peak voltage, and thus in a better utilization of the available supply. As far as possible, it is desirable to minimize the armature heating and the energy drawn from the supply. This is consistent with obtaining the maximum thrust per unit of stator current. As shown in Figure 6.1, this is achieved with a current phase angle near zero for motoring and near 180° for braking.

Simultaneously, the field current is held at its maximum value. In the low-speed region, power factor is not significant, since the required stator voltage is less than available from the dc supply. As speed is increased, a break point is reached at which the inverter is limited by the dc supply voltage. At and above this speed, the system should be controlled to achieve a near unity power factor to make best use of the

available supply voltage and current. This requires adjustment of the current phase angle as shown in Figure 6.1, and simultaneous control of the field current. Accordingly, a chopper is required for control of the dc supply to the field. The algorithm relating phase angle and field current to thrust and speed can be derived by use of the equivalent circuit of the motor and the experimental relationship between field current and modulated pole flux.

It is recognized that a variety of approaches can be taken to the detailed design of the control system for this motor. The above discussion indicates the important design criteria and suggests a possible approach. More detailed design is not needed to assess the relative merit of the HLSM versus alternative linear motors. It is sufficient to note that the control system appears to present no demands which are beyond known state-of-the-art technology.

6.3 References Related to Power-Conditioning and Control of Synchronous Drives

1. F. Harashima, M. Naitoh and Haneyoshi. "Dynamic Performance of Self-Controlled Induction Motors Fed by Current Source Inverters." IEEE Transactions on Industry Applications, Vol. IA-15, No. 1, January/February 1979, pp. 36-47.

2. G.R. Slemon, S.B. Dewan and J.W.A. Wilson. "Synchronous Motor Drive with Current Source Inverter." IEEE Transactions on Industry Applications, Vol. IA-10, No. 3, May/June 1974, pp. 412-416.

3. A. Jaloubowicz, M. Naugaret and R. Perret. "Simplified Model and Closed Loop Control of a Commutatorless D.C. Motor." IEEE Transactions on Industry Applications, Vol. IA-16, No. 2, March/April 1980, pp. 165-172.

4. Toshiaki Okayama, Takamasa Hori, Nobuyaki Morino, Toshio Migato, Koji Iwata and I.E. Suoshimizu. "Effects of Machine Constants on Steady-State and Transient Characteristics of Commutatorless Motors." IEEE IAS Annual Meeting Conference Record, 1977, pp. 272-279.

5. R.L. Steigerwald and T.A. Lipo. "Analysis of a Novel Force Commutation Starting Scheme for a Load Commutated Synchronous Motor Drive." IEEE IAS Annual Meeting Conference Record, 1977, pp. 739-747.

6. A.B. Plunkett and F.G. Turnbull. "Load Commutated Inverter/ Synchronous Motor Drive Without a Shaft Position Sensor." IEEE IAS Annual Meeting Conference Record, 1977, pp. 748-757.

7. K.J. Binns, M.A. Jabbar, G.E. Parry and S.W. Russel. "A Variable-Speed Drive Using Permanent Magnet A.C. Motor." 2nd International Conference on Electrical Variable-Speed Drives, September 25-27, 1979, IEE, London, pp. 84-87.

8. A.R. Stocken. "Synchronous Motor Variable-Speed A.C. Drive System." 2nd International Conference on Variable-Speed Drives, September 25-29, 1979, IEE, London, pp. 58-60.

9. W.R. Pearson and P.C. Sen. "Brushless D.C. Motor Propulsion Using Synchronous Motors for Transit Systems." IEEE IAS Annual Meeting Conference Record, 1983, pp. 285-290.

10. T.J.E. Miller, T.W. Neumann, E. Richter. "A Permanent Magnet Excited High Efficiency Synchronous Motor with Line Start Capability." IEEE IAS Annual Meeting Conference Record, 1983, pp. 455-461.

11. T.M. Johns. "Torque Production in Permanent Magnet Synchronous Motor Drives with Rectangular Current Excitation." IEEE IAS Annual Meeting Conference Record, 1983, pp. 476-487.

12. Toyori Himei, Shigayuki Funabiki, Yoshiaski Agari and Minoru Okada. "Analysis of Voltage Source Inverter-Fed Permanent Magnet Synchronous Motor Taking Account of the Converter Performance." IEEE IAS Annual Meeting Conference Record, 1983, pp. 574-579.

13. R.H. Miller, T.W. Nehl, N.A. Demerdash, B.P. Overton, C.J. Ford. "An Electronically Controlled Permanent Magnet Synchronous Machine Conditioning System for Electric Passenger Vehicle Propulsion." IEEE IAS Annual Meeting Conference Record, 1982, pp. 506-511.

14. G.R. Slemon and A.V. Gumaste. "Steady State Analysis of a Permanent Magnet Synchronous Motor Drive with Current Source Inverter." IEEE Transactions on Industry Applications, Vol. IA-19, No. 2, March/April 1983, pp. 190-197.

15. Jacques Davoine, Robert Perret and Hoang Le-Huy. "Operations of a Self-Controlled Synchronous Motor Without a Shaft Position Sensor." IEEE Transactions on Industry Applications, Vol. IA-19, No. 2, pp. 217-222.

16. H. Le-Huy, A. Jakubowicz and R. Perret. "A Self-Controlled Synchronous Motor Drive Using Terminal Voltage Sensing." IEEE IAS Annual Meeting Conference Record, 1980, pp. 562-569.

17. G.R. Slemon and A.V. Gumaste. "Steady-State Analysis of a Permanent Magnet Synchronous Motor Drive with Voltage Source Inverter." IEEE Transactions on Industry Applications, Vol. IA-17, No. 2, March/April 1981, pp. 143-151.

18. K.J. Binns, B. Sneyers, G. Maggetto and P.H. Lathire. "Rotor Position Controlled Permanent Magnet Synchronous Machines for Electrical Vehicles." Proceedings of the International Conference on Electrical Machines, Part 1, Athens, September 15-17, 1980, pp. 346-357.

19. Shoji Nishikata, Shoichi Muto and Teruo Kataoka. "Dynamic Performance Analysis of Self-Controlled Synchronous Motor Speed Control Systems." IEEE IAS Annual Meeting Conference Record, 1981, pp. 671-677.

20. Peter Hussels. "Flux and Torque Control of Synchronous Machine with Compensation of Inaccuracy Due to Variations in Motor Parameters." IEE Power Electronics and Drives Conference, 1984, pp. 377-380.

7. PERFORMANCE OVER DUTY CYCLES

It has been shown that an HLSM can be designed to meet the performance specifications of an urban transit drive, and that it can be controlled to maintain good armature terminal characteristics across the full speed range.

In addition to evaluating the characteristics of a drive over its specification, it is useful to evaluate its performance in actual vehicle system operation. This allows the peak power demand and energy profile of the vehicle to be determined, and the rms current loading and armature heating effects to be assessed. This has been achieved by simulating vehicle operation, with HLSM drive, over a typical 1 km duty cycle and over a route representing a typical transit line.

7.1 Simple Duty Cycle

7.1.1 Speed and Thrust Profiles

A simple duty cycle typical of urban transit systems was defined. A run between two stations of separation 1.0 km, followed by a dwell time of 20 seconds, was considered. Parameters for the vehicle and duty cycle are given in Table 7.1.

TABLE 7.1

PARAMETERS OF THE VEHICLE AND SIMPLE DUTY CYCLE

Station-to-station distance	1.0 km
Vehicle mass (crush-loaded)	19,600 kg
Initial acceleration	1.3 m/sec^2
Number of HLSMs	2
Initial thrust/motor	12.74 kN
Maximum grade (in cruise section)	±5%
Deceleration	1.1 m/sec^2
Station dwell time	20 seconds

A speed-distance profile was defined to be consistent with ICTS acceleration and deceleration requirements, and which would drive the HLSM close to its performance specification. Sections of +5 per cent and -5 per cent grade were added in the cruise portion.

The speed-time and grade profile is shown in Figure 7.1. The HLSM-driven vehicle is required to accelerate initially at 1.3 m/sec^2, to cruise at 20 m/sec, to climb a 5 per cent grade at full speed, to cruise along flat track, to descend a 5 per cent grade at full speed, to cruise along flat track, and finally to decelerate at 1.1 m/sec^2 into the station.

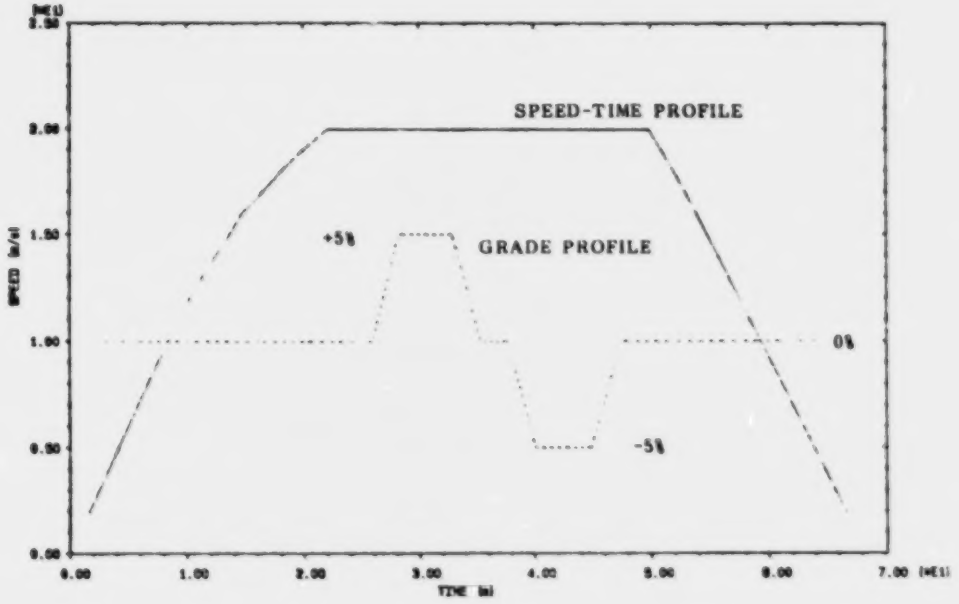

Figure 7.1 The speed-time and grade profile assumed for the simple duty cycle

The thrust requirements for the ICTS vehicle with HLSM drive were determined from the dynamic equation of motion:

$$\text{THRUST} = m\frac{dv}{dt} + T_R + T_A + G + C \qquad (7.1)$$

where: m = vehicle mass = 19,600 kg

v = instantaneous velocity (m/sec)

T_R = rolling resistance = 640 + 0.106 v Newtons

T_A = aerodynamic drag = 2.95 v^2 Newtons

G = grade resistance = M_g sin 0 = 1.92 kN/per cent of grade

C = curve resistance, assumed to be zero in this simulation.

The motor thrust profile, corresponding to the speed-time profile in Figure 7.1, is shown in Figure 7.2. Peak thrust is required for initial acceleration and for deceleration. The +5 per cent grade forces the HLSM to operate close to its performance specifications at full speed. The -5 per cent grade forces the HLSM to provide braking thrust at full speed.

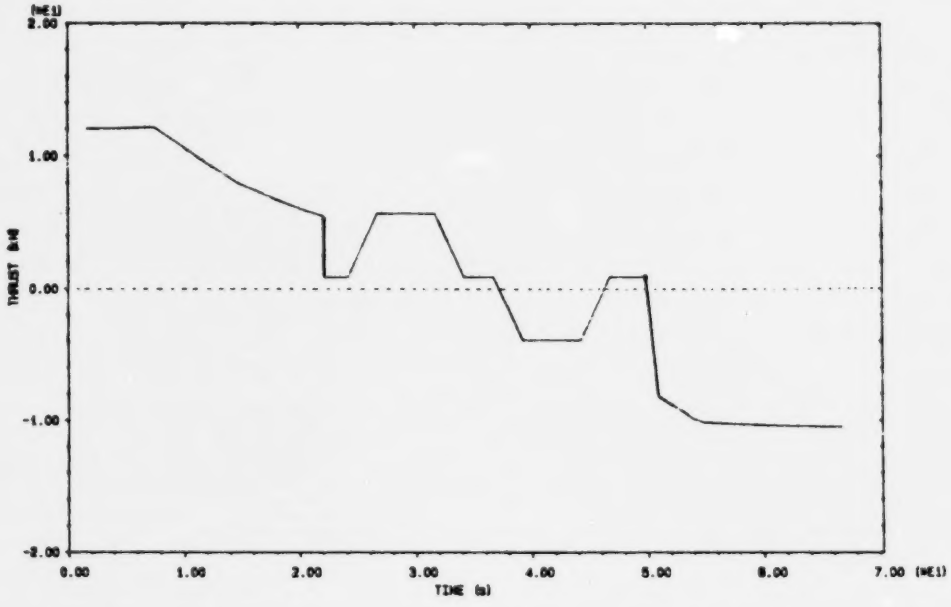

Figure 7.2 The motor thrust profile for the simple duty cycle

7.1.2 Performance Profiles

The performance of the HLSM over this simple duty cycle was evaluated using the equivalent circuit model, by means of the programs BETA and BETABRK, as described in Appendix D. The programs required the following input data:

- the equivalent circuit parameters of the HLSM
- the control angle versus speed characteristic, chosen to minimize armature current under maximum specified thrust conditions

- paired thrust and speed points as a function of distance and/or time
- the maximum field excitation versus speed characteristic
- the maximum available terminal voltage.

At each incremental time, the programs use the above data to solve for the armature phasor polygon that has the maximum terminal voltage, subject to the constraint that field excitation is less than or equal to its maximum value. This is consistent with the mode of control proposed for the HLSM.

While no analysis was conducted to evaluate the effect of eddy currents in the salient pole track, there is experimental evidence that this "end effect" is small. Slemon et al. (1980) observed a decrease in the open circuit voltage of about 20 per cent between zero and 20 m/sec in their three-pole test HLSM. Noting that the end effect should be less significant for the 11-pole urban transit HLSM design, the induced voltage/Hz is assumed to decrease by no more than 10 per cent from zero to cruising speed (20 m/sec) at nominal excitation:

$$\frac{V_{ei}(v)}{f} = \frac{V_{ei}(0)}{f}\left[\,1 - \frac{v}{200}\,\right] \quad \text{volts/Hz} \qquad (7.2)$$

The results of the simulation over the simple duty cycle are shown in Figures 7.3 through 7.7. Figure 7.3 shows the armature current profile. The maximum armature current of 247 A occurs at low speed while accelerating hard, and at high speed while decelerating hard. The rms armature current over the full duty cycle, including 20 second dwell time, is 164 A. This corresponds to an rms current density of 4.7 A/mm^2, i.e within the guidelines for the armature, based on thermal considerations.

Figure 7.4 shows the control angle profile. The angle at which the armature current is injected, relative to the phase angle of the induced voltage, is maintained constant at -8° to the brake point and is then made to rise to 50° while motoring at cruising speed. On the down grade at cruising speed, the control angle is changed to 130° to provide braking action While decelerating, the control angle is made to rise to its low speed value of 188°.

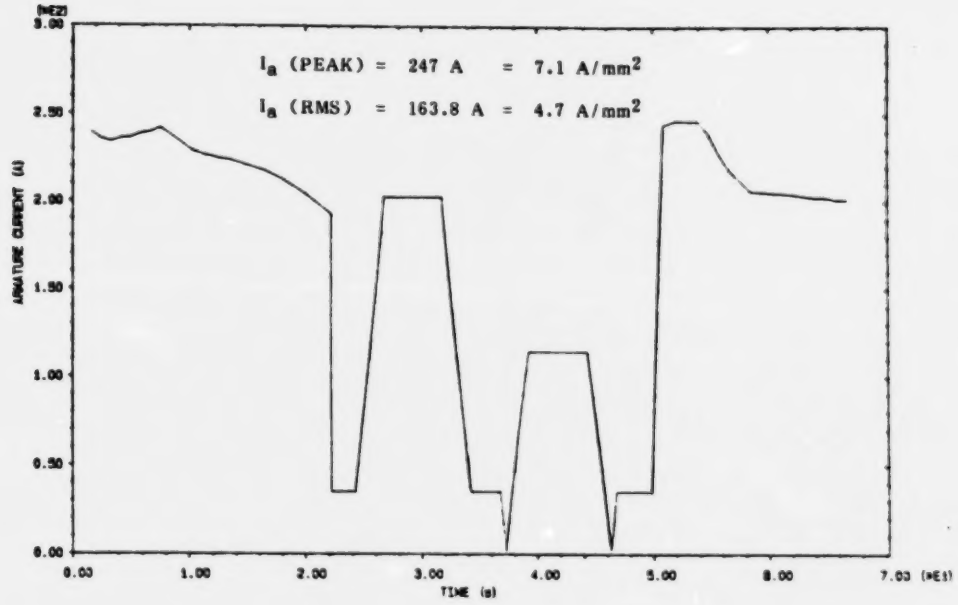

Figure 7.3 The armature current profile for the simple duty cycle

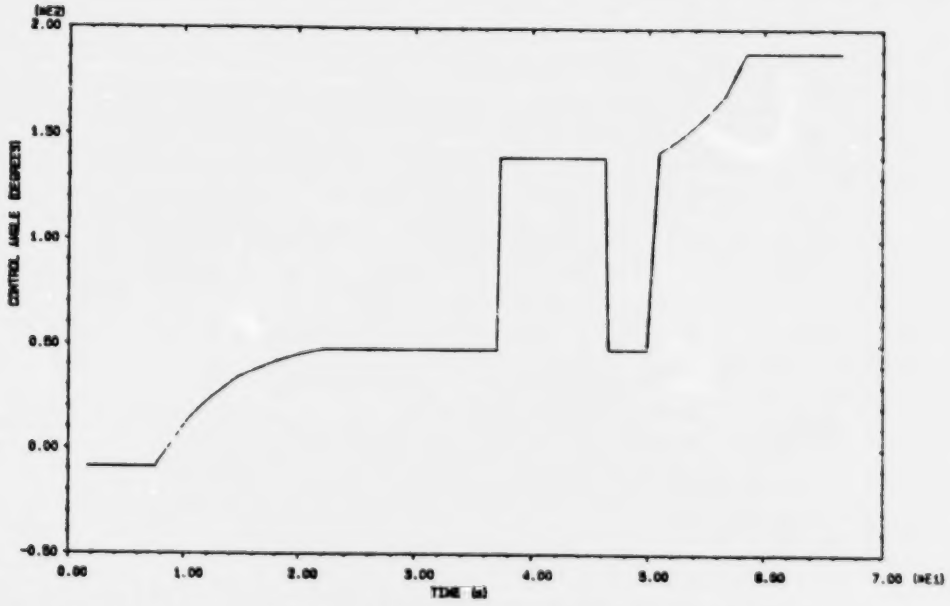

Figure 7.4 The control angle, γ, profile for the simple duty cycle

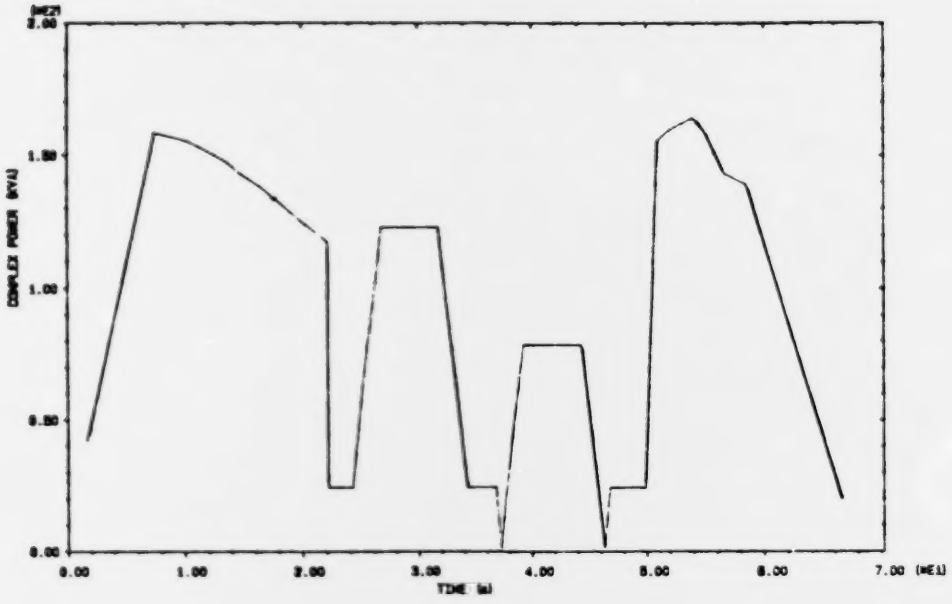

Figure 7.5 The kVA profile for the simple duty cycle

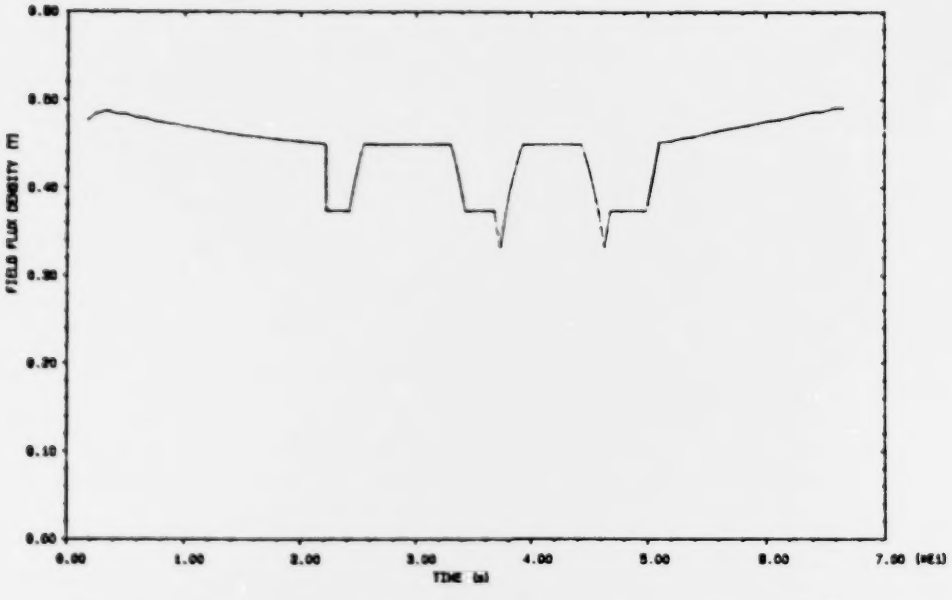

Figure 7.6 The induced voltage per Hertz, V_{ei}/Hz, profile for the simple duty cycle

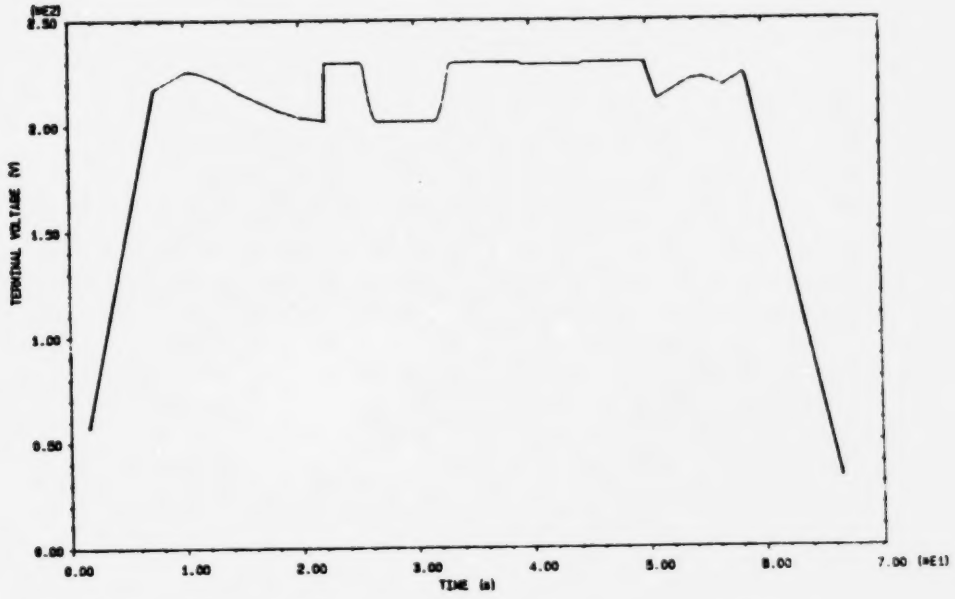

Figure 7.7 The armature terminal voltage profile for the simple duty cycle

The kVA profile is shown in Figure 7.5, while the induced voltage/Hz and terminal voltage profiles are shown in Figures 7.6 and 7.7, respectively. With regard to the V_{ei}/Hz profile, it may be noted that it is desirable to field weaken the HLSM, in order to minimize armature current, only during a limited range of operating conditions. Little performance would in fact be lost by maintaining constant field current. It would therefore appear possible to dispense with the chopper field control unit in the HLSM drive system for urban transit applications. This point will be considered further in the examination of the HLSM for integrated suspension/propulsion operation, as described in Section 9.

7.2 Transit Corridor Duty Cycle

To compare the performance of ICTS with the existing LIM drive and with the HLSM drive considered in this report, the operation of a four-car train was simulated over a typical transit corridor. The Vancouver ALRT alignment, which is scheduled for operation in 1986, was chosen. Detailed information on route characteristics was made available by UTDC. This 21 km corridor has fifteen stations with separations as short as 0.43 km and as long as 2.7 km. Dwell time at all stations was

taken to be 20 seconds. Grades are included, with a maximum of ±6 per cent.

7.2.1 Energy Management Model

An Energy Management Model (EMM) was used to conduct the comparison between LIM and HLSM drives. The basic software model was developed at Carnegie-Mellon University (by R.A. Uher and his associates at the Rail Systems Centre), and has been extensively modified at Queen's University. The model has the following input requirements:

- route characteristics, including station positions, grades, curves and local speed restrictions
- vehicle characteristics, including unloaded mass, passenger loading (which can be a function of distance), size, maximum acceleration and deceleration
- drive characteristics, including the maximum thrust versus speed capability in both motoring and braking, and a matrix of drive system efficiencies on a grid of thrust/speed points within the motor capabilities
- power supply characteristics, including substation regulation, and power distribution line impedance.

The first module of the EMM takes the above information and, by incrementally solving the dynamic equation of train motion (7.1), develops the speed versus distance/time profile of the train, taking into account available thrust, station position, speed restrictions, and acceleration/deceleration limits. The model may be used to follow the positions of many vehicles sent out from the terminals according to a specified schedule. For the purposes of this report, only one four-car train was considered.

The second module of the EMM is an electric network simulator. Knowing the thrust requirement, speed and efficiency of the drive system (motor and power conditioner), the power distribution network can be solved to yield the instantaneous power which is drawn from the feeder at the substation(s). Thus, the power profile of the vehicle can be developed, and the peak power requirements, averaged over the utility-

specified period for billing purposes, can be evaluated. The power profile can be used to develop a graph of cumulative electrical energy input versus distance/time, as the train is driven along the transit line.

7.2.2 Simulation Results

Characteristics of the 21 km Vancouver ALRT corridor are shown in Figure 7.8. The local speed restrictions (apart from stations) and the elevation profile are shown from Seabus (downtown Vancouver) to New Westminster.

To provide direct comparability between LIM and HLSM drives, common thrust versus speed capability curves in motoring and in braking were specified for both drives, as previously given in Figure 5.1. The four-car train then followed the same speed-distance profile, as shown in Figure 7.9.

The results of the Energy Management Model are shown in Figure 7.10 and in Table 7.2. In terms of power input, the higher efficiency of the HLSM drive results in lower input power requirement and somewhat higher regeneration in braking. The cumulative electrical energy profile shows this result more graphically. Over 21 km, the LIM-driven four-car train requires an energy of 202 kWh, while the HLSM-driven train (assuming full regenerative receptivity) requires 114 kWh, i.e. only 56 per cent of that for the LIM drive.

TABLE 7.2

POWER AND ENERGY CHARACTERISTICS OF LIM AND HLSM DRIVES OVER THE VANCOUVER ALRT CORRIDOR

	LIM	HLSM
Peak power demand for four-car train	1,580 kW	1,260 kW
Energy drawn by four-car train per km of corridor	9.6 kWh/km*	5.4 kWh/km*

* assumes full regenerative receptivity in the power line

(a) Speed restriction versus distance

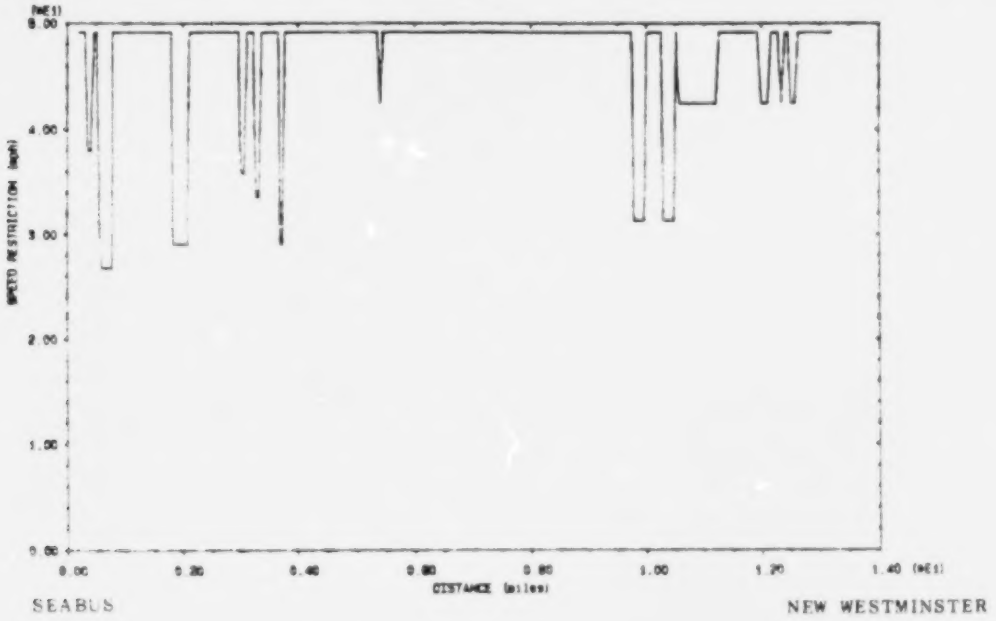

(b) Elevation versus distance

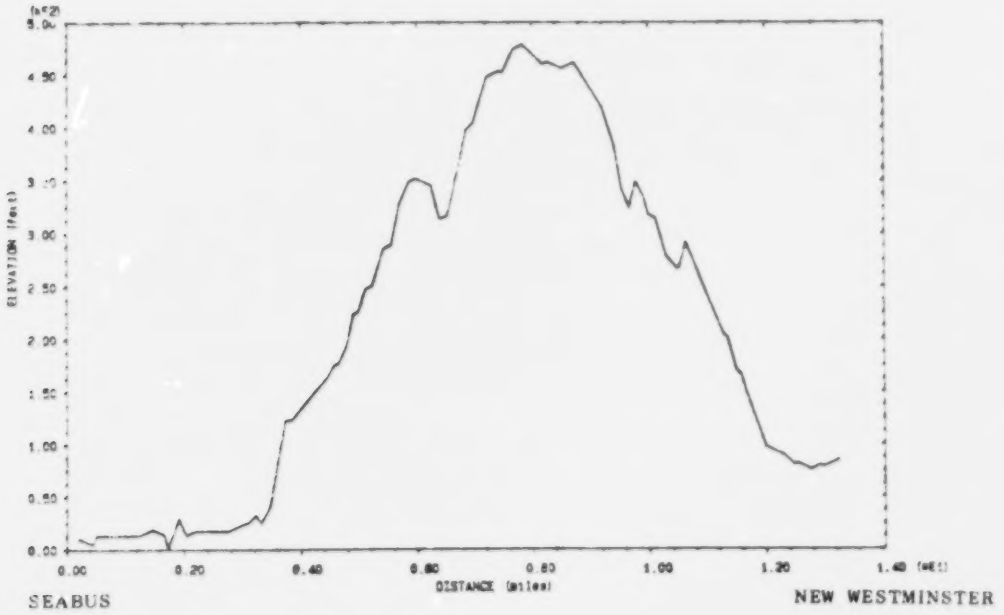

Figure 7.8 Characteristics of the Vancouver ALRT corridor

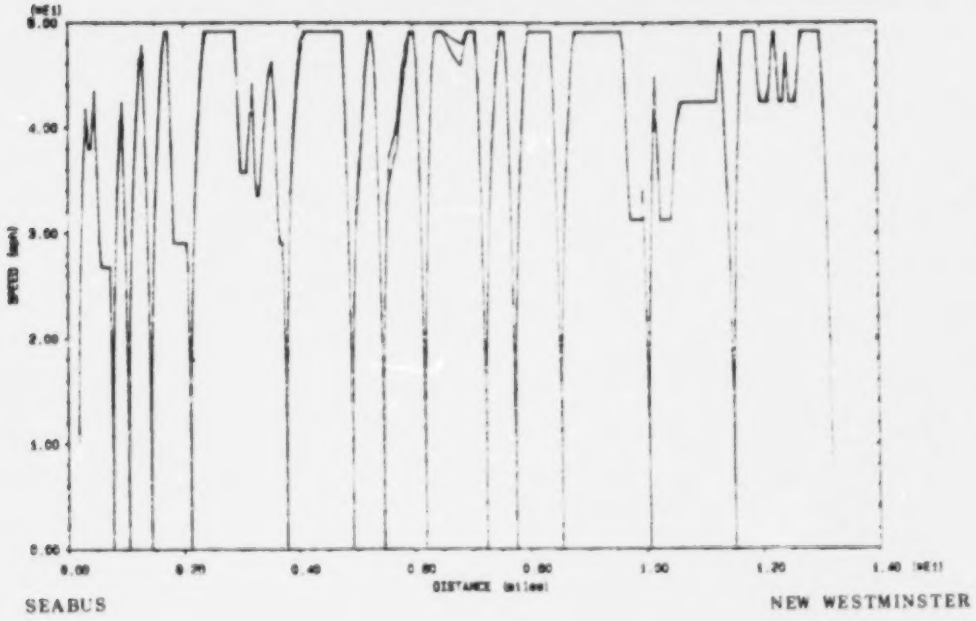

Figure 7.9 The speed-distance profile for vehicles with LIM drive and with HLSM drive along the Vancouver ALRT alignment

(a) Electrical power input versus distance

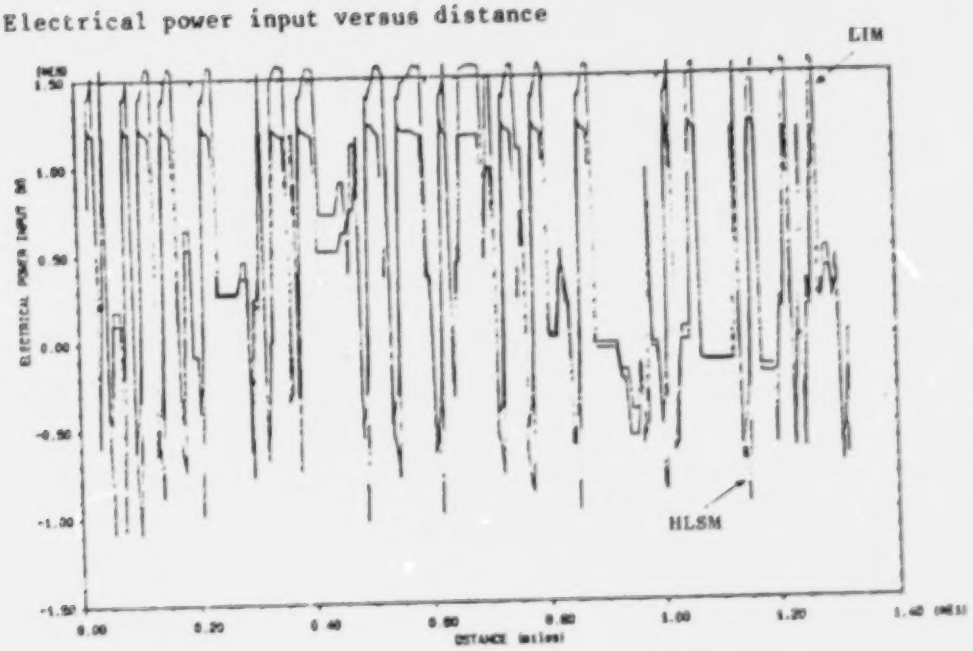

(b) Cumulative electrical energy input versus distance

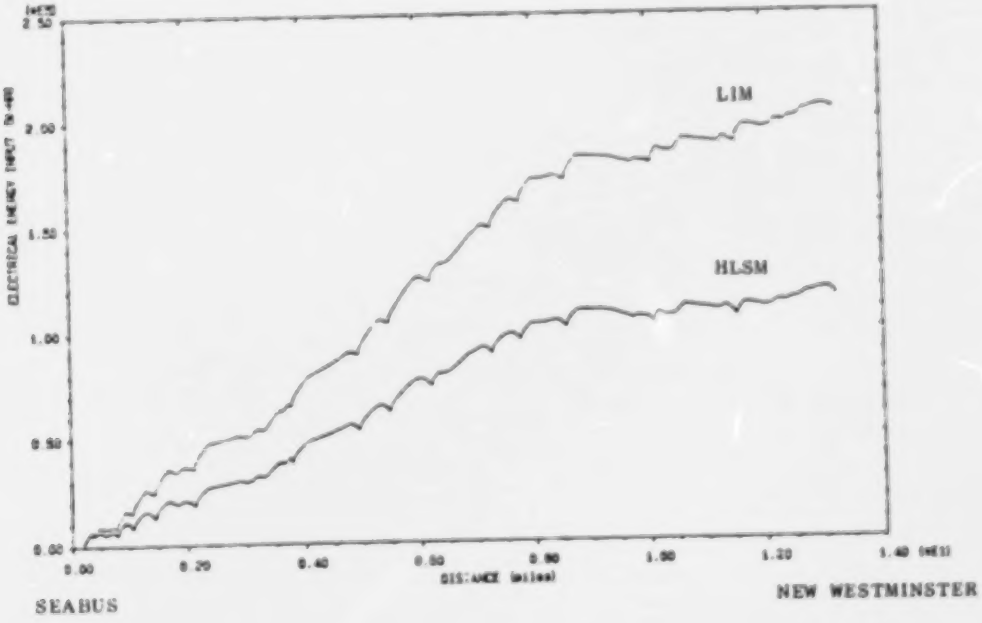

Figure 7.10 Electrical power and cumulative energy input profiles for a four-car train with LIM drive and with HLSM drive along the Vancouver ALRT alignment

8. COMPARISON BETWEEN HLSM AND LIM PROPULSION

8.1 Approach

One of the objectives of the work described in this report was to assess the homopolar linear synchronous motor as an urban transit drive, in comparison with the linear induction motor. In conducting this assessment, it is relevant to address three questions:

(i) can an HLSM be designed to meet the performance specifications for an urban transit system?

(ii) could the HLSM be retrofitted into an urban transit vehicle designed to operate with a LIM drive?

(iii) how do the capital and operating costs of an HLSM compared with the LIM drive?

The first question has already been answered positively in Section 5.3. The HLSM can be designed to meet urban transit drive specifications -- specifically those for UTDC's intermediate-capacity transit system.

As a result of the design studies reported in Section 5.3, it was determined that the HLSM required for an ICTS drive would be substantially larger and heavier than the installed LIM. It is clear, therefore, that the answer to the second question is no. The presently available space package could not accommodate the length, width or height of the HLSM.

It is still relevant to address the third question, since cost savings possible with the HLSM in comparison with the LIM might make it attractive to redesign the vehicle to accommodate the HLSM drive for the introduction of a more cost-effective second-generation ICTS.

The primary criterion used to judge the feasibility of the HLSM system was to consider its impact on the system capital cost. This was done by identifying the affected system components and predicting a cost increase/decrease for each, based on quantity and type of materials and manufacturing considerations.

Since knowledge of the proportion of each component cost relative to the overall vehicle cost or wayside cost permitted calculation of the cost ratio between systems, absolute figures were not employed. An indication of the confidence factor associated with each cost ratio is given by providing uncertainties in the relative costs.

8.2 Cost Analysis

8.2.1 Cost of the Primary

The HLSM design data indicate a materials weight of over three times that used in the ICTS linear induction motor. Since the materials used are similar in both cases (with the exception that part of the HLSM may be made of cheaper, non-laminated iron), it is concluded that the materials cost of the HLSM is higher than the LIM by a factor of 2.5, ±0.5

The experience of UTDC is that, because the LIM is not produced in large quantities, labour and tooling represent the greatest portion (about 70 per cent) of the cost. The HLSM is a somewhat more complicated structure because of its dual winding geometry, which would almost certainly increase the cost of manufacture, possibly by as much as 50 per cent. Therefore:

$$\begin{aligned}\text{HLSM cost} &= (2.5 \pm 0.5) \times \text{LIM material cost} + (1.5 \pm 0.2) \\ &\quad \times \text{LIM manufacturing cost} \\ &= (2.5 \pm 0.5) \times 0.3 + (1.5 \pm 0.2) \times 0.7 \\ &= 1.8 \pm 0.3 \text{ (where LIM cost} = 1.0)\end{aligned}$$

8.2.2 Cost of the Secondary

The materials used in the LIM secondary are extruded aluminum and mild steel bar stock. The HLSM uses solid steel only, the fabrication method as yet undetermined. While not the only factor, it is worthwhile noting that the volume of material per metre length is 2.5 times greater for HLSM rail. This implies a higher cost in both materials and handling.

Until approaches to HLSM rail fabrication have been evaluated, it is difficult to estimate or even compare costs against LIM rail very accurately; however, a range of (2.4 ± 0.5) times the cost of LIM rail seems possible. This cost disadvantage to the HLSM can be further

justified by considering the fixtures required to maintain structural integrity and track tolerances under the considerably higher HLSM normal forces.

8.2.3 Cost of the PCU

The superior efficiency and power factor of the HLSM would permit a reduction in the size or number of power devices in the inverter. This advantage, however, would be offset somewhat by the requirement for a dc/dc converter to control the field excitation which, despite its relatively small power rating, implies a higher component count.

A simple scaling of inverter cost according to the electrical rating may be overly optimistic when one considers that input conditioning, control logic, and packaging would not change dramatically.

The ICTS power conversion unit (PCU) is built in relatively small quantities as is the LIM; therefore, the dominant costs are associated with manufacturing and assembly rather than power component rating. This results in the selection of a cost ratio of 0.85 ± 0.15 as being representative.

8.2.4 Cost of Substations and Power Rail

There are different ways to view the impact of reduced power demand on the wayside costs. Because of the reduced current demand, power rails may be down-sized and substations may contain smaller, lower-cost transformers and rectifiers. Alternatively, similar power rail and substations may be used, but with substations spaced more infrequently along the transit corridor.

Again, a simple scaling of wayside power equipment by the reduction in power required would be optimistic. Certain costs, such as equipment housing, conduit, and protection, would not change. Other costs may increase due to the higher tendency for a substation to receive generated power[1] (e.g. an increase in the rating of the substation-placed, load-regulating resistor banks).

---

1 This statement is based on the assumption that the HLSM has superior regenerative efficiency, i.e. it would feed a higher proportion of the vehicle braking energy back to the line.

Keeping in mind that the peak power demand of the HLSM is about 80 per cent of the LIM, according to the supplied data, a cost ratio of 0.90 ± 0.1 in favour of the HLSM is justified.

8.2.5 Cost of the Truck and Friction Brakes

The increased weight and attractive force of the HLSM, and its increased length, would necessitate a redesign of the present ICTS truck. It is likely that the wheel diameter would need to be increased somewhat to accommodate the deeper structure, and that additional friction braking capac.ty would be needed to cover the increase in vehicle weight (approximately 4,000 kg, including the weight required in strengthening the truck).

The cost ratio of the new truck to the ICTS truck would be about 1.2 ± 0.1.

8.2.6 Cost Analysis Summary

Table 8.1 breaks down the HLSM/LIM comparison on a per-component basis and indicates the cost ratio for the vehicle. Table 8.2 does the same for wayside costs. The results show that in both cases the HLSM would result in higher capital costs.

TABLE 8.1

PER-VEHICLE COST COMPARISON

Subsystem	Per Cent of Total Vehicle Costs	Cost Ratio HLSM/LIM
1. Trucks and brakes	10	1.2 ± 0.1
2. Motor primaries	7	1.8 ± 0.3
3. Power conditioning	22	0.85 ± 0.15
4. Other (incl. assembly)	61	1.0

HLSM vehicle cost/LIM vehicle cost = 1.05 ± 0.05.

TABLE 8.2

WAYSIDE COST COMPARISON

Subsystem	Per Cent of Total Wayside Costs	Cost Ratio HLSM/LIM
1. Reaction rail	5	2.5 ± 0.5
2. Substations and power rail	17	0.9 ± 0.1
3. Other	78	1.0

HLSM wayside cost/LIM wayside cost = 1.05 ± 0.04.

8.3 Discussion

The above analysis considered only capital cost, not energy costs or maintenance costs. This may seem surprising in view of the fact that the one distinct advantage of the HLSM over the LIM is its significantly lower energy consumption.

Consider the following arguments:

(1) The performance of the HLSM in comparison with the LIM over a typical corridor (see Section 7.2.1) shows that, while the total energy consumed by the HLSM-driven vehicle is only 56 per cent of that consumed by the LIM-driven vehicle, the peak power demand of the HLSM is approximately 80 per cent of that for the LIM. Peak power demand determines the sizing and cost of vehicles and wayside power equipment, and does not offer as much of a capital cost saving as the energy consumption figures might indicate.

(2) One significant energy-saving factor of the HLSM over the LIM is its superior regenerative ability. This is really only a saving if the supply is assumed 100 per cent receptive. In systems such as those in which the ICTS vehicles will operate, 100 per cent receptivity is not achievable, especially if one presumes the higher efficiency vehicle in given typical operating scenarios.

(3) Energy costs are typically a minor component of total operating costs in any transit system.

The weakest area in the cost analysis exercise concerned the cost of HLSM reaction rail. It should be noted that despite the excess material, the use of a single material may permit a simpler, even automated, fabrication/installation procedure, which would make it more competitive with LIM rail.

The discussion regarding the power controller assumed a transistorized inverter similar to that presently used for the LIM drive. If a thyristor inverter is considered instead, the HLSM motor, being synchronous, would presumably permit load commutation, thereby simplifying the inverter design.

The greatest disadvantage of the HLSM is its size and weight, particularly of the reaction rail. The physical limits governing the size appear to be magnetic rather than thermal.

One aspect that could be considered is the economics of placing a few inverter stations in the power system such that regenerated power could be returned to the hydro grid. This would increase line receptivity and allow the HLSM to operate at its peak overall efficiency. Naturally, this advantage would need to be weighed against the additional costs of the inverter substations.

8.4 Conclusions

The positive features of the HLSM, in comparison with the LIM, are its superior efficiency and power factor. The negative features are its larger size and weight, which increase both vehicle and wayside costs by an estimated 5 per cent. On the basis of the capital cost analysis presented, the HLSM should not be considered as an alternative to LIM propulsion for ICTS-type applications.

One of the arguments in favour of the HLSM is its reduced energy consumption; however, since part of this improvement is due to the HLSM's better regenerative capability, the argument is only valid for installations which have receptive power distribution systems. This type of distribution system is not planned for the first intermediate-capacity transit system (ICTS) applications. It is therefore doubtful if the increased efficiency and power factor of the HLSM could be exploited to significantly reduce operating costs.

9. POTENTIAL OF HLSM FOR INTEGRATED SUSPENSION/PROPULSION

9.1 Normal Force

The HLSM was conceived as a linear drive which could operate at a high power factor. It has been shown that this objective can indeed be achieved, but at the expense of increased size and weight as compared with a LIM of equivalent mechanical power output.

To achieve a power factor approaching unity, the HLSM must be designed as a strong field/weak armature machine. As a consequence of this high power factor operation, a large normal force attracting the vehicle-borne component to the salient pole track is generated. This normal force, F_z, may be evaluated from the excitation field distribution determined by finite element analysis (see Figure 5.7(c)), by means of the "magnetic pressure" expression:

$$F_z = \int \frac{B_z^2}{2\mu_0} \, dA \qquad \text{over the surface area of the armature} \qquad (9.1)$$

Figure 9.1 shows the normal force per pole as a function of dc excitation for the urban transit HLSM design presented in Section 5.3. For a linear magnetic circuit, the normal force is proportional to the square of excitation. The non-linearity in Figure 9.1 indicates the onset of saturation.

For a nominal excitation of 24 kA turns, the normal force on the urban transit HLSM would be 93 kN (note that the 11-pole machine is longer than 11 because of half-filled end slots), in comparison with a maximum normal force of 25 kN for a single-sided LIM of equivalent power output (i.e. the ICTS LIM). For urban transit drive applications, implementation of the HLSM would result in the addition of at least one tonne per truck (in comparison with the LIM). This essentially unsprung mass would cause major problems in the dynamic stability of the wheeled trucks. In addition, the high normal force would almost double the axle load, imposing major penalties on both trackwork and vehicle. It has, therefore, been concluded that the HLSM is not viable as solely an urban transit drive.

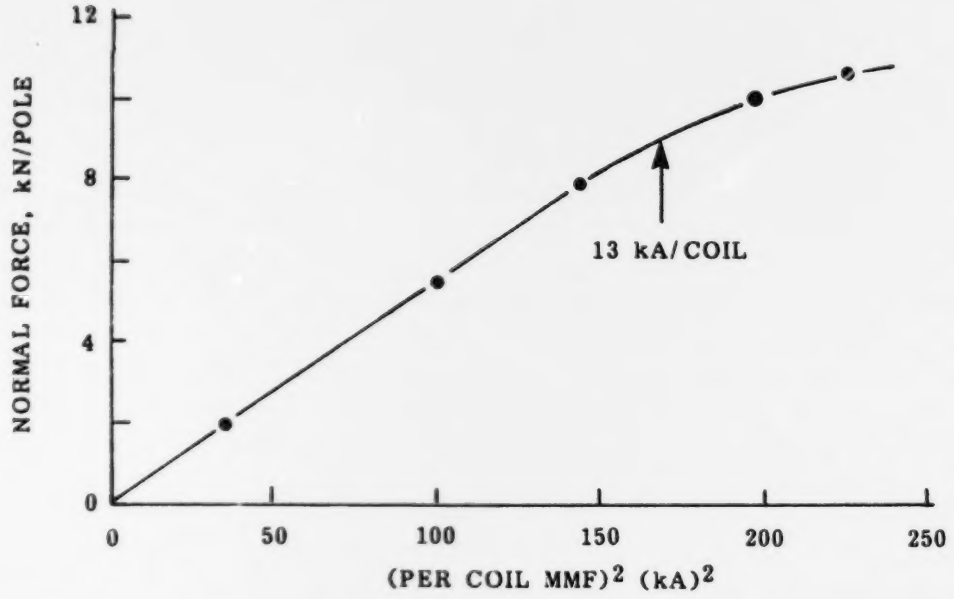

Figure 9.1 Normal force per pole as a function of (dc mmf/coil^2) for the urban transit HLSM

9.2 Integrated Suspension/Propulsion System

The HLSM presented in Section 5.3 was designed to produce a maximum thrust capability of 13 kN. This machine would have a normal force of 93 kN, giving a lift/thrust ratio of 7.1. With a mass of 1,410 kg, this HLSM would have a lift/weight ratio of 6.7, could support a payload of 8,000 kg, and could provide a vehicle with an acceleration of up to 0.14 g (1.37 m/sec^2). It is apparent, therefore, that the HLSM can generate the forces required for an integrated suspension/propulsion system (ISPS), as proposed by Boldea and Nasar (1978, 1979, 1982) and by El-Zawawi et al. (1981).

To make use of the normal force of the HLSM for vehicle suspension, the HLSM must be operated in a controlled electromagnetic mode. For ISPS applications, two salient pole "rails" would be mounted to the underside of the guideway structure, as shown in Figure 9.2, and each vehicle would carry at least four individually controlled HLSMs for stability.

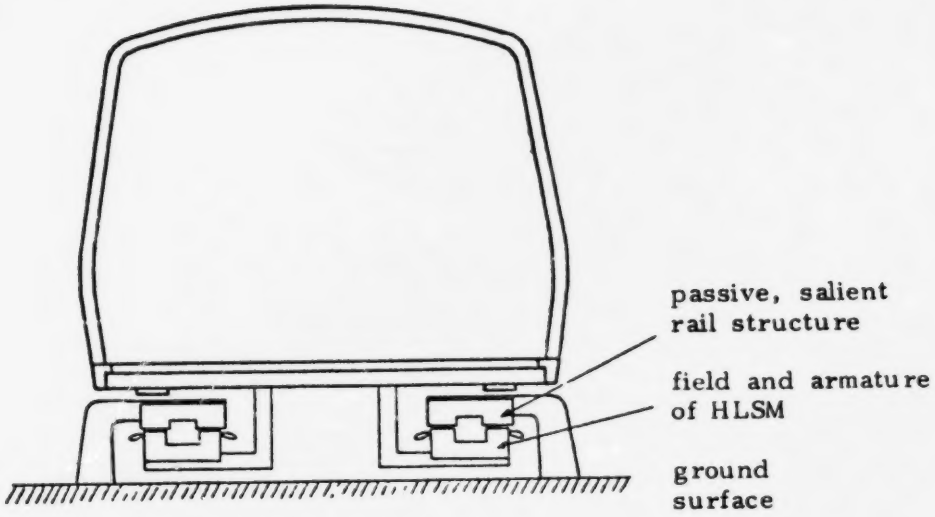

Figure 9.2 A cross-section of vehicle and guideway, showing how HLSMs may be used for integrated suspension and propulsion

9.3 Control

In the simulation of the urban transit HLSM over a typical corridor (see Section 7), it was apparent that the machine should be operated at close to full field flux in order to gain optimum performance (i.e. highest armature $\eta \cos \phi$). Under low thrust cruise conditions, it was desirable to reduce the field excitation by no more than 20 per cent. Under all conditions, the urban transit HLSM would, therefore, be operated with the excitation in the range 19-24 kA.t.

In the ISPS mode, it would be necessary to maintain constant field flux, and to dynamically control excitation in response to variations in the air gap and its time derivatives. Performance evaluation, using the equivalent circuit model, has shown that this mode of operation produces little degradation in the electrical characteristics of the HLSM under thrust control.

It is apparent, therefore, that independent normal force and thrust control would be achievable with the HLSM, and a schematic of an ISPS control system is shown in Figure 9.3. Chopper control of the field excitation, with feedback from gap sensors and accelerometers, can be used to maintain a dynamically stable electromagnetic suspension. This

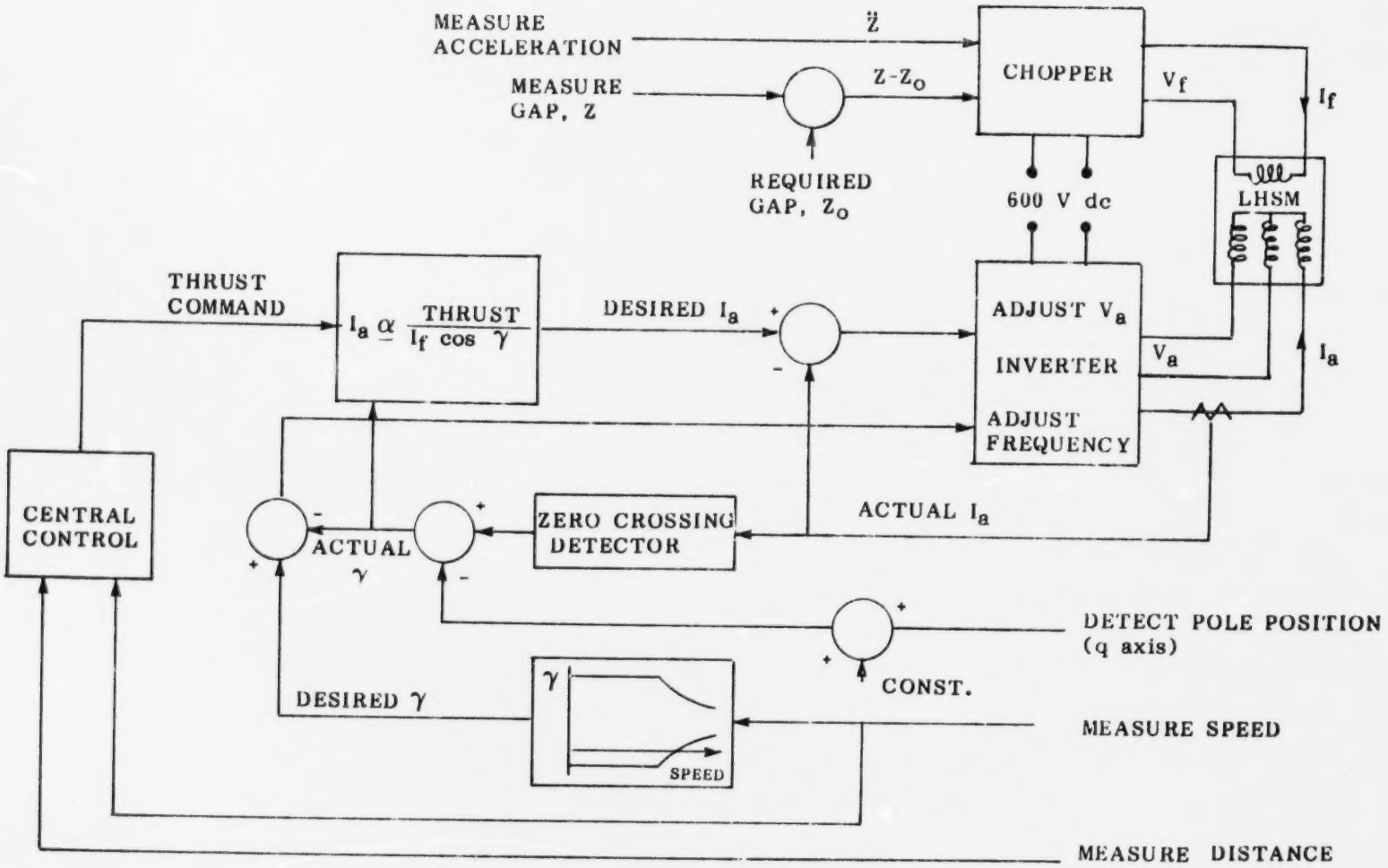

Figure 9.3 Schematic of ISPS control scheme for the HLSM

technology is now well established and demonstrated as a result of the TRANSRAPID, HSST and People Mover systems operating in the Federal Republic of Germany, in Japan, and in England, respectively.

To maintain optimum electrical characteristics at the armature terminals, under the constraint of constant field excitation, a current angle versus speed characteristic (similar to those in Figure 5.4(d)) can be defined. Thrust is then controlled, independently of normal force, simply by adjusting the magnitude of the armature current at the specified speed-dependent current angle, γ.

9.4 ISPS Design

It has been noted that the thrust and normal force characteristics of the urban transit HLSM design presented in Section 5 make it suitable for ISPS operation. In practise, the two centrally mounted 11-pole HLSMs of an urban transit drive would be replaced by four corner-mounted, six-pole HLSMs for integrated suspension and propulsion. The vehicle configuration would then be as shown in Figure 9.1.

Most of the design features of the urban transit HLSM, as presented in Section 5.3, could remain unchanged. The most significant necessary modification would be a doubling of the armature conductors per slot from 8 to 16 to keep the impedance of the machine compatible with the available power supply (up to 230 V sinusoidal/phase from a 600 V dc line). A representative design for an ISPS HLSM is given in Table 9.1.

Referring to Figure 9.1, a nominal dc mmf of 26 kA.turns is selected for ISPS operation. This excitation drives the magnetic circuit to a low level of saturation, leaving sufficient excess force at higher excitation to ensure dynamic stability of the suspension. The normal force for the ISPS machine design is 63 kN. Four HLMSs would, therefore, be capable of lifting a total vehicle mass of 25,600 kg.

9.5 Performance

The equivalent circuit parameters computed for the representative HLSM design for ISPS operation are listed in Table 9.1. These parameters may be used to define a current angle versus speed control curve and to

TABLE 9.1

DESIGN OF AN HLSM FOR ISPS OPERATION

(i) Cross-section

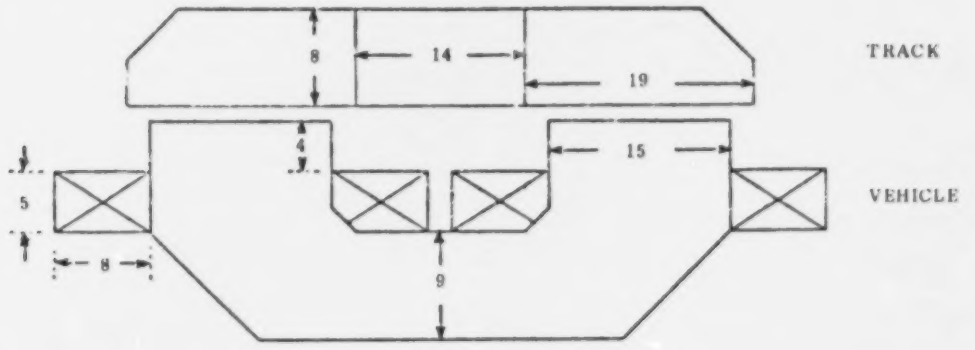

dimensions in cm

(ii) Field Winding

Total mmf		26 kiloamp. turns
Per coil:	Number of turns	500
	Current	26 A
	Cross-section	50 mm x 80 mm
	Fill factor (allowing for cooling passages)	0.75
	Conductor cross-section	6 mm^2
	Resistance	4.6 ohms
	Conductor current density	4.3 A/mm^2
Driving voltage (two coils in series)		260 volts
Winding loss		6.2 kW

(iii) Armature Winding

Number of phases	3
Number of poles	6
Pole pitch	183.3 mm
Active width of armature	150 mm (each side)
Number of slots	41 (each side)
Half-filled slots	5 (at each end)

TABLE 9.1 (cont'd)

DESIGN OF AN HLSM FOR ISPS OPERATION

(iii) Armature Winding (cont'd)	
Slot pitch	30.6 mm
Slot width	10.2 mm
Tooth width	20.4 mm
Slot depth	40.0 mm
Number of slots/pole/phase	2
Number of conductors/slot	16
Slot fill factor	0.67
Coil pitch	5/6
Coil overhang	80 mm (each side)
Conductor cross-section	17 mm^2
Number of turns/phase	96
Frequency range	0-60 Hz
Maximum available phase voltage	230 V
Voltage limit	8 m/sec
At peak thrust: current	120 A
conductor current density	7.1 A/mm^2

(iv) Equivalent Circuit Parameters (per phase, at 60 Hz)			
Armature resistance			0.186 ohms
Leakage reactance:	slot leakage	0.169 ohms	
	tooth-top leakage	0.071 ohms	
	end-winding leakage	0.041 ohms	
	harmonic leakage	0.023 ohms	
	central gap leakage	0.051 ohms	0.355 ohms
Direct axis, x_{ad}:	from stored energy expression		0.568 ohms
	from finite element computation		0.404 ohms
Quadrature axis,, x_{aq}:	from stored energy expression		0.410 ohms
	from finite element computation		0.649 ohms
Induced voltage			fundamental component of rate of change of flux linkage

determine the armature terminal characteristics of the ISPS HLSM. These characteristics for the urban transit HLSM were presented and discussed in Section 5.4.

The motoring characteristics for an ISPS HLSM, meeting the vehicle thrust specifications (for four ISPS machines) given in Figure 5.1, are shown in Figures 9.4(a)-(d). As for the urban transit drive, the control angle characteristic (9.4(a)) is chosen to minimize armature current across the speed range. The control angle varies from -7° to the break point (8 m/sec), rising to +60° at cruising speed.

For the HLSM meeting the thrust specification, armature current (9.4(b)) is approximately constant at 102-112 A, while maximum complex power is a modest 76 kVA (9.4(c)). The armature $\eta \cos \phi$ (9.4(d)) peaks at 0.93 at 14 m/sec, and is 0.87 at cruising speed.

Similar braking characteristics for the ISPS HLSM, again meeting the thrust specification in Figure 5.1, are shown in Figures 9.5(a)-(c). The control angle (9.5(a)) varies from 187° up to the break point, falling to 125° at cruising speed. Again, armature current (9.5(b)) is approximately constant at 105-112 A, while maximum complex power (9.5(c)) is 78 kVA.

9.6 Discussion

It is evident that the HLSM can be designed to provide not only sufficient motoring and braking thrust to meet the requirements of an urban transit vehicle, but also a normal force of sufficient magnitude to suspend this vehicle in a controlled electromagnetic mode. The high normal force which leads to major problems in the implementation of the HLSM for wheeled urban transit can be used to positive advantage for integrated suspension/propulsion systems.

It is concluded that ISPS operation offers the most appropriate application for the HLSM. This has been recognized by Boldea (1984). At the Polytechnic Institute in Timisoara, Romania, an experimental vehicle (MAGNIBUS-01) has been constructed, and controlled electromagnetic suspension by ISPS HLSM is reported to have been demonstrated. The results obtained to date indicate to Boldea that his MAGNIBUS system has a lower weight, noise and energy consumption per passenger-km, in

(a) Control angle versus speed

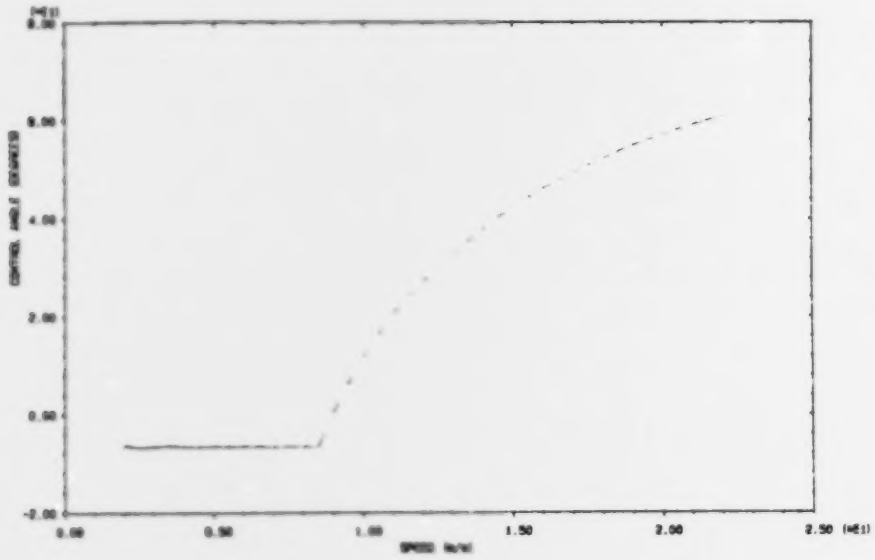

(b) Armature current versus speed

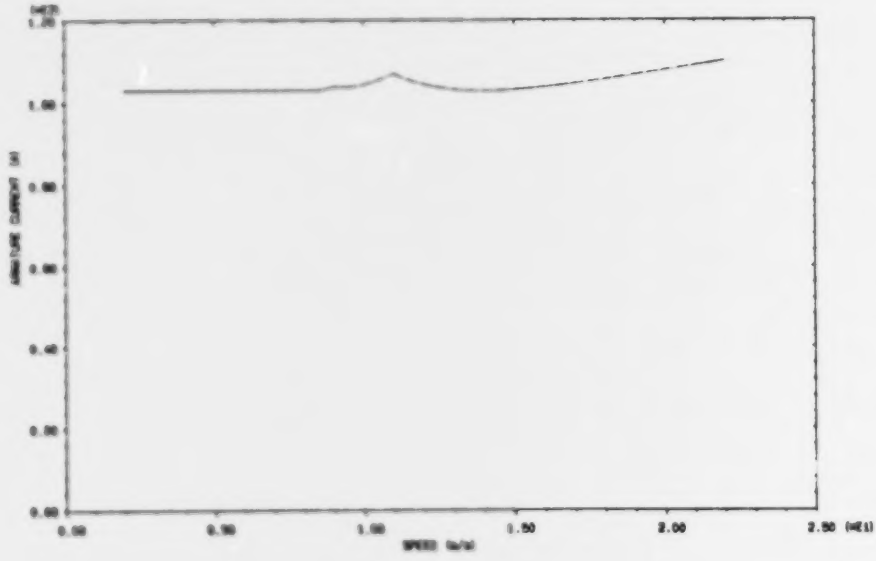

Figure 9.4 Performance characteristics of the ISPS HLSM with dc mmf of 26 kA.turns, meeting the performance specification in motoring

(c) Complex power versus speed

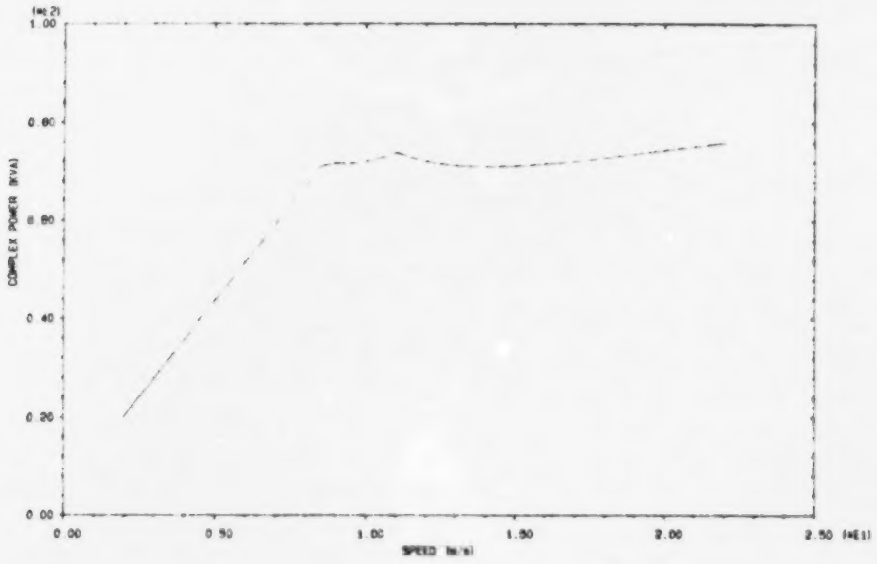

(d) Efficiency-power factor product versus speed

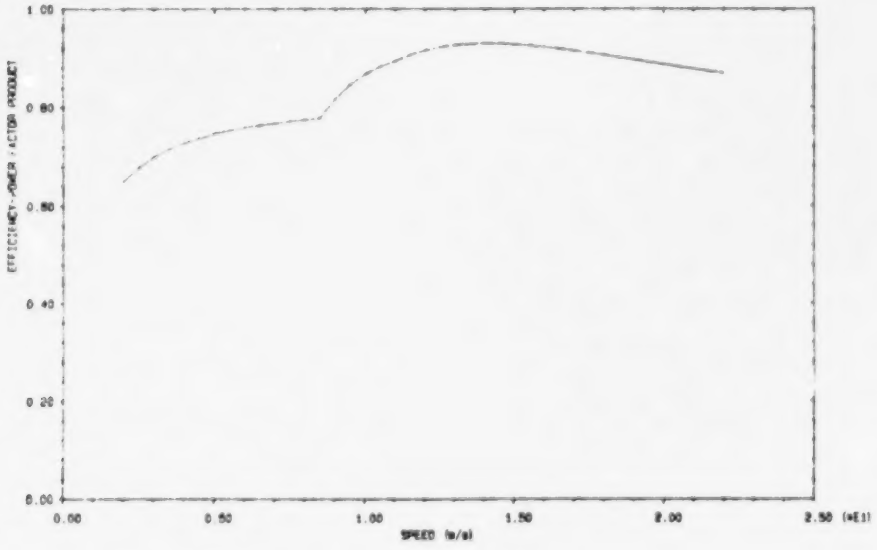

Figure 9.4 (Cont'd)

(a) Control angle versus speed

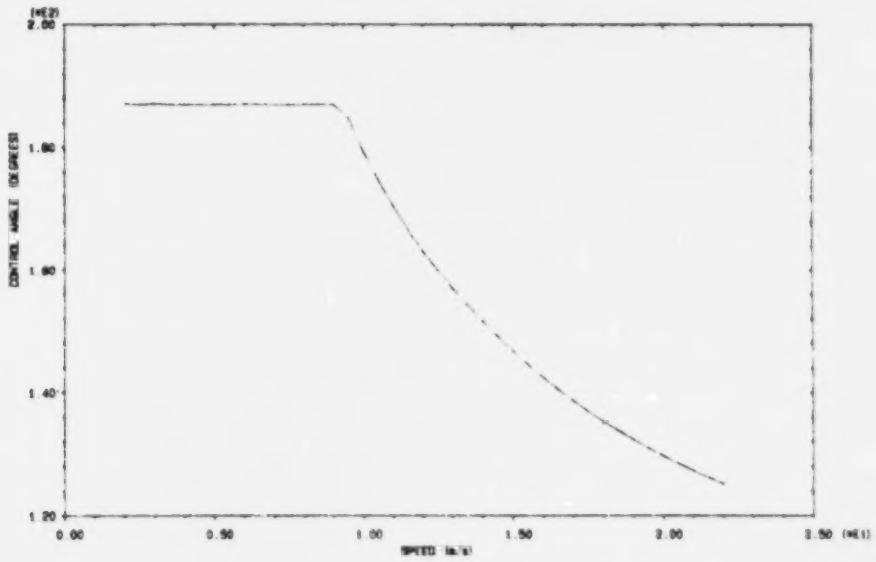

(b) Armature current versus speed

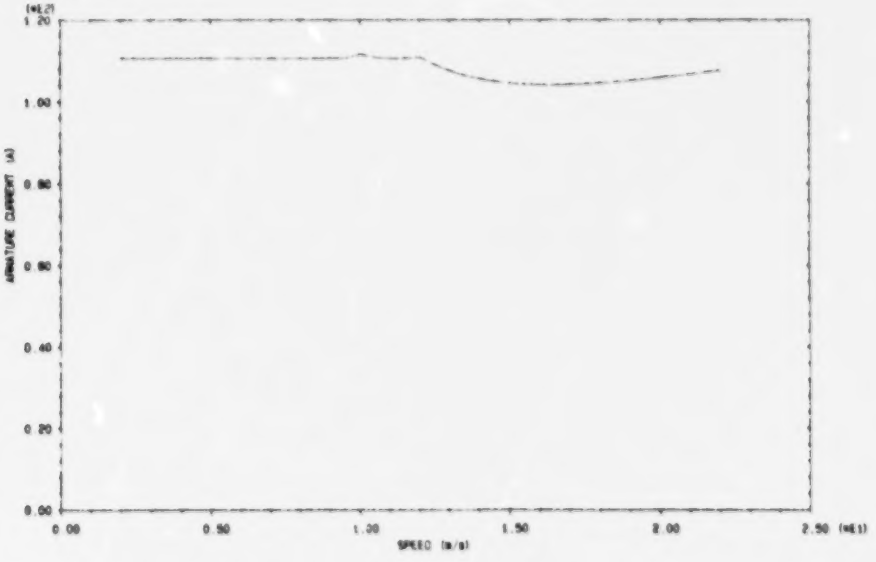

Figure 9.5 Performance characteristics of the ISPS HLSM with dc mmf of 26 kA.turns, meeting the performance specification in braking

(c) Complex power versus speed

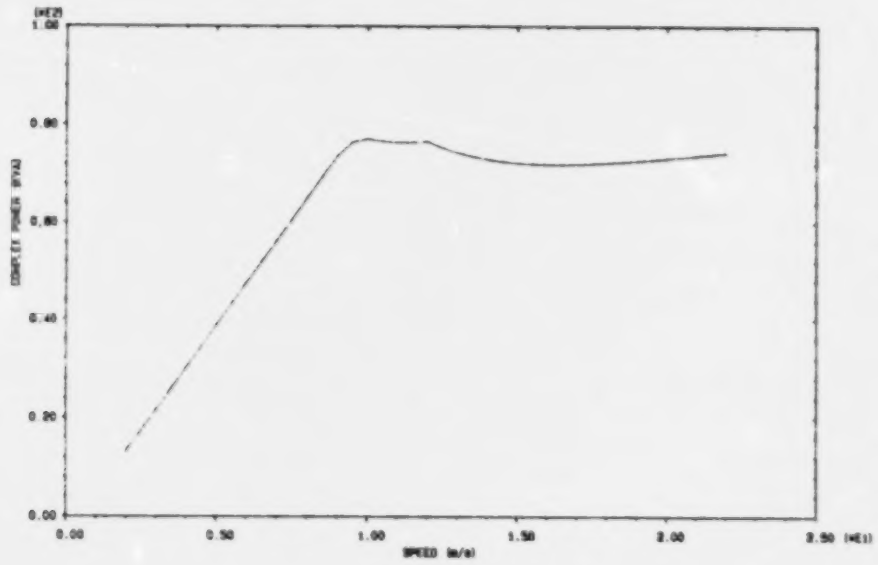

Figure 9.5 (cont'd)

comparison with existing systems (using wheels and rotary drives) and air modes, for similar operating speeds. Boldea considers the MAGNIBUS concept to be the least costly of the Maglev options, due primarily to lower guideway capital costs,, and it offers high energy efficiency through the use of ISPS HLSMs. The encouraging laboratory results with MAGNIBUS-01 have led to the hope to design and build a prototype vehicle for high-speed (up to 300 km/h) testing.

10. CONCLUSIONS AND RECOMMENDATIONS

10.1 Objectives and Achievements

The overall objectives of this project were to:

- conduct a comprehensive review of the state of knowledge of homopolar linear synchronous motors (HLSMs) and assess analytical approaches
- define a design specification for the HLSM, based on ICTS LIM propulsion requirements
- develop analytical techniques, as required
- conduct a design study for urban transit applications and evaluate performance capabilities of the proposed design
- evaluate the performance and control requirements of the HLSM over a typical transit vehicle duty cycle
- conduct an evaluation of the HLSM as a replacement for the LIM for ICTS-type applications
- evaluate the performance and control requirements of the HLSM as an integrated suspension and propulsion system.

All of these objectives have been achieved, as described in Sections 2 through 9 of this report.

Having reviewed the various analytical approaches used by other researchers, as reported in the literature, it was considered that most of the available techniques made use of assumptions that were too idealized and that did not take into account the non-linearities of iron saturation. Noting that a well designed machine should operate with some degree of saturation (to minimize mass), an analytical technique that includes the saturable characteristics of machine steels was considered desirable. The finite element method was selected for this purpose.

It was shown that a two-dimensional, non-linear model, applied to longitudinal and transverse sections and to a developed model of the

HLSM, could be used to gain a quantitative appreciation of the three-dimensional field distribution in the machine. This information was used to determine the per-phase induced voltage and good estimates of the d- and q-axis armature reactance parameters in the two-reactance equivalent circuit model of the HLSM. The finite element and equivalent circuit models were validated as effective tools for design studies and performance evaluation.

To make the assessment of the HLSM directly relevant to Canadian transit developments, a set of specifications and design guidelines were established, based on requirements and operating experience with UTDC's ICTS linear induction motor drive system. A design study was then conducted to identify an HLSM which was close to optimum in terms of high power factor operation, high efficiency, and minimum size and mass.

The equivalent circuit model of the HLSM was then used to evaluate control strategies. To minimize armature heating, it was shown that an armature-current-angle-versus-speed characteristic could be defined. In practice, this angle could be maintained by detecting the track pole position (by proximity or reluctance sensors) and by injecting an armature current of appropriate frequency, amplitude and delay to match the speed and thrust requirements of the transit vehicle. A power-transistorized voltage source inverter was shown to be appropriate. It would be necessary to control the shape of the current waveform to be close to sinusoidal, particularly at low speed, to minimize thrust harmonics. A chopper is also required to control the field current of the HLSM.

Having defined the HLSM design and its power-conditioning and control features, the performance of the HLSM over a typical duty cycle and over a route having the characteristics of a typical urban transit system was evaluated. A typical 1 km station-station duty cycle was defined such that the HLSM would be exercised over its full operating range. The results showed that the HLSM design could provide the specified performance within the design guidelines. An ICTS vehicle with HLSM drive was then run in simulation, using the Queen's Energy Management Model, over the Vancouver ALRT alignment. This allowed the net energy and peak power demand to be evaluated for direct comparison with a vehicle with LIM drive.

The design and performance information then allowed the HLSM to be evaluated as a replacement to the LIM drive system in ICTS-type applications. This assessment was conducted by engineers at UTDC Research & Development Ltd., and is summarized in the next subsection, giving conclusions to this project.

Finally, the HLSM was examined for a different application -- one in which the large normal force is controlled electromagnetically and used for vehicle suspension. The HLSM then becomes an integrated suspension and propulsion system (ISPS). It was shown that comparatively little design modification was required to allow the HLSM to operate in the ISPS mode. This HLSM was shown to be feasible, and indeed attractive, for a passive guideway Maglev system.

10.2 Conclusions

It has been shown that the HLSM can be designed and controlled to meet the specifications and design guidelines of an ICTS-type transit system. In this subsection, we will focus on the assessment of the HLSM in comparison with the LIM for urban transit drive systems.

A detailed comparison of the design features of the HLSM and the LIM propulsion units for UTDC's intermediate-capacity transit system has been given in Tables 5.2 and 5.3. A comparison of the general characteristics of the two machines is given in Table 10.1.

From an inspection of the comparative characteristics of the HLSM and LIM, the basic trade-offs become apparent. On the negative side, the HLSM is considerably larger, heavier, requires a deeper guideway component, and has an appreciably higher normal force than the LIM. However, on the positive side, the HLSM operates at a significantly higher power factor efficiency product, and therefore requires an inverter of lower capacity.

The effect of the latter characteristic has been quantified by means of an energy management model, in which the operation of a transit vehicle was simulated over the Vancouver ALRT corridor. LIM- and HLSM-propelled vehicles were run over the 21 km corridor, with 15 stations at varying separations, with a dwell time at each of 20 seconds. Grades, with a maximum of 6 per cent, and the mass differential (one

TABLE 10.1

RELATIVE FEATURES OF HLSM AND LIM

	HLSM	LIM
Motor size	2.35 m long x 0.65 m wide x 0.18 m high	1.90 m long x 0.52 m wide x 0.10 m high
Mass of electromagnetic components of motor	1,410 kg	422 kg
Depth of guideway component	8 cm	3 cm
Maximum normal force	90 kN	25 kN
Armature power factor times efficiency (above 15 m/sec)	0.92-0.94	0.40-0.42
Inverter capacity	200 kVA	325 kVA
Energy drawn by four-car train per km of corridor	5.4 kWh/km	9.6 kWh/km
Peak power demand of four-car train	1,260 kW	1,580 kW
Overall power factor times efficiency (above 15 m/sec)	typically 0.85	typically 0.40

* Assumes full regenerative receptivity.

tonne per motor) between the HLSM and the LIM were included. The corresponding energy drawn from the 600 V dc line (taking into account converter efficiencies) per km of corridor, and the peak power demand of a typical four-car train are given in Table 10.1.

In their assessment of the HLSM (see Section 8), UTDC note that one of the positive features of the HLSM is its reduced energy consumption. However, part of this improvement is due to the HLSM's better regenerative capability. While some of this energy could be used by other vehicles on the system, complete regeneration would require the installation of ac power line inverters rather than rectifiers at some substations. Alternatively, the regenerative energy could be absorbed by a bank of switched resistors at some substations. UTDC concludes

that it is doubtful if the positive features of the HLSM (i.e. its increased efficiency and power factor) could be exploited to significantly reduce capital or operating costs of ICTS-type transit systems.

With regard to the negative features of the HLSM, the increased size, mass and normal force would pose serious problems for urban transit. The addition of almost one tonne of unsprung mass to each axle would have major implications for truck dynamics. This, together with the high normal force, would impose unacceptable penalties on the track work and vehicle.

It must, therefore, be concluded that the HLSM, as a propulsion unit, is not viable for urban transit applications.

In reaching the above conclusion, it should be noted that the HLSM was designed to achieve high power factor operation. By making the HLSM a strong-field/weak-armature machine, unity power factor can be achieved. If a somewhat lower armature power factor, say 0.8, was acceptable, the number of ampere-turns on the field coil could be reduced (but with a corresponding increase in the required armature ampere-turns to maintain performance), effecting some economies in size and mass of the HLSM. While no detailed design studies have been conducted, the HLSM would still be considerably larger and heavier than an LIM of equivalent performance. It is doubtful that such a design would make the HLSM any more attractive as an urban transit drive.

During the design studies of the urban transit HLSM, it was noted that the strong field requirement for high power factor operation leads to a large normal force between motor and track. This force is of sufficient magnitude to provide vehicle suspension if controlled in an electromagnetic mode.

It has been shown that independent normal force and thrust control, at high $\eta \cos \phi$, is possible with the HLSM. Chopper control of the field excitation, with feedback from gap sensors and accelerometers, can be used to maintain a stable electromagnetic suspension. In order to maintain good armature terminal characteristics, a current-angle-versus-speed characteristic can be defined, and thrust can be controlled simply by adjusting the magnitude of the armature current at the specified speed-dependent angle.

Unlike the TRANSRAPID and M-BAHN drives, the HLSM, as an integrated suspension/propulsion system, uses an inexpensive passive guideway structure. While the ROMAG (now MAGTRANSIT, under development by Boeing Aerospace Company) system also has a passive guideway, using an LIM in an integrated suspension/propulsion mode, the HLSM operates at high $\eta \cos \phi$ and requires a power conditioner of lower capacity.

It appears that the application most suited to the characteristics of the HLSM is integrated suspension/propulsion. In this mode of operation, the HLSM offers ease of control and high energy efficiency. It merits detailed evaluation for urban transit and intermediate-speed (e.g. commuter, airport access) applications.

10.3 Recommendations

At the time at which this HLSM project was being planned, it was considered that a two-phase research program would be appropriate. The first phase would comprise analytical development, design studies, performance evaluation, and assessment. The second phase, contingent on the results of Phase I, would comprise the design and testing of a large-scale motor on the CIGGT rotating wheel test facility. In the light of the results of this work, it cannot be recommended that the project proceed to Phase II at this time. The HLSM, as designed to produce high power factor operation, is not viable as a propulsion unit for urban transit.

There remains the possibility that other configurations of the HLSM could offer certain better features than those of the HLSM system design reported here, particularly those including the use of permanent magnet materials instead of (or in addition to) dc field excitation. This area of investigation is under active study in the Physics Department at Queen's University (Atherton, 1982), and progress in analysis, design and experimentation is reported in Appendix E.

It has been shown that the most likely application for the HLSM is as an integrated suspension/propulsion system. The functions of suspension and propulsion in one integrated electromagnetic structure have been applied in the TRANSRAPID, M-BAHN and ROMAG (now MAGTRANSIT) vehicles. The HLSM offers this mode of operation with high $\eta \cos \phi$ and with a passive guideway.

The potential of ISPS HLSMs has been recognized by Boldea in his MAGNIBUS research and development program. It would appear that the HLSM, with its ease of independent suspension and propulsion control, is viable for low-to-intermediate-speed, non-contact vehicles. The People Mover System, recently installed in Birmingham to provide shuttle service between the airport terminal and railway station/ exhibition centre, is an example of the type of service which could benefit (in terms of reduced capital and operating costs) from the implementation of HLSMs.

While we are not recommending a research and development program on ISPS HLSMs at this stage, we recommend that the results of this work be reported at international transportation forums and that contact be made with interested parties in the U.S. (e.g. Mitre Corporation and Boeing Aerospace Company) to investigate the possibility of a collaborative research and development venture.

11. REFERENCES

11.1 A Bibliography of Iron-Cored Linear Synchronous Motors

Atherton, D.L., "A Magnetic Circuit Analysis of the Iron-Cored Homopolar Linear Synchronous Motor," IEEE Trans. on Magnetics, MAG-17, 1981, pp. 1305-10.

Atherton, D.L., and Fraser, S.D., "A Homopolar Linear Synchronous Test Motor Using Permanent Magnets," IEEE Trans. on Magnetics, MAG-18, 1982, pp. 1843-6.

Atherton, D.L., "Design and Control Studies of a Linear Synchronous Motor for Urban Transit Applications," IEEE Trans. on Magnetics, MAG-18, 1982, pp. 1847-55.

Balchin, M.J., "Operating Characteristics of a Heteropolar Linear Synchronous Motor," Proc. IEE Colloquium on Advanced Ground Transportation Systems, London, April 1979.

Balchin, M.J., and J.F. Eastham, "Characteristics of a Heteropolar Linear Synchronous Machine with Passive Secondary," Electric Power Applications, 2, 1979, pp. 213-8.

Baudon, Y., "Moteur Lineaire Synchrone," keport to D.G.R.S.T., No. 76-7-0126, July 1979.

Baudon, Y., A. El-Zawawi and M. Ivanes, "Numerical Study with a Finite Elements Method of a Homopolar Linear Synchronous Motor and Experimental Verification," Proc. ICEM 80, Athens, Vol. 1, September 1980, pp. 202-209.

Baudon, Y., A. El-Zawawi and M. Ivanes, "Homopolar Linear Synchronous Motor: Steady State Analysis and Experimental Results, Electr. Mach. & Electromech., 6, 1981, pp. 23-33.

Boldea, I., "An Experimental Study of LSHM," Bul. st. technic al I.P.T. "Tr. Vuia," Timisoara, 2, 1978.

Boldea, I., "Vehicule pe Perna Magnetica," Editura Academiei Republicii Socialiste Romania, Bucuresti, 1981.

Boldea, I., and S.A. Nasar, "Field Winding Drag and Normal Forces on Linear Synchronous Homopolar Motors," Electr. Mach. & Electromach., 2, 1978, pp. 253-68.

Boldea, I., and S.A. Nasar, "Linear Synchronous Homopolar Motor - Design Procedure for Propulsion and Levitation," Electr. Mach. & Electromech., 4, 1979, pp. 125-35.

Boldea, I., and S.A. Nasar, "Performance of Ideal Current Inverter-Fed Linear Inductor Motors: A Theoretical Study," Electr. Mach. & Electromech., 7, 1982, pp. 35-45.

Buchberger, H., and W. Leitgeb, "Fahrzeugantriebe mit Synchronen Linearmotoren," Electrische Bahnen, 4, 1975, pp. 82-5.

Chahal, J.S., "Linear Reluctance Machines for Urban Transport," Proc. ICEM 78, Part 1-L4, Brussels, 1978.

Chahal, J.S., and A.J. Davis, "A Study of Linear Reluctance Machines at Brush Electrical Machines Limited," Proc. IEE Colloquium on Advanced Ground Transportation Systems, London, April 1979.

Davis, A.J., J.S. Chahal and W. Ferrer, "A Study of Linear Synchronous Motors at Brush Electrical Machines Limited," Proc. IEE Colloquium on Advanced Ground Transportation Systems, London, April 1979.

Davis, A.J., "Linear Synchronous Motors," Ph.D. Thesis, Nottingham University, 1978.

Davis, R.M., S.A.E. El-Drieny and D.J. Rhodes, "Linear Synchronous Motor Design and Performance, Proc. IEE Colloquium on Advanced Ground Transportation Systems, London, April 1979.

Dawson, G.E. and E. Unteregelsbacher, "A Transverse Laminated Linear Synchronous Homopolar Machine," Proc. IEEE IAS Annual Meeting, 80CH1575-0, Chicinnati, October 1980, pp. 270-5.

Dawson, G.E., A.R. Eastham, and R. Ong, "Computer-Aided Design Studies of the Homopolar Linear Synchronous Motor," IEEE Trans. on Magnetics, MAG-20, to be published.

Deleroi, W., P. Grumbkow, H. Weh, U. Feldman, P.K. Sattler, G. Kratz, P. Appun, H. Buchberger, and M. Rentmeister, "Short-Stator Linear Motors - Present State of the Art and Future Development Trends," Elektrotech. Z. Ausg. A., 96, 1975, pp. 401-9.

Drake, J., R. Gee and J. Pierro, "Linear Electric Motors," Frontiers of Technology Study, Vol. 3, Section 10, North American Rockwell Corp., 1968.

Eastham, A.R., G.E. Dawson, R. Ong, and L.W. Coathup, "The Design and Operation of the Homopolar Linear Synchronous Motor for Linear Drive and for Integrated Suspension/Propulsion Applications," Proc. of Int. Conf. on "Maglev Transport: Now and for the Future," Solihull, England, October 1984, to be published.

Eastham, J.F., "Iron-Cored Linear Synchronous Machines," Electronics & Power, 23, 1977, pp. 239-42.

Eastham, J.F., and E.R. Laithwaite, "Linear Motor Topology," Proc. IEE, 120, 1973, pp. 337-43.

El-Zawawi, A., Y. Baudon and M. Ivanes, "Dynamic Analysis of an Electromagnetically Levitated Vehicle Using Linear Synchronous Motors," Electr. Mach. & Electromech., 6, 1981, pp. 129-141.

Haller, T.R., and W.F. Mischler, "A Comparison of Linear Induction and Linear Synchronous Motors for High Speed Ground Transportation, IEEE Trans. on Magnetics, MAG-14, 1978, pp. 924-6.

Kliman, G.B., D.G. Elliot, V.C. Honsinger, T.A. Lipo, W.R. Mischler, T.A. Nondahl, and W.R. Oney, "Performance of a Single-Sided Linear Induction Motor with Solid Back Iron and with Various Rail Configurations; Evaluation of the Claw-Pole Linear Synchronous Motor and Performance of the Homopolar Linear Synchronous Motor with Solid-Iron Poles," Report No. FRA/ORD-80/73-1, September 1980.

Kliman, G.B., and E.E. Von Zastrow, "Linear Electric Motors," Proc. IEEE IAS Annual Meeting, Cincinnati, 80CH1575-0, October 1980, pp. 256-61.

Levi, E., "Linear Synchronous Motors for High Speed Ground Transportation," IEEE Trans. on Magnetics, MAG-9, 1973, pp. 242-8.

Levi, E., "A Preliminary Evaluation of Electrical Propulsion by Means of Iron-Cored Synchronously Operating Linear Motors," Report to DOT-FRR, NTIS No. PB-258437, January 1975.

Levi, E., "Preliminary Design Studies on Iron-Cored Synchronously Operating Linear Motors," Report to DOT-FRR, No. POLY EE/EP 76-005, May 1976.

Levi, E., "High-Speed Iron-Cored Synchronously Operating Linear Motors," IEE Conf. Publ. No. 120, October 1974, pp. 155-60.

Levi, E., L. Birenbaum, and Z. Zabar, "Concerning the Design of Inductor Synchronous Motors Fed by Current Source Inverters," IEEE Trans. on Magnetics, MAG-13, 1977, pp. 1421-3.

Levi, E., J.P. Lee, F. Lalezari, and M. Gemalos, "Computer-Aided Conformal Mapping of Magnetic Fluxes in Saturated Inductor Motors," IEEE Trans. on Magnetics, MAG-14, 1978, pp. 927-9.

McLean, G.W., and W.O. Williams, "The Zig-Zag Linear Synchronous Motor," Proc. IEE Colloquium on Advanced Ground Transportation Systems, London, April 1979.

McLean, G.W., W.O. Williams and A.N. West, "The Zig-Zag Linear Synchronous Motor for Urban Transport," Proc. ICEM 80, Athens, Vol. 1, September 1980, pp. 218-25.

Meins, J., and H. Weh, "Determination and Stabilization of the Pole Angle in a Linear Synchronous Motor," Elektrotech. Zeitschrift, 6, 1977, pp. 414-8.

Mischler, W.R., and T.A. Nondahl, "Performance of a Linear Synchronous Motor with Laminated Track Poles and with Various Misalignments," Report No. FRA/ORD-80/52-1, September 1980.

Nondahl, T.A., "Design Studies for Single-Sided Linear Electric Motors: Homopolar Synchronous and Induction," Electr. Mach. & Electromech., 5, 1980, pp. 1-14.

Nasar, S.A., and I. Boldea, Linear Motion Electric Machines, New York: Wiley, 1976.

Ong, R., "Finite Element Analysis of a Linear Homopolar Synchronous Motor," M.Sc. Thesis, Queen's University, 1983.

Ooi, B.T., "Homopolar Linear Synchronous Motor Dynamic Equivalents," IEEE Trans. on Magnetics, MAG-13, 1977, pp. 1424-6.

Rummich, E., "Linear Synchronous Machines - Theory and Construction," Bull. ASE, 23, 1972, pp. 1338-44.

Slemon, G.R., "Linear Synchronous Motor Propulsion for Urban Systems," Proc. The Eighties: A New Rail Era, CIGGT Report No. 78-5, April 1978, pp. 179-87.

Slemon, G.R., "A Homopolar Linear Syhnchronous Motor," Proc. ICEM 78, Brussels, 1978.

Slemon, G.R., "An Experimental Study of a Homopolar Linear Synchronous Motor," Electr. Mach. & Electromech., 4, 1979, pp. 59-70.

Slemon, G.R , and R.P. Bhatia, "Linear Homopolar Synchronous Motor for Urban Transit Application," Can. Elec. Eng. J., 7, 1982, pp. 12-20.

Slemon, G.R., S.B. Dewan, P.E. Burke, A. Straughen, and R. Bhatia, "Study of an Analytical Model of the Homopolar Linear Synchronous Motor," Transport Canada Report No. TP-2856E, December 1980.

Slemon, G.R., and A. Straughen, Electric Machines, Addison-Wesley, 1980.

Unteregelsbacher, E., "A Linear Synchronous Homopolar Motor Design and Construction," M.Sc. Thesis, Queen's University, March 1980.

Weh, H., "Integrated Magnetic Levitation and Electric Propulsion," Electrotech. Zeitschrift, 96, 1975, pp. 131-5.

Weh, H., "Linear Synchronous Motor Development for Urban and Rapid Transit Systems," IEEE Tranr. on Magnetics, MAG-15, 1979, pp. 1422-7.

11.2 Other References

Alger, P.L., "The Nature of Induction Machines," Gordon & Breach, New York, 1965.

Carter, F.W., "Note on Airgap and Interpolar Induction," J. IEE, Vol. 29, 1900, p. 925.

Lawrenson, P.J., and Agu, L.A., "Theory and Performance of Polyphase Reluctance Machines," Proc. IEE, 111, 1964, pp. 1435-45.

Liwschitz-Garik, M., and Whipple, C.C., Electric Machinery; Volume I, DC Machines; Volume II, AC Machines, Van Nostrand, New York, 1946.

Trutt, F.C., Erdelyi, E.A., and Hopkins, R.E., "Representation of the Magnetisation Characteristics of DC Machines for Computer Use," IEEE Trans. Power Apparatus and Systems, Vol. PAS-87, 1968, pp. 665-9.

APPENDIX A

DETERMINATION AND COMPUTATION OF THE HLSM EQUIVALENT-CIRCUIT PARAMETERS

The homopolar linear synchronous machine was modelled by a conventional salient-pole synchronous machine per-phase equivalent circuit, as shown in Figure A.1. The parameters were determined in the following manner, and were computed by the program "EQUIVCIRC" included in this appendix. The equation numbers in the program correspond to those given below.

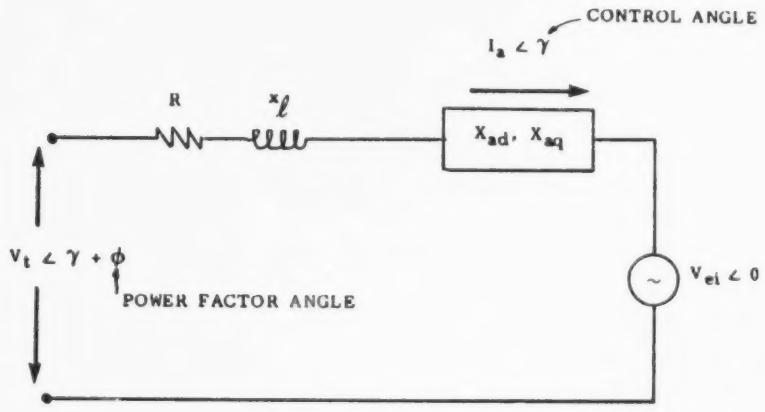

Figure A.1 The per-phase two-reactance equivalent circuit model of the HLSM

A.1 ARMATURE RESISTANCE, R

The armature resistance was determined from the armature winding configuration:

$$R = \frac{\rho L}{A} \qquad (A.1)$$

where: ρ = resistivity of copper at 120°C (2.4×10^{-8} ohm.m)

L = length of armature winding (per phase)

A = cross-section of armature winding (per turn)

A.2 LEAKAGE REACTANCE, X_L

The leakage reactance was determined from standard component expressions for rotary ac machines, as given by Liwschitz-Garik and Whipple (LGW) (1946), with an additional component due to the central crossover portion of the HLSM armature winding.

A.2.1 Slot Leakage, XSLOT

The parameter LEAK is defined for factors that occur repeatedly in leakage calculations:

$$LEAK = \frac{1.6\ \pi\ W^2}{P}\ 10^{-6}\ 2\ \pi\ f \qquad (A.2)$$

where: W = number of turns per phase

P = number of poles

f = electrical frequency (Hz)

In calculating slot leakage, LGW introduce the constants k_{xco} and k_{xt} for chorded windings. The following equations are approximations for k_{xco} and k_{xt} based on LGW Figure 5-8 (see below) for chording values greater than 0.7:

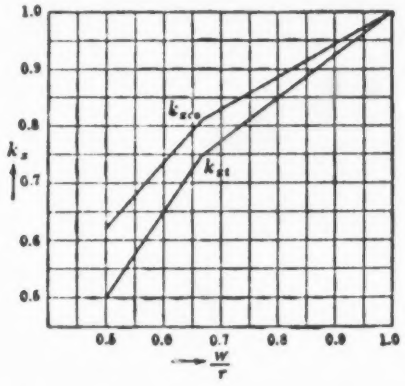

LGW Fig. 5-8 Reduction factors for slot leakage permeance of fractional-pitch 3-phase windings.

$$KXCO = 0.545\ CHORD + 0.455 \qquad (A.3)$$

$$KXT = 0.758\ CHORD + 0.242 \qquad (A.4)$$

where CHORD is the chording fraction of the winding.

The following formula is used to calculate slot leakage reactance. It is based on LGW formulae (5-24) and (5-26) with h_3 and h_4 set to zero. The parameters are defined in Figure A.2.

$$XSLOT = \frac{LEAK\ 4A}{SLPLPH}\left[\frac{0.95\ SD}{3\ SW}KXCO + \frac{0.05\ SD}{SW}KXT\right] \qquad (A.5)$$

where:

4A = active area width (m)

SLPLPH = number of slots per pole per phase

SD = slot depth (m)

SW = slot width (m)

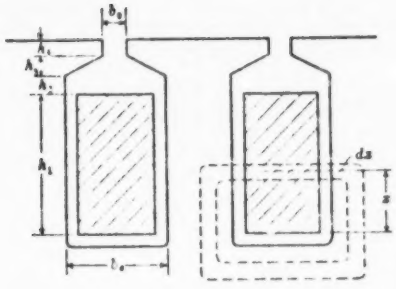

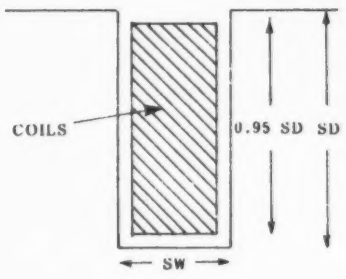

LGW Fig. 5-3. Determination of the slot leakage permeance.

(a) (b)

Figure A.2 Armature slot dimensions:
(a) modelled by LGW
(b) assumed for HLSM design studies

A.2.2 Tooth Top Leakage, XTTOP

The following formula is used to calculate tooth top leakage reactance, as based on LGW formulae (5-27) and (5-29):

$$XTTOP = \frac{LEAK\ 4A}{SLPLPH} \left[\frac{1}{\frac{SW}{KC1\ G1} + 0.8} \right] KXT \qquad (A.6)$$

where: G1 = smallest (polar) air gap between track and armature (m)

KC1 = Carter's coefficient for armature slotting.

A.2.3 End Winding Leakage, XEWIND

The following formula is used to calculate end winding leakage reactance, as based on LGW formula (5-34):

$$XEWIND = LEAK\ 1.2\ (KW)^2 \left[\ell_{e1} + \frac{\ell_{e2}}{2} \right] \qquad (A.7)$$

where KW = winding factor

ℓ_{e1} and ℓ_{e2} are defined in LGW Fig. 5-9 (see below).

In (A.7), ℓ_{e1} = 77 mm and ℓ_{e2} = (CHORD) (T) ÷ 2 for the HLSM.

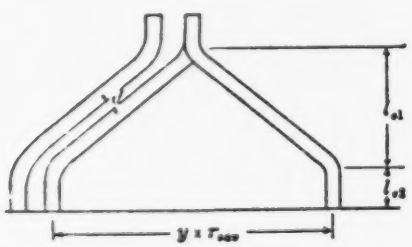

LGW Fig. 5-9. Determination of the end-winding leakage.

A.2.4 Harmonic Leakage, XHARM

The following formula was used for calculating harmonic leakage reactance, as based on LGW formulae (6-36) and (6-36a), and on LGW Fig. 6-10 with two slots per pole per phase and 5/6 chording:

$$XHARM = \frac{LEAK\ 3\ T\ \ 4A\ KC1\ G1\ 0.0205}{2} \qquad (A.8)$$

A.2.5 Central Gap Leakage, XCENT

The central gap leakage is not a reactance component in conventional machines, and is characteristic only of the geometry of the HLSM. The diamond-shaped armature winding crosses between the two active areas of the machine, and the central cross-over portion will have significant leakage. No analytical expressions exist for this component of leakage.

XCENT was estimated by first removing the iron structure and by calculating the magnitude of the travelling field which would be produced in the centre of the armature coil distribution shown in Figure A.3. This was achieved by calculating the magnetostatic field due to the distributed three-phase conductors, as shown, with currents frozen at one particular instant of the ac cycle. The leakage reactance is then given by:

$$XCENT = \frac{2}{\pi}\ \tau\ IG\ \frac{\hat{B}}{I_a}\ W\ KW\ 2\ \pi\ f\ k_{Fe}$$

where: τ is the pole pitch

IG is the inter-limb (central) gap of the HLSM

$\hat{B}$ is the peak value of the fundamental component of the travelling field

k_{Fe} is a factor which accounts for the presence of iron around the cross-over portion of the HLSM winding. An empirical value of 1.2 was used for computational purposes.

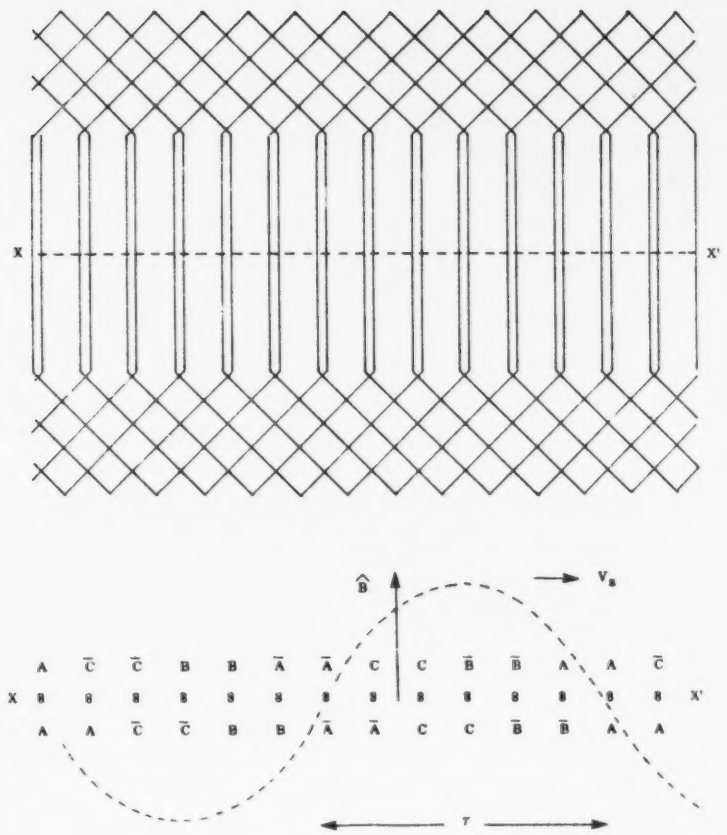

Figure A.3 Modelling of a 5/6 chorded armature winding to find the cross-over leakage reactance, XCENT

A.3 ARMATURE REACTANCES, X_{ad} AND X_{aq}

The magnetizing reactance, X_m, was first determined for a smooth air gap machine, using formula (9.20) in Nasar & Boldea (1976):

$$XM = \frac{48}{\pi} \mu_0 \; f \; W^2 \; (KW)^2 \; \frac{A \; T}{P \; KC1 \; G1} \times 2 \text{ sides} \qquad (A.9)$$

(Note that P is defined as the number of pole pairs in Nasar & Boldea.)

The direct axis and quadrature axis armature reactances were calculated from the stored energy/Fourier series analytical expressions for

comparison with values computed by the finite element method. Before calculating X_{ad} and X_{aq}, the program uses Carter's and Green's coefficients to allow for armature slotting and track saliency.

A.3.1 Direct Axis Armature Reactance, X_{ad}

From equation (2.9):

$$XAD = \frac{2}{\pi} \left[\left(\frac{ALPHA}{2} + \frac{1}{4} SIN (2 \times ALPHA) \right) K1 + \frac{\pi}{2\ K11} \right] XM \qquad (A.10)$$

where: ALPHA = B/T (see equation (2.4)) (A.11)

$$K1 = 1 - \frac{1}{K11} \qquad (A.12)$$

$$K11 = \frac{KC2\ G2}{KC2\ G1} \qquad (A.13)$$

where B/T is the ratio of track pole length to pole pitch.

A.3.2 Quadrature Axis Armature Reactance, X_{aq}

From equation (2.10):

$$XAQ = \frac{2}{\pi} \left[\left(\frac{ALPHA}{2} - \frac{1}{4} SIN (2 \times ALPHA) \right) K1 + \frac{\pi}{2\ K11} \right] XM \qquad (A.14)$$

The total direct and quadrature axis reactances were then determined by adding the sum of all the leakage reactances to the armature reactances.

A.4 EXCITATION VOLTAGE, VEI

From equation (2.15):

$$\frac{VEI}{BL1} = 8\sqrt{2}\ f\ KW\ W\ A\ T \qquad (A.15)$$

where BLI is the amplitude of the fundamental flux density linking the armature coils.

VEI/BL1, rather than VEI, was computed, as (A.15) is an exact expression, and it proved useful to be able to determine VEI for particular values of BL1 as computed by finite element analysis.

A.5 PROGRAM "EQUIVCIRC"

```
C                          EQUIVCIRC
C*************************************************************************
C       THIS PROGRAM WILL COMPUTE THE EQUIVALENT CIRCUIT PARAMETERS OF A
C       HOMOPOLAR LINEAR SYNCHRONOUS MOTOR, GIVEN THE FOLLOWING INPUT
C       SPECIFICATIONS:
C       DESIGN YIELD:                                   YIELD
C       FREQUENCY AT DESIGN SPEED:                      F
C       SLOTS PER POLE PER PHASE:                       SLPLPH
C       TOOTH TO SLOT WIDTH RATIO ON THE ARMATURE:      TS
C       SLOT DEPTH TO SLOT WIDTH RATIO:                 SLDPWD
C       SLOT FILL FACTOR:                               FLFCTR
C       CONDUCTORS PER SLOT:                            CONDSL
C       COILS PER PHASE:                                COILPH
C       VALUE OF CHORDING:                              CHORD
C       STACK WIDTH PER SIDE, 2A: INPUT A               A
C       WIDTH OF CENTRAL GAP:                           W
C       B/T RATIO (SEE FIGURE 9.11 IN NASAR & BOLDEA):  B1
C       RATIO OF LARGE GAP TO SMALL GAP                 N
C       SMALL GAP (FIGURE 9.11)                         G1
C       NUMBER OF POLES:                                P
C*************************************************************************
C       IF THE USER WISHES, THE NUMBER OF POLES CAN BE DETERMINED USING
C       THE ABOVE DATA AND INPUTED DIRECTLY. OTHERWISE, A NEGATIVE
C       NUMBER MUST BE INPUT FOR THE NUMBER OF POLES AND THE PROGRAM
C       WILL THEN EQUATE THE NUMBER OF POLES TO COILPH/SLPLPH.THIS
C       APPROXIMATION IS CORRECT TO WITHIN ONE POLE.
C*************************************************************************
C       THE PROGRAM WILL OUTPUT THE FOLLOWING PARAMETERS:
C       RESISTANCE OF THE ARMATURE:                     R1
C       MAGNETISING REACTANCE ALONG THE DIRECT AXIS:    XDM
C       MAGNETISING REACTANCE ALONG THE QUADRATURE AXIS: XQM
C       LEAKAGE REACTANCE                               XL
C           COMPONENTS OF XL:
C                 SLOT                                  XSLOT
C                 TOOTH-TOP                             XTTOP
C                 END-WINDING                           XEWIND
C                 HARMONIC                              XHARM
C                 CENTRAL GAP                           XCENT
C       POLE PITCH:                                     T
C       SLOT WIDTH:                                     SW
C       TOOTH WIDTH:                                    TW
C       SLOT DEPTH:                                     SD
C       NUMBER OF TURNS PER PHASE:                      W
C       RATIO OF FIELD VOLTAGE TO AMPLITUDE OF FLUX
C       DENSITY MODULATION (VIE/BL1):                   VIEBL1
C*************************************************************************
C       VARIABLES USED:
C       LENGTH OF CONDUCTOR:                            L
C       AREA OF CONDUCTOR:                              AR
C       RESISTIVITY OF COPPER:                  2.4 E-8 OHM M
C       LARGE GAP:                                      G2
C       WINDING FACTOR:                                 KW
C       REACTANCE FOR A SMOOTH AIR GAP MACHINE:         XM
C       CARTER'S COEFFICIENT (SMALL GAP):               KC1
C       CARTER'S COEFFICIENT (LARGE GAP):               KC2
```

```
C       RATIO OF SMALL GAP TO LARGE GAP AFTER
C             CARTER'S CORRECTION:                    K11
C       DIRECT AXIS MAGNETISING REACTANCE:            XDM
C       QUADRATURE AXIS MAGNETISING REACTANCE:        XQM
C       CONSTANTS THAT OCCUR IN LEAKAGE CALCULATIONS: LEAK
C                                                     KXCO
C                                                     KXT
C       HALF TRACK POLE LENGTH                        T
C*************************************************************************
      REAL US,F,SLPLPH,TS,SLOPWD,FLECTR,CONDSL,COILPH,CHORD,A,S,ET,G1
     1 ,XAQ,XAD,L,SW,T,KW,XM,KC1,XDM,XQM,P,PI,ALPHA,K1,UO,W,K11,KC,TW,SD,P
     1 ,XSLOT,XTTOP,XEWIND,XHARM,LEAK,XCENT,KXCO,KXT,XL,G2,K11,KC2,WIDTH
      PI=3.141592654
      UO=4*PI*1E-7
      READ(5,1) US,F,SLPLPH,TS,SLOPWD,FLECTR,CONDSL,COILPH,CHORD,A,S,ET,
     2 K,G1,P
    1 FORMAT(F10.6,/,F10.6,/,F10.6, ,F10.6,/,F10.6, ,F10.6,/,F10.6, ,F10.6, ,
     1 F10.6,/,F10.6,/,F10.6,/,F10.6, ,F10.6,/,F10.6,/,F10.6, ,F10.6,/)
C*************************************************************************
C       CALCULATION OF CONDUCTOR RESISTANCE:
      T=US/2/F
      W=COILPH*CONDSL/2
      L=(8*A+2*K+CHORD*SQRT(8.)*T)*W+4*0.007*K
      SW=T/3*SLPLPH/(TS+1)
      TW=SW*TS
      SD=SW*SLOPWD
      AK=SW*SD/CONDSL*FLECTR
      R1=2.4E-8*L/AK                                          (A.1)
C*************************************************************************
C       CALCULATION OF MAGNETISING REACTANCES:
C  INTERMEDIATE CALCULATION OF KW AS THE PRODUCT OF THE DISTRIBUTION
C  FACTOR AND THE PITCH FACTOR.
      KW=SIN(PI/2*CHORD)*SIN(PI/6)*SLPLPH/SIN(PI/6/SLPLPH)
C  CALCULATION OF CARTER'S COEFFICIENT(P.269 IN NASAR & ZOLDAN)
      G2=G1*K
      KC1=1/(1-(SW/(TS+1)/(5*G1+SW)))
      KC2=1/(1-(SW/(TS+1)/(5*G2+SW)))
      K11=KC2*G2/KC1/G1                                       (A.13)
C  DETERMINE THE VALUE OF 'P' TO BE USED
      IF(F.LT.0.0) P=COILPH/SLPLPH
C  DETERMINE XM USING AN ADAPTATION OF EQUATION 9-20 FROM NASAR
      XM=96*UO*F*T*W*W*KW*KW/PI/PI/KC1/G1                     (A.9)
C  DETERMINE XDM,XQM USING ADAPTATIONS OF 9-24,9-25
      ALPHA=PI*BT                                             (A.11)
      K1=1.-1./K11                                            (A.12)
      XQM=2/PI*XM*((ALPHA/2-SIN(2*ALPHA)/4)*K1+PI/2/K11)      (A.10)
      XDM=2/PI*XM*((ALPHA/2+SIN(2*ALPHA)/4)*K1+PI/2/K11)      (A.14)
C*************************************************************************
C       THE LEAKAGE REACTANCE WILL NOW BE CALCULATED FROM EXPRESSIONS
C       GIVEN IN LIWSCHITZ-GARIK & WHIPPLE.
C*************************************************************************
      LEAK=1.6*PI*W*W/P*1E-6*2*PI*F                           (A.2)
C  SLOT LEAKAGE REACTANCE:(EQUATIONS 5-24,5-26)
      KXCO=0.545*CHORD+0.455                                  (A.3)
      KXT=0.750*CHORD+0.242                                   (A.4)
      XSLOT=LEAK/SLPLPH*4*A*(0.95*SD/3/SW*KXCO+0.05*SD/SW*KXT)  (A.5)
C  TOOTH-TOP LEAKAGE REACTANCE:(EQUATIONS 5-27,5-29)
      XTTOP=LEAK/SLPLPH*4*A/(0.8+SW/G1/K11)*KXT               (A.6)
C  END-WINDING LEAKAGE REACTANCE:(EQUATION 5-36 WITH LE1=CHORD*1/2
C  AND LE2=7mm)
      XEWIND=LEAK*1.2*KW*KW*(0.007+CHORD*T/4)                 (A.7)
C  HARMONIC LEAKAGE REACTANCE:(EQUATIONS 6-36,6-36A; FIGURE 6-10)
      XHARM=LEAK*3/PI/PI*T*4*A/G1/KC1*0.0205                  (A.8)
C  CENTRAL GAP LEAKAGE REACTANCE (FROM SEPARATE ANALYSIS):
      XCENT=0.0792
C  CALCULATION OF XL:
      XL=XSLOT+XTTOP+XEWIND+XHARM+XCENT
C*************************************************************************
```

```
C       CALCULATION OF THE RATIO OF INDUCED FIELD VOLTAGE TO
C  FIELD FLUX DENSITY.
        VIEBL1=8*SQRT(2.)*F*RW*W*RA*1                                    (A.15)
C*****************************************************************************
C       OUTPUT FOR THIS PROGRAM WILL BE SENT TO FOR010 WHICH IS ASSIGNED
C       TO OUTPUT.DAT IN THE LOGIN ROUTINE. IT WILL ALSO BE OUTPUT IN
C       FREE FORMAT TO FOR011 WHICH WILL ACT AS INPUT DATA FOR
C       SUBSEQUENT PROGRAMS.
C*****************************************************************************
        M=N1*N2
        A=A*2.
        WRITE(11,8) US,F,R1,XDM,XQM,XL,XSLOT,XTTOP,XEWIND,XHARM,XCENT,
     1              VIEBL1
        WRITE(10,3) US,F,SLPLPH,FLFCTR,CONDSL,COILPH,CHORD,A,S,R,G1,G2
     1  ,T,SW,TW,SD,W,P
  3     FORMAT('            MLSM DESIGN CHARACTERISTICS:'//,
     3  '   DESIGN SPEED (m/s)                        ',F10.4,/,
     4  '   FREQUENCY AT DESIGN SPEED (Hz)            ',F10.6,/,
     5  '   SLOTS PER POLE PER PHASE                  ',F10.4,/,
     6  '   SLOT FILL FACTOR                          ',F10.6,/,
     7  '   CONDUCTORS PER SLOT                       ',F10.6,/,
     8  '   COILS PER PHASE                           ',F10.6,/,
     9  '   VALUE OF CHORDING                         ',F10.6,/,
     1  '   STACK WIDTH (m)                           ',F10.6,/,
     2  '   WIDTH OF CENTRAL GAP (m)                  ',F10.6,/,
     3  '   TRACK POLE LENGTH (m)                     ',F10.6,/,
     4  '   SMALL GAP (m)                             ',F10.6,/,
     5  '   LARGE GAP (m)                             ',F10.6,/,
     6  '   POLE PITCH (m)                            ',F10.6,/,
     7  '   SLOT WIDTH (m)                            ',F10.6,/,
     8  '   TOOTH WIDTH (m)                           ',F10.6,/,
     9  '   SLOT DEPTH (m)                            ',F10.6,/,
     1  '   TURNS PER PHASE                           ',F10.6,/,
     2  '   EFFECTIVE NUMBER OF POLES                 ',F10.6)
        WRITE(10,2) R1,XSLOT,XTTOP,XEWIND,XHARM,XCENT,XL,XDM,XQM,VIEBL1
  2     FORMAT(/,/,/,'       EQUIVALENT CIRCUIT PARAMETERS (OHMS):'//,
     3  '   ARMATURE RESISTANCE                       ',F10.6,/,
     7  '       SLOT LEAKAGE                          ',F10.6,/,
     8  '       TOOTH-TOP LEAKAGE                     ',F10.6,/,
     9  '       END-WINDING LEAKAGE                   ',F10.6,/,
     1  '       HARMONIC LEAKAGE                      ',F10.6,/,
     2  '       CENTRAL GAP LEAKAGE                   ',F10.6,/,
     4  '   TOTAL LEAKAGE REACTANCE                   ',F10.6,/,
     4  '   DIRECT AXIS MAGNETISING REACTANCE         ',F10.6,/,
     5  '   QUADRATURE AXIS MAGNETISING REACTANCE     ',F10.6,/,
     3  '   RATIO OF FIELD VOLTAGE TO FIELD FLUX      ',F10.5)
        STOP
        END
```

APPENDIX B

DESIGN PARAMETERS OF THE UNIVERSITY OF TORONTO TEST HLSM

Experimental results obtained from the HLSM designed, built and tested at the University of Toronto (Slemon et al., 1980) were used to validate the finite element method as an effective tool for CAD of homopolar linear synchronous motors. The dimensions and winding characteristics of this machine are shown in Figure B.1 and/or are listed below:

(i) Motor

Arc length of iron structure	441 mm
Stack width, 2a	55.0 mm
Slot depth	38.0 mm
Slot width	9.2 mm
Tooth width	9.2 mm
Pole pitch, τ	110.4 mm
Coil pitch	93 mm (5/6)
No. of poles, P	3
Slot/pole/phase	2
Turns/coil	8
Turns/phase, N_{ph}	48
Overhang width, l_{e1}	92 mm
Protrusion beyond stack, l_{e2}	20 mm
Inter-limb gap, IG	110 mm
Field coil width	48.0 mm
Field coil depth	48.5 mm
Field turns/coil	453

(ii) Track and Air Gaps

Pole length	109.2 mm
Interpolar space	111.8 mm
Pole width	55 mm
Effective pole depth*	58 mm
Pole air gap, g_1	10 mm
Effective interpolar air gap, g_2*	68 mm

* These values were determined by the equal reluctance finite element method, as discussed in Section 4.2.3.

(a) Transverse section of motor

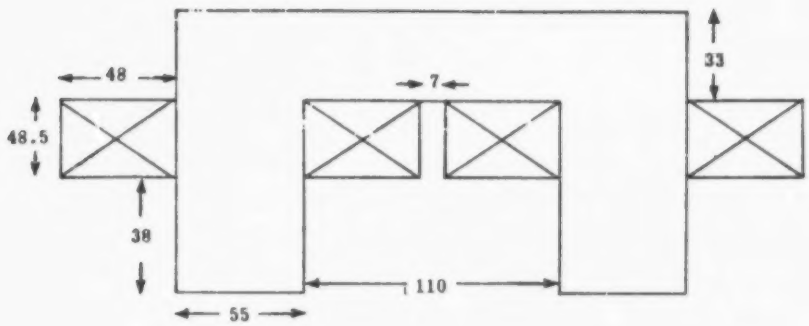

(b) Longitudinal section of track

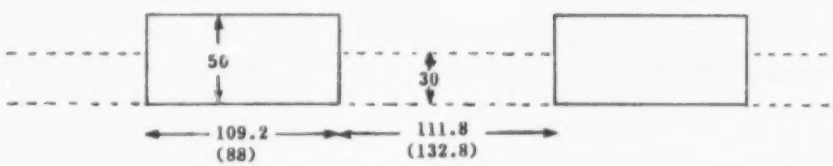

(c) Transverse section of track

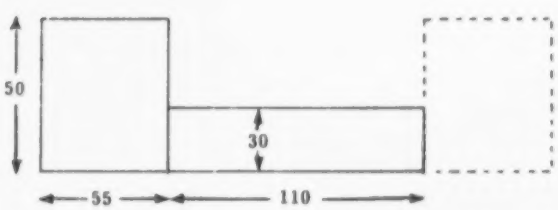

(not to scale; dimensions in millimetres)

Figure B.1 Dimensions of the University of Toronto test HLSM

APPENDIX C

DETERMINATION OF THE CONTROL ANGLE REQUIRED FOR MINIMUM CURRENT, FOR ANY GIVEN SET OF THRUST, SPEED AND FIELD EXCITATION

C.1 CAPABILITY OF PROGRAMS

If the thrust, speed and field excitation of an HLSM are specified, a set of phasor polygons are defined with different armature currents and terminal voltages. In order to minimize Joule heating losses, the optimal phasor polygon for the specific conditions is that which minimizes armature current.

The program IMIN, included in this appendix, was formulated for the motoring regime, and takes the following quantities as input:

- a set of equivalent circuit parameters provided by EQUIVCIRC or by direct input
- a specific thrust-speed profile
- a level of field excitation; various levels can be specified for different passes along the thrust-speed profile by the HLSM
- a maximum terminal voltage.

IMIN uses the above input to solve for the optimal phasor polygon at each operating point. It outputs the following data at the specified levels of field excitation, any one of which can be plotted as a function of speed:

- control angle
- armature current
- apparent power
- armature efficiency-power factor product
- terminal voltage.

The program IMINBRK, also included in this appendix, performs the same function in the braking regime.

C.2 DEVELOPMENT OF FORMULAE USED IN "IMIN"

Figure C.1 shows a typical motoring phasor polygon. The following equations can be derived:

$$V_t \cos\gamma = V_{ie} + I_q R - I_d x_d \qquad (C.1)$$

$$V_t \sin\gamma = I_d R + I_q X_q \qquad (C.2)$$

$$I_d = I_q \tan\beta \qquad (C.3)$$

$$I_a^2 = I_d^2 + I_q^2 \qquad (C.4)$$

$$\text{OUTPUT POWER, } P = 3 V_t I_a \cos(\gamma - \beta) - 3 I_a^2 R \qquad (C.5)$$

Solving (C.1) and (C.2) for I_d and I_q gives:

$$I_d = \frac{V_t (R \sin\gamma - X_q \cos\gamma) + V_{ie} X_q}{X_d X_q + R^2} \qquad (C.6)$$

$$I_q = \frac{V_t (X_q \sin\gamma + R \cos\gamma) - R V_{ie}}{R^2 + X_d X_q} \qquad (C.7)$$

(Note that IMIN uses the negative of (C.6).)

Using $$\cos(\gamma - \beta) = \cos\gamma \cos\beta + \sin\gamma \sin\beta, \qquad (C.8)$$

one can eliminate the γ and β terms from (C.5) using (C.1) and (C.2) to obtain:

$$P = 3 I_q [V_{ie} - I_d (X_d - X_q)] \qquad (C.9)$$

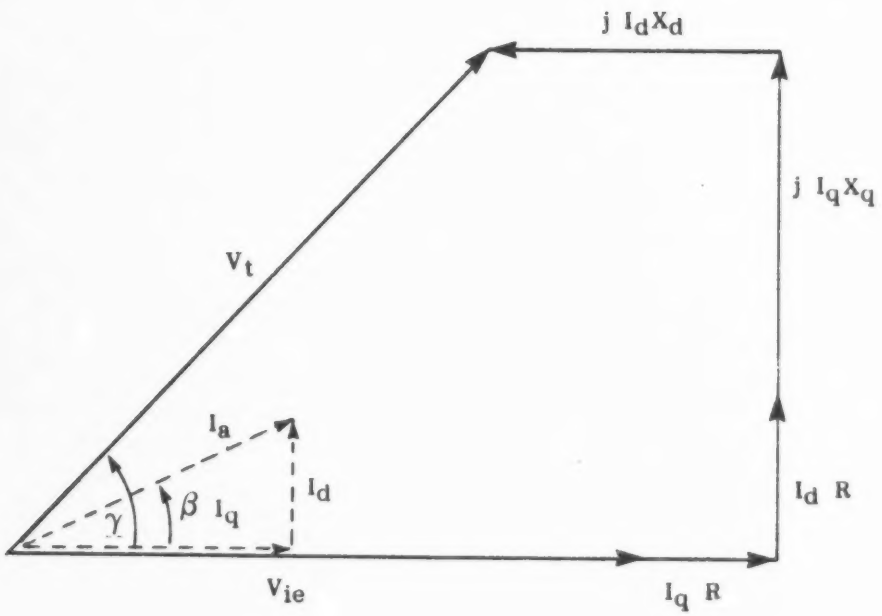

Figure C.1 Phasor polygon in the motoring regime. (Arrowheads indicate positive polarity on voltages and currents.)

One can now eliminate I_d and I_q from (C.9) using (C.7) and (C.8) to obtain:

$$F2 = F3 = 0 = 3 \left[\frac{V_t (X_q \sin\gamma + R \cos\gamma) - R V_{ie}}{X_d X_q + R^2} \right]$$

$$\left\{ V_{ie} + (X_d - X_q) \left[\frac{V_t (X_q \cos\gamma \; R \sin\gamma) - V_{ie} X_q}{X_d X_q + R^2} \right] \right\}$$

$$- P \qquad (C.10)$$

The algorithm that computes the minimum current is presented in the comments of IMIN.

C.3 PROGRAM "IMIN"

```
C                              IMIN
C*************************************************************************
C       This program takes the equivalent circuit data for the HLSM
C provided by EQUIVCIRC from FOR011.DAT. It is also given a field flux
C densities (BL). The program moves through operating speeds incremented
C from 2 to 22 m/s and determines an operating thrust at each speed. For
C each operating point involving a fixed BL, speed and thrust the program
C determines the minimum armature current, complex power (KVA), control angle
C (between armature current and the q axis), efficiency, power factor product
C and terminal voltage. IMIN is intended to give these output parameters as
C a function of speed.
C       The computation proceeds identically to THRUST.
C       The user may use a different thrust-speed profile by changing the
C appropriate section of the program marked between the lines with
C exclamation marks.
C*************************************************************************
C       VARIABLES USED:
C       MOST ARE THE SAME AS IN 'EQUIVCIRC' WITH THE FOLLOWING ADDITIONS:
C       TERMINAL VOLTAGE:(LINE-NEUTRAL)                          VT
C       MAXIMUM TERMINAL VOLTAGE:                                VTMAX
C       OUTPUT POWER:                                            POWER
C       INDUCED FIELD VOLTAGE:                                   VIE
C       ARMATURE CURRENT:                                        IA
C       DIRECT AXIS ARMATURE CURRENT:                            ID
C       QUADRATURE AXIS ARMATURE CURRENT:                        IQ
C       ANGLE BETWEEN VT AND VIE:                                GAMMA
C       TOTAL DIRECT AXIS REACTANCE (XAD+XL):                    XD
C       TOTAL QUADRATURE AXIS REACTANCE (XAQ+XL):                XQ
C       EFFICIENCY:                                              EFF
C       POWER FACTOR:                                            PWRFCT
C       EFFICIENCY-POWER FACTOR PRODUCT:                         NCOS
C       FREQUENCY AT ANY SPEED:                                  FREQ
C       OPERATING THRUST:                                        THRUST
C       OPERATING SPEED:                                         SPEED
C       CONTROL ANGLE:                                           BETA
C       COMPLEX POWER:                                           KVA
C       EQUIVALENT FIELD FLUX DENSITY (AMPLITUDE OF
C               THE FIRST HARMONIC):                             BL1
C       MAXIMUM POSSIBLE BL1:                                    BLMAX
C       SUBROUTINE VARIABLES:                  GAMMA2,GAMMA3,F2,F3,GMANEW
C       ITERATION VARIABLES FOR MINIMIZATION:
C                       VT1,VT2,IA1,IA2,IA3,ID1,ID2,IQ1,IQ2,GAMMA4,GAMMA5
C*************************************************************************
C       ARRAYS USED:
C       FIELD FLUX DENSITY:                                      BL
C       ARMATURE CURRENT:                                        C
C       COMPLEX POWER (KVA):                                     VA
C       EFFICIENCY-POWER FACTOR PRODUCT:                         NCS
C       TERMINAL VOLTAGE:                                        VTEE
C*************************************************************************
      REAL US,F,R1,XDM,XQM,XL,XSLOT,XTTOP,XEWIND,XHARM,XCENT,VIEBL1,
     1       VT,POWER,VIE,IA,ID,IQ,GAMMA,XD,XQ,EFF,PWRFCT,NCOS,PI,UO,
     2       FREQ,THRUST,SPEED,BETA,KVA,IA1,IA2,VT1,VT2,GAMMA3,GAMMA4,
     3       IA3,GAMMA5,ID1,ID2,IQ1,IQ2,GAMMA2,F2,F3,GMANEW
      REAL BL(4),C(4),VA(4),BTA(4),NCS(4),VTEE(4)
      PI=3.141592654
      UO=4*PI*1E-7
      READ(11,*) US,F,R1,XDM,XQM,XL,XSLOT,XTTOP,XEWIND,XHARM,XCENT,
     1           VIEBL1
      XL=XSLOT+XTTOP+XEWIND+XHARM+XCENT
```

```
C       Input the number of values of BL that are to be used. Each value
C cycles through the thrust-speed profile once. Also input the maximum
C terminal voltage in volts and BL in Tesla.
        READ(16,*) N,VTMAX
        DO 567 I=1,N
                READ(16,*) BL(I)
 567    CONTINUE

C       This loop will cycle through the speed range from 2 to 22 m/s.
        SPEED=2.
        DO 45 J=1,41

C!!!!!!!!!!!!!!!!!!!!!!!!!!!!!!!!!!!!!!!!!!!!!!!!!!!!!!!!!!!!!!!!!!!!!!!!!!!
C       This is the thrust-speed profile:
        IF(SPEED.LT.10.15) THEN
             THRUST=13000.
           ELSE
             THRUST=132000./SPEED
        END IF
C!!!!!!!!!!!!!!!!!!!!!!!!!!!!!!!!!!!!!!!!!!!!!!!!!!!!!!!!!!!!!!!!!!!!!!!!!!!

        POWER=THRUST*SPEED

C       Note that frequency is directly proportional to speed.
        FREQ=F*SPEED/US

C       Note that XD, XQ and VIE are frequency dependent.
        XD=(XDM+XL)*FREQ/F
        XQ=(XQM+XL)*FREQ/F

C       This loop will perform calculations with each field flux density
C value at the present operating speed.
        DO 234 I=1,N
        VIE=VIEBL1*BL(I)/F*FREQ
C*************************************************************************************
C       Solve for IA with terminal voltages of VTMAX and (VTMAX-0.2) volts.
C If IA is decreasing, then continue decrementing terminal voltage by 0.2
C volts until a minimum current is obtained.
        VT1=VTMAX
        CALL IFIND(XD,XQ,R1,VIE,VT1,POWER,GAMMA4,ID1,IQ1,IA1)
        VT2=VTMAX-0.2
        CALL IFIND(XD,XQ,R1,VIE,VT2,POWER,GAMMA5,ID2,IQ2,IA2)
        IA3=IA1-IA2
 53     IF(IA3.LT.0.0)THEN
        GO TO 57
        END IF
           IA1=IA2
           VT1=VT2
           VT2=VT2-0.2
           GAMMA4=GAMMA5
           ID1=ID2
           IQ1=IQ2
           CALL IFIND(XD,XQ,R1,VIE,VT2,POWER,GAMMA5,ID2,IQ2,IA2)
           IA3=IA1-IA2
           GO TO 53
 57     IA=IA1
        ID=ID1
        IQ=IQ1
        VT=VT1
        GAMMA=GAMMA4*180/PI
C*************************************************************************************
C       Calculate the other output parameters that are consistent with the
```

```
C solution found above. See notes for derivation of these formulae.
C Division by 1000 indicates conversion of output to units with prefix
C kilo-. Output angles in degrees.
      EFF=1/(143*IA*IA*R1/POWER)
      PWRFCT=(POWER+3*IA*IA*R1)/3/VT/IA
      NCOS=EFF*PWRFCT
      BETA=ATAN(ID/IQ)*180/PI
      KVA=3*VT*IA/1000
      THRUST=THRUST/1000

C     Store outputs in their corresponding array and then continue on
C to the next field flux density value. Note that THRUST must be
C converted back to Newtons.
      C(I)=IA
      VA(I)=KVA
      BTA(I)=-BETA
      NCS(I)=NCOS
      VTEE(I)=VT
      THRUST=THRUST*1000
  234 CONTINUE
      WRITE(20,*) SPEED,(C(L),L=1,N)
      WRITE(21,*) SPEED,(VA(L),L=1,N)
      WRITE(22,*) SPEED,(BTA(L),L=1,N)
      WRITE(23,*) SPEED,(NCS(L),L=1,N)
      WRITE(24,*) SPEED,(VTEE(L),L=1,N)
      SPEED=SPEED+0.5
   45 CONTINUE
      STOP
      END
C*******************************************************************************
C     This subroutine solves for GAMMA by iteration using the secant method
C given the equivalent circuit, VIE, VT and POWER. Then IA is calculated.
C The result is correct to six decimal places. This method attempts to
C find a radian value of GAMMA that makes F2 and F3 zero.
      SUBROUTINE IFIND(XD,XQ,R1,VIE,VT,POWER,GAMMA,ID,IQ,IA)
      REAL XD,XQ,R1,VIE,VT,GAMMA,GAMMA2,GAMMA3,F2,F3,GMANEW,ID,IQ,IA
     1 ,POWER
      GAMMA2=0.1
      GAMMA3=0.15
      F2=(VT*(XD*SIN(GAMMA2)+R1*COS(GAMMA2))-R1*VIE)/(XD*XQ+R1*R1)*    (C.10)
     1    ((VT*(XQ*COS(GAMMA2)-R1*SIN(GAMMA2))-VIE*XQ)/(XD*XQ+R1*R1)*
     2    (XD-XQ)+VIE)*3-POWER
      F3=(VT*(XD*SIN(GAMMA3)+R1*COS(GAMMA3))-R1*VIE)/(XD*XQ+R1*R1)*    (C.10)
     1    ((VT*(XQ*COS(GAMMA3)-R1*SIN(GAMMA3))-VIE*XQ)/(XD*XQ+R1*R1)*
     2    (XD-XQ)+VIE)*3-POWER
  777 IF(ABS(GAMMA2-GAMMA3).LT.1E-6)GO TO 666
          GMANEW= GAMMA3-F3*(GAMMA2-GAMMA3)/(F2-F3)
          GAMMA2=GAMMA3
          F2=F3
          GAMMA3=GMANEW
          F3=(VT*(XD*SIN(GAMMA3)+R1*COS(GAMMA3))-R1*VIE)/
     1       (XD*XQ+R1*R1)*((VT*(XQ*COS(GAMMA3)-R1*SIN(GAMMA3))       (C.10)
     2       -VIE*XQ)/(XD*XQ+R1*R1)*(XD-XQ)+VIE)*3-POWER
          GO TO 777
  666 CONTINUE
      GAMMA=GMANEW
      IQ=(VT*(XD*SIN(GAMMA)+R1*COS(GAMMA))-R1*VIE)/(XD*XQ+R1*R1)       (C.7)
      ID=(VT*(XQ*COS(GAMMA)-R1*SIN(GAMMA))-VIE*XQ)/(XD*XQ+R1*R1)       (C.6)
      IA=SQRT(ID*ID+IQ*IQ)                                             (C.4)
C*******************************************************************************
      RETURN
      END
```

C.4 DEVELOPMENT OF FORMULAE USED IN "IMINBRK"

Figure C.2 shows a typical braking phasor polygon. The following equations can be derived:

$$V_t \cos\gamma = V_{ie} + I_d X_d - I_q R \qquad (C.11)$$

$$V_t \sin\gamma = I_q X_q + I_d R \qquad (C.12)$$

$$P = 3 V_t I_a \cos(\gamma + \beta) - 3 I_a^2 R \qquad (C.13)$$

Using these equations, together with (C.3) and (C.4), the following formulae can be developed in a manner similar to that for IMIN:

$$I_d = \frac{V_t (X_q \cos\gamma + R \sin\gamma) - X_q V_{ie}}{X_d X_q + R^2} \qquad (C.14)$$

$$I_q = \frac{V_t (X_q \sin\gamma - R \cos\gamma) + R V_{ie}}{X_d X_q + R^2} \qquad (C.15)$$

$$P = - 3 I_q [V_{ie} + I_d (X_d - x_d)] \qquad (C.16)$$

$$F2 = F3 = 0 = 3 \left[\frac{V_t (X_d \sin\gamma) - R \cos\gamma) + R V_{ie}}{X_d X_q + R^2} \right]$$

$$\left\{ V_{ie} + (X_d - X_q) \left[\frac{V_t (X_q \cos\gamma + R \sin\gamma) - X_q V_{ie})}{X_d X_q + R^2} \right] \right\}$$

$$- \left| P \right| \qquad (C.17)$$

The algorithm that computes the minimum current is presented in the comments for IMINBRK.

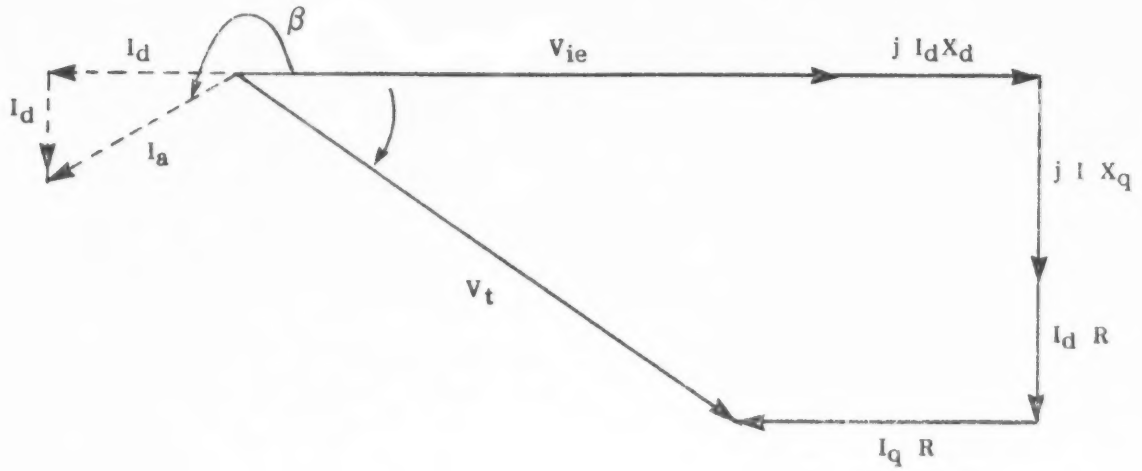

Figure C.2 Phasor polygon in the braking regime

C.5 PROGRAM "IMINBRK"

```
C                              IMINBRK
C*****************************************************************************
C       This program performs the same function as IMIN but in the braking
C region rather than the motoring region. It does not output
C efficiency-power factor product. The other outputs are the same as those
C from IMIN. This program has only three input field flux densities.
C*****************************************************************************
C       VARIABLES USED:                                    SAME AS IN IMIN
C*****************************************************************************
        REAL US,F,R1,XDM,XQM,XL,XSLOT,XTTOP,XEWIND,XHARM,XCENT,VIEBL1,
     1       VT,POWER,VIE,IA,ID,IQ,GAMMA,XD,XQ,EFF,PWRFCT,NCOS,PI,
     2       U0,F1,FREQ,THRUST,SPEED,BETA,KVA,IA1,IA2,VT1,VT2,GAMMA3,
     3       GAMMA4,IA3,GAMMA5,ID1,ID2,IQ1,IQ2,GAMMA2,F2,F3,GMANEW
        REAL BL(3),C(3),VA(3),BTA(3),VIEE(3)
        PI=3.141592654
        U0=4*PI*1E-7
        READ(11,*) US,F,R1,XDM,XQM,XL,XSLOT,XTTOP,XEWIND,XHARM,XCENT,
     1             VIEBL1
        XL=XSLOT+XTTOP+XEWIND+XHARM+XCENT

C       Input the number of values of BL that are to be used. Each value
C cycles through the thrust-speed profile once. Also input the maximum
C terminal voltage in volts and the values of BL in Tesla.
        READ(16,*) N,VTMAX
        DO 567 I=1,N
                READ(16,*) BL(I)
 567    CONTINUE

C       This loop will cycle through the speed range from 2 to 22 m/s.
        SPEED=2.
        DO 45 J=1,41

C!!!!!!!!!!!!!!!!!!!!!!!!!!!!!!!!!!!!!!!!!!!!!!!!!!!!!!!!!!!!!!!!!!!!!!!!!!!
C       This is the thrust-speed profile:
        IF(SPEED.LT.10.15) THEN
            THRUST=14000.
          ELSE
            THRUST=140000./SPEED
        END IF
C!!!!!!!!!!!!!!!!!!!!!!!!!!!!!!!!!!!!!!!!!!!!!!!!!!!!!!!!!!!!!!!!!!!!!!!!!!!
```

```
      POWER=THRUST*SPEED

C     Note that frequency is directly proportional to speed.
      FREQ=F*SPEED/US

C     Note that XD, XQ and VIE are frequency dependent.
      XD=(XDM+XL)*FREQ/F
      XQ=(XQM+XL)*FREQ/F

C     This loop will perform calculations with each field flux density
C value at the present operating speed.
      DO 234 I=1,N
      VIE=VIEBL1*BL(I)/F*FREQ
C*****************************************************************************
C     Solve for IA with terminal voltages of VTMAX and (VTMAX-0.2) volts.
C If IA is decreasing, then continue decrementing terminal voltage by 0.2
C volts until a minimum current is obtained.
      VT1=VTMAX
      CALL IFIND(XD,XQ,R1,VIE,VT1,POWER,GAMMA4,ID1,IQ1,IA1)
      VT2=VTMAX-0.2
      CALL IFIND(XD,XQ,R1,VIE,VT2,POWER,GAMMA5,ID2,IQ2,IA2)
      IA3=IA1-IA2
         VT2=VT2-0.2
 53   IF(IA3.LT.0.0)THEN
      GO TO 57
      END IF
         IA1=IA2
         VT1=VT2
         VT2=VT2-0.2
         GAMMA4=GAMMA5
         ID1=ID2
         IQ1=IQ2
         CALL IFIND(XD,XQ,R1,VIE,VT2,POWER,GAMMA5,ID2,IQ2,IA2)
         IA3=IA1-IA2
         GO TO 53
 57   IA=IA1
      ID=ID1
      IQ=IQ1
      VT=VT1

C     Output angles in degrees.
      GAMMA=GAMMA4*180/PI
C*****************************************************************************
C     Calculate the other output parameters that are consistent with the
C solution found above. See notes for derivation of these formulae.
      BETA=180+ATAN(ID/IQ)*180/PI
      KVA=3*VT*IA/1000

C     Store outputs in their corresponding array and then continue on
C to the next field flux density value.
      C(I)=IA
      VA(I)=KVA
      BTA(I)=BETA
      VTEE(I)=VT
 234  CONTINUE
      WRITE(60,*) SPEED,(C(L),L=1,N)
      WRITE(61,*) SPEED,(VA(L),L=1,N)
      WRITE(62,*) SPEED,(BTA(L),L=1,N)
      WRITE(64,*) SPEED,(VTEE(L),L=1,N)
      SPEED=SPEED+0.5
 45   CONTINUE
      STOP
      END
C*****************************************************************************
```

```
C       This subroutine solves for GAMMA by iteration using the secant method
C given the equivalent circuit, VIE, VI and POWER. Then IA is calculated.
C It will produce a result correct to six decimal places. This method
C attempts to find a radian value of GAMMA that makes F2 and F3 zero.
        SUBROUTINE IFIND(XD,XQ,R1,VIE,VI,POWER,GAMMA,ID,IQ,IA)
        REAL XD,XQ,R1,VIE,VI,GAMMA,GAMMA2,GAMMA3,F2,F3,GMANEW,ID,IQ,IA
     1  ,POWER
        GAMMA2=0.1
        GAMMA3=0.15
        F2=(VI*(XD*SIN(GAMMA2)-R1*COS(GAMMA2))+R1*VIE)/(XD*XQ+R1*R1)*    (C.17)
     1     ((VI*(XQ*COS(GAMMA2)+R1*SIN(GAMMA2))-VIE*XQ)/(XD*XQ+R1*R1))*
     2     (XD-XQ)+VIE)*3-POWER
        F3=(VI*(XD*SIN(GAMMA3)-R1*COS(GAMMA3))+R1*VIE)/(XD*XQ+R1*R1)*    (C.17)
     1     ((VI*(XQ*COS(GAMMA3)+R1*SIN(GAMMA3))-VIE*XQ)/(XD*XQ+R1*R1))*
     2     (XD-XQ)+VIE)*3-POWER
 777    IF(ABS(GAMMA2-GAMMA3).LT.1E-6)GO TO 666
            GMANEW=GAMMA3-F3*(GAMMA2-GAMMA3)/(F2-F3)
            GAMMA2=GAMMA3
            F2=F3
            GAMMA3=GMANEW
            F3=(VI*(XD*SIN(GAMMA3)-R1*COS(GAMMA3))+R1*VIE)/              (C.17)
     1        (XD*XQ+R1*R1)*((VI*(XQ*COS(GAMMA3)+R1*SIN(GAMMA3))
     2        -VIE*XQ)/(XD*XQ+R1*R1)*(XD-XQ)+VIE)*3-POWER
            GO TO 777
 666    CONTINUE
        GAMMA=GMANEW
        ID=(VI*(XD*SIN(GAMMA)-R1*COS(GAMMA))+R1*VIE)/(XD*XQ+R1*R1)       (C.15)
        IQ=(VI*(XQ*COS(GAMMA)+R1*SIN(GAMMA))-VIE*XQ)/(XD*XQ+R1*R1)       (C.14)
        IA=SQRT(ID*ID+IQ*IQ)                                             (C.4)
C*****************************************************************************
        RETURN
        END
```

APPENDIX D

SIMULATION OF THE HLSM RUNNING ON A DUTY CYCLE

D.1 CAPABILITY OF PROGRAMS

After using the programs in Appendix C to determine the optimal control angle for specified maximum thrust requirements, one can simulate the performance of an HLSM over a duty cycle. The programs BETA and BETABRK, included in this appendix, were formulated to compute the terminal characteristics of the HLSM over a duty cycle as a function of time and/or distance. BETA applies to the motoring regime; BETABRK to the braking regine. The programs use the following input quantities:

- a set of equivalent-circuit parameters provided by EQUIVCIRC or by direct input
- a control-angle/speed characteristic that is chosen to minimize current under maximum expected thrust conditions
- a set of paired thrust and speed points that are functions of distance and/or time
- a maximum field excitation/speed characteristic
- a maximum terminal voltage.

The programs use the above data to solve for a phasor polygon at each operating point that has the maximum terminal voltage subject to the constraint that field excitation is less than or equal to its maximum value. The outputs from BETA are: terminal voltage, armature current, field excitation, electrical input power, apparent power, and armature efficiency/power factor product. The outputs from BETABRK are: terminal voltage, armature current, field excitation, electrical output power, and apparent power.

D.2 DEVELOPMENT OF FORMULAE USED IN "BETA"

From Figure C.1, the following equation can be derived:

$$V_t^2 = (V_{ie} + I_q R - I_d X_d)^2 + (I_d R + I_q X_q)^2 \qquad (D.1)$$

Also, equation (C.9) can be rewritten:

$$V_{ie} = \frac{P}{3 I_q} + I_d (X_d - X_q) \qquad (D.2)$$

Now, (C.3) and (D.2) can be used to eliminate I_d and V_{ie} from (D.1) to obtain a quadratic in I_q^2.

$$I_q = \sqrt{\frac{-(BB) - \sqrt{(BB)^2 - 4(AA)(CC)}}{2(AA)}} \qquad (D.3)$$

where: $$AA = \frac{X_q^2 + R^2}{\cos^2 \beta} \qquad (D.4)$$

$$BB = \frac{2P}{3} (R - X_q \tan \beta) - V_t^2 \qquad (D.5)$$

$$CC = \frac{P^2}{9} \qquad (D.6)$$

The root of the quadratic is chosen to give minimum armature current.

D.3 PROGRAM "BETA"

```
C                              BETA
C*****************************************************************************
C       This program takes the equivalent circuit data for the HLSM
C provided by EQUIVCIRC from FOR011.DAT. A tabulation of points on the
C required thrust vs. speed characteristic is also given. Using each
C input speed, a control angle (the angle between the armature current
C and the e-axis) that is best suited for an eleven pole machine is
C calculated. These inputs allow a fourth degree polynomial expression
C in IQ to be solved for any given terminal voltage.
C       The program begins computation with the maximum terminal voltage.
C After computing IQ and the equivalent field flux density (BL1), the
C program compares BL1 with its maximum possible value. If BL1 is less
C than its maximum, then a realistic solution has been obtained. If not,
C then the terminal voltage is decremented and the iteration process
C continues until a realistic solution is obtained.
C       The following parameters are calculated by the program: output
C power, armature current, complex power (KVA), input power from the line,
C angle between the terminal voltage and the e-axis, field excitation
C voltage, efficiency (of armature only), power factor, and the efficiency
C of the whole HLSM system including power conditioner.
```

```
C       The user can alter the control angle versus speed characteristic
C and the maximum field flux density by changing the statements surrounded
C by the lines of exclamation marks.
C!!!
```

```
C       Solve for IQ with a VT=VTMAX. Then check that BL1 is less than
C BLMAX. If BL1 is greater than BLMAX, decrement VT by 0.2 volts and repeat
C until a solution is obtained with BL1 less than BLMAX.
        VT=VTMAX
 57     CALL IQFIND(XD,XQ,R1,BETA,VT,POWER,ID,IQ,IA)
        VIE=POWER/3/IQ+IQ*TAN(BETA)*(XD-XQ)                              (D.2)

C       Note the frequency dependence of VIE.
        BL1=VIE/VIEBL1*F/FREQ
        IF(BL1.GT.BLMAX)THEN
        VT=VT-0.2
        GO TO 57
        END IF
C*******************************************************************************
C       Calculate the other output parameters that are consistent with the
C solution found above. See notes for derivation of these formulae.
C Division by 1000 indicates conversion of output to units with the prefix
C kilo-. In the calculation of EFF1, the following losses are assumed:
C 5% of the power conditioning unit kW and 12.74 kW for the Joule heating
C of the field coil. Output angles in degrees.
        GAMMA=(ATAN((IQ*XQ+ID*R1)/(VIE+IQ*R1-ID*XD)))*180/PI
        EFF=1/(1+3*IA*IA*R1/POWER)
        PWRFCT=(POWER+3*IA*IA*R1)/3/VT/IA
        NCOS=EFF*PWRFCT
        BETA=BETA*180/PI
        KVA=3*VT*IA/1000
        THRUST=THRUST/1000
        PIN=(POWER+3*IA*IA*R1)/1000
        POWER=POWER/1000
        EFF1=POWER/(PIN+12.74)/1.05
C*******************************************************************************
        WRITE(20,*) SPEED,THRUST,POWER,PIN,KVA,ID,IQ,IA,VT,GAMMA,BETA,BL1,
     1              BLMAX,VIE,NCOS,PWRFCT,EFF,EFF1
 456    CONTINUE
        STOP
        END
C*******************************************************************************
C       This subroutine solves a fourth degree polynomial for IQ using the
C quadratic formula given the equivalent circuit, BETA, POWER and VT. The
C quadratic formula solves for IQ**2. See notes for derivation of formulae.
        SUBROUTINE IQFIND(XD,XQ,R1,BETA,VT,POWER,ID,IQ,IA)
        REAL XI,XQ,R1,VT,ID,IQ,IA,POWER,BETA,AA,BB,CC,ROOT,IQSQ
        IQSQ=IQ**2
C*******************************************************************************
        AA=(R1*R1+XQ*XQ)/COS(BETA)/COS(BETA)                             (D.4)
        BB=2.*(POWER/3.*(R1-XQ*TAN(BETA))-VT*VT                          (D.5)
        CC=(POWER/POWER/9.                                               (D.6)
        ROOT=BB*BB-4.*AA*CC

C       Check for complex roots.
        IF(ROOT.LT.0.) THEN
                WRITE(6,*)'NO ROOT FOUND'
                GO TO 11
        END IF

C       This root gives the solution with the smallest current.
        IQSQ=-(BB+SQRT(ROOT))/2/AA                                       (D.3)

C       Check that IQ**2 is greater than zero.
        IF(IQSQ.LT.0.) THEN
                WRITE(6,*)'NO ROOT FOUND'
                GO TO 11
        END IF

C       Calculate IQ, ID and IA.
        IQ=SQRT(IQSQ)
        ID=IQ*TAN(BETA)                                                  (D.3)
        IA=SQRT(IQ*IQ+ID*ID)                                             (D.4)
C*******************************************************************************
 11     RETURN
        END
```

D.4 DEVELOPMENT OF FORMULAE USED IN BETABRK

From Figure C.2, the following equation can be derived:

$$V_t^2 = (V_{ie} + I_d X_d - I_q R)^2 + (I_q X_q + I_d R)^2 \qquad (D.7)$$

Also, (C.16) can be rewritten:

$$V_{ie} = \frac{|P|}{3 I_q} - I_d (X_d - X_q) \qquad (D.8)$$

(C.3), (D.7) and (D.8) again lead to the following solution for I_q:

$$I_q = \sqrt{\frac{-(BB) - \sqrt{(BB)^2 - 4(AA)(CC)}}{2(AA)}} \qquad (D.3)$$

where: $$AA = \frac{X_q^2 + R^2}{\cos^2\beta} \qquad (D.4)$$

$$BB = \frac{2|P|(X_q \tan\beta - R)}{3} - V_t^2 \qquad (D.5)$$

$$CC = \frac{P^2}{9} \qquad (D.6)$$

The root of the quadratic is chosen to given minimum armature current.

D.5 PROGRAM "BETABRK"

```
C                                  BETABRK
C*************************************************************************
C       This program performs the same function as BETA, but for the
C braking region rather than the motoring region. It does not output
C efficiency or power factor of the armature. The other outputs are the
C same as those from BETA. EFF1 is redefined for the HLSM acting as a
C regenerative brake.
C*************************************************************************
C       VARIABLES USED: (SAME AS IN BETA EXCEPT)
C       REGENERATED POWER RETURNED TO THE LINES                  POUT
C*************************************************************************
        REAL US,F,R1,XDM,XQM,XL,XSLOT,XTTOP,XEWIND,XHARM,XCENT,VIEBL1,
     1       VT,POWER,VIE,IA,ID,IQ,GAMMA,XD,XQ,PI,UO,FREQ,THRUST,SPEED,
     2       BETA,KVA,BLMAX,AA,BB,CC,ROOT,IQSQ,POUT,EFF1
        PI=3.141592654
        UO=4*PI*1E-7
        READ(11,*) US,F,R1,XDM,XQM,XL,XSLOT,XTTOP,XEWIND,XHARM,XCENT,
     1             VIEBL1
        XL=XSLOT+XTTOP+XEWIND+XHARM+XCENT

C       Input N, the number of thrusts and speeds in the list and VTMAX.
        READ(16,*) N,VTMAX
        DO 456 I=1,N

C       Repeat the calculation for each thrust and speed on the list.
C Input speed in metres per second and the absolute value of thrust in
C Newtons.
        READ(16,*) SPEED,THRUST
        POWER=THRUST*SPEED

C       Note that frequency is directly proportional to speed.
        FREQ=F*SPEED/US

C       Note that XD and XQ are frequency dependent.
        XD=(XDM+XL)*FREQ/F
        XQ=(XQM+XL)*FREQ/F

C*************************************************************************
C       Find BLMAX and BETA (degrees) given the speed.
        BLMAX=0.5-SPEED/200
        IF(SPEED.LT.12.1) THEN
                BETA=190.*PI/180.
           ELSE
                BETA=((0.26*SPEED-13.34)*SPEED+312.64)*PI/180.
        END IF
C*************************************************************************

C       Solve for IQ with VT=VTMAX. Then check that BL1 is less than
C BLMAX. If BL1 is greater than BLMAX, decrement VT by 0.2 volts and repeat
C until a solution is obtained with BL1 less than BLMAX.
        VT=VTMAX
 57     CALL IQFIND(XD,XQ,R1,BETA,VT,POWER,ID,IQ,IA)
        VIE=POWER/3/IQ-IQ*TAN(BETA)*(XD-XQ)
        BL1=VIE/VIEBL1*F/FREQ                                    (D.8)
        IF(BL1.GT.BLMAX)THEN
        VT=VT-0.2
        GO TO 57
        END IF
C*************************************************************************
C       Calculate the other output parameters that are consistent with the
C solution found above. See notes for derivation of these formulae.
```

```
C Division by 1000 indicates conversion of output to units with the prefix
C kilo-. In the calculation of EFF1, the following losses are assumed:
C 5% of the power conditioning unit kW and 12.74 kW for the Joule heating
C of the field coil. Output angles in degrees.
      GAMMA=ATAN((IQ*XQ+ID*R1)/(VIE-IQ*R1+ID*XD))
      POUT=3*VT*IA*COS(BETA+GAMMA)/1000
      POWER=POWER/1000
      BETA=BETA*180/PI
      GAMMA=GAMMA*180/PI
      KVA=3*VT*IA/1000
      EFF1=-(POUT/1.05+12.74*1.05)/POWER
      THRUST=THRUST/1000
C*************************************************************************
      WRITE(30,*) SPEED,THRUST,POWER,POUT,KVA,ID,IQ,IA,VT,GAMMA,BETA,BL1,
     1            BLMAX,VIE,EFF1
 456  CONTINUE
      STOP
      END
C*************************************************************************
C     This subroutine solves a fourth degree polynomial for IQ using the
C quadratic formula given the equivalent circuit, BETA,POWER and VT. The
C quadratic formula solves for IQ**2. See notes for derivation of formulae.
      SUBROUTINE IQFIND(XD,XQ,R1,BETA,VT,POWER,ID,IQ,IA)
      REAL XD,XQ,R1,VT,ID,IQ,IA,POWER,BETA,AA,BB,CC,ROOT,IQSQ
C     IQSQ=IQ**2
C*************************************************************************
      AA=(R1*R1+XQ*XQ)/COS(BETA)/COS(BETA)                          (D.4)
      BB=2.*POWER/3.*(XQ*TAN(BETA)-R1)-VT*VT                        (D.9)
      CC=POWER*POWER/9.                                             (D.6)
      ROOT=BB*BB-4.*AA*CC

C     Check for complex roots.
      IF(ROOT.LT.0.) THEN
            WRITE(6,*)'NO ROOT FOUND'
            GO TO 11
      END IF

C     This root gives smaller armature current.
      IQSQ=-(BB+SQRT(ROOT))/2/AA                                    (D.3)

C     Check that IQ**2 is greater than zero.
      IF(IQSQ.LT.0.) THEN
            WRITE(6,*)'NO ROOT FOUND'
            GO TO 11
      END IF

C     Calculate IQ, ID and IA.
      IQ=SQRT(IQSQ)
      ID=IQ*TAN(BETA)                                               (D.3)
      IA=SQRT(IQ*IQ+ID*ID)                                          (D.4)
C*************************************************************************
 11   RETURN
      END
```

APPENDIX E

PERMANENT MAGNET HLSMS

E.1 Previous Work

A small Alnico permanent magnet HLSM was constructed and tested (Atherton and Fraser, 1982) in order to gain experience with these motors. The conclusions at that time were relatively pessimistic, namely that:

(i) demagnetization is a problem with Alnico magnets

(ii) the relatively poor mechanical tolerance typical of Alnico magnets can lead to difficulties when used in large numbers to build an HLSM

(iii) Alnico magnets tend to increase the motor mass and should only be used to supply part of the mmf required for the field

(iv) since the field coil power may be less than the armature power requirements, the savings resulting from Alnico magnets may only be small.

E.2 Changes During the Present Study

Two important changes have occurred during the present study which, together, may do much to reverse the previous pessimism: the improved availability, geometric configuration and cost of cobalt-rare earth magnets, and the change from a transverse flux to a diagonal flux geometry for the permanent magnet HLSM.

Comparative typical demagnetization curves for Alnico, Ferrite and Cobalt-Samarium magnets are shown in Figure E.1. It is clear that Cobalt-Samarium resists demagnetization even better than ferrite and produces a flux density only slightly less than Alnico at its maximum energy density. Recent advances in the commercial application of powder metallurgy now enable cobalt rare-earth magnets of reasonable size (about 10 cm diameter) to be fabricated at modest cost, though

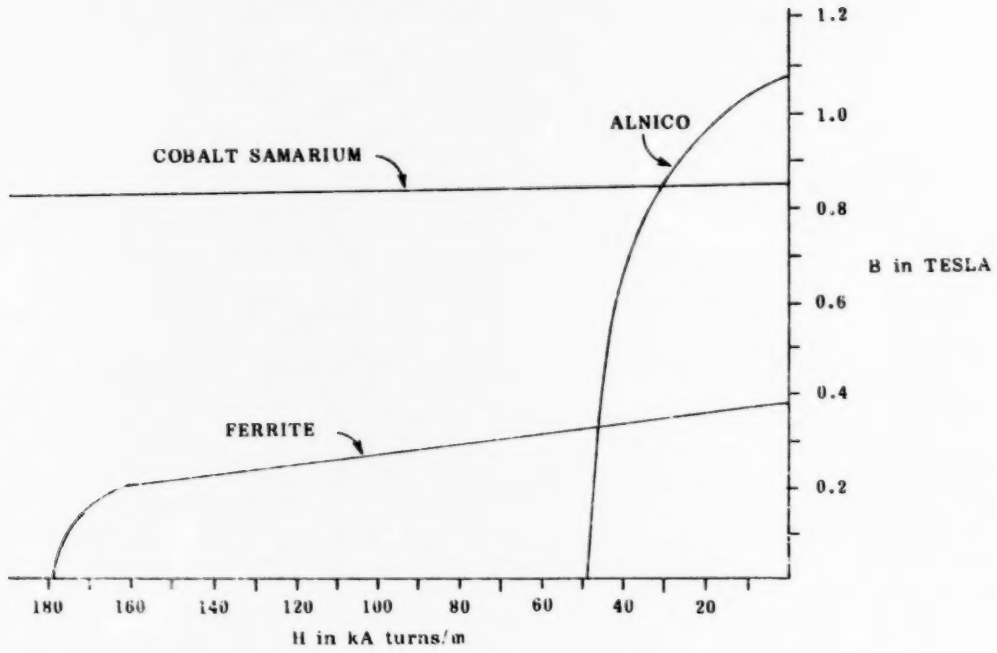

Figure E.1 Demagnetization curve for Alnico, Cobalt-Samarium, and Ferrite permanent magnets

still somewhat higher than ferrites. Cobalt rare-earth magnets are now a reasonable proposition for HLSMs, and could be used in a test motor.

The previous study of permanent magnet HLSMs used a transverse flux geometry with spacers between each tooth stack section. The use of permanent magnets, which have lower flux densities than can be achieved in iron, required an increased cross-section of the magnetic circuit, which was then tapered at the teeth to obtain air gap flux density similar to a comparable iron-cored HLSM. This required increasing the stack height or width, resulting in an increase in motor mass (see Atherton and Fraser, 1982, Figures 2 and 3). This was essentially a two-dimensional geometry. The diagonal flux motor enables the use of the third dimension, with permanent magnets running the length of the motor covering both teeth and slots, and having their flux density

concentrated into just the teeth. The simple conventional armature winding, without the "figure-of-eight" crossover required in a transverse flux machine, also takes advantage of the very high magnetic induction, H, available with cobalt-rare earth magnets and allows the two sides of the motor to be moved closer, since no central region need be left for crossovers.

E.3 Cobalt-Rare Earth Permanent Magnet Motor Design Concept

Since the potential of a cobalt-rare earth permanent magnet HLSM only became apparent very late in this study, no detailed designs have yet been investigated. Instead, consideration has been given to what changes should be made to the design in order to incorporate permanent magnets and what major results could be expected.

Transverse and longitudinal sections of the conceptual cobalt-rare earth permanent magnet HLSM are shown in Figure E.2. The changes to the study final design are as follows:

(1) The field coils are omitted and a strip of cobalt-rare earth permanent magnet 1.3 to 4 cm deep runs the full length of each side of the motor. (The exact depth depends on the cobalt-rare earth magnet used, and is an important design parameter.) The permanent magnets provide an mmf equivalent to that of the final design field coils.

(2) The slot width/tooth width ratio is changed from 1:2 to 2:1 to ensure that the magnet flux density is adequate to saturate the teeth. The number of armature conductors per slot is doubled.

These changes are likely to have the following effects:

(i) The tooth flux density is assumed to be unchanged (because the armature mmf remains smaller than the field mmf) and consequently the tooth flux is halved (because the width is halved). The armature flux linkage is unchanged (because the armature turns are doubled). Thrust and armature-induced voltage, therefore, remain approximately unchanged.

(ii) The doubling of the armature turns per phase will increase leakage reactance. This, and the reduced excitation flux modulation, will result in a lower operational power factor. The increased length of armature winding will lead to some loss in efficiency.

(iii) Because of the reduced flux, yoke height and the depth of the guideway can be reduced.

(iv) Because there is no space required for field windings, the sides of the motor can be brought closer together (until leakage flux becomes a serious problem).

(v) Because of the increased cross-section of the armature coils, there will be a tendency for them to run hotter. However, the permanent magnet design now has an unobstructed central slot which would appear ideally suited to supplying forced-air cooling to the armature windings. These changes are expected to compensate each other.

E.4 RESULTS

The principal physical changes to the final reference design resulting from the use of cobalt-rare earth permanent magnets would appear to be as follows:

(i) motor mass would be reduced from 1,410 kg to 830 kg (steel and magnets, 610 kg; armature, 220 kg)

(ii) the HLSM size will change:

	2.35 m long		2.25 m long
from:	x 0.65 m wide	to:	x 0.60 m wide
	x 0.18 m high		x 0.13 m high

(iii) the depth of the guideway component will be reduced from 8 cm to 4 cm

(iv) the power dissipation per motor will be reduced from 19 kW to about 13 kW.

The reductions in the motor mass and height are particularly significant, because these appear to be major problems with an HLSM when

compared to an LIM. It should be stressed that these potential reductions occur partly as a result of substituting magnets for the field coils and partly because of the change from wide teeth to wide slots. The consequence, however, will be a lower $\eta \cos \phi$ as compared to that of the study reference design.

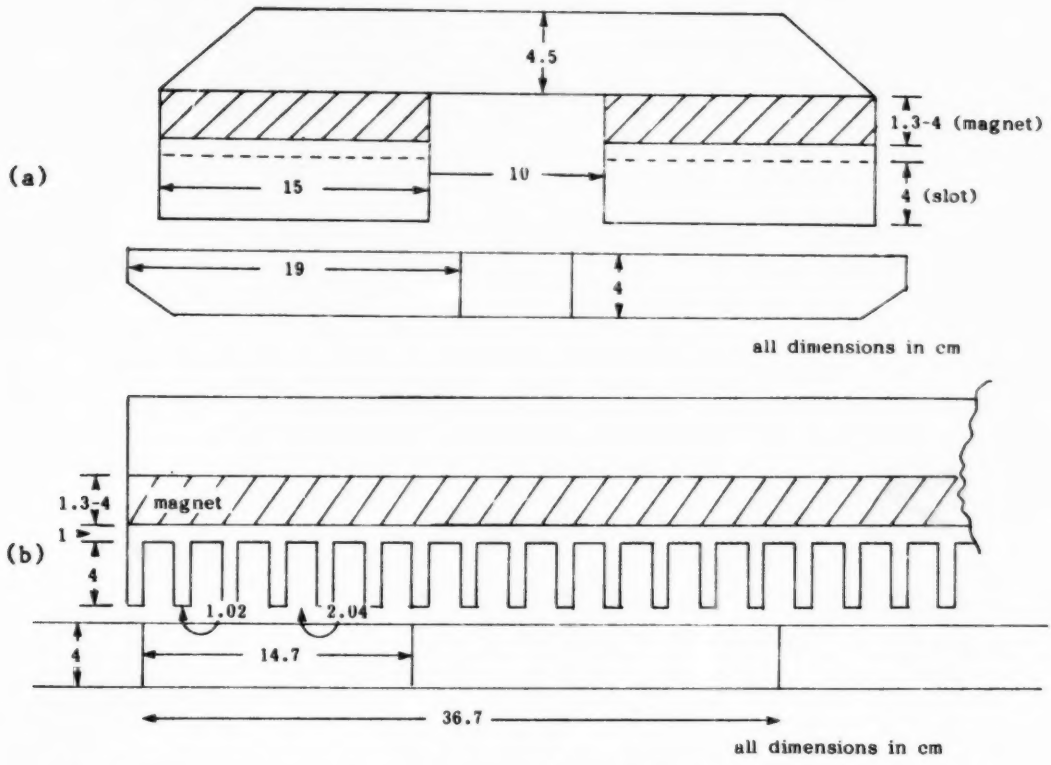

Figure E.2 A conceptual design of an HLSM with cobalt-rare earth permanent magnet excitation:
(a) transverse section
(b) longitudinal section

E.5 DISCUSSION

E.5.1 ISPS

It has been suggested that the high normal forces typically associated with an HLSM make it a natural candidate for integrated suspension and propulsion systems. This necessitates field control which is, of

course, not possible with a permanent magnet HLSM. The addition of a control field coil to a permanent magnet HLSM does not appear to be a viable solution because it would have little effect on the permanent magnet flux density, particularly for cobalt-rare earth magnets.

E.5.2 Slot Width/Tooth Width Ratio

Changing this ratio from 1:2 to 2:1 to allow for the relatively low permanent magnet flux density will approximately halve the air gap field modulation, necessitating a doubling of armature mmf to maintain the thrust capability. This will need to be evaluated in detail. Previous comparative design studies suggested that there should be a slight increase in thrust and a decrease in normal force (Atherton, 1982, Figure 15).

The final reference design is unusual in its use of a slot/tooth width ratio of 1:2. Other HLSM designs have aimed for a higher linear current density in the armature, typically by using ratios of 1:1 or greater (the G.E. motor used 1.17:1). Higher ratios have the important additional requirement of reducing the iron required, i.e. reducing the motor mass and height and the guideway rail depth. This is, therefore, a very significant parameter and is worth further study.

E.5.3 Permanent Magnet Performance

The performance of a permanent magnet HLSM is more difficult to calculate than that of an HLSM using field coils because of the non-linear demagnetizing characteristic of the permanent magnet. For a material like cobalt-rare earth, there is a tendency to operate in a constant field mode, producing low field modulation. There are several possible approaches to this potential problem:

- Use either guideway magnets and a moving armature, or use vehicle-borne magnets and a wound guideway armature. Neither of these approaches is thought to be economically viable in the present situation.

- Divert the flux through an alternative path (as in a magnetic chuck). Since the "alternate path" must not thread the armature windings, this proposal seems impactical in this instance.

- Operate the magnets with a linear demagnetization/recoil response. This seems to be the best solution in this case, but will require careful material selection or specification, careful motor design and optimization of the magnet recoil lines.

Permanent magnet proposals naturally raise concerns about the motor collecting tramp iron from the guideway. Permanent magnets cannot be de-energized, but even high-strength ones can be easily cleared of ferromagnetic pick-up by shear rather than tensile forces. The motor magnets are well protected. If tramp iron on the guideway proves to be a problem, a sweeper magnet can be mounted ahead of the motors. This problem is not likely to prove serious.

E.6 CONCLUSIONS

A high-strength cobalt-rare earth permanent magnet version of the HLSM now appears to merit more detailed study. It is recognized that a lot more effort will be required to select the optimum magnet specifications and operating points.

The potential advantages of a permanent magnet HLSM are a significant reduction in motor mass and height compared with a conventional HLSM, which could make it a stronger competitive alternative to the LIM for ICTS. However, the permanent magnet HLSM is not likely to operate with as high an efficiency/power factor product as the reference design presented in the body of this report, and integrated suspension/propulsion is no longer an option.

POOR
QUALITY
ORIGINAL